

Dissertation zur Erlangung des Doktorgrades

der Fakultät für Chemie und Pharmazie

der Ludwig-Maximilians-Universität München

Nitrogen-rich and Thiophene-containing Covalent Organic Framework Bulk and Films

—

Synthesis, Properties and Function

Laura Frey

aus

Ingolstadt, Deutschland

2022

Erklärung

Diese Dissertation wurde im Sinne von § 7 der Promotionsordnung vom 28. November 2011 von Herrn Prof. Dr. Thomas Bein betreut.

Eidesstattliche Versicherung

Diese Dissertation wurde eigenständig und ohne unerlaubte Hilfe bearbeitet.

München, den 12.09.2022

(Laura Frey)

Dissertation eingereicht am: 12.09.2022

1. Gutachter: Prof. Dr. Thomas Bein

2. Gutachter: Prof. Dr. Achim Hartschuh

Mündliche Prüfung am: 24.10.2022



**Nitrogen-rich and Thiophene-containing
Covalent Organic Framework Bulk and
Films**

Synthesis, Properties and Function

Laura Frey

2022

Acknowledgement

I would like to use this platform, to thank everyone who supported me during the work for my thesis and who helped with the completion of the dissertation.

I wish to thank my PhD supervisor Prof. Thomas Bein, for giving me the opportunity to accomplish my dissertation in his research group. Thank you, for your support throughout my PhD in your group and for meaningful discussions during (sub)group meetings.

A big thank you goes to Dr. Dana Medina for being my central contact person and advisor during my PhD. Thank you so much for all the insightful discussions, for guiding my way through all the different projects and of course for the proof-reading of my manuscripts and this thesis. I very much enjoyed working on such a diverse research field. Thank you for always taking time for our nearly daily phone calls, for always having an open ear and of course for supporting me throughout my whole PhD 😊!

Furthermore, I want to thank Prof. Achim Hartschuh for taking over the second evaluation of my thesis.

Thank you to the rest of my examination board: Prof. Konstantin Karaghiosoff, Prof. Thomas Klapötke, Prof. Knut Müller-Caspary, Prof. Andreas Kornath.

I also want to thank all my collaboration partners. First, Roman Guntermann for the nice collaboration on our different projects. Thanks for the great teamwork, I really enjoyed our time together in the lab. Next, I want to thank Dr. Laura Salonen and her students Jenni Jarju, Soraia P. S. Fernandes, Krystal M. Cid-Seara and Orlando Oliveira for the cooperation on the review chapter and the two very interesting Dione- and Aza-COF projects. Thank you to my cooperation partners at the University of Göttingen Jonas Pöhls and Prof. Thomas Weitz and at the University of Erlangen Dr. Matthias Hennemann and Prof. Timothy Clark for the cooperation on the Ninja Star project. Also, I want to thank Alexander Biewald for supporting me with complementary PL measurements.

A big thank you also goes to Tina Reuther and Corinna Heidt for keeping everything running smoothly in our group and of course also to Markus Döblinger and Steffen Schmidt for the great TEM and SEM measurements.

Further, I also want to thank my lab mates Derya Bessinger, Stephan Reuter, Katharina Muggli, Roman Guntermann, Laura Spies, Melisande Kost for the nice times we had in the lab such that with the right company even tiring column chromatographies became fun 😊. A big thank you goes to the COF/MOF subgroup and of course to the whole AK Bein for the hiking trips, barbecue parties and all activities

outside of the university. I want to thank my office colleagues Roman Guntermann, Andreas Weis, Rik Hoojer and Apeksha Singh (Office 27) for all the interesting discussions we had on all kinds of topics and for always taking time to chat 😊. I was really lucky to have you as my office colleagues. I want to thank Marcella Günther (Team Career) for always whining together with me and for pushing through the last part of the PhD together. Next, of course I also want to thank the guys of our South Tyrol trip (Patricia Scheurle, Laura Spies, Andreas Weis and Maximilian Sirtl). I really enjoyed our trips together. A big thank you also goes to Patricia Scheurle who became a really good friend during my PhD. Thank you for all the breaks together, the nice work and most of all thank you for our friendship outside of the university.

I especially want to thank Tim for his tireless support during the last years. Thank you for always cheering me up, for always having an open ear and for just being there for me.

Last but not least, I want to thank my family. Thank you for your support and love all these years! Without you, this would not have been possible.

Abstract

Covalent Organic Frameworks (COFs) have been explored as an intriguing class of crystalline, highly ordered, porous polymers that are formed by the condensation of purely organic aromatic building blocks. The covalent bond-formation is slightly reversible which allows for building block assembly faults to be corrected, and thereby highly structurally defined products are formed. Tailor-made COFs are accessible using a large variety of organic building blocks. Owing to that, key properties such as pore structure, optical properties and conjugation of monomers can be tailored to feature specific functionalities by fine-tuning of the chemical structure and geometry of the building blocks which in turn enables their utilization for a large variety of potential applications such as gas storage, sensing, catalysis, and separation. Even though, COFs have been studied for almost 20 years now, there are still challenges that need to be overcome in order to increase the number of possible and functional frameworks. Synthesizing large aromatic building blocks always requires their solubility, shape as well as their packing in the COF to be considered. Therefore, during the course of this thesis, new synthetic methodologies are introduced that can help diversifying the field of COFs.

Typically, the functionalities of the resulting COF structures can be altered by using different approaches such as (i) pre-modification, i.e., using building blocks that have been modified prior to the framework formation or (ii) post-synthetic modification (PSM) strategies by installing chemical functional groups at the COFs' pore walls which serve as anchor groups for subsequent modification resulting in ordered frameworks. Thereby, the design of new synthetic methods or design principles that may be generalized for many molecular frameworks, especially to alter optical properties is of high interest to advance the progress in the field of COFs. In this thesis, the main focus lies on studying the impact of fundamental structural alterations achieved *via* different synthetic approaches on the overall photophysical properties and the electrical properties of 2D COFs.

Addressing these aspects, in the first part of the thesis (chapter 3 and 4), the focus is on the synthesis of boronate ester-azaacene-based COFs. Thereby, different strategies are described for the synthesis of pyrene fused azaacene containing functional COFs. The first part of this thesis (chapter 3) describes a post-synthetic modification strategy for the extension of building block π -conjugation in covalent organic framework (COF) backbones. Thereby, by using the chemistry of the pyrene dione-COF, known as Dione-COF, the dione moieties at the pore walls were allowed to react with different di-amines, namely *o*-phenylenediamine (Ph) and 2,3-diaminonaphthalene (Naph), to form extended pyrene-fused azaacenes. Optimized catalyst-free reaction conditions yielded COFs post-synthetically modified with up to 33% conversion, termed Dione-Ph- and Dione-Naph-COF, and corresponding intriguing optical

properties such as a red-shift of the absorption onsets for Dione-Ph-COF and Dione-Naph-COF compared to the pristine Dione-COF, which is attributed to the extension of π -conjugation of part of the dione moieties.

Following this conceptual line of thought and to boost the conversion yield of the reaction of dione functional groups to azacenes introduced in chapter 3, in chapter 4, the development of a three-component synthesis approach is described which was used for the formation of COFs containing extended, fused aromatics in high yield. Thereby, using two types of building block components, namely the pyrene dione-diboronic acid as aggregation inducing COF precursor, and di-amines such as *o*-phenylenediamine (Ph), 2,3-diaminonaphthalene (Naph) or (1*R*,2*R*)-(+)-1,2-diphenyl-ethylenediamine (2Ph) as lateral extending building units resulted in the formation of pyrene fused azaacenes in high yield of 100 %. Including HHTP in the reaction mixture as a catechol counterpart, namely by three-component synthesis, enables the formation of boronate ester COF products comprising pyrene-fused azaacenes building blocks. Thereby, COFs featuring long-range order and high surface areas coined Aza-Ph-, Aza-Naph- and Aza-2Ph-COF were obtained. Strikingly, using the three-component approach, framework formation and functionalization take place in parallel reactions and therefore building block and COF assembly occurs *in chorus*. Importantly, this methodology was applicable to the rather labile boronate-ester based COF, whereas framework formation was not hindered despite the use of strong nucleophiles present in the reaction mixture. In the chapter, a systematic study of the three-component synthesis traced by NMR is given. Further, highly oriented thin films of the functional COFs featuring nanostructured surfaces were successfully grown on different substrates by applying the non-epitaxial solvothermal *in situ* approach and the newly developed three-component synthesis. With the novel three-component approach, systematic modification of the photophysical properties of Dione-COF is in reach. Thereby, the main absorption maxima are red-shifted with Aza-2Ph-COF exhibiting the absorption maximum with the shortest wavelength at around 420 nm, followed by Aza-Ph-COF at around 450 nm and lastly Aza-Naph-COF with an absorption maximum at around 480 nm, which was attributed to the extension of the π -conjugation.

One of the potential issues of boronate ester-based COFs is their instability in aqueous/ acidic media or towards moisture. Therefore, in chapter 5 a new class of COFs which instead feature vinylene linkages is introduced. Here, we show the synthesis of two novel highly crystalline, porous, luminescent and stable vinylene-linked COFs, termed TMT BDTOEt and TMT BDTOPr, which were synthesized using a Knoevenagel polycondensation reaction with trimethyltriazine (TMT) and different alkoxy-functionalized benzodithiophene (BDT) aldehydes as building blocks. Subsequently, the frameworks were grown successfully as porous and highly crystalline films on different substrates using the vapor-

assisted conversion (VAC) method that was already established in our group for boronate-ester based COFs but has not yet been shown for vinylene-linked COFs. The resulting films showed interesting properties upon interaction with different solvents. The addition of a droplet of ethanol or water led to a drastic blue-shift in the photon emission wavelength of up to 200 nm, changing from 690 nm for the pristine TMT COF to 480 nm upon interaction with ethanol. Further, lifetimes of the excited states were strongly enhanced upon interaction with solvents, increasing from 0.7 ns (pristine TMT BDTOPr COF) to 9.97 ns (addition of water) for the largest contributions.

The last part of the thesis (chapter 6) deals with charge carrier migration in covalent organic frameworks (COFs) which is a key aspect for the incorporation of this class of porous materials in advanced applications where COFs serve as active materials. To utilize COFs in devices, unraveling COFs' conductive pathways and mechanisms is vital and still a great challenge. In this chapter, the synthesis of novel electroactive COFs based on a newly synthesized thiophene-extended benzotrithiophene (BTT) building block is described. In combination with triazine-based amines we obtained novel, highly crystalline and porous imine-linked COFs, BTT TTA and BTT TTTBA, with distorted hexagonal pores and surface areas as high as 932 m² g⁻¹ and 1200 m² g⁻¹, respectively. Moreover, the frameworks were grown successfully on different substrates as highly oriented thin films, with varying thicknesses from 320 to 590 nm for BTT TTA and 290 to 480 nm for BTT TTTBA, as indicated by grazing incidence diffraction (GID) and electron microscopy analyses. BTT films on quartz substrates show light absorption in the 300-600 nm spectral region and emission at 740 and 705 nm. Room-temperature in-plane electrical conductivity of up to 10⁻⁴ S m⁻¹ was measured for both COFs. Temperature-dependent electrical conductivity measurements indicate activation energies of ~123.3 meV for BTT TTA and ~137.5 meV for BTT TTTBA and trap-dominated charge transport *via* a hopping mechanism for both COFs. Moreover, conductive atomic force microscopy revealed strongly directional, defect-dominated charge transport in the oriented BTT COF films, with a strong preference for the in-plane direction within the molecular 2D-planes over the out-of-plane direction. Quantum mechanical calculations predict BTT TTTBA to conduct holes and electrons effectively in both the in-plane and out-of-plane directions. In-plane, charge carrier transport is of hopping character where the triazine cores represent the barrier. Out-of-plane, a continuous charge-carrier pathway is calculated that is hampered by an imposed structural defect simulated by a rotated molecular COF layer.

Table of Contents

1. Introduction	1
1.1 Introduction	2
1.2 Synthesis and Structure	4
1.2.1 Installation of the Boronic Acid Functional Group	4
1.2.2 Formation of Boroxine and Boronate Ester Compounds	6
1.2.3 COF Synthesis and Mechanism of Formation	8
1.2.4 COF Structures and Properties	12
1.2.5 Post-synthetic Modification of Boronic-Acid-derived COFs	28
1.2.6 Processing	31
1.2.7 Applications	37
1.3 Summary and Outlook	47
1.4 References	47
1.5 Exploring New Linkage Motifs	55
1.6 Tailoring Optical Properties	56
1.7 References	57
2. Characterization Methods	60
2.1 X-ray Diffraction (XRD)	60
2.2 Grazing-Incidence Wide-Angle X-ray Scattering (GIWAXS)	62
2.3 Gas Sorption	63
2.4 Thermogravimetric Analysis (TGA)	65
2.5 Electron Microscopy (EM)	66
2.5.1 Scanning Electron Microscopy (SEM)	66
2.5.2 Transmission Electron Microscopy (TEM)	67
2.6 Infrared Spectroscopy (IR)	68
2.7 Nuclear-Magnetic-Resonance Spectroscopy (NMR)	68
2.8 Mass Spectrometry	69
2.9 Ultraviolet-Visible Spectroscopy (UV-vis)	70
2.10 Photoluminescence Spectroscopy (PL)	71
2.11 Time-Correlated Single Photon Counting (TCSPC)	72
2.12 Atomic Force Microscopy (AFM)	73
2.13 References	75
3. A Post-synthetic Modification Strategy for the Synthesis of Pyrene-fused Azaacene COFs	77

3.1	Abstract.....	78
3.2	Introduction	78
3.3	Results and Discussion	79
3.4	Conclusion.....	83
3.5	References	83
3.6	Appendix	86
3.6.1	Materials and Methods	86
3.6.2	Synthetic Procedures	88
3.6.3	NMR Spectra	94
3.6.4	Crystal Structure Simulation	99
3.6.5	N ₂ Physisorption	111
3.6.6	Fourier-transform Infrared (FT-IR) Spectroscopy.....	114
3.6.7	Thermogravimetric Analysis (TGA)	115
3.6.8	Scanning Electron Microscopy (SEM).....	116
3.6.9	Optical Properties of the Dione Building Block.....	117
3.6.10	References.....	118
4.	Building Blocks and COFs formed <i>in chorus</i>.....	119
4.1	Abstract.....	120
4.2	Introduction	120
4.3	Results and Discussion	122
4.3.1	Synthesis	122
4.3.2	Oriented Thin Films of Fully Modified Aza COFs	127
4.3.3	Photophysical Properties	128
4.4	Conclusion.....	129
4.5	References	130
4.6	Appendix	133
4.6.1	Materials and Methods	133
4.6.2	Synthetic Procedures	135
4.6.3	NMR Spectra	140
4.6.4	Structural Analysis.....	144
4.6.5	Fourier-transform Infrared (FT-IR) Spectra	148
4.6.6	N ₂ Physisorption	149
4.6.7	Thermogravimetric Analysis (TGA)	150
4.6.8	Transmission Electron Microscopy (TEM).....	150
4.6.9	Thin Film Analysis	151
4.6.10	Photophysical Properties	151

4.6.11	References.....	152
5.	Thiophene-based Vinylene-Linked COF Films	153
5.1	Abstract.....	154
5.2	Introduction	154
5.3	Results and Discussion	156
5.3.1	Synthesis.....	156
5.3.2	Structural Investigations	157
5.3.3	Film Synthesis via Vapor-assisted Conversion	159
5.3.4	Photophysical Properties	162
5.4	Conclusion.....	164
5.5	References	165
5.6	Appendix	169
5.6.1	Methods	169
5.6.2	Materials and Building Block Synthesis	171
5.6.3	Vinylene-linked COFs – Acidic Conditions.....	175
5.6.4	Structural Analysis.....	175
5.6.5	Nitrogen Sorption	181
5.6.6	Thermogravimetric Analysis	182
5.6.7	Grazing-Incidence Wide-Angle X-ray Scattering – VAC Films.....	182
5.6.8	SEM and X-Ray Diffraction Analysis – VAC Films	183
5.6.9	Krypton Sorption – VAC films	186
5.6.10	Optical Characterization – Bulk and Films	186
5.6.11	Solvatochromic Effect – VAC films	188
5.6.12	References.....	190
6.	Benzotrithiophene COF Thin Films –	191
	Directional Electrical Conductivity	191
6.1	Abstract.....	192
6.2	Introduction	192
6.3	Results and Discussion	194
6.3.1	Synthesis.....	194
6.3.2	Oriented Thin Films of BTT TTA and BTT TTTBA.....	197
6.3.3	Photophysical Properties	198
6.3.4	Electrical Conductivity of BTT TTA and BTT TTTBA COFs.....	199
6.3.5	Charge-Carrier Pathway Simulations	201
6.4	Conclusion.....	202
6.5	References	203

6.6 Appendix	207
6.6.1 Methods	207
6.6.2 Materials and Building Block Synthesis	209
6.6.3 Structural Analysis.....	216
6.6.4 IR Spectroscopy.....	221
6.6.5 Sorption	222
6.6.6 Thermogravimetric Analysis	223
6.6.7 Electron Microscopy.....	224
6.6.8 Grazing Incidence Diffraction Patterns	226
6.6.9 Photoluminescence Spectroscopy.....	227
6.6.10 Electrical Conductivity – Stability Measurements	227
6.6.11 Computational Simulations	228
6.6.12 NMR Spectra	230
6.6.13 Solid-state NMR Spectra	236
6.6.14 References.....	237
7. Conclusion	238
8. Appendix.....	241
8.1 Curriculum Vitae	241
8.2 Publications	242
8.3 Conference Contributions.....	244

List of Abbreviations

AFM	atomic force microscope
2D	two-dimensional
3D	three-dimensional
BDT	benzodithiophene
BET	Brunauer-Emmett-Teller
BTT	benzotrithiophene
COF	covalent organic framework
DMF	dimethyl formamide
DMSO	dimethyl sulfoxide
EtOH	ethanol
eq.	equivalents
GIWAXS	grazing-incidence wide angle X-ray scattering
H ₂ O	water
MeOH	methanol
PL	photoluminescence
ppm	parts per million
PXRD	powder X-ray diffraction
N ₂	nitrogen
QSDFT	quenched solid density functional theory
SEM	scanning electron microscopy
TCSPC	transmission electron microscopy
TGA	thermogravimetric analysis
THF	tetrahydrofuran
TT	thieno thiophene
UV-vis	ultraviolet-visible

VAC

vapor-assisted conversion

1. Introduction

This chapter is **published as:**

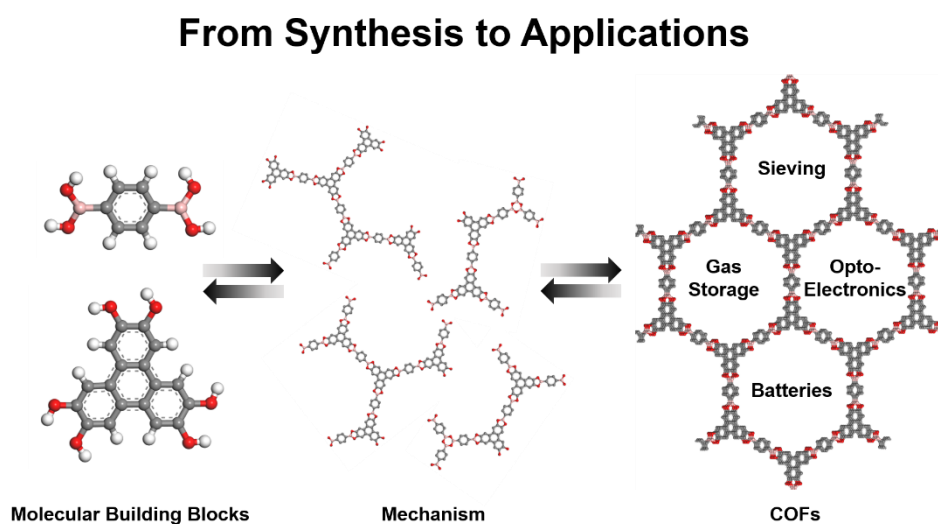
Boronic-acid-derived covalent organic frameworks: from synthesis to applications

Laura Frey,^{‡a} Jenni J. Jarju,^{‡b} Laura M. Salonen^{*b} and Dana M. Medina^{*a}, *New J. Chem.*, **2021**, *45*, pp 14879-14907.

^a Department of Chemistry, Ludwig-Maximilians-Universität (LMU) & Center for NanoScience (CeNS), Butenandtstr. 11, 81377 Munich, Germany. E-mail: dana.medina@cup.lmu.de

^b International Iberian Nanotechnology Laboratory (INL), Av. Mestre José Veiga, 4715-330 Braga, Portugal. E-mail: laura.salonen@inl.int

[‡] These authors contributed equally.



Modular, well-defined, and robust hierarchical functional materials are targets of numerous synthesis endeavors. Covalent organic frameworks (COFs) are crystalline and porous materials with a vast chemical and structural diversity, and they are synthesized in a bottom-up approach from molecular building blocks by condensation polymerization reactions to form layered or spatial complex structures. Boronic-acid-containing building blocks were the first to be employed as monomers in the synthesis of COFs, setting the foundations for an exceedingly growing, exciting field of research. Here, an overview is provided on boronic-acid-derived COFs, including synthesis, building block design and mechanism of COF formation, structures and properties, processing and implementation into functional devices, as well as examples of application for which these materials have been studied.

1.1 Introduction

Boronic acids, $\text{RB}(\text{OH})_2$, have central roles in synthetic, analytical, and bioorganic chemistry, and they are common precursors in organic chemistry, widely used for catalytic cross-coupling reactions to give saturated carbon–carbon bonds.¹ Therefore, these compounds are broadly commercially available and various synthesis methods have been developed to gain access to them. Boronic acids react through a reversible condensation reaction both with diols to give boronate esters as well as self-condense to yield boroxines. Due to the reversibility of these reactions, the use of boronic acid compounds has been demonstrated for the formation of macromolecular structures, such as macrocycles, molecular cages, and extended frameworks.^{2–4} Both boronate esters and boroxines are planar, thus allowing for predictable connectivity in macromolecule design. The reversible bond formation enables ‘proof-reading’ and ‘error-checking’ of the forming structure in a thermodynamically controlled process, thus providing highly structurally defined products.

The two key features of linkage reversibility and planarity have enabled the preparation of boronic-acid-derived highly defined two-dimensional (2D) and three-dimensional (3D) frameworks, the so-called covalent organic frameworks (COFs). COFs are crystalline, light-weight porous materials featuring well-defined pore shape and aperture. The principle of construction of 2D COFs includes the judicious selection of typically aromatic building blocks with a defined geometry and connecting functional groups, which eventually direct the addition of building blocks in-plane. Upon condensation polymerization, 2D sheets are formed, continuously extending the number aromatic units at the backbone. These extended molecular sheets form aggregates, guided by π – π interactions, resulting in a crystalline layered 2D structure and well-defined porous channels, aligned along the stacking direction.⁵

In contrast to layered COFs, where planar molecular monomers are employed, 3D COFs are constructed by employing spatial building blocks, where the connecting vertices are pointing out-of-plane, thus forming extended 3D networks with different topologies and degree of network interpenetration. In a pioneering work in 2005, Yaghi and co-workers reported the synthesis of 2D-COFs⁶ through the self-condensation reaction of linear 1,4-benzenediboronic acid (BDDBA) to form boroxines as well as co-condensation of boronic acid compounds with planar catechols to give boronate ester COFs (**Figure 1.1**). In a following work, the same group synthesized extended 3D frameworks employing spatial precursors such as boronic-acid-functionalized tetraphenylmethane.⁷ These reports laid the foundations for the discovery of numerous crystalline porous frameworks with vast chemical and physical properties and structural diversity that are known to date.

In this review, we aim to give an overview of boronic-acid-derived COF materials. First, we will focus on the installation of boronic acid moieties to form COF building blocks with the desired functionality and symmetry. Afterwards, the synthesis of boronic-acid-derived frameworks will be discussed with an

emphasis on their properties and mechanism of formation. In addition, different synthesis approaches for the formation of COFs as well as post-synthetic modification methods will be described. Then, the processing of boronic-acid-derived COF powders and thin films will be discussed and the review will conclude with examples of the utilization of these materials for a variety of applications. As an aid to the readers, abbreviations for the most commonly appearing building blocks in this review are presented in **Table 1.1**.

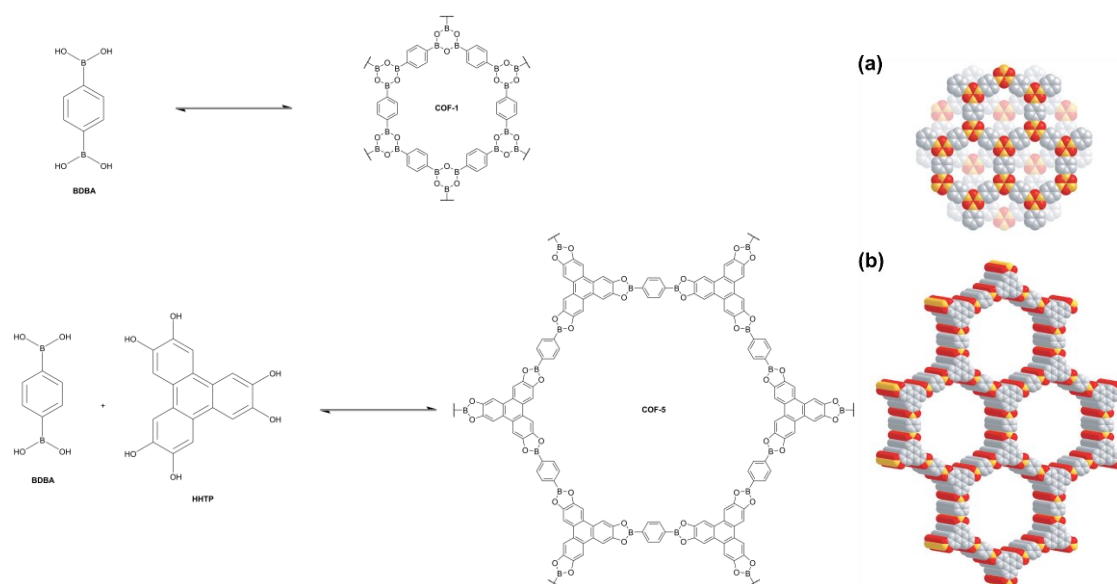


Figure 1.1. Synthesis scheme and structures of (a) COF-1 and (b) COF-5.⁶ Reprinted with permission from AAAS.

Table 1.1. Abbreviations for frequently appearing building blocks.

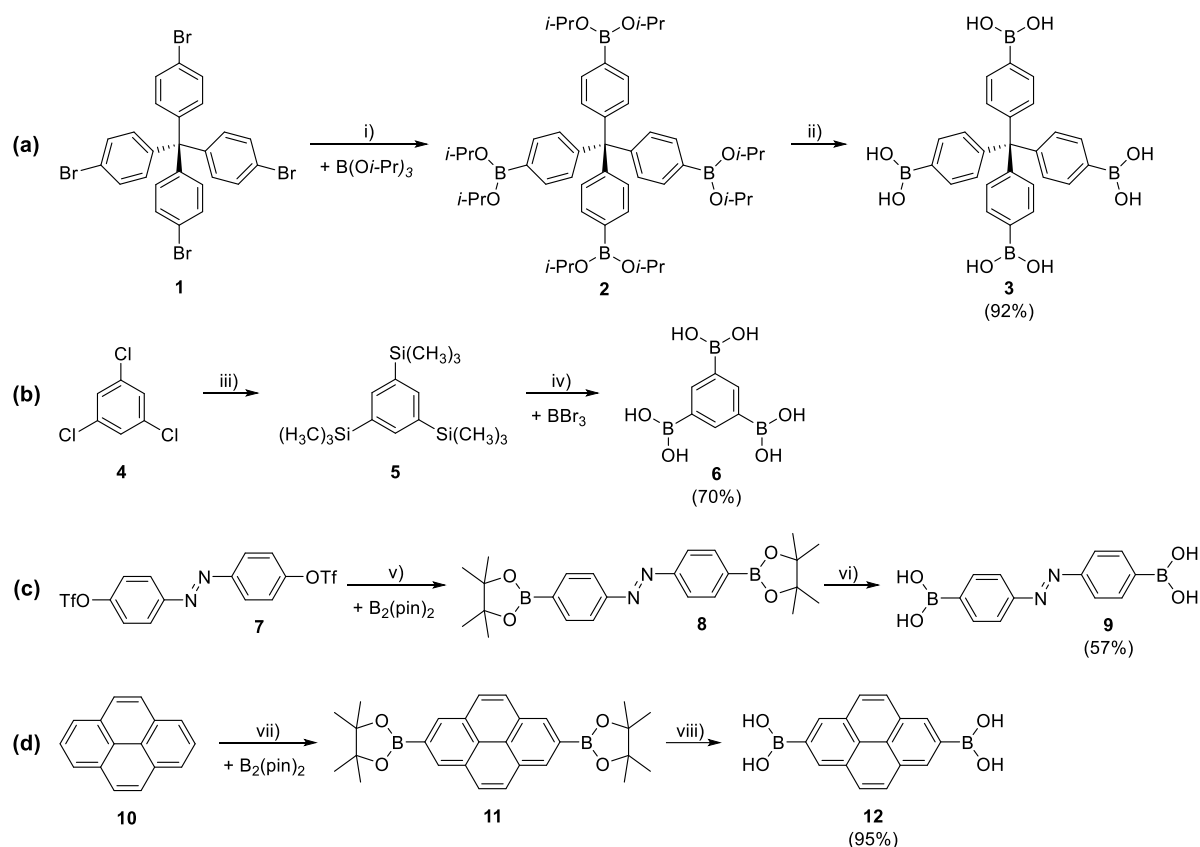
AEM	arylene–ethynylene	NDIDA	naphthalene tetracarboxylic acid diimide
BDBA	1,4-dibenzeneboronic acid	PCBM	[6,6]-phenyl-C ₆₁ -butyric acid methyl ester
BDT	benzo[1,2- <i>b</i> :4,5- <i>b'</i>]dithiophene	Pc	phthalocyanine
BPDA	4,4'-biphenyldiboronic acid	PDBA	pyrene-2,7-diboronic acid
BPA	borophosphonic acid	PPTODB	4,5,9,10-tetraone-pyrene-2,7-diboronic acid
BTDA	1,4-benzothiadiazole diboronic acid	PyrDIDA	pyromellitic tetracarboxylic acid diimide
CTC	cyclotricatechylene	TBPM	tetra(4-dihydroxyborylphenyl)methane
DBA	dehydrobenzoannulene	TBPS	tetra(4-dihydroxyborylphenyl)silane
H4TDB	2,5-thiophene diboronic acid	TCAT	4- <i>tert</i> -butylcatechol
HHTP	2,3,6,7,10,11-hexahydroxytriphenylene	THB	tetrahydroxybenzene
MPc	Metallophthalocyanine		

1.2 Synthesis and Structure

1.2.1 Installation of the Boronic Acid Functional Group

Boronic acids are trivalent boron-containing organic compounds with one alkyl- or aryl- substituent and two hydroxyl groups. The neutral, sp^2 -hybridized boron center has an empty p -orbital, which confers Lewis acidity.^{8,9} Boronic acids are key building blocks for Suzuki Miyaura cross-coupling reactions,¹ they can function as selective anion sensors,¹⁰ and form the basis of a myriad of saccharide receptors.¹¹ Their dynamically reversible condensation reactions, which yield boroxines and boronate esters (see **section 1.2.2**), enable the synthesis of complex molecular and supramolecular compounds and materials, such as macrocycles,² capsules,³ polymers,⁴ cages, and COFs.^{12,13} The increasing importance of boronic acids as synthetic building blocks has led to the development of new mild and efficient synthesis methods to provide a wide range of these compounds with desired functionalities.

In the context of COFs, boronate ester and acid moieties have been incorporated into robust and well-defined building blocks, facilitating COF formation.⁶ One of the first, probably the most common, and least expensive method for the synthesis of arylboronic acids involves the treatment of aryl halides with Grignard or organolithium reagents to produce arylmetal intermediates,⁸ followed by a reaction with trialkylborate $B(OR)_3$ and subsequent hydrolysis of the boronic ester to yield the arylboronic acid (**Scheme 1.1a**). Using this method, tetrakis(4-bromophenyl)methane (**1**) was borylated with triisopropyl borate, $B(Oi-Pr)_3$, to produce compound **2**, the hydrolysis of which yielded tetraboronic acid **3**.¹³ This compound has served as a building block for the synthesis of 3D boroxine COF-102 (**section 1.2.4**).⁷ Although this synthesis approach is effective for simple systems with small number to no functional groups, finding optimal conditions for high yields can be difficult due to the formation of by-products such as undesired boronic acids and boranes.⁸ In addition, the high reactivity of the organometallic intermediates requires inert anhydrous conditions at cryogenic temperatures.



Scheme 1.1. Synthesis of boronic acids **3**, **6**, **9**, and **12**. Reaction conditions: i) *n*-butyllithium in hexane, dry THF; then, triisopropyl borate, dry THF;¹³ ii) 1 M HCl; iii) Mg, Me₃SiCl, dry THF; then H₂O;¹⁴ iv) BBr₃, hexane; then, H₂O; v) KOAc, dppf, 1,4-dioxane, PdCl₂(dppf)·CH₂Cl₂;¹⁵ vi) NaIO₄, 1 M HCl, THF/H₂O; vii) [Ir(μ-OMe)cod]₂, 4,4'-di-*tert*-butyl-2,2'-bipyridine, dry THF;¹⁶ viii) NaIO₄, 1M HCl, THF/H₂O. dppf: 1,1'-bis(diphenylphosphino)ferrocene; pin: pinacolato; cod: 1,5-cyclooctadiene.

Another common method for preparing relatively simple arylboronic acid derivatives involves the transmetalation of aryl stannanes or silanes⁸ with boron tribromide, BBr₃, yielding arylboron dibromide as intermediate,¹² which can be then converted to arylboronic acid *via* aqueous acidic workup. Some boronic acids have also been prepared starting from trimethylsilyl derivatives (**Scheme 1.1b**). For example, silylation of 1,3,5-trichlorobenzene (**4**) produced compound **5**, which was then borylated with BBr₃ and subsequently hydrolyzed to yield triboronic acid **6**. This compound has been employed together with 2,3,6,7-tetrahydroxyanthracene to give access to a photoresponsive boronate ester COF (**section 1.2.4**).¹⁴

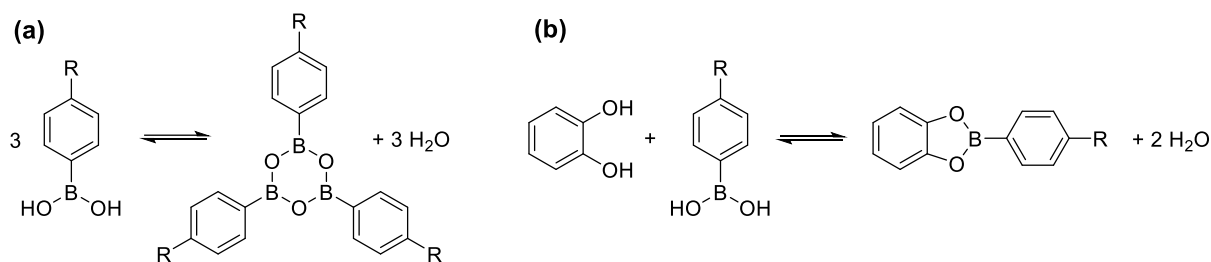
Palladium-catalyzed coupling of an aryl halide or triflate with B₂(OR)₂ or HB(OR)₂, such as bis(pinacolato)diboron (B₂(pin)₂) or pinacolborane, is an efficient method to provide boronic ester derivatives (**Scheme 1.1c**). Hydrolysis of the pinacol ester to the boronic acid proceeds using NaIO₄ under acidic conditions.⁸ The method is compatible with a wide variety of haloarene compounds and tolerates the presence of reactive chemical groups such as ketones, esters, nitriles, benzophenones, and benzaldehydes. The reaction is typically completed in less than 24 h. Using this approach, triflate **7** was borylated with B₂(pin)₂ to yield boronic ester **8**, which was hydrolyzed to azobenzene diboronic acid **9**

that, together with 2,3,6,7,10,11-hexahydroxytriphenylene (HHTP, **Figure 1.1**), was used in the synthesis of boronate ester Azo-COF.¹⁵

A convenient way to prepare boronic acid derivatives is through direct borylation *via* a transition-metal-catalyzed C-H activation⁸ in the presence of a boron donor. This borylation method was first demonstrated on alkanes using photochemical conditions.¹⁷ For arene compounds, several research groups, including those of Marder,¹⁸ Hartwig,^{19,20} and Smith,²¹ have reported several efficient procedures using iridium and rhodium catalysts. The main challenge in this method is the regioselectivity of the aromatic C-H activation with mono- and polysubstituted arenes. Marder and co-workers¹⁶ utilized the selectivity of the Ir-catalyzed aromatic borylation of pyrene (**10**) to produce pyrene-2,7-bis(boronate) (**11**) in 97% yield, providing direct borylation of positions that are otherwise difficult to derivatize (**Scheme 1.1d**). Perylene-2,5,8,11-tetra(boronate) ester was prepared through a similar procedure in 83% yield. The selectivity is likely obtained owing to the sterics of the bulky Ir-containing intermediate, which is proposed to be the key intermediate performing the rate-determining C-H activation step. Subsequently, compound **11** was hydrolyzed to boronic acid **12**. This compound together with HHTP has been employed in the synthesis of luminescent and semiconductive boronate ester-linked TP-COF (**section 1.2.4**).²² In addition, compound **11** can be further converted into 2,7-bis(R)-pyrenes, where R = BF₃K, Br, OH or OTf.²³

1.2.2 Formation of Boroxine and Boronate Ester Compounds

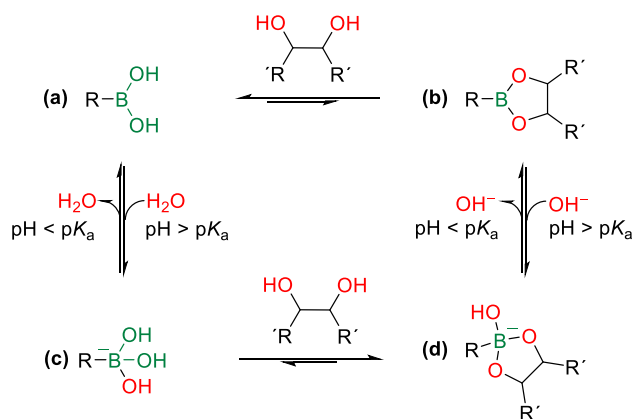
The self-condensation of boronic acids yields planar six-membered boroxine anhydride (B₃O₃) rings (**Scheme 1.2a**), whereas the condensation of boronic acids with 1,2-diols results in planar five-membered boronic ester (BO₂C₂) rings (**Scheme 1.2b**).²⁴ Both boroxine and boronic ester formation are thermodynamically reversible despite the formation of a strong B-O covalent bond, accompanied by the entropically favorable release of water molecules as by-product, and the bond dissociation energy being 124 kcal mol⁻¹ for the B-O bond in boronic esters.²⁵ According to Le Chatelier's principle, the thermodynamic equilibrium of the reactions can be pushed towards products, *e.g.*, by azeotropic removal of water, employing dehydrating agents, and product precipitation. The formation of boroxine anhydrides and boronate esters is fast, with reaction rates of 10²–10³ M⁻¹ s⁻¹ for boronate ester formation,⁸ which are influenced by the conditions under which the reaction takes place, including the type of solvent employed in the reaction and functional groups decorating the reactants.



Scheme 1.2. Formation of (a) boroxine and (b) boronate ester compounds.

In nonpolar solvents, many boronic acid derivatives easily self-condense to produce the corresponding less polar boroxines.²⁴ Boron compounds functionalized with electron-donating groups have been reported²⁴ to promote boroxine formation by decreasing the electrophilicity of the boron. The resulting ring is therefore less prone to hydrolysis, whereas electron-withdrawing groups have a destabilizing effect on the formed ring.²⁶ Compounds with nitrogen Lewis-base donors, such as pyridine, facilitate the self-condensation of boronic acids by forming a boroxine-N-donor adduct, the formation of which is thermodynamically more favorable than that of uncoordinated boroxine.^{8,24}

The water stability of boronate esters is significantly influenced by the structure of the diol precursor, with cyclic and hindered *cis*-1,2-diols, typically giving access to more stable products.²⁷ The lower polarity of boronate esters compared to the corresponding boronic acids can be used to shift the equilibrium towards ester formation in nonpolar solvents.²⁴ In aqueous medium, the ionic equilibrium between boronic acid (**a**) and boronate anion (**c**) is shown on the left of **Scheme 1.3**. Acidic conditions favor the formation of electron-accepting boronic acid, while under basic conditions the electron-donating boronate anion dominates.²⁸ Since (**a**) and (**c**) have different electronic properties, the reactions involving boronic acids are dependent on the equilibrium between the boronic acid and the boronate anion. The reaction of boronic acids with diols forms both boronate esters (**b**) and boronate ester anions (**d**), which exist in ionic equilibrium. The formation of the tetrahedral boronate anion (**c**) has been assumed to favor complexation with diols at higher pH values, yielding boronate esters, while under acidic conditions boronate esters tend to hydrolyze.²⁷ The reactivity and formation constant of boronic acids (**a**) increase with their increasing acidity, whereas the opposite is found for the conjugate base (**c**): the higher basicity of **c** leads to higher reactivity with diol forming boronate ester anion **d**.²⁸ Additional stability to the boronate ester is provided by *o*-substitution of the phenylboronic acid. The pK_a of phenylboronic acid is 8.8, which is slightly more acidic than boric acid ($pK_a = 9.2$) and less acidic than 3,5-dichlorophenylboronic acid ($pK_a = 7.4$) or 4-nitrophenylboronic acid ($pK_a = 7.1$).⁸ Boronic acids become more acidic upon diol binding, with the pK_a values of the boronate esters being 2-4 units lower compared to the pK_a of the corresponding boronic acid.²⁹



Scheme 1.3. The pH-dependent formation equilibrium of a boronic ester in an aqueous solution.

1.2.3 COF Synthesis and Mechanism of Formation

Although many building blocks and synthesis routes have been developed to obtain crystalline COFs, finding suitable reaction conditions under which a COF forms is still not trivial.²⁹ Regulating the thermodynamic equilibrium during covalent bond formation is a key to obtain highly crystalline and porous COFs, where temperature, pressure, and solvents all play a pivotal role.

Solvothermal synthesis is the most typical preparation method of boronic-acid-derived COF materials, and it often requires several days within a sealed vessel at a constant elevated temperature, ranging from 80–120 °C.³⁰ Solvent combinations and ratios chosen for the COF synthesis are important factors, as they affect the polarity of the medium and thereby the solubility of the building blocks, the reaction rate, crystal nucleation, crystal growth rate, and reversibility of the reaction, which in turn allows for self-healing and ‘error-correction’ in the process. During an optimal COF synthesis, should a linkage form in an undesired direction, reversible bond formation grants access to its repair, thus ultimately leading to a crystalline, stable product.³¹ Mixtures of apolar and polar solvents, such as mesitylene/dioxane or *o*-dichlorobenzene/dimethylacetamide (DMAc), are commonly employed in the synthesis of boronate ester- and boroxine-linked COFs. A suitable concentration of the building blocks in the solvent system is essential for the reaction to proceed under thermodynamic control.

Although solvothermal synthesis is widely used and leads to highly crystalline and porous COF materials, the challenges include the relatively long reaction times and scale-up of COF synthesis.⁵ An approach to overcome these challenges was reported by Cooper and co-workers,³² who synthesized 2D COF-5 (**Figure 1.1b**) and 3D COF-102 (**section 1.2.4**) using microwave heating in only 20 min. The reaction proceeded over 200 times faster for both COFs as compared to the solvothermal method and resulted in nearly double Brunauer–Emmett–Teller (BET) surface area for COF-5. The possibility of conducting the reaction in an open vessel facilitates the optimization of the conditions and paves the way for industrial production. In another approach, COFs were produced through sonochemical

synthesis.³³ The use of ultrasound irradiation forms micrometer-sized bubbles in the solvent, which grow and collapse in a cavitation process. This leads to high local temperatures and pressures in the solution, and thus accelerates chemical reactions. This method was used for the preparation of COF-1 and COF-5, and materials with BET surface areas of over 2000 m² g⁻¹ were obtained in a short reaction time of 0.5-2 h. The scalability of this technique was demonstrated up to 0.5 L batch size, showing potential for the synthesis of highly porous products on a large scale with a space-time yield of COF-5 being 45 kg m⁻³ day⁻¹. The sonochemical method was also used to deposit COF-5 on carbon nanotubes (CNTs) and graphene.⁵

Despite intense research in COF materials, the nucleation and growth processes of the frameworks remain poorly understood. In most COF syntheses, the monomers are only partially soluble under the reaction conditions and the product and intermediates precipitate from the reaction mixture. Therefore, the reaction solution is heterogeneous at all times, which excludes the use of most *in situ* spectroscopic characterization techniques that would give important information of COF polymerization and crystallization processes.³⁴ To shed light on the COF formation processes, several mechanistic studies on boronate ester 2D COFs have been carried out by Dichtel and co-workers.³⁴⁻³⁷ Here, COF-5 was synthesized starting from clear, fully-soluble monomer solutions, which provided COF material with high crystallinity and surface area, and allowed for the measurement of the rate of formation of COF-5 and determination of its formation under varied reaction conditions.³⁴ Homogeneous solutions were obtained by the addition of a small amount of MeOH as modulator to a 4:1 dioxane/mesitylene solvent mixture, from which COF-5 started to precipitate upon heating to 90 °C, enabling the quantification of its formation rate from optical turbidity measurements. The precipitation of crystalline COF-5 was found to begin already after a two min induction period and proceed at a constant rate for several minutes, after which the COF precipitation started to slow down. The growth rate was further studied under various homogeneous reaction conditions to provide information on the bond-forming and crystallization processes, controlling the temperature, concentration, as well as the concentration of the modulator and the co-solvent.³⁴ The obtained insights led to a model for COF-5 formation (**Figure 1.2**), which suggests that the early stages of boronic-acid-derived COF synthesis involve monomer condensation into soluble oligomers, followed by a nucleation step yielding COF crystallites, which further grow by bond-formation and stacking processes. The small crystallites aggregate and precipitate as polycrystalline powders with high surface areas, confirming the hypothesized COF precipitation process. The precipitation happens in minutes when reaction-rate-inhibiting additives, such as H₂O, an excess of MeOH, or monofunctional 4-*tert*-butylcatechol (TCAT), are not present in the reaction mixture. The TCAT modulator serves as a steric capping agent of the boronic acid precursor, lengthening the nucleation induction period and inhibiting precipitation, thus suppressing further COF nucleation without preventing seeded growth. Furthermore, dynamic boronate ester exchange occurs among soluble monomers and oligomers and probably at the edges of the growing crystals prior to precipitation. The study suggested that 2D and 3D boronate ester and boroxine COF syntheses proceed through

reversible bond-formation processes, which are capped by at least one irreversible step associated with the precipitation of a nanocrystalline product.

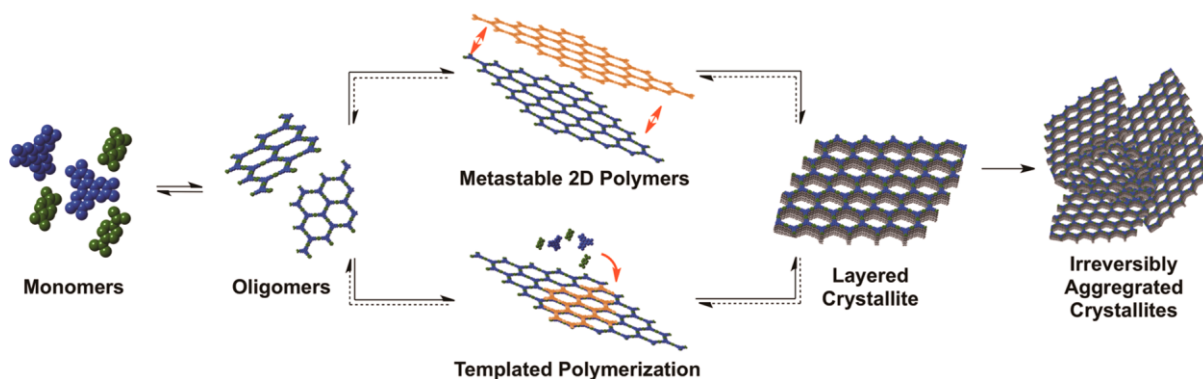


Figure 1.2. Proposed models of boronate ester COF-5 growth. Reprinted with permission.³⁴ Copyright (2014) American Chemical Society.

The proposed COF formation model was further studied by systematically varying monomer length and aromatic domain size of 2D boronate ester COFs, namely COF-5 (**Figure 1.1b**), COF-10 (**Table 1.2**), HHTP-DPB COF (**Table 1.2**), and TP-COF (**Table 1.2**).³⁵ Turbidity measurements indicated that the formation of all four COFs begins with a fully soluble monomer induction period that is followed by a rapid increase in turbidity associated with COF precipitation. The COF formation rate depends on both pore size and the interlayer attractive forces: the growth rate was found to increase with enhanced van der Waals surface of the linkers, whereas larger pore size and the corresponding higher percentage of empty space per unit cell, decreasing the interlayer attraction, led to a decreased rate of formation. To determine the overall activation energies for the COF formation reactions, the syntheses were carried out at different temperatures. The cause of activation energy differences between the COFs was further studied by examining the formation of molecular boronate esters in condensation reaction of the respective boronic acid monomers, used in the synthesis of TP-COF, and COF-5 with TCAT modulator under similar conditions. The activation energies for boronate formation are similar for both linkers, ca. 7 kcal mol⁻¹, which is significantly lower than the COF formation energies (COF-5: 22-23 kcal mol⁻¹, TP-COF: 12 kcal mol⁻¹), indicating that the initial boronate ester formation is not the rate-determining step for these COFs. Furthermore, the water stability of the COFs was examined and the results are consistent with the relative growth rates, showing that COFs with smaller pore size and greater intermolecular interactions also demonstrated greater water stability. These results indicate that interlayer stacking of the 2D polymers is the rate-determining step, and that COF formation occurs through nucleation-elongation type mechanism, in which a 2D polymer templates the growth of a subsequent COF layer.

Experimental and theoretical studies were combined to estimate the rate parameters associated with the nucleation and growth of COF-5.³⁶ A kinetic Monte Carlo (KMC) model was used to describe the

formation of the COF from its monomers in solution, deriving the key rate parameters from experimental measurements when possible. To understand the structure of the nuclei and the nucleation process, KMC simulations were carried out monitoring all generated intermediate structures once they had reached a certain number of monomer units (N). The model suggested that small oligomers, for example with $N = 15$, rarely grow into COF-5 crystals, with the majority decomposing back to smaller units. In contrast, larger oligomers with $N \geq 30$ almost always grow into crystals. The nucleation process includes the formation of stable stacked structures that are able to grow further before they dissociate to oligomers and monomers. The rate of the stacking process is fast with negligible energy barrier, frequently giving rise to multi-layered structures, while COF layer defoliation rate is highly dependent on the size of the oligomers. Larger oligomers have larger lateral sizes, and thus increased stability.

In the same study,³⁶ the nucleation process of COF-5 was found to have several stages, resulting in multilayer structures. The first stage is the formation of small oligomers, which influences the length of the induction period. The oligomers formed in the first step, then follow two different nucleation pathways (**Figure 1.3**). In nucleation pathway 1, stacking of the small oligomers results in larger structures, from which the majority dissociates back to oligomers, and a smaller population successively grows laterally. The nucleation pathway 2 includes lateral growth of the small oligomers to form larger ones, which can then stack and produce stable nuclei that can grow further. One pathway does not rule out the other: if one pathway fails, the oligomers formed in it are able to participate as building blocks in the second nucleation pathway. After the formation of a nucleus, the growth continues into a COF-5 crystal in a process, where both lateral diameter and height increase linearly with time. The lateral growth occurs *via* bond formation with monomers and small oligomers, while vertical growth, corresponding to the formation of new layers, is dominated by the assembly of oligomers. Adding water to the reaction mixture gives rise to COF-5 crystals with larger diameters by shifting the equilibrium from large oligomers towards monomers, thereby favoring lateral (pathway 1) over vertical growth (pathway 2). The crystallization of COF-5 is non-classical and can be considered similar to crystallization by particle attachment (CPA),³⁸⁻⁴⁰ since oligomers are the key precursors in the nucleation process and dominate vertical growth. On the other hand, as opposed to the CPA mechanism, COF-5 crystallization involves several metastable species like oligomers and stacked structures in the nucleation process, different mechanisms in vertical and lateral growth, and simultaneous presence of the classical monomer-by-monomer addition mechanism that dominates the lateral growth of the COF-5 crystals.

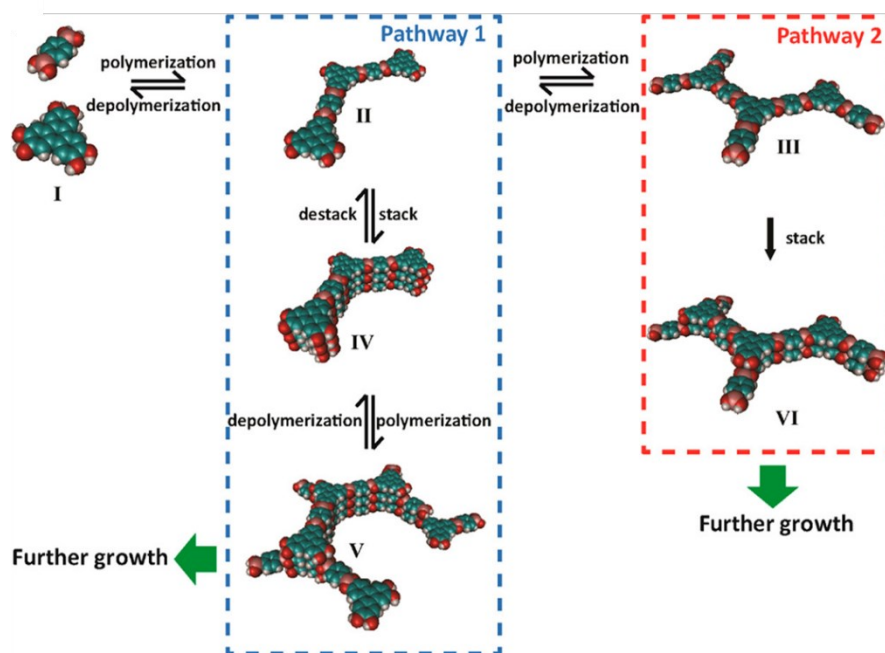


Figure 1.3. Two observed nucleation pathways for COF-5. Reprinted with permission.³⁶ Copyright (2017) American Chemical Society.

Further experimental studies of nucleation and growth mechanisms included a quantitative analysis of the nucleation–elongation dynamics of 2D COFs. The rate dependence of COF-5 nucleation and growth was investigated by *in situ* small/medium/wide-angle X-ray synchrotron scattering (SAXS/MAXS/WAXS) measurements, which allow for monitoring of the size and crystallinity of the particles as the reaction proceeds.³⁷ To examine the nucleation and growth processes independently, particular monomer concentrations were selected under which one process is dominating. The results indicated that the nucleation and growth processes have second-order and first-order dependences on the monomer concentration, respectively, meaning there exists a critical monomer concentration (C^*) below which nucleation is slower than growth. This result is in line with earlier findings that nucleation is suppressed when adding monomers slowly to a colloidal COF suspension,⁴¹ and because of that, lower monomer concentration yields fewer but larger crystallite domains. In contrast, if the monomer concentration is higher than C^* , the successive nucleation takes place with the growth process, resulting in a smaller average crystal size.

1.2.4 COF Structures and Properties

Through the combination of multidentate building blocks, various COF pore systems can be designed using the principles of reticular chemistry, resulting in a broad range of pore sizes, topologies, and geometries. This way, hexagonal, quadratic, pseudo-quadratic/rhombic, trigonal, or dual-pore/star-shaped pore systems can be achieved. Additionally, vast opportunities for the pre-design of COF pore-wall surfaces are presented through the selection of functional groups decorating the organic building blocks. Following the pioneering report⁶ of boroxine and boronic ester COF syntheses by Yaghi

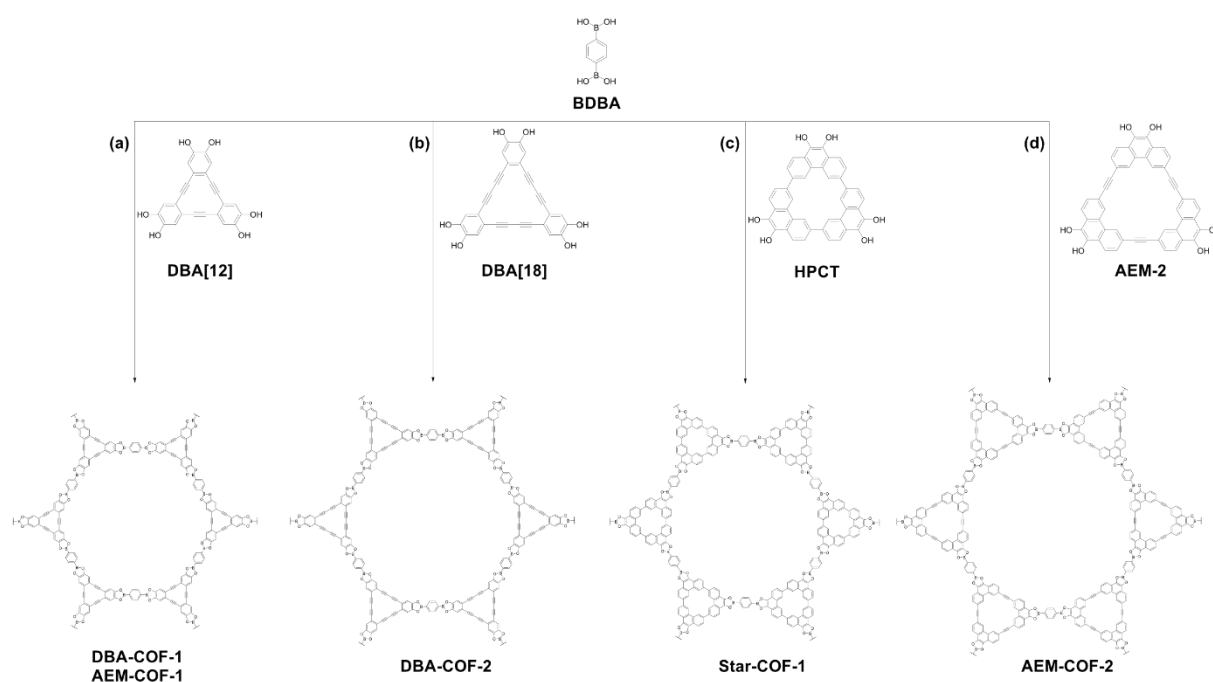
and co-workers (**Figure 1.1**), a wide variety of different structures have been presented. Two-dimensional boronate ester COFs (**Table 1.2** and **Table 1.3**) are by far the most common boronic-acid-derived COFs, although interesting examples have also been reported on 2D boroxine (**Table 1.4**) and 3D COF structures (**Table 1.5**). Selected structures of these COF classes will be presented in the following, and this section is concluded with examples of double-linkage COFs, which feature an additional linkage type to the boronic ester (**Table 1.6**).

The synthesis of one of the first COFs, COF-1, was based on a simple molecular dehydration process of BDBA at 120°C for 72 h in a mesitylene/dioxane mixture, resulting in a highly crystalline boroxine-linked framework.⁶ Comparing the experimental powder X-ray diffraction (PXRD) pattern to the one of the simulated model revealed that the 2D organic sheets arrange in a staggered manner (AB), analogous to the packing of graphite sheets, where the vertex of one layer is located at the pore opening of the successive layer (**Figure 1.1a**). This layer arrangement was attributed to the presence of residual mesitylene within the pores and upon removal of the solvent guest molecules, the layers shifted towards an eclipsed AA stacking mode, where the successive layers are fully overlapped. In the case of COF-5 (**Figure 1.1b**), eclipsed AA stacking model of the 2D layers was suggested, which was attributed to the presence of conjugated HHTP building blocks, inducing favorable π - π interactions between successive layers.

Eclipsed layer arrangement was also found for boroxine-linked PPy-COF (**Table 1.4**), formed by the self-condensation of pyrene-2,7-diboronic acid (**12**) (PDBA, **Scheme 1.1d**) units, which was attributed to the extended π -system of pyrene.⁴² This COF exhibited interesting photophysical properties by visible light absorption: upon excitation at 414 nm photon-emission at $\lambda = 484$ nm was observed. Additionally, PPy-COF triggered photocurrent generation upon illumination, therefore representing the first example of a photoconductive COF. Luminescent and semiconducting properties were also found when the same pyrene building block was combined with HHTP, resulting in the belt-shaped TP-COF,²⁰ which, similarly to PPy-COF, was found to be highly luminescent and being electrically conductive.

Dual-pore COFs with alternating triangular and hexagonal pores based on the combination of C_3 -symmetric π -conjugated dehydrobenzoannulenes (DBAs) with BDBA (**Scheme 1.4a,b**) were reported to feature luminescent properties ($\lambda_{\text{max}} = 530$ nm, with $\lambda_{\text{exc}} = 365$ nm) with an absorption range of 310-380 nm.⁴³ DBAs are planar macrocycles that form strong metal complexes with Li, Ca, and low-oxidation-state transition metals by donating 2-4 electrons per alkyne as required by the electronic demands of the metals. The small DBA[12] macrocycle has also been converted to a 3D COF with tetra(4-dihydroxyborylphenyl) methane (TBPM).⁴⁴ COFs with luminescent properties have been obtained from DBA[12] and DBA[18] in combination with PDBA, yielding Py-DBA-COF 1 and Py-DBA-COF 2, respectively.⁴⁵ In addition, a mixed-linker approach using both DBA[12] and DBA[18] gave access to Py-MV-DBA-COF. All three COFs were highly luminescent in the solid state. For

DBA-COF 2, a blue-greenish luminescence was observed with $\lambda_{\text{max}} = 483$ nm upon excitation at 365 nm. In contrast to that, Py-DBA-COF 1 and Py-MV-DBA-COF both revealed red-shifted luminescence at $\lambda_{\text{max}} = 530$ nm and $\lambda_{\text{max}} = 528$ nm, respectively, leading to the conclusion that the luminescence of the multicomponent structures is mostly dominated by the DBA[12] units. Other dual-pore COFs have been reported using C_3 -symmetric 9,10-hydroxyphenanthrene trimeric macrocycle (HPCT, **Scheme 1.4c**),⁴⁶ the condensation of which with BDBA, PDBA, and biphenyldiboronic acid led to a series of COFs with star-shaped dual-pore structure. This macrocycle-to-framework strategy was expanded by using tritopic arylene-ethynylene macrocycles (AEMs, **Scheme 1.4d**).⁴⁷



Scheme 1.4. Examples of COFs with a dual-pore structure: (a) DBA-COF-1⁴³/AEM-COF-1,⁴⁷ (b) DBA-COF-2,⁴³ (c) Star-COF-1,⁴⁶ and (d) AEM-COF-2.⁴⁷

In all of the above-mentioned dual-pore macrocycle COFs, the presence of the micropores could not be confirmed by N_2 sorption experiments, indicating limited accessibility of the smaller pores. Contrarily, TPE-Ph COF formed from the boronic acid analog of 1,1,2,2-tetraphenylethylene (TPE) with tetrahydroxybenzene (THB) exhibited a dual-pore system with accessible trigonal pores, featuring different pores of 1.3 and 2.6 nm in size (**Figure 1.4a,b**).⁴⁸ This COF also features aggregation-induced emission (AIE), meaning that the chromophores become emissive in an aggregated state, thus overcoming aggregation-caused quenching (ACQ) that had typically limited the availability of highly emissive COFs, thus granting access to ordered, porous structures for sensing and imaging applications. The TPE building block provides a specific docking site for successive layers owing to its highly defined locked propeller shape. Thus, rotation-induced excitation-energy dissipation is hindered, resulting in an absolute fluorescence quantum yield as high as 32% for the COF. The fluorescence microscopy images

of TPE-Ph COF samples prepared at different reaction times show that the synthesis time, and thus the crystal shape did not alter the luminescent properties of the material (**Figure 1.4c–f**).

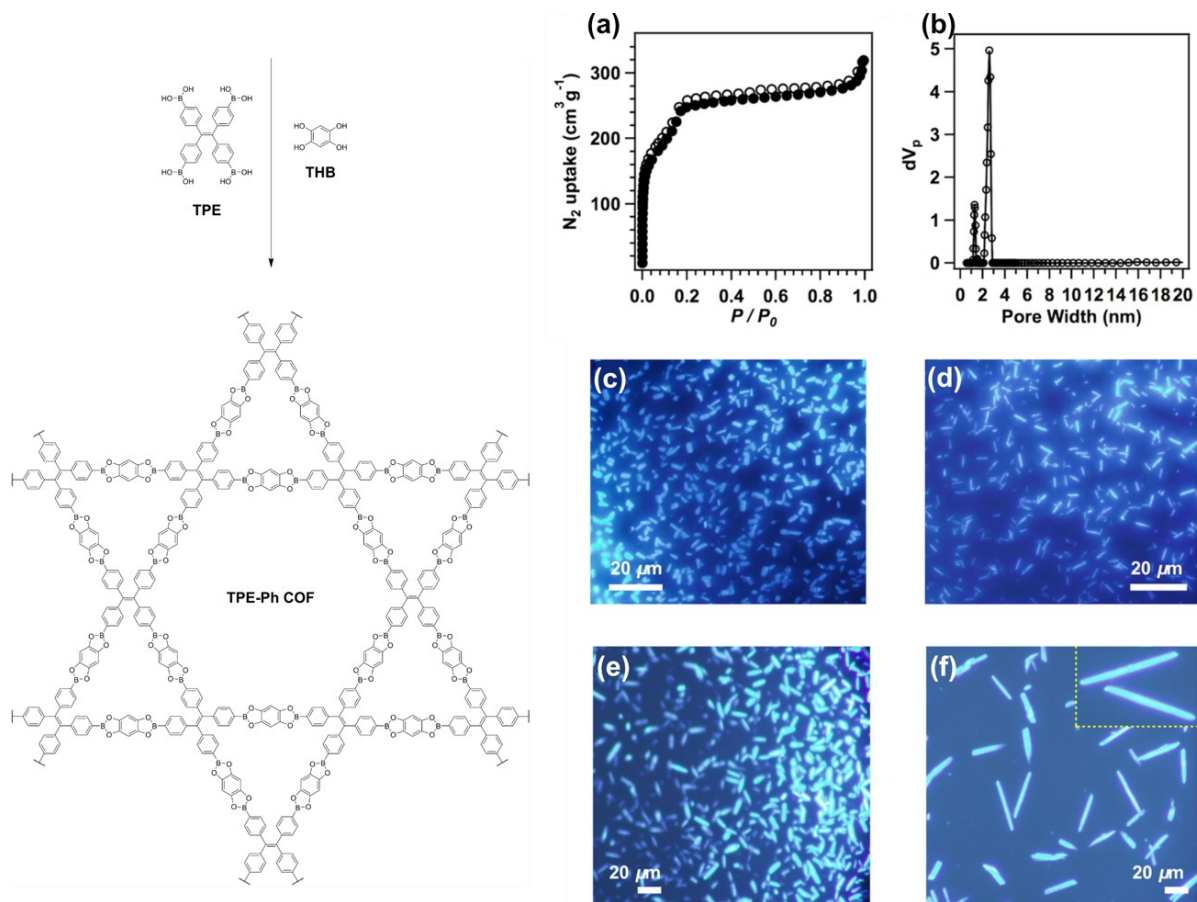
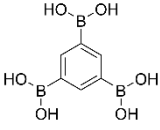
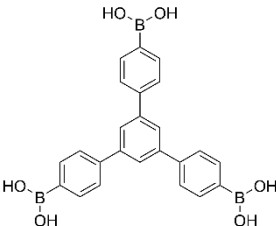
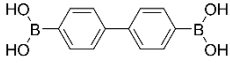
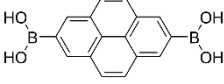
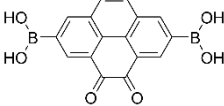
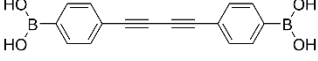
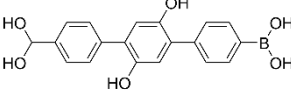
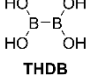
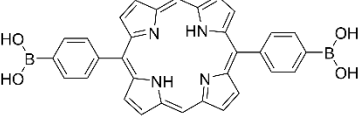
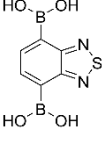
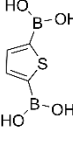
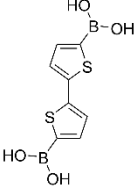
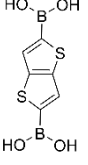
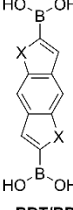
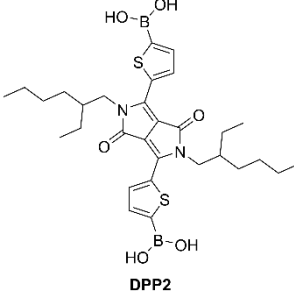
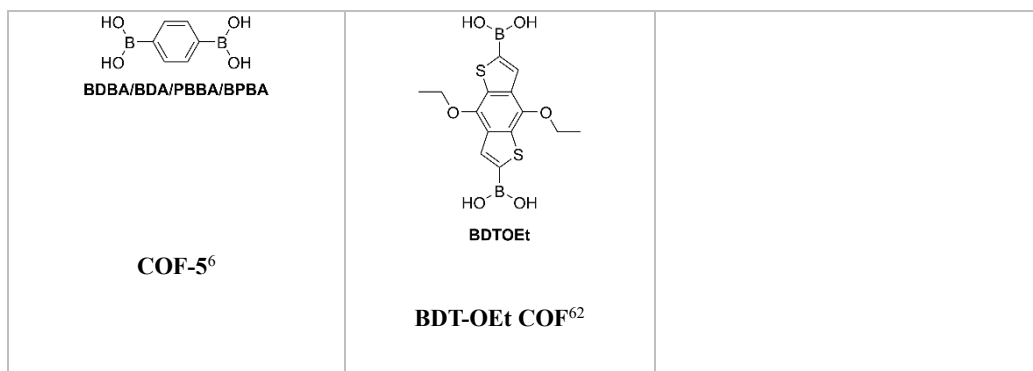


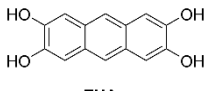
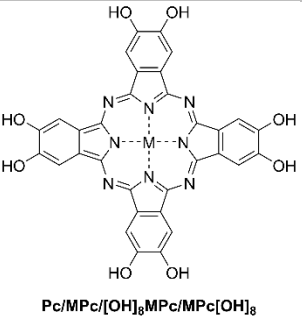
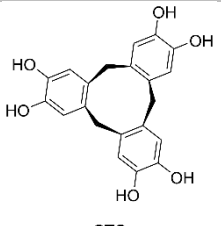
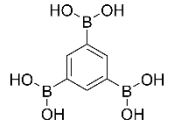
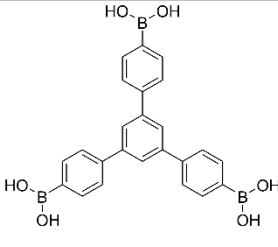
Figure 1.4. Synthesis of dual-pore TPE-Ph COF, (a) N_2 adsorption and desorption isotherms and (b) pore size distribution profile of TPE-Ph COF and the fluorescence microscopy images of TPE-Ph COF samples prepared at different reaction times of (c) 3 days, (d) 10 days, (e) 20 days, and (f) 30 days. Adapted with permission.⁴⁸ Copyright (2016) American Chemical Society.

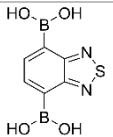
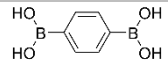
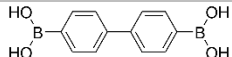

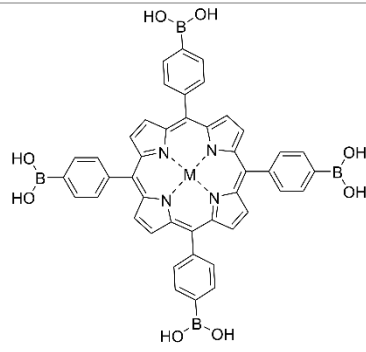
Table 1.2. Examples of HHTP-based 2D boronate ester COFs.

 <p>BTBA/TBA</p> <p>COF-6⁴⁹</p>	 <p>BTPB/BTPA</p> <p>COF-8⁴⁹</p>	 <p>BPBA/BPDA/DPDA</p> <p>COF-10⁴⁹</p>
---	--	--

 <p>PDBA/PDA</p> <p>TP-COF²²</p>	 <p>Dione-COF⁵⁰</p>	 <p>DPBA/DPBDDA</p> <p>HHTP-DPB COF⁵¹</p>
 <p>DHTBA</p> <p>T-COF-OH⁵²</p>	 <p>THDB</p> <p>HTCOF⁵³</p>	 <p>Por</p> <p>TP-Por COF⁵⁴</p>
 <p>BTDADA</p> <p>2D D-A sCOF⁵⁵</p>	 <p>H₄TDB</p> <p>T-COF-1⁵⁶</p> <p>T-COF-2⁵⁶</p>	 <p>H₄BTDB</p> <p>T-COF-3⁵⁶</p>
 <p>H₄TTDB/TTBA/TTDA</p> <p>TT-COF^{57,58}</p> <p>T-COF-4⁵⁶</p>	 <p>X = S: BDT/BDTBA/ H₂BDS/BDTBA</p> <p>X = Se: H₂BDSe</p> <p>X = Te: H₂BDTe</p> <p>X = S BDT-COF⁵⁹⁻⁶² 1-S⁶³</p> <p>X = Se 1-Se⁶³</p> <p>X = Te 1-Te⁶³</p>	 <p>DPP2</p> <p>DPP2-HHTP-COF⁶⁴</p>

**Table 1.3.** 2D boronic ester COFs.

	 <p>THAn</p>	 <p>Pc/MPc/[OH]₈MPc/MPc[OH]₈</p>	 <p>CTC</p>
 <p>BTBA/TBA</p>	<p>R = H COF-18Å⁶⁵</p> <p>R = CH₃ COF-16Å⁶⁵</p> <p>R = CH₂CH₃ COF-14Å⁶⁵</p> <p>R = CH₂CH₂CH₃ COF-11Å⁶⁵</p>	Ph-An COF¹⁴	
 <p>BTPB/BTPA</p>		BTP-COF⁶⁶	

 <p>BTDA</p>			<p>M = Ni 2D-NiPc-BTDA COF⁶⁷</p>	
 <p>BDBA/BDA/PBBA/BPBA</p>				<p>CTC-COF^{68,69}</p>
 <p>BPBA/BPDA/DPDA</p>				<p>CTC-COF-2⁷⁰</p>
 <p>PDBA/PDA</p>				<p>CTC-COF-3⁷⁰</p>
 <p>MP (M = H₂, Zn, Cu)</p>	<p>H₂P-COF^{71,72} ZnP-COF⁷¹ CuP-COF⁷¹</p>			

Owing to their stability, planarity and rigidity, free-base and metallophthalocyanines (MPcs) have been widely used across the fields of material science as components in semiconductors, electrochromic and non-linear optical devices, and catalysis.⁷³ However, polymeric phthalocyanine materials usually lack either the control of molecular alignment or long-range order. These elements are crucial when designing functional materials since device performance can be strongly dependent on the structural order of the active material. Thus, incorporation of these molecules into COFs is an attractive way to control their chemical environment. To date, phthalocyanines (Pcs) have been widely used as core building blocks for boronate ester COFs, which, in combination with linear building blocks, led to tetragonal pore structures.⁷⁴ In addition to the typical condensation reaction between boronic acids and diols, a successful preparation of Pc-containing COFs from acetonide-protected octahydroxyphthalocyanine by Lewis-acid catalyzed *in situ* deprotection has been reported.⁷⁵

Pcs feature great electron-donating properties, they readily engage in π - π stacking interactions, and their properties can be easily tuned by the choice of the core metal. MPc COFs having different central metal species ($M = \text{Co}, \text{Cu}, \text{Zn}$) have been reported to provide good pathways for charge-carrier transport.⁷⁶ Flash-photocatalysis time-resolved microwave conductivity (FP-TRMC) measurements showed that the different central metals led to different charge carrier mobilities, meaning that the charge carrier transport throughout the framework is strongly influenced by the metal species. These metal species are coordinated in the phthalocyanine by four nitrogen atoms leading to a lower electron density of the macrocycles in the following way: CuPc-COF < ZnPc-COF < CoPc-COF. MPc COFs also give rise to *n*-channel semiconductors featuring broad absorption range, panchromatic photoconductivity, high near infra-red (NIR) sensitivity, as well as high charge carrier mobility.⁶⁷ 2D-NiPc-BTDA COF (**Table 1.3**) formed from the electron-withdrawing 1,4-benzothiadiazole diboronic acid (BTDA) and a Ni-based Pc gave access to AA-stacked layers, which provided pathways for charge carrier transport.⁶⁷

A series of studies have focused on constructing COFs containing both electron donor and acceptor units within their framework to provide highly ordered heterojunctions within the COF lattice. A COF consisting of HHTP donor and benzothiadiazole acceptor units showed large on/off photoconductive response and a high-rate charge carrier transport, demonstrating the advantages of combining donor and acceptor units within the framework.⁵⁵ Charge carrier mobility of $1.51 \times 10^{-4} \text{ cm}^2 \text{ V}^{-1} \text{ s}^{-1}$ under Ar and photocarrier generation yield of 3×10^{-3} were determined using FP-TRMC measurements. TP-Por COF (**Table 1.2**) consists of HHTP building blocks and linear porphyrin linkers, giving access to highly defined interdigitated donor–acceptor heterojunctions.⁵⁴ The π -stacked columns of the layered 2D COF provide a path for hole and electron migration in opposite directions in an oriented thin film to the respective electrode. Electrical conductivity and high thermal stability have also been achieved with tetra(*p*-boronic acid phenyl)porphyrin in combination with tetrahydroxyanthracene building block.⁷⁷

Another approach to expand the versatility of chemical reaction routes used for forming COFs as well as to enhance their structural diversity is to use multiple-condensation systems, where one knot and two or three linkers give access to hexagonal and tetragonal multiple-component COFs.⁷⁸ This way, multiple-component electron donor–acceptor systems have been achieved, such as those shown in **Figure 1.5**.

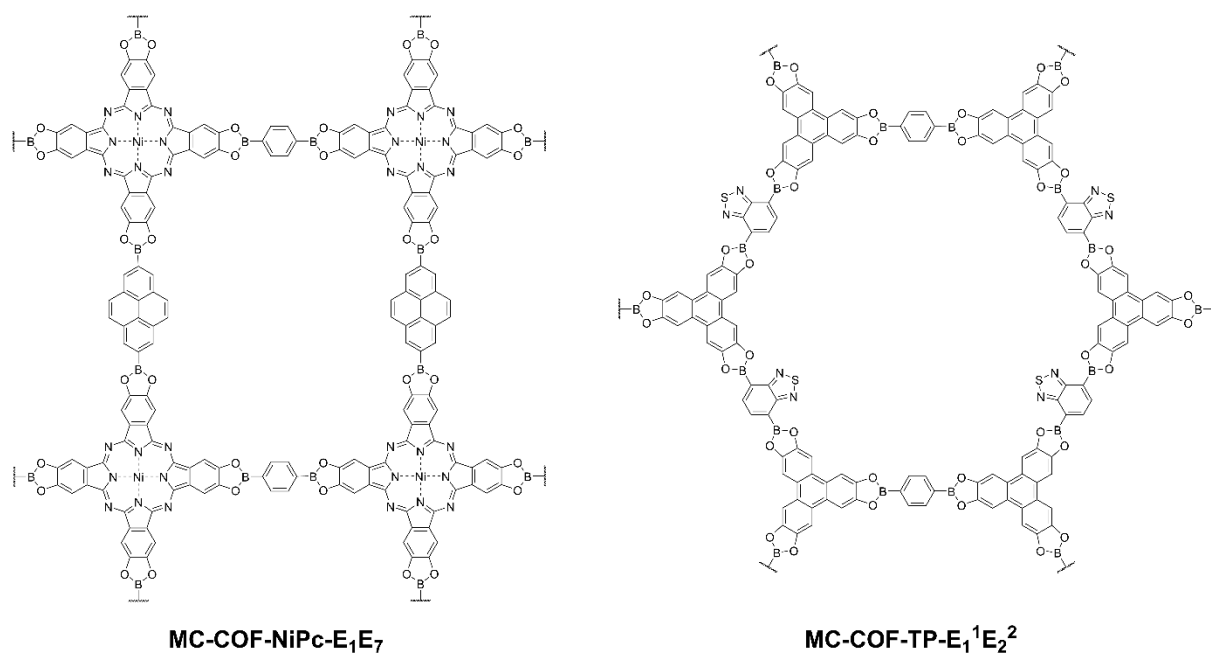


Figure 1.5. Two examples of multiple-component COFs.⁷⁸

HHTP has also been employed as donor in conjunction with naphthalenetetracarboxylic acid diimide (NDIDA) and its pyromellitic derivative (PyrDIDA), resulting in $D_{TP-A_{NDI}}\text{-COF}$ and $D_{TP-A_{PyrDI}}\text{-COF}$, respectively.⁷⁹ Both structures are formed by periodically aligned columnar triphenylene-on-triphenylene and diimide-on-diimide arrays. Steady-state electronic absorption spectra revealed that for $D_{TP-A_{NDI}}\text{-COF}$ no clear charge-transfer band was observed, whereas contrarily, the formation of a charge-transfer complex was observed for $D_{TP-A_{PyrDI}}\text{-COF}$. The differences in charge transfer and charge separation observed for the NDI and PyrDI acceptors highlighted the necessity of appropriate donor–acceptor pairing to obtain efficient structures for optoelectronic and photovoltaic applications. In a similar approach,⁸⁰ donor–acceptor MPc structures were synthesized *via* the co-condensation of metallophthalocyanines containing different central metals as donors, including copper, nickel, and zinc, with a variety of different acceptor molecules, such as naphthalene diimide or perylene diimide building blocks (**Figure 1.6**). Time-resolved transient absorption (TA) spectroscopy and electron spin resonance revealed long-lived charge carrier lifetime, indicating that efficient charge separation at the molecular junctions is possible with these donor–acceptor COFs. Lifetimes reaching up to $\tau_{CS1} = 4.8 \mu\text{s}$ and $\tau_{CS2} = 33 \mu\text{s}$ for $D_{CuPc-A_{PyrDI}}\text{-COF}$ were obtained, showing the potential of these materials to serve as active materials in light-harvesting applications.

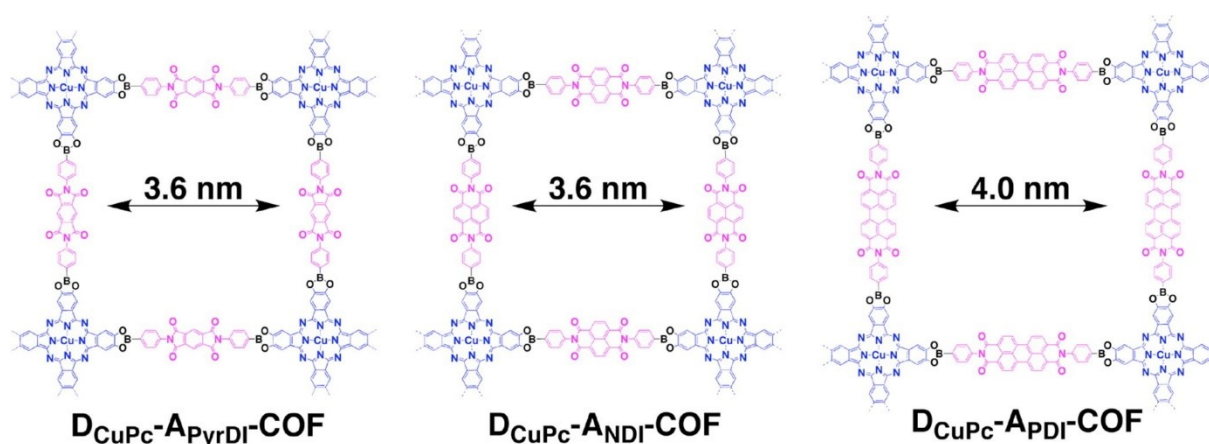


Figure 1.6. Structures of donor–acceptor COFs synthesized through the co-condensation of CuPc with diimide acceptor units. Adapted with permission.⁸⁰ Copyright (2015) American Chemical Society.

Thiophene-based polymers are commonly used as semiconducting active material in organic photovoltaic devices.⁸¹ However, structural disorder of the donor and acceptor phases in such polymers can limit charge-carrier mobility and charge separation in organic bulk heterojunctions.⁵⁷ To overcome these limitations and to obtain deterministic control over the semiconducting segment interactions, the incorporation of thiophene units into COFs has been an attractive goal.

A series of thiophene-containing COFs was synthesized by the co-condensation of HHTP with thiophene-based diboronic acids, such as 2,5-thiophene diboronic acid (H₄TDB) and thieno[3,2-*b*]thiophene-2,5-diboronic acid (H₄TTDB) (for examples, see **Table 1.2**), leading to T-COF-1–4.⁵⁶ Interestingly, using H₄TDB as a building block, the co-condensation with HHTP resulting in the formation of boronate ester linked T-COF-1 was only possible under the strict exclusion of water and 3:2 ratio of the diboronic acid and HHTP. Deviations from these conditions resulted in mixed products, where the diboronic acid units formed boroxine rings that subsequently co-condensed with HHTP to give access to T-COF-2. Several thiophene-based COF structures, *e.g.* based on thieno[2,3-*b*]thiophene,⁵⁷ benzo[1,2-*b*:4,5-*b'*]dithiophene,⁵⁹ and ethoxy-functionalized benzo[1,2-*b*:4,5-*b'*]dithiophene,⁶² have been studied in the context of photovoltaics (see **section 1.2.7.4**).

Duhović and Dincă described the effect of incorporating heteroatoms such as S, Se, and Te into COFs by using benzodithiophene and the respective heavier chalcogen analogs as building blocks with HHTP to give 1-S, 1-Se, and 1-Te COFs.⁶³ Pressed pellets of the materials revealed that the electrical conductivity, measured with a two-point probe setup, increased by a factor of two for the Se-containing COF ($8.4 \times 10^{-9} \text{ S cm}^{-1}$) and nearly by a factor of three for the Te-based COF ($1.3 \times 10^{-7} \text{ S cm}^{-1}$) as compared to thiophene ($3.7 \times 10^{-10} \text{ S cm}^{-1}$). Later, Bein, Medina and co-workers reported a highly crystalline DPP2-HHTP-COF consisting of diketopyrrolopyrrole bithiophene and HHTP building blocks. The DPP2-HHTP-COF revealed electrical conductivity of up to $2.2 \times 10^{-6} \text{ S cm}^{-1}$.⁶⁴ In addition, the DPP2-HHTP-COF features intriguing optical properties including strong absorption over the visible

spectral range, broad emission into the NIR and a singlet lifetime of over 5 ns attributed to the formation of molecular stacks with J-type interactions between the DPP successive building blocks in the COF scaffold.

In terms of possible applications for COFs not only optical or electronic properties of the building blocks play an important role but also structural features can be crucial for certain applications. To this end, curvature in the COF structure can give access to new architectures and properties, such as chirality, high surface areas, or enhanced charge-carrier mobilities.⁸² Cyclotricatechylene (CTC) has been used as building block with BDBA to obtain undulated 2D CTC-COF (**Table 1.3**).⁶⁸ Interestingly, the bowl-shaped core unit of the COF led to a larger surface area as compared to its planar analogue COF-5, resulting in higher hydrogen uptake owing to its wavy structure and despite its smaller pore volume. The series of CTC-COFs was later expanded by co-condensing CTC with 4,4'-biphenyldiboronic acid (BPDA) and PDBA to yield CTC-COF-2 and CTC-COF-3, respectively.^{68,70} Both COFs featured smaller pore size distributions compared to their planar analogues COF-10 and TP-COF, which was attributed to the curved twisted structure of the respective CTC-COFs.

A wavy 2D COF structure based on core-twisted hexabenzocoronene (HBC) was recently reported by Melle-Franco, Khlobystov, Mateo-Alonso, and co-workers (**Figure 1.7**).⁸² The high order of the structure was attributed to the self-complementary concave-convex nature of the building block, which gave access to chair-like honeycomb facets and aligned mesoporous channels. Moreover, a full 3D analysis by transmission electron microscopy (TEM) was carried out from both face-on and edge-on perspective, confirming the presence of both free-standing individual chair-like hexagons as well as zigzag and armchair edges. Furthermore, using TEM tomography the correlations between the observed hexagons, the channel cross sections, and chair-like features of the COF were indicated. Interestingly, no disruption of the interlayer π - π stacking distance was observed as a result of the twisted nature of the framework.

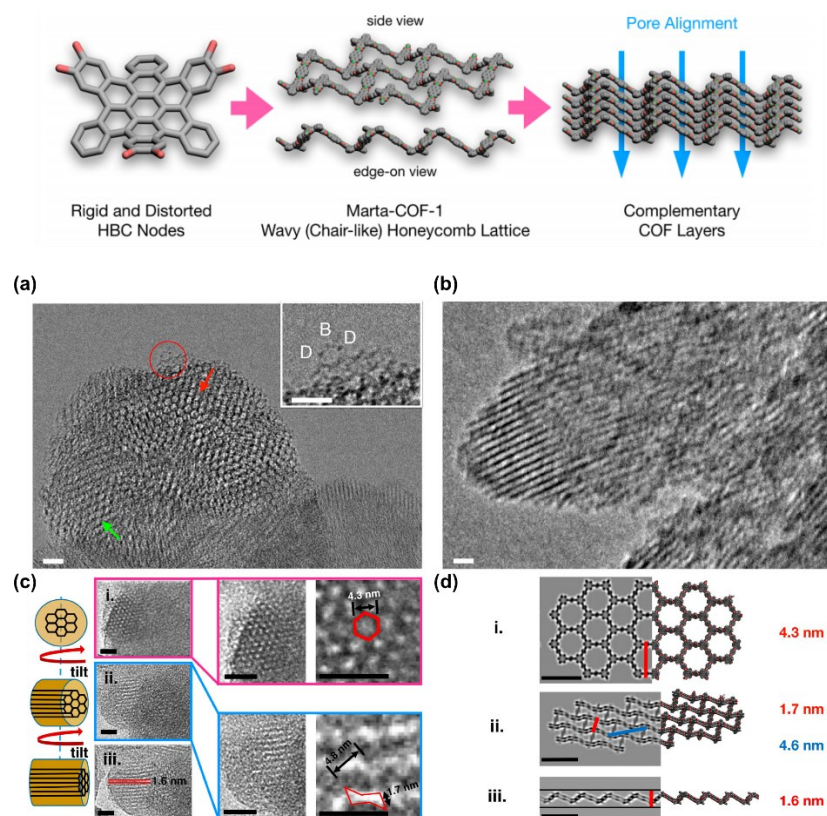


Figure 1.7. Schematic representation of the rigid and distorted HBC nodes and incorporation into Marta-COF-1. HR-TEM images of highly crystalline domains of the COF are shown: (a) face-on and (b) edge-on (scale bars 10 nm). (c) HR-TEM images showing the COF particle rotated and imaged at 70° tilt angle within the plane of the page (panels i–iii) (scale bars 10 nm). (d) Merged quantitative scanning transmission electron microscopy (QSTEM) HR-TEM simulations (left) with the respective geometry-optimized models (right) in face-on (i), chair-like (ii), and edge-on (iii) configuration (scale bars 5 nm). Adapted with permission.⁸² Copyright (2019) American Chemical Society.

Although some examples of 3D boronic-acid-derived COFs have been reported (**Table 1.5**), they remain significantly rarer compared to the related 2D structures. The first 3D COFs were synthesized by Yaghi and co-workers by the combination of triangular and tetrahedral nodes *via* the self-condensation of tetrahedral TBPM and its silicon-derivative tetra(4-dihydroxyborylphenyl)silane (TBPS), giving access to boroxine-linked COF-102 and COF-103, respectively, both of **ctn** topology.⁷ Additionally, COF-105 (**ctn**) and COF-108 (**bor**) have been obtained by co-condensation of HHTP with TBPM or TBPS, respectively. All structures showed high thermal stabilities, high surface areas, up to $4210 \text{ m}^2 \text{ g}^{-1}$ for COF-103, as well as extremely low densities (for the simulated structures of selected 3D COFs, see **Figure 1.8**). High surface area of $5083 \text{ m}^2 \text{ g}^{-1}$ has also been reported for DBA-3D COF (**bor**), which features the DBA[12] building block, opening access to the possibility of incorporating a metal within the DBA cavity (**Table 1.5**).⁴⁴ High uptake of ethane and ethylene gas was observed for this COF.

Table 1.4. Boroxine-based COFs. t.b.n = to be named.

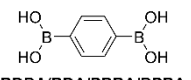
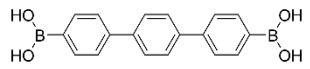
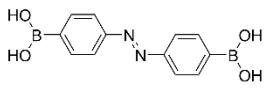
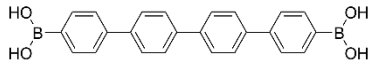

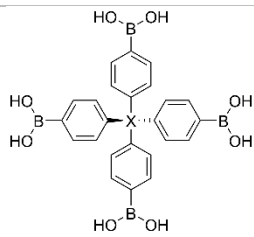
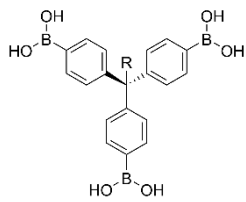
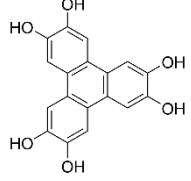
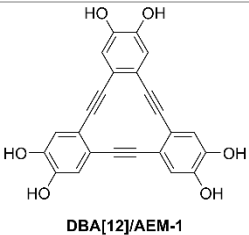
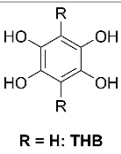
 <p>BDBA/BDA/PBBA/BPBA</p> <p>COF-1,^{6,33,47,83-103}</p>	 <p>TPDA</p> <p>t.b.n.⁸⁵</p>	 <p>ABBA/ABDA</p> <p>surface COF ABBA¹⁰⁴</p>
 <p>QPDA</p> <p>t.b.n.⁸⁵</p>	 <p>PDBA</p> <p>PPy-COF,^{42,85} Pyrene-COF⁶⁰</p>	

Table 1.5. 3D boronate ester COFs.

	 <p>X=C: TBPM</p> <p>X=Si: TBPS</p>	
self-condensation	X = C COF-102 ^{7,32,105-107}	R = tolyl COF-102-tolyl ¹⁰⁸
(boroxine formation)	X = Si COF-103 ^{7,105}	R = allyl COF-102-allyl ¹⁰⁶
		R = -(CH₂)₁₁-CH₃ COF-102-C₁₂ ¹⁰⁶
 <p>HHTP</p>	X = C COF-105 ^{7,105}	
	X = Si COF-108 ^{7,105}	

 <p style="text-align: center;">DBA[12]/AEM-1</p>	X = C DBA-3D-COF 1⁴⁴	
 <p style="text-align: center;">R = H: THB</p>	X = C MCOF-1¹⁰⁹	

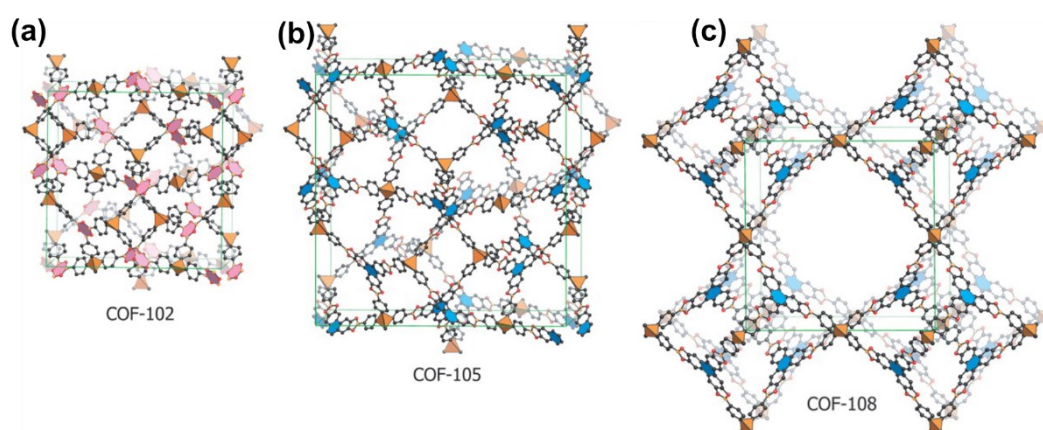
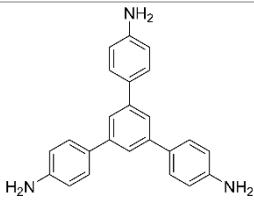
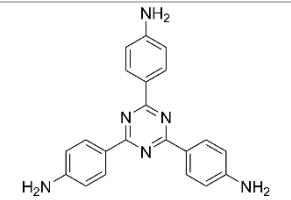
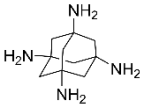
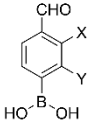
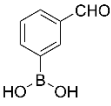
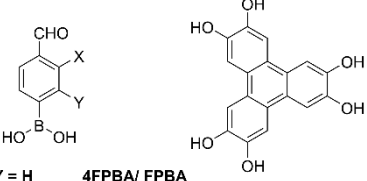
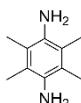
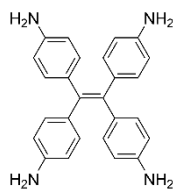
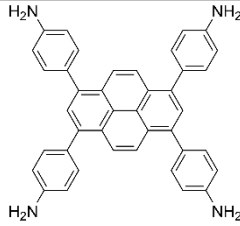
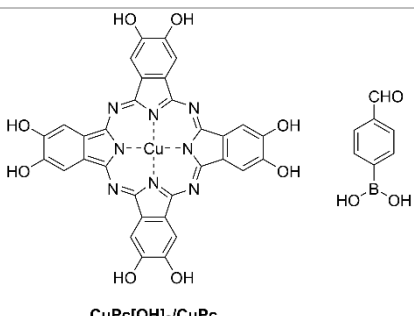


Figure 1.8. Structure and connectivity of different 3D COFs based on PXRD and modeling. (a) COF-102, (b) COF-105, and (c) COF-108. Adapted with permission.⁷ Reprinted with permission from AAAS.

To expand the versatility and structural diversity and to overcome limitations arising from the availability of only a few chemical reactions suitable for COF synthesis, the development of new approaches and reaction systems is a crucial task. To this end, double-stage connection approaches using two types of covalent bonds have been reported, featuring both an imine bond and a boronate ester or boroxine linkage, leading to COFs with enhanced structural complexity and diversity (**Table 1.6**). These materials have revealed high surface areas as well as high hydrogen adsorption capacity,^{110,111} and the obtained materials feature pore geometries ranging from hexagonal (NTU-COF-1¹¹⁰) and tetragonal (*e.g.* CuPc-FPBA-ETTA COF¹¹¹) to 3D structures (DL-COF-1 and DL-COF-2¹¹²). Interestingly, as compared to boroxine linked COFs, such hybrid COF structures, such as sCOFA (**Table 1.6**), have been reported to feature higher stability,¹¹³ with retention of high crystallinity of the material even after storage under ambient conditions for 20 days.

Table 1.6. COFs prepared by a double linkage motif.

	 <p>TAPB/ Tab/ TPB/ 3PB/ TPBA</p>	 <p>TAPT/ TATTA/ Tta/ TT-amine/ TTA</p>	 <p>TAA</p>
 <p>X = H, Y = H 4FPBA/ FPBA X = F, Y = H FFPBA X = H, Y = F FFPBA X = F, Y = F DFFPBA</p>	<p>X = H, Y = H NTU-COF-1¹¹⁰</p> <p>X = H, Y = H sCOFA¹¹³</p>	<p>X = H, Y = H TATTA-FPBA COF¹¹¹</p> <p>X = F, Y = H TATTA-FFPBA COF¹¹¹</p> <p>X = F, Y = F TATTA-DFFPBA COF¹¹¹</p>	<p>X = H, Y = H DL-COF-1¹¹²</p> <p>X = H, Y = F DL-COF-2¹¹²</p>
 <p>3FPBA</p>	<p>sCOFB¹¹³</p>		
 <p>X = H, Y = H 4FPBA/ FPBA X = F, Y = H FFPBA X = F, Y = F DFFPBA</p> <p>HHTP/ TP</p>	<p>X = H, Y = H NTU-COF-2¹¹⁰</p>	<p>X = H, Y = H HHTP-FPBA-TATTA COF¹¹¹</p> <p>X = F, Y = H HHTP-FFPBA-TATTA COF¹¹¹</p> <p>X = F, Y = F HHTP-DFFPBA-TATTA COF¹¹¹</p>	

	 <p style="text-align: center;">TMBDA</p>	 <p style="text-align: center;">ETTA/ 4PE</p>	 <p style="text-align: center;">Py/ PyTTA</p>
 <p style="text-align: center;">CuPc[OH]₈/CuPc</p>	<p>CuPc-FPBA-TMBDA COF¹¹¹</p>	<p>CuPc-FPBA-ETTA COF¹¹¹</p>	<p>CuPc-FPBA-PyTTA COF¹¹¹</p>

COFs are typically limited to lower valencies of 3 and 4 as a result of sp^2 - and sp^3 -hybridization of the light element constructing the COFs. Very recently, the diversity of COFs was expanded using the concept of higher valency,¹¹⁴ where valency of 8 was introduced using building blocks with phosphonic acid groups (**Figure 1.9**). The synthesis of BP-COF-1 is based on a molecular dehydration reaction, in which eight borophosphonic acid BPA-1 linkers react to form a cubic borophosphonate node under elimination of eight water molecules per cube. The generality of the concept was shown using BPA-linkers 2–5 to obtain a series of related COFs (**Figure 1.9a**). Addition of aqueous concentrated HCl to a reaction mixture containing BPA-1 resulted in the formation of a new crystalline phase of large single crystals with infinite-rod topology (**Figure 1.9d**), where the cubic borophosphonates were replaced by infinite 1D B–O–P rods of alternating tetrahedral boron and phosphorus building units connected by phenyl groups with an interlayer spacing of 5.47 Å.

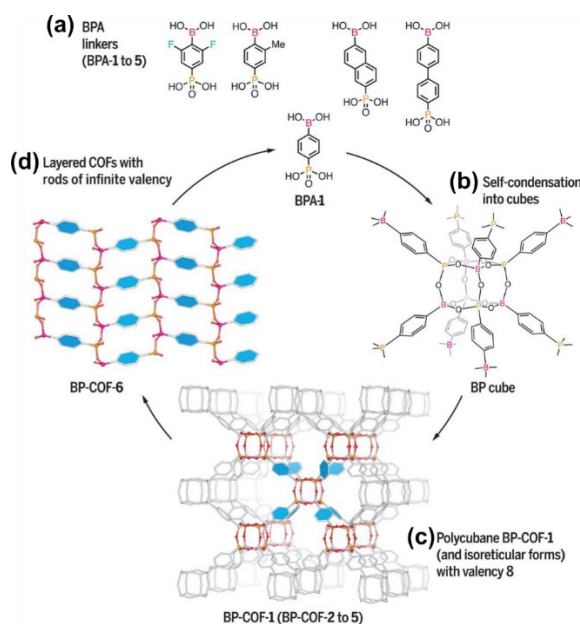


Figure 1.9. (a) BPA linkers 1–5 with two different functionalities (boronic acid and phosphonic acid groups); (b) and (c) self-condensation of BPA-1 to form BP cubes with a valency of 8, (c) and the resulting polycubane BP-COF-1. (d) Upon addition of acid, BP-COF-1 rearranges to form layered BP-COF-6 with infinite rod valency. Reprinted¹¹⁴ with permission from AAAS.

1.2.5 Post-synthetic Modification of Boronic-Acid-derived COFs

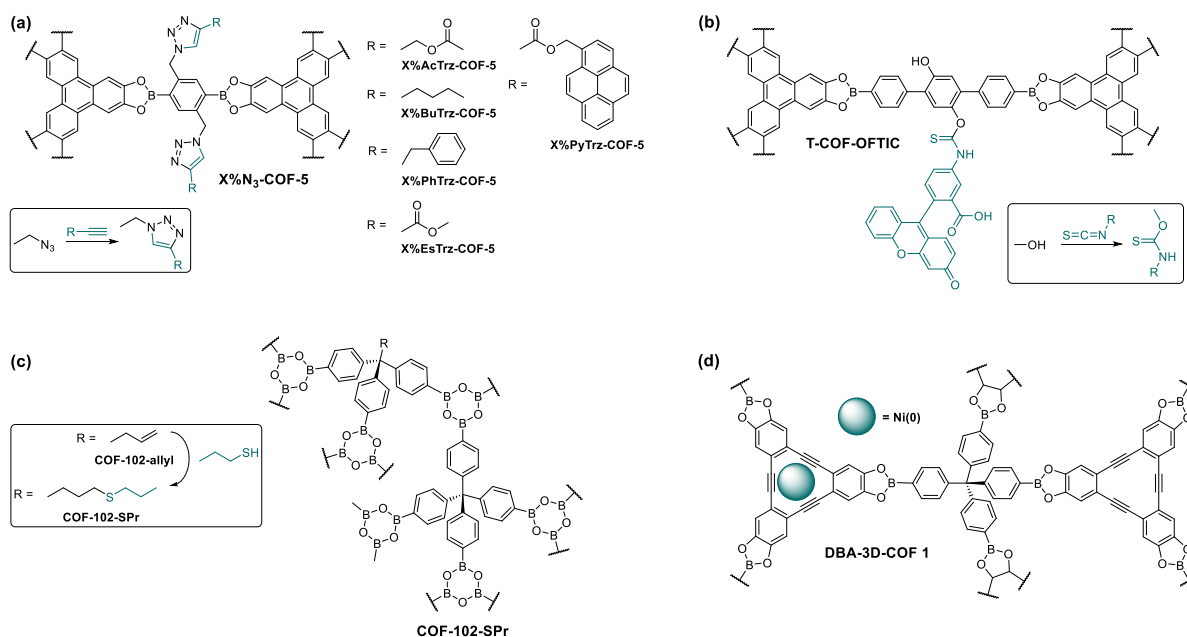
Post-synthetic modification (PSM) of COFs allows to systematically modify the pore chemical environment in a bottom-up approach⁵ by further converting pre-installed functional groups to a desired function or by incorporating metal ions or particles into the COF backbone after its formation.¹¹⁵ This approach enables the introduction of a wide range of functional moieties into the COF structures and minimizes the involvement of undesired side reactions during reticulation. Thus, a careful design of the post-synthesis scheme is required, where the integrity of the COF structure is maintained during the process.

Using the post-synthetic route, boroxine and boronate ester COFs have been modified through several strategies, such as metal incorporation, covalent-bond formation, and monomer truncation.¹¹⁶ The most common reactions for pore-wall modifications are addition and substitution reactions. The first PSM of COFs by covalent-bond formation was demonstrated by employing azide-alkyne cycloaddition.¹¹⁷ To tune the density of the wall-anchored groups, a mixed-linker strategy was employed, in which a mixture of azide-functionalized benzenediboronic acid (N_3 -BDBA, **Scheme 1.5a**) and BDBA was converted with HHTP to boronate ester $X\%N_3$ -COF-5 ($X = 5, 25, 50, 75, \text{ and } 100$). Subsequently, the COFs were functionalized through click chemistry by various alkynes containing long alkyl chains, polar ester groups, and pyrene in quantitative yields. This approach has also been used to functionalize Pc-containing boronate ester N_3 -NiPc-COF and donor-acceptor $[C_{60}]_y$ -ZnPc-COF,¹¹⁸ the latter having phthalocyanine as an electron donor and fullerene as an electron acceptor.

Hydroxyl groups have been used as anchoring sites for PSM of COFs due to their small size, diverse reactions with other functional groups, and great variety of available linker molecules. Medina, Bein, and co-workers⁵² synthesized hydroxyl-functionalized mesoporous boronate ester T-COF-OH (**Scheme 1.5b**), which was post-synthetically labeled with fluorescein-isothiocyanate (FTIC) by forming *o*-thiocarbamate bonds. The fluorescent dye allowed for the visualization of the material in a fluorescence microscope, indicating a successful PSM reaction.

Monomer-truncation strategy was employed for the functionalization of boroxine-linked 3D COF-102.¹⁰⁶ Tetrahedral TBPM building block was modified by replacing one of its four arylboronic acid groups with a dodecyl or an allyl functional group. The co-condensation of the modified TBPM linkers with pristine TBPM led to boroxine-linked 3D COF-102-C₁₂ and COF-102-allyl structures, respectively. High loading levels of >30% of the truncated building blocks still resulted in crystalline COF structures with high surface areas. In a similar approach, tolyl-functionalized COF-102 was formed by the co-condensation of 4-tolylboronic acid and TBPM.¹⁰⁸ The PSM¹¹⁹ of COF-102-allyl was carried out under typical thiol-ene reaction conditions by adding propanethiol to a solution containing a photoinitiator and COF-102-allyl. The resulting thio-modified COF-102-SPr (**Scheme 1.5c**) retained the long-range order and identical **ctn** network topology with COF-102-allyl.

The periodic structure of COFs provides a platform for uniform ligand distribution with catalytically active metals throughout the structures, allowing for the effective isolation of the active sites of the catalyst.¹¹⁶ Different metals have been incorporated into COFs taking advantage of metal-ligand interactions. McGrier and co-workers¹²⁰ metalated a mesoporous 3D COF prepared from C₃-symmetric π -electron conjugated triangular DBA (**Scheme 1.5d**) and four-fold symmetric TBPM building blocks. Treatment of the COF with a nickel complex resulted in a material with 10 wt% of Ni, with retention of COF crystallinity and minimal reduction of surface area.



Scheme 1.5. PSM approaches for the synthesis of (a) X%N₃-COF-5,¹¹⁷ (b) T-COF-OFTIC,⁵² (c) COF-102-SPr,¹⁰⁶ and (d) DBA-3D-COF 1.¹²⁰

An elegant approach to modify the COF skeleton was demonstrated using cycloaddition reaction. A photoresponsive anthracene unit was used with BTBA (**Table 1.3**) to synthesize a structurally dynamic boronic ester Ph-An-COF (**Figure 1.10**).¹⁴ The anthracene columns in the COF were situated in eclipsed stacking mode with an interlayer distance of 3.4 Å, which is favorable for photoinduced [4π+4π] cycloaddition reactions. Thus, irradiation of Ph-An-COF deposits induced the cycloaddition reaction of the anthracene units forming concave–convex shaped dimers. The dimerization resulted in drastic conformational changes in the COF backbone and triggered a structural modification of layers (**Figure 10d**). The XRD pattern of the modified COF was similar to that of Ph-An-COF but with decreased reflection intensity, which was attributed to the relatively flexible conformation of concave–convex skeletons. The cycloaddition reaction was thermally reversible, and heating regenerated the planar anthracene units and the Ph-An-COF structure. The structural transformations led to profound changes in the properties and functions, including gas adsorption, photo-absorption, and luminescence.

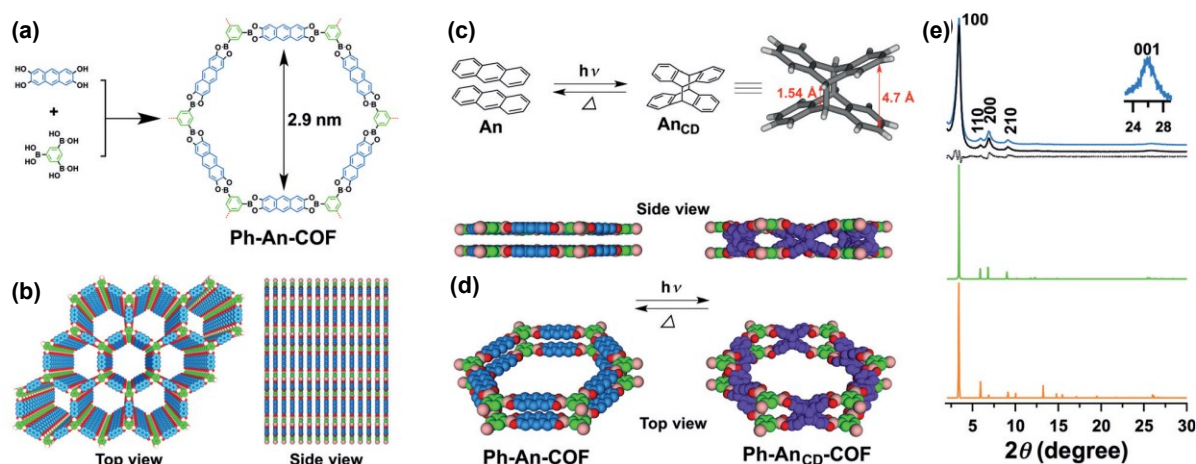


Figure 1.10. (a) Synthesis of PH-An-COF. (b) Top and side views of Ph-An-COF. (c) $[4\pi + 4\pi]$ Cycloaddition reaction upon irradiation, the formation of an anthracene dimer, and thermal reversibility of the reaction. (d) Side and top views of the structural changes of the COF upon photoirradiation and thermal stimulation. (e) PXRD patterns of Ph-An-COF: experimentally observed (blue curve), Pawley refined (black curve), their difference (dotted curve), and the patterns simulated using the eclipsed AA (green curve) and staggered AB (orange curve) stacking modes. Reprinted with permission.¹⁴

1.2.6 Processing

Typically, COFs are obtained as insoluble microcrystalline powder precipitates from reactive precursor solutions. This feature imposes a great challenge for their processing and surface growth. To enable the utilization and performance assessment of COFs for applications, particularly as functional devices, developing synthesis routes that provide ordered COF-on-surface deposition is essential. In the following, we will briefly present different methodologies developed for the preparation of colloidal COF particles and thin films.

Colloidal COFs

One route to gain control over the COF growth process is aiming at limiting the fast precipitation of agglomerated COF crystallites, namely stabilizing COF particle suspensions. Addressing this challenge, Dichtel and co-workers¹²¹ demonstrated the stabilization of four boronate ester-linked COFs, COF-5, COF-10, TP-COF, and HHTP-DPB COF, as colloidal suspensions by adding nitrile-containing co-solvents to the reaction mixture. Acetonitrile serves as a surface stabilization agent of the COF crystallites by interacting with the boronate linkages to suppress the attractive forces between the crystallites, disrupting the aggregation and precipitation without inhibiting polymerization. For example, in the presence of 55% acetonitrile relative to the solvent volume, crystalline COF-5 was observed within 15 min reaction time with relatively uniform particle size distribution. Mean radius of 21 nm at 25 min and 30 nm at 2 h was determined by line broadening calculation of the SAXS data. The particle sizes of the COFs were comparable to the 20–40 nm crystallite sizes of COF-5 precipitates prepared from initially homogeneous conditions in the presence of TCAT modulator in 5 days and determined by

X-ray diffraction.³⁴ At a longer reaction time of 20 h at 90°C, the average particle size of the COFs synthesized with varying monomer and acetonitrile concentrations was measured by dynamic light scattering (DLS). Stable colloidal COF particles with average sizes of 240 nm, 100 nm, and 45–60 nm were observed with acetonitrile concentrations of 15, 35, and >55 vol%, respectively. With acetonitrile concentrations >55 vol%, the average size was relatively invariant, being comparable to the 20–40 nm crystalline domains of precipitated COF-5 powders. After colloidal COF formation, the particle sizes were not affected by dilution with non-nitrile solvents or by exposure to different acetonitrile concentrations, even at elevated temperatures. This synthesis approach provides stable colloidal COF suspensions when acetonitrile is used at volume fractions of 15–95%. Interestingly, the COF suspensions were reported to be stable for several weeks at room temperature with no apparent precipitation (*i.e.* particle aggregation).

The ability to obtain well-dispersed colloidal COF solutions has also allowed access to single-crystalline boronate ester-linked⁴¹ and boroxine-linked¹²² COFs. Controlled COF formation was studied using a two-step approach, in which the nucleation and growth processes are essentially separated, resulting in three boronate ester single crystal 2D COFs: COF-5, COF-10, and TP-COF. First, using acetonitrile as co-solvent, crystalline COF colloids with an average diameter of 30 nm were prepared to serve as seeds for the growth of larger crystals. Slow addition of monomer solutions at 0.10 equiv./h to the existing colloidal COF crystals allowed for crystal growth without the formation of new nuclei, whereas the opposite was found for fast addition at 1.0 equiv./h, eventually leading to a large particle size distribution. HR-TEM showed that the obtained COF-5 particles have six-fold symmetry and hexagonal faceting in projection along the *c*-crystal axis. The singled-out COF-5 crystals were between 300 and 500 nm in diameter.

The well-dispersed, single-crystalline COF colloids enabled the characterization of their photophysical properties by optical transient absorption spectroscopy.¹²³ An improved signal quality of three orders of magnitude in comparison to polycrystalline powders was found, enabling the study of excited state dynamics and optical signatures of COF crystals. The studies revealed that excitons in smaller COF particles undergo exciton-exciton annihilation more easily due to their confinement to smaller effective volume in comparison with larger particles. In a later study,¹²² the synthesis of COF crystallites was expanded to boroxine-linked colloidal frameworks including four 2D (Ph-COF, BPh-COF, Py-COF, DBD-COF) COFs and one 3D COF (TMPh-COF) (**Figure 1.11**). The syntheses were carried out under solvothermal conditions in the presence 50 vol% of acetonitrile. Colloidal stabilization enabled detailed structural analysis by HR-TEM, and an investigation of the optoelectronic nature of these materials with excitation–emission matrix fluorescence spectroscopy (EEMS). The EEMS studies of PPy-COF, for example, indicated the formation of J-aggregates and excited charge-transfer complexes, where interlayer pyrenes are in proximity through the COF matrix. Additionally, colloidal COF solutions were

used for the synthesis of free-standing transparent COF films¹²¹ and the preparation of spray-coated 2D COF coatings.¹²⁴ For further details, see **sections 1.2.6.2** and **1.2.7.5**.

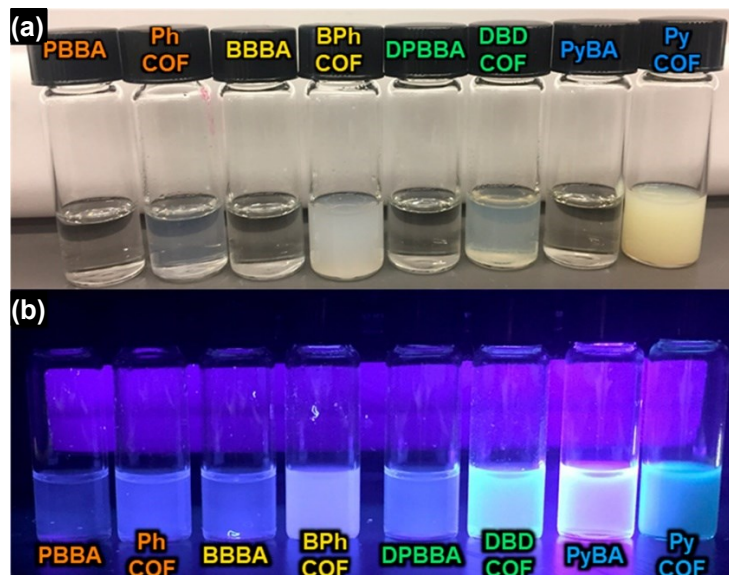


Figure 1.11. COF monomer solutions and the respective COF nanocrystal suspensions (a) under natural light and (b) under UV irradiation. Reprinted with permission.¹²² Copyright (2019) American Chemical Society.

An alternative synthetic method to prepare boronate-ester-linked colloidal COFs was realized in the presence of a monofunctional modulator, TCAT, a capping agent, which suppresses successive nucleation but permits seeded growth.¹²⁵ The inhibition of colloid nucleation was found to be concentration dependent, where TCAT loadings of 0-5 equivalents relative to PDDBA failed to suppress successive nucleation, resulting in large particles, whereas the presence of 10 and 15 equivalents of TCAT resulted in the formation of stable colloidal COF suspensions. To expand the size of the existing 2D COF colloidal seeds, 15 equivalents of the TCAT modulator with varying amounts of COF building blocks were added to the suspension, showing an increase in crystallinity and particle size over the course of 2 days. Varying the monomer concentration from 0 to 4.5 equivalents, relative to that present in the initial colloids, resulted in an average particle size increase from 60 to 450 nm, respectively, in 2 days. TEM studies of the COF colloids grown in the presence of TCAT confirmed that the colloids primarily expand vertically by oriented attachment of oligomers in the out-of-plane direction.

Thin Films

The first COF thin films were introduced by Dichtel and co-workers and were obtained under solvothermal conditions, where COF powders and films were produced simultaneously in the same reactor using the so-called *in situ* approach. The inclusion of single-layer graphene (SLG) modified

surfaces in the reaction mixture, which served as a preferred site for film nucleation, allowed for epitaxial growth of COF films (**Figure 1.12**).¹²⁶ Oriented 2D COF thin films on SLG of COF-5, TP-COF (**Table 1.2**), and NiPc-PBBA COF were prepared supported by several different substrates, such as polycrystalline Cu films on Si wafers (SLG/Cu), fused SiO₂ (SLG/SiO₂), or SiC (SLG/SiC). All resulting films were crystalline and oriented with the 2D aromatic molecular planes stacked perpendicular to the substrate with a full coverage of the surface. To evaluate the photophysical properties, COF films grown on transparent fused SLG/SiO₂ as substrate material were employed, enabling UV/Vis/NIR spectroscopy. The same approach was used to prepare oriented thin films of HHTP-DPB COF (**Table 1.2**) on SLG modified transparent fused SiO₂ substrate.⁵¹ Later, Dichtel and co-workers monitored the growth of ZnPc-based COF thin films on SLG-modified fused SiO₂, where the crystallite orientation in the film was strongly dependent on the solvents used for the synthesis.⁷⁴ Solvent mixture of DMAc/*o*-dichlorobenzene (DCB) led to crystalline but unoriented films, whereas dioxane, MeOH, DMAc, and DCB in 3:1:2:1 (v/v) ratio resulted in the formation of oriented and crystalline films.

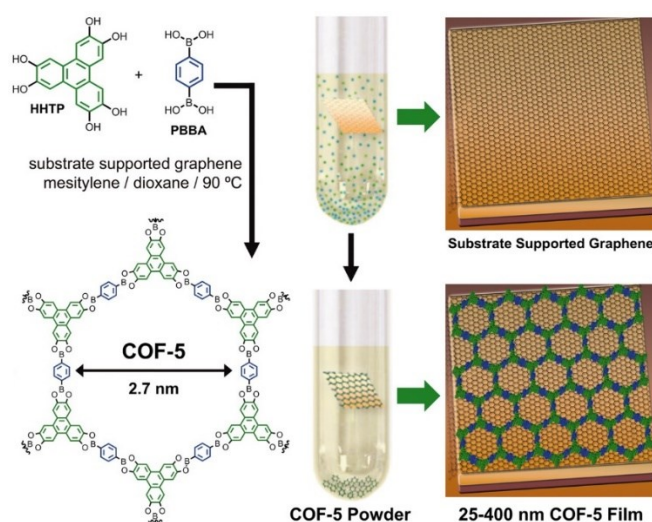


Figure 1.12. An illustration of the solvothermal synthesis of COF thin films on substrate-supported single layer graphene. Co-condensation of HHTP and PBBA leads to both COF-5 powder as well as film on the graphene-modified surface. Reprinted¹²⁶ with permission from AAAS.

Using solvothermal conditions, Medina et al.⁵⁹ demonstrated the non-epitaxial synthesis of oriented COF films on SLG-free substrates, such as transparent conductive oxides (TCO), *i.e.* indium-doped tin oxide (ITO), gold substrates, and even fused silica, as an example for amorphous substrates. Thin films of BDT-COF (**Table 1.2**) were synthesized in a bottom-up approach using a stainless-steel autoclave equipped with a Teflon liner and substrate holder. The substrates were inserted horizontally in the substrate holder allowing them to be evenly immersed in the reactive precursor solutions. In this way, thin, porous, and highly oriented BDT-COF films were obtained (**Figure 1.13**), grazing incidence diffraction (GID) measurements of which revealed the preferential horizontal alignment of the 2D COF sheets relative to the substrate. Furthermore, halting the film synthesis reaction at 2 h revealed films consisting of free-standing pillars in close vicinity of each other, indicating island-growth mechanism with crystal domain sizes in the *c*-direction being smaller than those obtained at longer reaction times. In addition, the ability of the electron donor BDT-COF to host an electron acceptor phase in the oriented COF channels was investigated by TA measurements, which indicated the stabilization of hole-polaron charge carriers at the COF backbone, featuring elongated life-time upon inclusion of an electron-accepting phase.

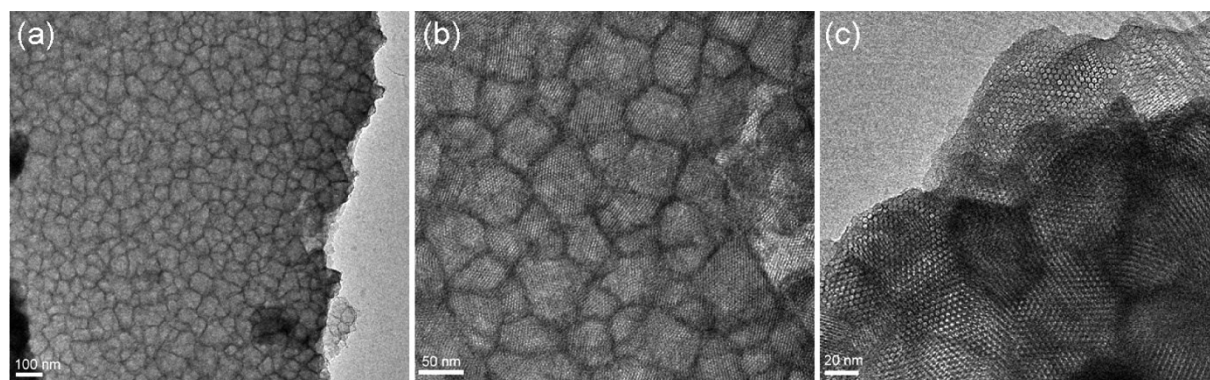


Figure 1.13. TEM micrographs of a BDT-COF thin film fragment grown on a gold surface showing the hexagonal structure along the *c*-axis at different magnifications. Reprinted with permission.⁵⁹ Copyright (2014) American Chemical Society.

Boronate ester and boroxine COF films and powders have also been shown to form under mild conditions through vapor-assisted conversion (VAC) at room temperature.⁶⁰ In the VAC procedure, a COF precursor solution was deposited on a substrate, such as glass, TCOs, or gold, providing a thin reactive layer solution. The substrates were then placed in a desiccator equipped with a small vessel containing mesitylene and dioxane for 72 h. After the given reaction time, evenly covered, porous, and highly crystalline films of boronate ester BDT-COF (**Table 1.2**), COF-5 (**Table 1.2**), and boroxine PPy-COF (**Table 1.4**) were obtained with a precise thickness, controlled by the amount of the precursor solution deposited on the substrate, ranging from a few hundred nanometers to several microns. The film morphology was found to be dependent on the film thickness, and thin films of about 300 nm were observed as continuous films, whereas thicker films featured agglomeration of the COF particles with evident textural porosity.

Using a continuous flow synthesis, where constant rates of monomer precursor mass was deposited at constant elevated temperatures, crystalline thin films with preferred crystal orientation of COF-5 (**Table 1.2**), DPB-COF (**Table 1.2**), TP-COF (**Table 1.2**), and COF-10 (**Table 1.2**) were achieved with a fine control over the film thickness.¹²⁷ For the synthesis of COF-5 in a flow-cell, the building blocks HHTP and BDBA were mixed at 25°C in a dioxane/mesitylene solvent mixture, after which rising the temperature to 90°C resulted in the formation of COF-5 after 2 min. The resulting reaction mixture was pumped through a heated tubing for a given residence time and passed through a flow cell over a substrate. The deposited mass was monitored by a quartz crystal microbalance (QCM). High crystallinity of the resulting COF films was observed at residence times of 80 and 100 s, indicating that crystalline films are likely to form through the addition of larger oligomeric species to the substrates rather than monomers. Using the continuous flow method, thicker films (374 nm for DPB-COF) were accessed compared to films obtained by a static film growth (261 nm).

Recently, electrophoretic deposition (EPD, **Figure 1.14**) has been reported by Medina and co-workers for the synthesis of 2D or 3D COF films linked by boronate ester or imine bonds.¹²⁸ External electric field induced to a parallel electrode set-up immersed in COF-5 nanoparticle suspension of a low dielectric constant solvent, such as ethyl acetate, led to the migration of COF particles, which bear a negative intrinsic surface charge, to the electrode's surface of opposite charge to give a continuous film of gathered crystallites. Notably, the COF particle suspensions were obtained either by a top-down approach by breaking down large, agglomerated COF particles by sonication, or re-suspending COF powders in the respective solvents. This way, COF films with an inherent textural porosity were formed on a time scale of minutes. Using EPD, the thickness and the covered surface area of the resulting films was precisely controlled by controlling parameters such as the deposition time, applied potential, and concentration of the COF particles, in a short time scale. For COF-5, in 2 min a film with 14 μm thickness was obtained. Furthermore, this method also allowed for the co-deposition of different COFs as well as COF/Pt nanoparticles from mixed suspensions.

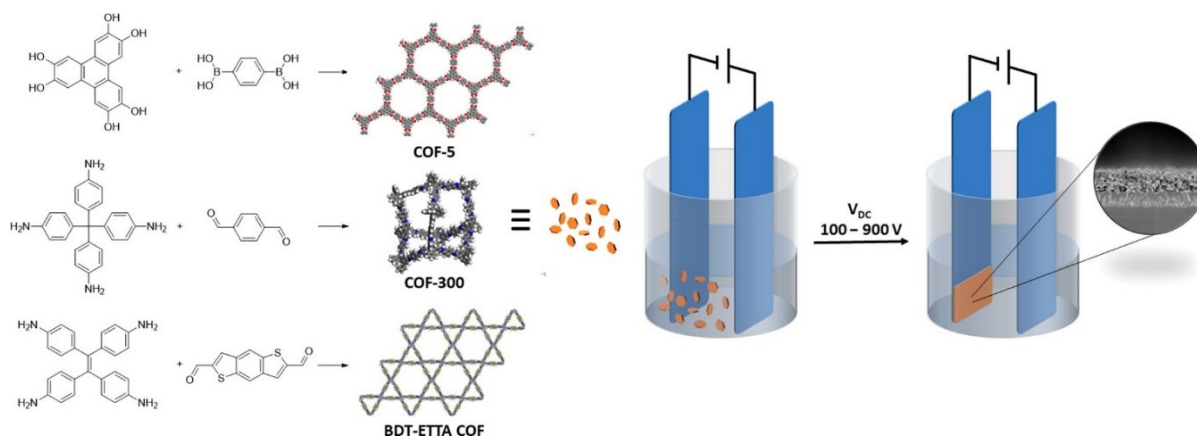


Figure 1.14. COF building blocks and the resulting frameworks used for electrophoretic deposition. A schematic representation of the EPD set-up is shown together with a representative cross-section SEM image of the resulting COF thin film. Reprinted with permission.¹²⁸ Copyright (2019) American Chemical Society.

Free-standing transparent crystalline and porous COF films with preferential crystallite orientation, where the aromatic planes are positioned perpendicular to the film surface have been reported by solution-casting of stable colloidal suspensions of 2D COF nanoparticles and drying.¹²¹ Such colloidal COF suspensions have also been used as ink for spray coating of 2D COF thin films.¹²⁴ Five different boronic-ester-COF-based colloidal inks were spray-coated at high speed, large-scale, and micrometer-scale resolution, either in isolation or as mixtures, onto several substrates, such as metal, polymer, and oxide substrates, subsequently introducing film-based devices with mixed 2D COFs.

1.2.7 Applications

The high porosity, tunable pore size and structure, and light weight of COFs combined with the immense number of organic molecules render COF materials as a unique platform to design a specific spatial orientation of organic ligands. Therefore, boronate ester COFs have been studied for a wide range of applications, such as gas storage, sieving, batteries, and optoelectronics. In the following section, the exploration of boronic acid derived COFs for different applications will be discussed.

Sieving/ Separation of Molecules

Compared with inorganic zeolites, COFs feature the advantage of providing a more versatile chemical diversity due to the immense number of different organic building blocks that can be used for their synthesis. Moreover, their properties, such as tunable pore sizes and shapes as well as easily customizable functionalities, make them perfect candidates for application in molecular separation.

The pore wall modification of COF-1 using pyridine (Py) gave access to Py@COF-1, which enabled the separation of isotope mixtures of H₂ by highly selective quantum sieving as described by Oh *et al.*⁸⁶ Py@COF-1 was synthesized by Lewis-base-assisted self-condensation reaction of BDBA in the

presence of one equivalent of pyridine. Using this approach, the pore aperture size and the pore volume of Py@COF-1 were significantly decreased compared to the parent COF-1: gas adsorption measurements revealed that neither N_2 at 77 K nor H_2 at 19.5 K could penetrate the structure due to its high density, resulting in BET surface areas of $20.5 \text{ m}^2 \text{ g}^{-1}$ and $48 \text{ m}^2 \text{ g}^{-1}$ for N_2 and H_2 , respectively, greatly reduced from that of COF-1 of $711 \text{ m}^2 \text{ g}^{-1}$. Interestingly, Py@COF-1 exhibits unique sorption behavior at low temperatures (19.5–70 K). Analyzing the H_2 uptake at different temperatures, an increase in the surface area from $20.5 \text{ m}^2 \text{ g}^{-1}$ at 19.5 K to $250 \text{ m}^2 \text{ g}^{-1}$ at 77 K was observed, indicating framework flexibility with changes in the effective aperture size and gating effects, meaning that already at low temperatures (>30 K) the system showed cryogenic flexibility. Since the cryogenic flexibility produces a kinetic hindrance at the aperture, this allowed for highly size-selective quantum sieving of D_2 from a 1:1 H_2/D_2 isotope mixture using Py@COF-1 in a temperature range of 20–100 K (**Figure 1.15**). The different H_2 isotopes display a difference in adsorption strength at low temperatures as a result of a strong isotope effect, which is used in quantum sieving in order to separate the different H_2 isotopes.¹²⁹

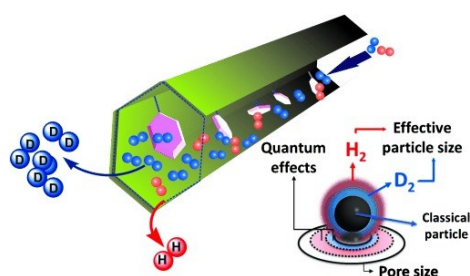


Figure 1.15. Schematic representation of the quantum sieving process of D_2 from a 1:1 mixture of H_2/D_2 . Reprinted with permission.⁸⁶ Copyright 2013, John Wiley and Sons.

Homogeneous and ultra-thin COF membranes were obtained from COF nanosheets, where the as-synthesized COF-1 was immersed in dichloromethane and subjected to sonication, resulting in exfoliated COF nanosheets (**Figure 1.16**).⁹⁶ Then, a membrane was produced by depositing the COF-1 nanosheet solution onto the outer surface of a macroporous ceramic support. The single-gas permeation study of the membrane for H_2 , N_2 , and SF_6 at 350°C gave nearly constant rates of permeance, indicating that the membrane was highly stable under high temperatures.

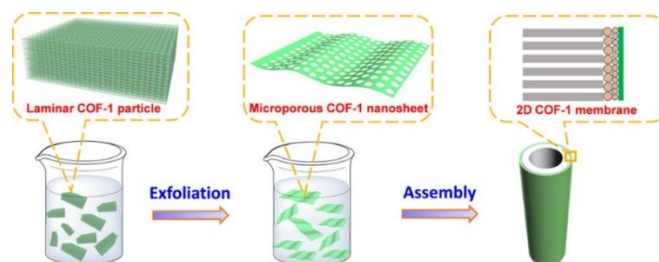


Figure 1.16. Schematic representation of the fabrication of a COF-1 membrane produced via the exfoliation of COF-1 to nanosheets. Reprinted with permission.⁹⁶ Copyright (2017) American Chemical Society.

Graphene oxide (GO)/COF-1 nanocomposite prepared through the *in situ* growth route showed excellent water permeation as a membrane material for water treatment.¹⁰¹ High rejection rates were observed for water-soluble dyes (>99%) and lower rejection rates for salts (<12%), which was attributed to the physical size sieving of COF-1 and the suitable interlayer spacing between the adjacent GO sheets of 1.03 nm, resulting from the presence of the COF as spacer, making the composite a promising material for the extraction of dyes from wastewater.

Boronic-acid-derived COFs have also been probed as stationary phases for gas and liquid chromatography. COF-5 was grown on the inner wall of a fused silica capillary *via* polydopamine (PDA) supported method, where the catechol moieties of the immobilized dopamine on the surface of the tube served as anchoring sites for the successive COF growth.¹³⁰ The obtained COF-5-PDA@capillary stationary phase was used for open-tubular capillary electrochromatography (OT-CEC) and showed high column efficiencies, stability, and repeatability in baseline separation of neutral, acidic, and basic small organic molecules. For example, baseline separation of ethylbenzene, *n*-propylbenzene, and *n*-butylbenzene was achieved, whereas for the non-COF-containing PDA@capillary no separation was observed, indicating that an interaction between the neutral analytes with the COF-5 layers led to the separation of the three alkyl benzenes. PDA-based functionalization has also been employed to immobilize COF-1 on the surface of magnetic nanoparticles (M-COF-1).⁹¹ Selective extraction of paclitaxel, a known anti-cancer drug in clinical chemotherapy, was carried out using this composite with good linearity in the range of 0.1–200 ng mL⁻¹ with a low limit of detection of 0.02 ng mL⁻¹.

A COF composite based on a CTC-COF shell (**Table 1.3**) and magnetic nanoparticles inside carbon nanotubes (MCNT), CTC-COF@MCNT, was employed for magnetic solid-phase extraction (MSPE) of heterocyclic aromatic amines (HAA) from complex food samples.⁶⁹ The composite was prepared through a photochemical reaction of MCNT, BDBA, and CTC in dioxane and 3-aminopropyltriethoxysilane (APTES), and featured specific surface area of 430 m² g⁻¹ and enhanced moisture stability as compared to pristine CTC-COF. Thus, CTC-COF@MCNT was used as adsorbent for MSPE to enrich HAAs prior to their analysis with ultra-high-performance liquid chromatography-tandem mass spectrometry. To this end, the processed food sample and CTC-COF@MCNT composite were combined, shaken, and after a specific time, the CTC-COF@MCNT composite was separated from the solution using an external magnetic field. HAAs were subsequently desorbed from the adsorbent by addition of methanol, and limit of detection (LOD) of 0.0058–0.025 ng g⁻¹ was obtained.

Gas Storage

Porous materials have attracted a great deal of interest as possible storage materials for gases, such as hydrogen, carbon dioxide, methane, or ammonia. The storage of methane and hydrogen is especially

important owing to their potential to serve as alternative energy sources, replacing fossil fuels. To this end, the regular pore structures and large surface areas of light-weight COFs are particularly beneficial.

Hydrogen storage was one of the first applications investigated for boronate ester COFs. In a theoretical study, the hydrogen storage properties of a series of 2D and 3D COFs were studied, and the hydrogen storage capacity of 3D COFs was found to be almost three times as high as that of 2D COFs as a result of their higher surface area and free volume,¹⁰² with a maximum H₂ uptake of 18.9 wt% at 77 K calculated for COF-108. In a study by Ghosh *et al.*, using density functional theory (DFT) and grand canonical Monte Carlo (GCMC) simulations, the H₂ adsorption of COF-1 (**Table 1.4**), COF-5 (**Table 1.2**), and porphyrin-containing H₂P-COF (**Table 1.3**) was theoretically predicted.⁷² COF-5 was simulated to have the highest hydrogen adsorption capacity among the analyzed COFs, which was attributed to its high free volume (2.45 cm³ g⁻¹) and the high binding energy of the boronic ester ring towards H₂. The inclusion of pyridine units inserted between the layers of 2D H₂P-COF allowed for an increased interlayer spacing, and thus enhanced the accessible volume for hydrogen adsorption. The highest storage capacity among the studied 2D COFs was achieved for H₂P-COF doped with four pyridine molecules with a gravimetric and volumetric uptake of ~5.1 wt% and 20 g H₂/L at room temperature and 100 bar. The hydrogen storage capacity of COF-1 has also been calculated to be enhanced by decorating the framework with lithium atoms.⁹⁹ Ab initio molecular dynamics (MD) simulations showed that six Li atoms were uniformly dispersed on a COF-1 layer and three hydrogen molecules were adsorbed per Li-atom in the Li-COF-1 system. At 300 K, 12 hydrogen molecules were adsorbed on the Li-COF-1 layer, which led to a hydrogen hosting capacity of 5.26 wt%.

Metal species have been included in the COF pores to improve their hydrogen storage ability.¹⁰⁷ The inclusion of ultra-small palladium nanoparticles into COF-102 by photodecomposition of [Pd(η^3 -C₃H₅)(η^5 -C₅H₅)]@COF-102 yielded hybrid material Pd@COF-102, which featured monodispersed Pd nanoparticles in the size of 2.4 nm evenly distributed inside the COF. Hydrogen sorption measurements showed that the inclusion of Pd nanoparticles led to an improvement in the hydrogen hosting capacities by a factor of 2–3 at room temperature and 20 bar (**Figure 1.17**). High hydrogen uptake has also been shown for the bowl-shaped CTC-COF, which with 1.12 wt% at low pressure outperformed other 2D frameworks with similar structures (COF-5 0.84 wt%, COF-10 0.82 wt%), owing to its larger surface area.^{68,70}

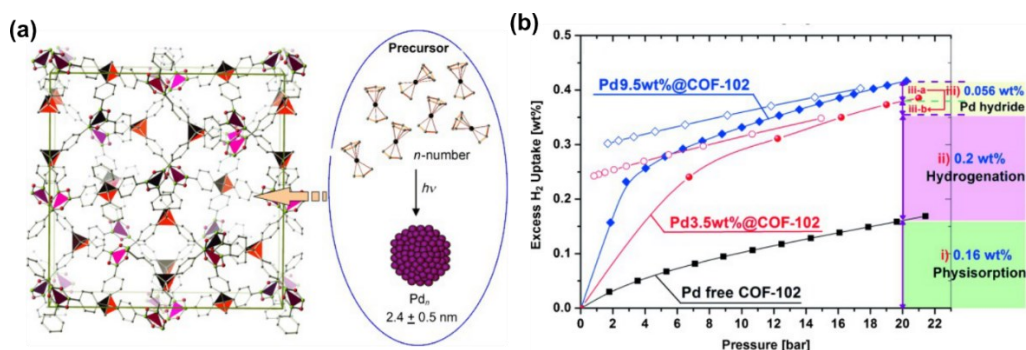


Figure 1.17. (a) Schematic representation of the synthesis of Pd@COF-102 hybrid material. (b) Excess hydrogen storage sorption isotherms of pristine COF-102, Pd3.5wt%@COF-102, and Pd9.5wt%@COF-102 at 298 K. Adapted with permission.¹⁰⁷ Copyright 2012, John Wiley and Sons.

Batteries/ Energy Storage

Robust COFs with enhanced structural stability, low solubility, and open pore channels are suitable for the transport of ions and electrons. In addition, the COF backbone can be modified with redox-active centers for storing or liberating lithium or sodium ions, which makes them interesting materials for application in batteries or energy storage.

In this context, Jiang and co-workers reported the synthesis of a hybrid carbon-based COF material. Here, a redox-active, crystalline, mesoporous D_{TP}-A_{NDI}-COF was deposited on the outer surface of carbon nanotubes (CNTs) *via* the *in situ* condensation of D_{TP}-A_{NDI}-COF in the presence of CNT wires under solvothermal conditions.¹³¹ The COF was found to be insoluble in the electrolyte solution, giving electrodes with robust structural stability. Moreover, owing to the presence of aligned open mesoporous channels provided by the 2D COF skeleton, ion transport was facilitated, with the redox-active COF walls undergoing multi-electron oxidation and reduction processes and the carbon nanotube wires contributing to enhanced electrical conductivity compared to the pristine COF (**Figure 1.18**). Furthermore, the great availability of different redox-active building blocks and the versatility of COF synthesis in combination with conducting carbons make this approach a very important step towards facilitating the synthesis of electrode materials for energy storage.

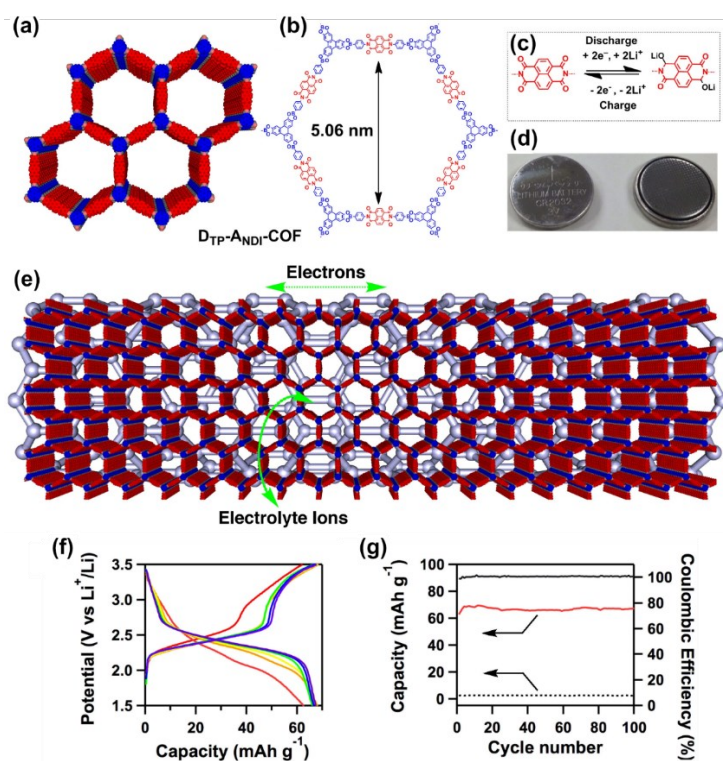


Figure 1.18. (a) Schematic illustration of the AA-stacking of D_{TP} -ANDI-COF with redox-active naphthalene diimide walls. (b) Chemical structure of D_{TP} -ANDI-COF. (c) Electrochemical redox reaction of the naphthalene diimide building block. (d) Photographs of a coin-type battery. (e) Graphical representation of D_{TP} -ANDI-COF@CNT, electron conduction, and ion transport. CNTs are depicted in grey. (f) Discharge-charge curves of D_{TP} -ANDI-COF@CNTs upon 100 cycles at the rate of 2.4 C (red, 1st cycle; orange, 10th cycle; yellow, 20th cycle; green, 50th cycle; blue, 80th cycle; purple, 100th cycle). (g) Capacities of D_{TP} -ANDI-COF@CNTs (red line) and CNT (dotted black line) batteries and Coulombic efficiency of D_{TP} -ANDI-COF@CNTs for 100 cycles (black line). Adapted with permission.¹³¹ Copyright 2015, Springer Nature.

Boroxine-linked 2D PPTODB COF, prepared from 4,5,9,10-tetraone-pyrene-2,7-diboric acid, featuring redox active tetraone sites protruding the pore walls was reported by Yao *et al.*¹³² By mixing 70 wt% of the PPTODB COF with 30 wt% CNTs as a conductive additive, a binder-free organic cathode material for lithium-ion storage was obtained. Lithium-ion batteries (LIBs) with a high electrochemical performance, specific capacity of 198 mAh g⁻¹, rate ability (76%, 1000 mA g⁻¹ vs. 100 mA g⁻¹), and stable coulombic efficiency (CE, ~99.6% at 150th cycle) were obtained, which was attributed to the high electrochemical activity (4 redox electrons) of the tetraone sites combined with an enhanced π - π interaction between PPTODB and the CNTs.

COFs were reported by Vazquez-Molina *et al.* to be mechanically pressed into shaped objects, leading to an anisotropic crystallographic ordering of the COF sheets in the pellet with the (001) crystallographic planes being oriented parallel to the plane of the pellet.¹³³ Different boronic-acid-derived COFs with different functionality and symmetry (COF-1, COF-5, ZnPc-PBBA) were analyzed using this approach showing exceptional stability and similar crystallographic plane alignment for all the investigated structures. Room temperature conductivity of up to 0.26 mS cm⁻¹ was obtained for a pressed pellet made from LiClO₄-impregnated bulk COF-5 powders. Later, Chen and co-workers reported the use of COF-

1 as functional additive in solid polymer electrolytes for LIBs.¹⁰² In that report, poly(vinylidene fluoride) (PVDF) composites containing LiClO₄ and COF-1 were prepared by a solution casting technique. Thereby, polymer electrolyte PVDF was dissolved in *N*-methyl-2-pyrrolidone, COF-1 powder was subsequently added to the polymer solution, the solution was stirred at room temperature for 1 day, and afterwards spread on a clean glass plate using a doctor blade apparatus. After solidifying and drying, the membranes were peeled off from the glass plate. The presence of boron-containing COF-1 in the electrolytes enabled a strong adsorption of the anions of the lithium salt by the boron groups in the framework, resulting in an improved Li ion transference number when using the COF-containing polymer electrolytes. In this way, decreased overpotentials as well as improved rate performances were achieved for the solid-state cells with COF-containing polymer electrolytes. For example, Li/PVDF/H-COF-1@10/LiFePO₄ exhibited an initial capacity of 128 mAh g⁻¹ and a capacity retention of 94% after 80 cycles. Moreover, it showed discharge capacities of ~145, 138, 128, 122, and 107 mAh g⁻¹ at 0.25 C, 0.5 C, 1 C, 2 C, and 4 C rates, respectively. The authors postulate that by using functionalized COF structures that contain electron-withdrawing groups, the Li ion transference number may be even further improved.

Yoo *et al.* utilized a hybrid material consisting of COF-1 or COF-5 on CNTs as a hierarchical porous chemical trap for lithium polysulfides (Li₂S_x) for Li-S batteries.⁹⁰ A CNT-templated *in situ* COF synthesis assisted by the favorable CNT/COF π - π interactions was employed, giving access to microporous-COF-on-mesoporous-CNT hybrids. DFT calculations revealed that the combination of microporous COFs as Li₂S_x traps with mesoporous CNTs as ion-conducting channels had a beneficial influence on the electrochemical performance of the Li-S-cells, attributed to the boron-mediated chemical affinity for selectively binding Li₂S. As opposed to COF-5 with its larger pore size of 2.7 nm, COF-1 with smaller micropores of 0.7 nm allowed for the exclusive penetration of Li₂S, leading to its selective adsorption. The COF-1 composite also facilitated the solid-liquid conversion of Li₂S, leading to an improvement in the electrochemical reversibility, and thus an exceptional improvement in the cell performance was observed, *i.e.* a capacity retention after 300 cycles (at a rate of 2.0 C/2.0 C) of 84% was obtained compared to 15% for a control cell without COF interlayer.

Using the *in-situ* growth approach, an anode material for potassium-ion batteries (PIBs) was prepared consisting of COF-10 (**Table 1.2**) and carbon nanotubes (COF-10@CNT).¹³⁴ The enhanced π - π stacking in the hybrid COF-10@CNT structure facilitates the access to the exposed active sites, and accordingly, ion/electron diffusion was shortened and the insertion/extraction kinetics of potassium ions were improved. High capacities of 288 mAh g⁻¹ after 500 cycles at 0.1 A g⁻¹ and 161 mAh g⁻¹ after 4000 cycles at 1 A g⁻¹ were detected.

Optoelectronics

A prominent feature of 2D COFs is the precise alignment of aromatic, photoactive, and semiconducting molecular slabs into defined molecular stacks guided by π - π interactions between successive COF layers. The tight arrangement of the molecular stacks is expected to grant access to a charge-carrier path and facilitate charge migration along the stacking direction, making these materials attractive for optoelectronic applications. Furthermore, available pores in the mesoporous scale are suitable for hosting guest molecules with matching electronic properties to create an ordered photoactive blend. To this end, boronate ester COFs have been designed and synthesized aiming at the formation of a photoactive backbone and structurally defined donor-acceptor blends as powder bulk materials,¹³⁵ and their deposition as oriented thin films on conductive substrates has allowed for their exploration as photoactive devices (**section 1.2.6.2**).

The first COF-based photovoltaic device was reported by Bein and co-workers using TT-COF (**Table 1.2**), which combines thieno[2,3-b]thiophene diboronic acid building block as electron donor with HHTP.⁵⁷ The obtained COF featured high surface area of up to 1810 m² g⁻¹ and open pore system, which was used for the infiltration of a complementary electron acceptor [6,6]-phenyl-C₆₁-butyric acid methyl ester (PCBM). A light-induced charge transfer from the photoactive TT-COF electron donor powder to the acceptor PCBM encapsulated in the pores was observed in spectroscopic measurements. Photoluminescence measurements revealed drastic quenching upon inclusion, indicating a charge transfer from the COF backbone to the included guest (**Figure 1.19**). Thereafter, a photovoltaic device was constructed by depositing TT-COF on glass-modified ITO substrate electrode as an oriented thin film by the non-epitaxial *in situ* method (for more details, see **section 1.2.3.2**). Subsequently, PCBM was infiltrated into the open and vertically aligned COF pores by soaking and spin coating. To finalize the photovoltaic device, a thin Al layer was deposited as a top electrode. With the obtained photovoltaic COF device, charge migration and collection were observed for the first time. Under simulated AM1.5G full sun illumination, an open-circuit voltage of 622 mV, a short-circuit current density of 0.213 mA cm⁻², and 40% fill factor were obtained, giving a power conversion efficiency of 0.053%.

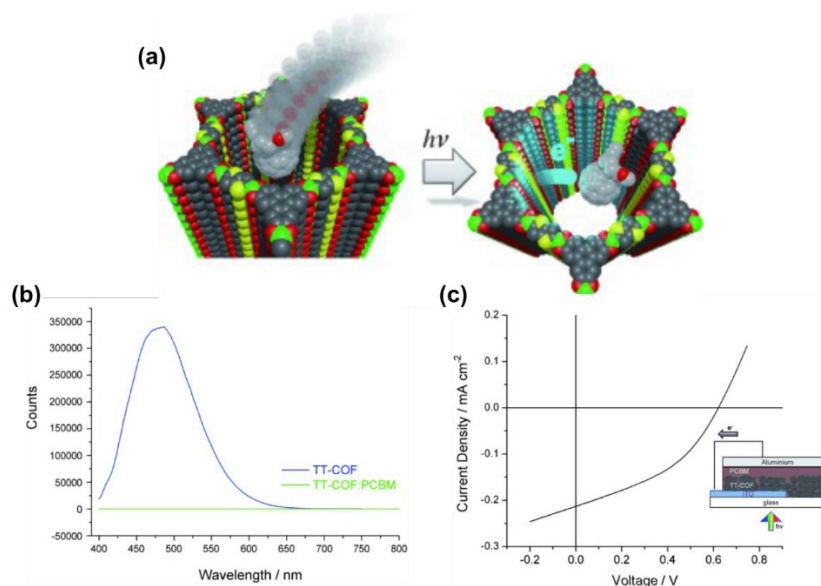


Figure 1.19. (a) Schematic representation of the encapsulation of a PCBM molecule into the pore of TT-COF and the light-induced charge transfer from the TT-COF electron donor to the acceptor molecule. (b) Fluorescence emission of TT-COF (blue) upon excitation at $\lambda = 380$ nm and after encapsulation of PCBM (green). (c) J–V characteristics of the TT-COF-based photovoltaic cell measured under illumination with simulated solar light. Adapted with permission.⁵⁷ Copyright 2013, John Wiley and Sons.

In a later work, employing an approach combining both the donor and acceptor within the framework, TP-Por COF (**Table 1.2**) containing both electron-donor porphyrin and electron-acceptor HHTP was synthesized resulting in a highly defined interdigitated donor–acceptor heterojunction.⁵⁴ To examine the charge migration properties of the COF, oriented thin films of the material were grown using the non-epitaxial *in situ* approach on patterned ITO substrates covered with a 10 nm layer of vacuum-deposited MoO_x. To complete the device, ZnO/Al served as the top electrode. Upon irradiation with simulated solar light, an open-circuit voltage of 312 mV and a short-circuit current density of 44.6 $\mu\text{A cm}^{-2}$ were obtained.

To estimate the hole charge carrier transport in boronate ester COFs exclusively along the layer stacks, hole-only devices were constructed by Medina *et al.*⁶¹ For this purpose, oriented thin films of photoactive BDT-COF were grown on glass-supported ITO with hole-selective layer of MoO_x (**Figure 1.20**). Subsequently, a top MoO_x layer and gold electrode were deposited on top of the oriented film to complete the device. The directional charge transport of the oriented BDT-COF thin films was exclusively examined along the π -columnar arrays and electrical conductivity was examined in the COF planes. Depending on the thickness of the COF films, different hole mobilities were observed, and thinner films revealed higher average hole mobilities ($3 \times 10^{-7} \text{ cm}^2 \text{ V}^{-1} \text{ s}^{-1}$ for a thickness of 80–100 nm) than the respective thicker (~ 200 nm) ones. This variation was attributed to transport barriers that appear within the BDT-COF stacks. Moreover, for the 200 nm thick sample, an increase of one order of magnitude in hole mobility was observed under illumination ($3 \times 10^{-8} \text{ cm}^2 \text{ V}^{-1} \text{ s}^{-1}$) compared to the measurement in the dark ($5 \times 10^{-9} \text{ cm}^2 \text{ V}^{-1} \text{ s}^{-1}$), revealing the photoactive nature of BDT-COF.

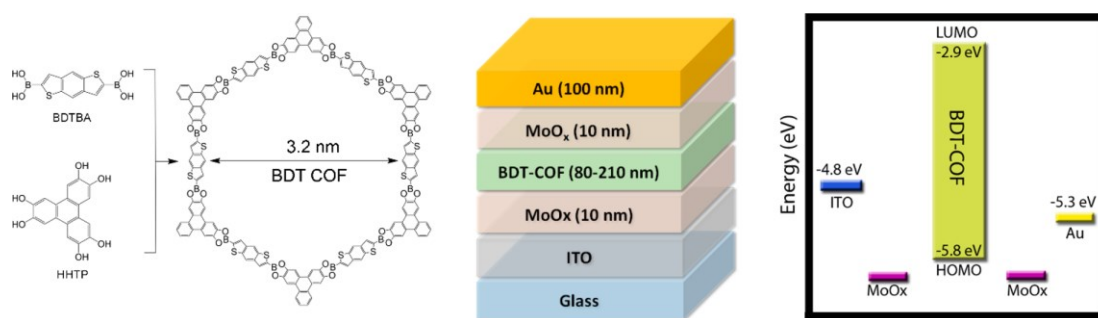


Figure 1.20. Schematic representation of BDT-COF-based hole-only device, the COF structure, and the corresponding energy diagram. Reprinted with permission.⁶¹ Copyright (2017) American Chemical Society.

Other Applications

In addition to the applications described above, examples for the use of boronic-acid-derived COFs have been reported for a variety of other applications as well. Recently, boroxine-linked COF-1 was shown to facilitate nitrogen accessibility in nitrogen reduction reaction (NRR) to ammonia through electrochemical excitation.¹³⁶ Simulations showed outstanding electronic structure of COF-1 for N_2 absorption and a reduced energy barrier of the rate-determining step, N_2 dissociation, over the boron-sites of the COF. Therefore, when a suitable potential was applied, boron atoms easily bonded with the nitrogen species, causing distortions in the lattice planes of the COF, which led to enhanced nitrogen adsorption towards the framework. The whole NRR reaction was facilitated due to the localized high nitrogen concentration that promotes the probability of collisions of nitrogen molecules with the boron sites. The conclusions from this study were verified by proof-of-concept experiments on COF-1 on nitrogen-doped carbon nanosheet support. PXRD measurements indicated that the COF transformed from crystalline to amorphous, while *in situ* Raman experiments verified the formation of the B-N bond during electrochemical excitation. The ability to facilitate the NRR due to the transformations in the COF structure was demonstrated by linear sweep voltammetry studies, showing that COF-1 on nitrogen-doped carbon nanosheet produced ammonia with Faradaic efficiency of 45.43%.

Spray-coated 2D COF thin films (**section 1.2.6.2**) were incorporated as an active layer in acoustic sensors by Evans *et al.*¹²⁴ To this end, COF-5 ink was spray-coated onto Ti-coated QCM acoustic resonators, and the resulting 2D COF QCM-based volatile amine sensor was employed for the detection of volatile amines in meat and seafood, such as trimethylamine (TMA). Here, remarkable performance was observed, which was attributed to the high surface area of the COF and Lewis acidity provided by the boron where concentrations as low as 10 ppb of TMA were detected, placing these 2D COF-based sensors among the most sensitive sensors for food spoilage.

1.3 Summary and Outlook

Boronic-acid-containing building blocks have paved the way for the construction of robust and thermally stable hierarchical materials with key features, such as long-range order and well-defined cavities, the so-called covalent organic frameworks. The reversible nature of the boronic acid condensation reaction, allowing for “proof-reading” processes during the synthesis, has thus resulted in the synthesis of complex structures not attainable through other methods. Thereafter, the field of COFs has expanded to feature a much larger diversity of linkages.

Boronic-acid-bearing building blocks have played a pivotal role in giving the first insights into the formation of COFs, their crystallization, growth as bulk and films, and their utilization. Although the COF field is currently dominated by structures featuring more chemically stable linkages, such as imine or enamine bonds, boronic-acid-derived COFs offer exceptional opportunities of atomically precise design owing to their excellent crystallinity. They are particularly suitable for studying the mechanism of COF formation owing to their high reactivity under mild conditions, sometimes at room temperature, without the need of a catalyst, such as acid or base, which facilitates the interpretation of the COF formation process. In addition, boronate ester and boroxine moieties are in-plane linkages, which position the typically planar aromatic COF building blocks at an optimal geometry for π - π stacking, forming closely packed aggregates in a solid matrix. Additionally, in contrast to imine or vinylene linkages, boroxine and boronate ester are junctions of limited conjugation, enabling the creation of ordered interdigitated molecular aggregates of different properties, such as electron donor-acceptor. Also, highly sensitive sensors can be constructed from boronate ester COF materials based on the strong affinity of boron to electron-donating elements, such as nitrogen-containing compounds. In addition, recent reports on catalysis show that these materials can be used as pre-catalysts to give access to highly active materials.

In addition to holding promise for several applications, boronic-acid-derived COFs allow not only the study of the formation of COF materials, but interactions within the COFs and other relevant fundamental behavior. Therefore, we believe that exciting examples on the synthesis and application of these materials will continue appearing and the boronic-acid-derived COFs will hold their place within the expanding field of COFs.

1.4 References

- (1) A. Suzuki, *Angew. Chem. Int. Ed.* **2011**, *50*, 6722–6737.
- (2) G. Zhang, O. Presly, F. White, I. M. Oppel and M. Mastalerz, *Angew. Chem. Int. Ed.* **2014**, *53*, 1516–1520.

- (3) N. Nishimura and K. Kobayashi, *J. Org. Chem.* **2010**, *75*, 6079–6085.
- (4) E. Sheepwash, N. Luisier, M. R. Krause, S. Noé, S. Kubik and K. Severin, *Chem. Commun.*, **2012**, *48*, 7808–7810.
- (5) M. S. Lohse and T. Bein, *Adv. Funct. Mater.* **2018**, *28*, 1705553.
- (6) A. P. Côté, A. I. Benin, N. W. Ockwig, M. O’Keeffe, A. J. Matzger and O. M. Yaghi, *Science* **2005**, *310*, 1166–1170.
- (7) H. M. El-Kaderi, J. R. Hunt, J. L. Mendoza-Cortés, A. P. Côté, R. E. Taylor, M. O’Keeffe and O. M. Yaghi, *Science* **2007**, *316*, 268–272.
- (8) D. Hall, in *Boronic Acids: Preparation and Applications in Organic Synthesis and Medicine*, **2006**, pp. 1–99.
- (9) D. G. Hall, *Chem. Soc. Rev.* **2019**, *48*, 3475–3496.
- (10) R. Nishiyabu, Y. Kubo, T. D. James and J. S. Fossey, *Chem. Commun.* **2011**, *47*, 1106–1123.
- (11) X. Wu, Z. Li, X.-X. Chen, J. S. Fossey, T. D. James and Y.-B. Jiang, *Chem. Soc. Rev.*, **2013**, *42*, 8032–8048.
- (12) M. K. Smith and B. H. Northrop, *Chem. Mater.* **2014**, *26*, 3781–3795.
- (13) J.-H. Fournier, T. Maris, J. D. Wuest, W. Guo and E. Galoppini, *J. Am. Chem. Soc.* **2003**, *125*, 1002–1006.
- (14) N. Huang, X. Ding, J. Kim, H. Ihee and D. Jiang, *Angew. Chem. Int. Ed.* **2015**, *54*, 8704–8707.
- (15) J. Zhang, L. Wang, N. Li, J. Liu, W. Zhang, Z. Zhang, N. Zhou and X. Zhu, *CrystEngComm* **2014**, *16*, 6547–6551.
- (16) D. N. Coventry, A. S. Batsanov, A. E. Goeta, J. A. K. Howard, T. B. Marder and R. N. Perutz, *Chem. Commun.* **2005**, 2172–2174.
- (17) K. M. Waltz and J. F. Hartwig, *Science* **1997**, *277*, 211.
- (18) S. Shimada, A. S. Batsanov, J. A. K. Howard and T. B. Marder, *Angew. Chem. Int. Ed.* **2001**, *40*, 2168–2171.
- (19) H. Chen, S. Schlecht, T. C. Semple and J. F. Hartwig, *Science* **2000**, *287*, 1995.
- (20) T. Ishiyama, J. Takagi, K. Ishida, N. Miyaura, N. R. Anastasi and J. F. Hartwig, *J. Am. Chem. Soc.* **2002**, *124*, 390–391.
- (21) J.-Y. Cho, C. N. Iverson and M. R. Smith, *J. Am. Chem. Soc.* **2000**, *122*, 12868–12869.
- (22) S. Wan, J. Guo, J. Kim, H. Ihee and D. Jiang, *Angew. Chem. Int. Ed.* **2008**, *47*, 8826–8830.
- (23) A. G. Crawford, Z. Liu, I. A. I. Mkhaliid, M.-H. Thibault, N. Schwarz, G. Alcaraz, A. Steffen, J. C. Collings, A. S. Batsanov, J. A. K. Howard and T. B. Marder, *Chemistry* **2012**, *18*, 5022–5035.
- (24) A. R. Goldberg and B. H. Northrop, *J. Org. Chem.* **2016**, *81*, 969–980.
- (25) O. R. Cromwell, J. Chung and Z. Guan, *J. Am. Chem. Soc.* **2015**, *137*, 6492–6495.

- (26) K. L. Bhat, G. D. Markham, J. D. Larkin and C. W. Bock, *J. Phys. Chem. A* **2011**, *115*, 7785–7793.
- (27) J. P. M. António, R. Russo, C. P. Carvalho, Cal, Pedro M. S. D. and P. M. P. Gois, *Chem. Soc. Rev.* **2019**, *48*, 3513–3536.
- (28) B. Marco-Dufort and M.W. Tibbitt, *Mater. Today Chem.* **2019**, *12*, 16–33.
- (29) X. Wu, Z. Li, X.-X. Chen, J. S. Fossey, T. D. James and Y.-B. Jiang, *Chem. Soc. Rev.* **2013**, *42*, 8032–8048.
- (30) X. Feng, X. Ding and D. Jiang, *Chem. Soc. Rev.* **2012**, *41*, 6010–6022.
- (31) S. Kandambeth, K. Dey and R. Banerjee, *J. Am. Chem. Soc.* **2019**, *141*, 1807–1822.
- (32) N. L. Campbell, R. Clowes, L. K. Ritchie and A. I. Cooper, *Chem. Mater.* **2009**, *21*, 204–206.
- (33) S.-T. Yang, J. Kim, H.-Y. Cho, S. Kim and W.-S. Ahn, *RSC Adv.* **2012**, *2*, 10179–10181.
- (34) B. J. Smith and W. R. Dichtel, *J. Am. Chem. Soc.* **2014**, *136*, 8783–8789.
- (35) B. J. Smith, N. Hwang, A. D. Chavez, J. L. Novotney and W. R. Dichtel, *Chem. Commun.* **2015**, *51*, 7532–7535.
- (36) H. Li, A. D. Chavez, H. Li, H. Li, W. R. Dichtel and J.-L. Bredas, *J. Am. Chem. Soc.* **2017**, *139*, 16310–16318.
- (37) H. Li, A. M. Evans, I. Castano, M. J. Strauss, W. R. Dichtel and J.-L. Bredas, *J. Am. Chem. Soc.*, **2020**, *142*, 1367–1374.
- (38) M. Niederberger and H. Cölfen, *Phys. Chem. Chem. Phys.* **2006**, *8*, 3271–3287.
- (39) D. D. Medina and Y. Mastai, *Cryst. Growth Des.* **2008**, *8*, 3646–3651.
- (40) H. Cölfen, *Crystals*, **2020**, *10*, 61.
- (41) A. M. Evans, L. R. Parent, N. C. Flanders, R. P. Bisbey, E. Vitaku, M. S. Kirschner, R. D. Schaller, L. X. Chen, N. C. Gianneschi and W. R. Dichtel, *Science* **2018**, *361*, 52–57.
- (42) S. Wan, J. Guo, J. Kim, H. Ihee and D. Jiang, *Angew. Chem. Int. Ed.* **2009**, *48*, 5439–5442.
- (43) L. A. Baldwin, J. W. Crowe, M. D. Shannon, C. P. Jaroniec and P. L. McGrier, *Chem. Mater.* **2015**, *27*, 6169–6172.
- (44) L. A. Baldwin, J. W. Crowe, D. A. Pyles and P. L. McGrier, *J. Am. Chem. Soc.* **2016**, *138*, 15134–15137.
- (45) J. W. Crowe, L. A. Baldwin and P. L. McGrier, *J. Am. Chem. Soc.* **2016**, *138*, 10120–10123.
- (46) X. Feng, Y. Dong and D. Jiang, *CrystEngComm* **2013**, *15*, 1508–1511.
- (47) H. Yang, Y. Du, S. Wan, G. D. Trahan, Y. Jin and W. Zhang, *Chem. Sci.* **2015**, *6*, 4049–4053.
- (48) S. Dalapati, E. Jin, M. Addicoat, T. Heine and D. Jiang, *J. Am. Chem. Soc.* **2016**, *138*, 5797–5800.

- (49) A. P. Côté, H. M. El-Kaderi, H. Furukawa, J. R. Hunt and O. M. Yaghi, *J. Am. Chem. Soc.* **2007**, *129*, 12914–12915.
- (50) L. M. Salonen, D. D. Medina, E. Carbó-Argibay, M. G. Goesten, L. Mafra, N. Guldris, J. M. Rotter, D. G. Stroppa and C. Rodríguez-Abreu, *Chem. Commun.* **2016**, *52*, 7986–7989.
- (51) E. L. Spitler, B. T. Koo, J. L. Novotney, J. W. Colson, F. J. Uribe-Romo, G. D. Gutierrez, P. Clancy and W. R. Dichtel, *J. Am. Chem. Soc.* **2011**, *133*, 19416–19421.
- (52) S. Rager, M. Dogru, V. Werner, A. Gavryushin, M. Götz, H. Engelke, D. D. Medina, P. Knochel and T. Bein, *CrystEngComm* **2017**, *19*, 4886–4891.
- (53) P. P. Ramees, P. K. Mondal and D. Chopra, *J. Chem. Sci.* **2018**, *130*, 51.
- (54) M. Calik, F. Auras, L. M. Salonen, K. Bader, I. Grill, M. Handloser, D. D. Medina, M. Dogru, F. Löbermann, D. Trauner, A. Hartschuh and T. Bein, *J. Am. Chem. Soc.* **2014**, *136*, 17802–17807.
- (55) X. Feng, L. Chen, Y. Honsho, O. Saengsawang, L. Liu, L. Wang, A. Saeki, S. Irle, S. Seki, Y. Dong and D. Jiang, *Adv. Mater.* **2012**, *24*, 3026–3031.
- (56) G. H. V. Bertrand, V. K. Michaelis, T.-C. Ong, R. G. Griffin and M. Dincă, *Proc. Natl. Acad. Sci. U. S. A.* **2013**, *110*, 4923–4928.
- (57) M. Dogru, M. Handloser, F. Auras, T. Kunz, D. Medina, A. Hartschuh, P. Knochel and T. Bein, *Angew. Chem. Int. Ed.* **2013**, *52*, 2920–2924.
- (58) Y. Chen, H. Cui, J. Zhang, K. Zhao, D. Ding, J. Guo, L. Li, Z. Tian and Z. Tang, *RSC Adv.* **2015**, *5*, 92573–92576.
- (59) D. D. Medina, V. Werner, F. Auras, R. Tautz, M. Dogru, J. Schuster, S. Linke, M. Döblinger, J. Feldmann, P. Knochel and T. Bein, *ACS Nano* **2014**, *8*, 4042–4052.
- (60) D. D. Medina, J. M. Rotter, Y. Hu, M. Dogru, V. Werner, F. Auras, J. T. Markiewicz, P. Knochel and T. Bein, *J. Am. Chem. Soc.* **2015**, *137*, 1016–1019.
- (61) D. D. Medina, M. L. Petrus, A. N. Jumabekov, J. T. Margraf, S. Weinberger, J. M. Rotter, T. Clark and T. Bein, *ACS Nano* **2017**, *11*, 2706–2713.
- (62) M. S. Lohse, J. M. Rotter, J. T. Margraf, V. Werner, M. Becker, S. Herbert, P. Knochel, T. Clark, T. Bein and D. D. Medina, *CrystEngComm* **2016**, *18*, 4295–4302.
- (63) S. Duhović and M. Dincă, *Chem. Mater.* **2015**, *27*, 5487–5490.
- (64) S. Rager, A. C. Jakowetz, B. Gole, F. Beuerle, D. D. Medina and T. Bein, *Chem Mater* **2019**, *31*, 2707–2712.
- (65) R. W. Tilford, W. R. Gemmill, H.-C. zur Loye and J. J. Lavigne, *Chem. Mater.* **2006**, *18*, 5296–5301.
- (66) M. Dogru, A. Sonnauer, A. Gavryushin, P. Knochel and T. Bein, *Chem. Commun.* **2011**, *47*, 1707–1709.
- (67) X. Ding, L. Chen, Y. Honsho, X. Feng, O. Saengsawang, J. Guo, A. Saeki, S. Seki, S. Irle, S. Nagase, V. Parasuk and D. Jiang, *J. Am. Chem. Soc.* **2011**, *133*, 14510–14513.
- (68) J.-T. Yu, Z. Chen, J. Sun, Z.-T. Huang and Q.-Y. Zheng, *J. Mater. Chem.* **2012**, *22*, 5369–5373.

- (69) R. Liang, Y. Hu and G. Li, *J. Chromatogr., A* **2020**, 460867.
- (70) J. Zhen, S. Ding, W. Wang, J. Liu, J. Sun, Z. Huang and Q. Zheng, *Chin. J. Chem.* **2016**, *34*, 783–787.
- (71) X. Feng, L. Liu, Y. Honsho, A. Saeki, S. Seki, S. Irle, Y. Dong, A. Nagai and D. Jiang, *Angew. Chem. Int. Ed.* **2012**, *51*, 2618–2622.
- (72) S. Ghosh and J. K. Singh, *Int. J. Hydrog. Energy* **2019**, *44*, 1782–1796.
- (73) A. B. Sorokin, *Chem. Rev.* **2013**, *113*, 8152–8191.
- (74) E. L. Spitler, J. W. Colson, F. J. Uribe-Romo, A. R. Woll, M. R. Giovino, A. Saldivar and W. R. Dichtel, *Angew. Chem. Int. Ed.* **2012**, *51*, 2623–2627.
- (75) E. L. Spitler and W. R. Dichtel, *Nat. Chem.* **2010**, *2*, 672–677.
- (76) X. Ding, X. Feng, A. Saeki, S. Seki, A. Nagai and D. Jiang, *Chem. Commun.* **2012**, *48*, 8952–8954.
- (77) S. Wan, F. Gándara, A. Asano, H. Furukawa, A. Saeki, S. K. Dey, L. Liao, M. W. Ambrogio, Y. Y. Botros, X. Duan, S. Seki, J. F. Stoddart and O. M. Yaghi, *Chem. Mater.* **2011**, *23*, 4094–4097.
- (78) N. Huang, L. Zhai, D. E. Coupry, M. A. Addicoat, K. Okushita, K. Nishimura, T. Heine and D. Jiang, *Nat. Commun.* **2016**, *7*, 12325.
- (79) S. Jin, K. Furukawa, M. Addicoat, L. Chen, S. Takahashi, S. Irle, T. Nakamura and D. Jiang, *Chem. Sci.* **2013**, *4*, 4505–4511.
- (80) S. Jin, M. Supur, M. Addicoat, K. Furukawa, L. Chen, T. Nakamura, S. Fukuzumi, S. Irle and D. Jiang, *J. Am. Chem. Soc.* **2015**, *137*, 7817–7827.
- (81) W. Budiawan, K.-W. Lai, P. Karuppuswamy, T. S. Jadhav, Y.-A. Lu, K.-C. Ho, P.-C. Wang, C.-C. Chang and C.-W. Chu, *ACS Appl. Mater. Interfaces* **2020**, *12*.
- (82) M. Martínez-Abadía, C. T. Stoppiello, K. Strutynski, B. Lerma-Berlanga, C. Martí-Gastaldo, A. Saeki, M. Melle-Franco, A. N. Khlobystov and A. Mateo-Alonso, *J. Am. Chem. Soc.* **2019**, *141*, 14403–14410.
- (83) M. A. A. Musa, C.-Y. Yin and R. M. Savory, *Mater. Chem. Phys.* **2010**, *123*, 5–8.
- (84) J. F. Dienstmaier, A. M. Gigler, A. J. Goetz, P. Knochel, T. Bein, A. Lyapin, S. Reichlmaier, W. M. Heckl and M. Lackinger, *ACS Nano* **2011**, *5*, 9737–9745.
- (85) J. F. Dienstmaier, D. D. Medina, M. Dogru, P. Knochel, T. Bein, W. M. Heckl and M. Lackinger, *ACS Nano* **2012**, *6*, 7234–7242.
- (86) H. Oh, S. B. Kalidindi, Y. Um, S. Bureekaew, R. Schmid, R. A. Fischer and M. Hirscher, *Angew. Chem. Int. Ed.* **2013**, *52*, 13219–13222.
- (87) S. B. Kalidindi, C. Wiktor, A. Ramakrishnan, J. Weßing, A. Schneemann, G. van Tendeloo and R. A. Fischer, *Chem. Commun.* **2013**, *49*, 463–465.
- (88) D. Cui, J. M. MacLeod, M. Ebrahimi and F. Rosei, *CrystEngComm* **2017**, *19*, 4927–4932.
- (89) J. Plas, O. Ivasenko, N. Martsinovich, M. Lackinger and S. de Feyter, *Chem. Commun.* **2016**, *52*, 68–71.

- (90) J. Yoo, S.-J. Cho, G. Y. Jung, S. H. Kim, K.-H. Choi, J.-H. Kim, C. K. Lee, S. K. Kwak and S.-Y. Lee, *Nano Lett.* **2016**, *16*, 3292–3300.
- (91) Y. Chen and Z. Chen, *Talanta* **2017**, *165*, 188–193.
- (92) Y. Du, D. Calabro, B. Wooler, Q. Li, S. Cundy, P. Kamakoti, D. Colmyer, K. Mao and P. Ravikovitch, *J. Phys. Chem.* **2014**, *118*, 399–407.
- (93) Y. Du, K. Mao, P. Kamakoti, B. Wooler, S. Cundy, Q. Li, P. Ravikovitch and D. Calabro, *J. Mater. Chem. A* **2013**, *1*, 13171–13178.
- (94) Y. Du, D. Calabro, B. Wooler, P. Kortunov, Q. Li, S. Cundy and K. Mao, *Chem. Mater.* **2015**, *27*, 1445–1447.
- (95) D. Cui, J. M. MacLeod, M. Ebrahimi, D. F. Perepichka and F. Rosei, *Chem. Commun.* **2015**, *51*, 16510–16513.
- (96) G. Li, K. Zhang and T. Tsuru, *ACS Appl. Mater. Interfaces* **2017**, *9*, 8433–8436.
- (97) S. Spitzer, A. Rastgoo-Lahrood, K. Macknapp, V. Ritter, S. Sotier, W. M. Heckl and M. Lackinger, *Chem. Commun.* **2017**, *53*, 5147–5150.
- (98) T. Pham, K. A. Forrest, M. Mostrom, J. R. Hunt, H. Furukawa, J. Eckert and B. Space, *Phys. Chem. Chem. Phys.* **2017**, *19*, 13075–13082.
- (99) H. Zhao, Y. Guan, H. Guo, R. Du and C. Yan, *Mater. Res. Express* **2020**, 35506.
- (100) J. Sun, A. Iakunkov, I. A. Baburin, B. Joseph, V. Palermo and A. V. Talyzin, *Angew. Chem. Int. Ed.* **2020**, *59*, 1087–1092.
- (101) X. Zhang, H. Li, J. Wang, D. Peng, J. Liu and Y. Zhang, *J. Membr. Sci.* **2019**, *581*, 321–330.
- (102) D. Dong, H. Zhang, B. Zhou, Y. Sun, H. Zhang, M. Cao, J. Li, H. Zhou, H. Qian, Z. Lin and H. Chen, *Chem. Commun.* **2019**, *55*, 1458–1461.
- (103) J. Sun, A. Klechikov, C. Moise, M. Prodana, M. Enachescu and A. V. Talyzin, *Angew. Chem. Int. Ed.* **2018**, *57*, 1034–1038.
- (104) C. Liu, W. Zhang, Q. Zeng and S. Lei, *Chemistry* **2016**, *22*, 6768–6773.
- (105) S. S. Han, H. Furukawa, O. M. Yaghi and W. A. Goddard, *J. Am. Chem. Soc.* **2008**, *130*, 11580–11581.
- (106) D. N. Bunck and W. R. Dichtel, *Angew. Chem. Int. Ed.* **2012**, *51*, 1885–1889.
- (107) S. B. Kalidindi, H. Oh, M. Hirscher, D. Esken, C. Wiktor, S. Turner, G. van Tendeloo and R. A. Fischer, *Chemistry* **2012**, *18*, 10848–10856.
- (108) S. D. Brucks, D. N. Bunck and W. R. Dichtel, *Polymer* **2014**, *55*, 330–334.
- (109) H. Ma, H. Ren, S. Meng, Z. Yan, H. Zhao, F. Sun and G. Zhu, *Chem. Commun.* **2013**, *49*, 9773–9775.
- (110) Y. Zeng, R. Zou, Z. Luo, H. Zhang, X. Yao, X. Ma, R. Zou and Y. Zhao, *J. Am. Chem. Soc.* **2015**, *137*, 1020–1023.

- (111) X. Chen, M. Addicoat, E. Jin, H. Xu, T. Hayashi, F. Xu, N. Huang, S. Irle and D. Jiang, *Sci. Rep.*, **2015**, *5*, 14650.
- (112) H. Li, Q. Pan, Y. Ma, X. Guan, M. Xue, Q. Fang, Y. Yan, V. Valtchev and S. Qiu, *J. Am. Chem. Soc.* **2016**, *138*, 14783–14788.
- (113) J.-Y. Yue, Y.-P. Mo, S.-Y. Li, W.-L. Dong, T. Chen and D. Wang, *Chem. Sci.* **2017**, *8*, 2169–2174.
- (114) C. Gropp, T. Ma, N. Hanikel and O. M. Yaghi, *Science* **2020**, 370.
- (115) Y. Yusran, X. Guan, H. Li, Q. Fang and S. Qiu, *Natl. Sci. Rev.* **2019**, *7*, 170–190.
- (116) J. L. Segura, S. Royuela and M. Mar Ramos, *Chem. Soc. Rev.* **2019**, *48*, 3903–3945.
- (117) A. Nagai, Z. Guo, X. Feng, S. Jin, X. Chen, X. Ding and D. Jiang, *Nat. Commun.* **2011**, *2*, 536.
- (118) L. Chen, K. Furukawa, J. Gao, A. Nagai, T. Nakamura, Y. Dong and D. Jiang, *J. Am. Chem. Soc.* **2014**, *136*, 9806–9809.
- (119) D. N. Bunck and W. R. Dichtel, *Chem. Commun.* **2013**, *49*, 2457–2459.
- (120) L. A. Baldwin, J. W. Crowe, D. A. Pyles and P. L. McGrier, *J. Am. Chem. Soc.* **2016**, *138*, 15134–15137.
- (121) B. J. Smith, L. R. Parent, A. C. Overholts, P. A. Beaucage, R. P. Bisbey, A. D. Chavez, N. Hwang, C. Park, A. M. Evans, N. C. Gianneschi and W. R. Dichtel, *ACS Cent. Sci.* **2017**, *3*, 58–65.
- (122) A. M. Evans, I. Castano, A. Brumberg, L. R. Parent, A. R. Corcos, R. L. Li, N. C. Flanders, D. J. Gosztola, N. C. Gianneschi, R. D. Schaller and W. R. Dichtel, *J. Am. Chem. Soc.* **2019**, *141*, 19728–19735.
- (123) B. J. Smith, L. R. Parent, A. C. Overholts, P. A. Beaucage, R. P. Bisbey, A. D. Chavez, N. Hwang, C. Park, A. M. Evans, N. C. Gianneschi and W. R. Dichtel, *ACS Cent. Sci.* **2017**, *3*, 58–65.
- (124) A. M. Evans, N. P. Bradshaw, B. Litchfield, M. J. Strauss, B. Seckman, M. R. Ryder, I. Castano, C. Gilmore, N. C. Gianneschi, C. R. Mulzer, M. C. Hersam and W. R. Dichtel, *Adv. Mater.* **2020**, *32*, 2004205.
- (125) I. Castano, A. M. Evans, H. Li, E. Vitaku, M. J. Strauss, J.-L. Brédas, N. C. Gianneschi and W. R. Dichtel, *ACS Cent. Sci.* **2019**, *5*, 1892–1899.
- (126) J. W. Colson, A. R. Woll, A. Mukherjee, M. P. Levendorf, E. L. Spitler, V. B. Shields, M. G. Spencer, J. Park and W. R. Dichtel, *Science* **2011**, *332*, 228–231.
- (127) R. P. Bisbey, C. R. DeBlase, B. J. Smith and W. R. Dichtel, *J. Am. Chem. Soc.* **2016**, *138*, 11433–11436.
- (128) J. M. Rotter, S. Weinberger, J. Kampmann, T. Sick, M. Shalom, T. Bein and D. D. Medina, *Chem. Mater.* **2019**, *31*, 10008–10016.
- (129) J. Cai, Y. Xing and X. Zhao, *RSC Adv.* **2012**, *2*, 8579–8586.
- (130) T. Bao, P. Tang, D. Kong, Z. Mao and Z. Chen, *J. Chromatogr. A* **2016**, *1445*, 140–148.

- (131) F. Xu, S. Jin, H. Zhong, D. Wu, X. Yang, X. Chen, H. Wei, R. Fu and D. Jiang, *Sci. Rep.* **2015**, *5*, 8225.
- (132) C.-J. Yao, Z. Wu, J. Xie, F. Yu, W. Guo, Z. J. Xu, D.-S. Li, S. Zhang and Q. Zhang, *ChemSusChem* **2020**, *13*, 2457.
- (133) D. A. Vazquez-Molina, G. S. Mohammad-Pour, C. Lee, M. W. Logan, X. Duan, J. K. Harper and F. J. Uribe-Romo, *J. Am. Chem. Soc.* **2016**, *138*, 9767–9770.
- (134) X. Chen, H. Zhang, C. Ci, W. Sun and Y. Wang, *ACS Nano* **2019**, *13*, 3600–3607.
- (135) N. Keller and T. Bein, *Chem. Soc. Rev.* **2021**, *50*, 1813–1845.
- (136) S. Liu, M. Wang, T. Qian, H. Ji, J. Liu and C. Yan, *Nat. Commun.* **2019**, *10*, 3898.

1.5 Exploring New Linkage Motifs

As described in **section 1.2.3** and **1.2.4**, covalent organic frameworks (COFs) have been established as a new class of crystalline, highly ordered, porous materials. The frameworks are formed using reversible condensation reactions, a large variety of organic building blocks and the means of reticular chemistry. They have gained immense attention since the first report of 2D COFs by Yaghi and co-workers in 2005¹. Owing to their large surface areas, high crystallinity, and well-defined pore systems, they have been used for different applications such as gas storage^{2,3}, sensing⁴⁻⁶, catalysis^{7,8}, separation^{9,10} and optoelectronics^{11,12} as mentioned in **section 1.2.7** for boronate ester and boroxine based COFs. Moreover, due to the great variety in the organic chemistry toolbox, the construction of COFs featuring tailor-made design becomes possible. Thereby, by a well-chosen selection of the building blocks, their chemical structure and geometry, COFs with tailored pore structures, optical or electronic properties can be accessed. The formation of highly structurally defined products can be ensured due to the slightly reversible nature of the covalent bond formation which allows for building block assembly faults to be corrected during the framework formation process. To date, diverse linkage chemistries have been used for constructing these materials, based on the reversible formation of B–O^{1,13-17}, B–N¹⁸ and C–N¹⁹⁻²¹ bonds (for more details see **Figure 1.21**). Boronate ester and boroxine-based COFs were described thoroughly in **section 1.2.4**. However, these COFs although thermally stable tend to be much less stable in aqueous/ acidic media or towards moisture, which is a big drawback in terms of implementation of such structures as active materials for certain applications.²² Therefore, in the following years, other types of linkage motifs were introduced. The most prominent one is the imine linkage which can be accessed by an acid-catalysed *Schiff-base* imine condensation reaction. To date, a great variety of imine-based COFs have been reported and used for all kinds of applications similar to boronate ester and boroxine based COFs as described in **section 1.2.7**. Additionally, to achieve frameworks that are highly stable and/ or fully conjugated various strategies such as keto-enol-tautomerization²³ or post-synthetic modifications²² (see **section 1.2.5**) have been employed. Thereby, in the past few years vinylene-linked COFs²⁴⁻³⁰ (sp²-carbon linked COFs), which are synthesized using a Knoevenagel polycondensation reaction, have become more and more common. These new structures tend to be much more stable towards hydrolysis compared to commonly known imine- or boronate ester-linked COFs.²⁴ Additionally, they feature non-polar in-plane π -conjugation.²⁸ In the following chapters, COFs featuring different kinds of linkage motifs will be described starting with boronate ester based COFs, followed by vinylene-linked and lastly imine-based COFs. Thereby, the development of new synthetic strategies for tuning optical properties in COFs will be of major interest throughout this thesis.

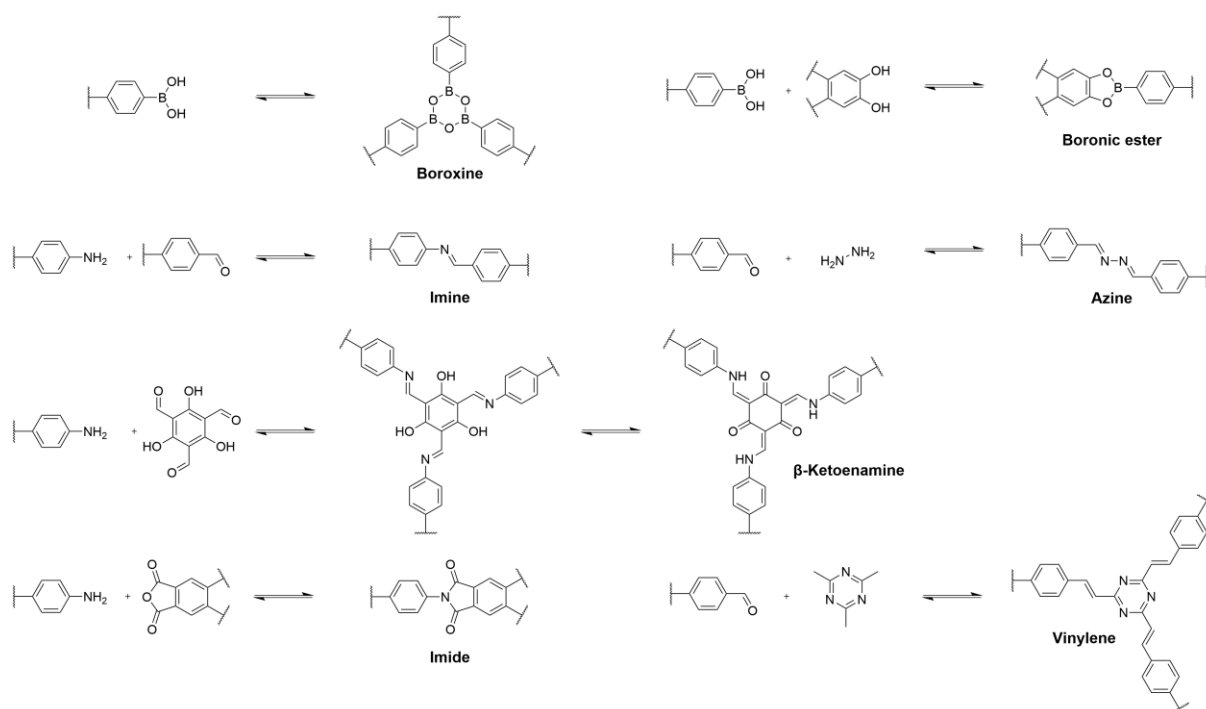


Figure 1.21. Examples for applied condensation reactions for the formation of COFs.

1.6 Tailoring Optical Properties

One of the key features of COFs that makes them attractive for a great variety of different applications is their tunability. Thereby, due to the vast choice of organic building blocks together with different possible linkage motifs as discussed in **section 1.5**, it is possible to form a large variety of different structures with tailor-made absorption and photoluminescence behaviour. There are several different ways of altering the optical properties of COFs such as, (i) the implementation of chromophores into the framework, (ii) the exchange of the linkage motif which can lead to improved conjugation throughout the framework, (iii) altering the stacking distance in 2D COFs which then can have an effect on the electronic overlap of adjacent layers and can thereby promote the formation of long-lived excited species or (iv) the implementation of donor-acceptor systems into the framework.³¹ Moreover, functionalities in COFs altering the optical properties or in general for synthesizing COFs tailored for specific applications, can be introduced using different strategies, whereas to date, two main synthetic strategies have been considered: (i) pre-modification, i.e. using building blocks that have been modified prior to the formation of the frameworks or (ii) post-synthetic modification (PSM, see **section 1.2.5**) where the framework functionalities are introduced only after the successful formation of the frameworks. In this thesis, additional methodologies will be described that can be used for the tailoring of optical properties in COFs, starting with a new post-synthetic modification approach, followed by a three-component reaction forming both fused aromatics and the frameworks *in chorus* and thereby altering the photophysical properties in COFs.

1.7 References

- (1) Côté, A. P.; Benin, A. I.; Ockwig, N. W.; O’Keeffe, M.; Matzger, A. J.; Yaghi, O. M. Porous, Crystalline, Covalent Organic Frameworks. *Science* **2005**, *310*, 1166–1170.
- (2) Li, Z.; Feng, X.; Zou, Y.; Zhang, Y.; Xia, H.; Liu, X.; Mu, Y. A 2D azine-linked covalent organic framework for gas storage applications. *Chem. Commun.* **2014**, *50*, 13825–13828.
- (3) Fan, H.; Mundstock, A.; Feldhoff, A.; Knebel, A.; Gu, J.; Meng, H.; Caro, J. Covalent Organic Framework–Covalent Organic Framework Bilayer Membranes for Highly Selective Gas Separation. *J. Am. Chem. Soc.* **2018**, *140*, 10094–10098.
- (4) Ascherl, L.; Evans, E. W.; Gorman, J.; Orsborne, S.; Bessinger, D.; Bein, T.; Friend, R. H.; Auras, F. Perylene-Based Covalent Organic Frameworks for Acid Vapor Sensing. *J. Am. Chem. Soc.* **2019**, *141*, 15693–15699.
- (5) Jhulki, S.; Evans, A. M.; Hao, X.-L.; Cooper, M. W.; Feriante, C. H.; Leisen, J.; Li, H.; Lam, D.; Hersam, M. C.; Barlow, S.; et al. Humidity Sensing through Reversible Isomerization of a Covalent Organic Framework. *J. Am. Chem. Soc.* **2020**, *142*, 783–791.
- (6) Wang, Y.; Zhao, Z.; Li, G.; Yan, Y.; Hao, C. A 2D covalent organic framework as a sensor for detecting formaldehyde. *J. Mol. Model.* **2018**, *24*, 153.
- (7) Wang, Y.; Liu, H.; Pan, Q.; Wu, C.; Hao, W.; Xu, J.; Chen, R.; Liu, J.; Li, Z.; Zhao, Y. Construction of Fully Conjugated Covalent Organic Frameworks via Facile Linkage Conversion for Efficient Photoenzymatic Catalysis. *J. Am. Chem. Soc.* **2020**, *142*, 5958–5963.
- (8) Shen, J.-C.; Jiang, W.-L.; Guo, W.-D.; Qi, Q.-Y.; Ma, D.-L.; Lou, X.; Shen, M.; Hu, B.; Yang, H.-B.; Zhao, X. A rings-in-pores net: crown ether-based covalent organic frameworks for phase-transfer catalysis. *Chem. Commun.* **2020**, *56*, 595–598.
- (9) Khan, N. A.; Zhang, R.; Wu, H.; Shen, J.; Yuan, J.; Fan, C.; Cao, L.; Olson, M. A.; Jiang, Z. Solid–Vapor Interface Engineered Covalent Organic Framework Membranes for Molecular Separation. *J. Am. Chem. Soc.* **2020**, *142*, 13450–13458.
- (10) Cui, W.-R.; Zhang, C.-R.; Jiang, W.; Li, F.-F.; Liang, R.-P.; Liu, J.; Qiu, J.-D. Regenerable and stable sp² carbon-conjugated covalent organic frameworks for selective detection and extraction of uranium. *Nat. Commun.* **2020**, *11*, 436.
- (11) Calik, M.; Auras, F.; Salonen, L. M.; Bader, K.; Grill, I.; Handloser, M.; Medina, D. D.; Dogru, M.; Löbermann, F.; Trauner, D.; et al. Extraction of Photogenerated Electrons and Holes from a Covalent Organic Framework Integrated Heterojunction. *J. Am. Chem. Soc.* **2014**, *136*, 17802–17807.
- (12) Guo, J.; Xu, Y.; Jin, S.; Chen, L.; Kaji, T.; Honsho, Y.; Addicoat, M. A.; Kim, J.; Saeki, A.; Ihee, H.; et al. Conjugated organic framework with three-dimensionally ordered stable structure and delocalized π clouds. *Nat. Commun.* **2013**, *4*, 2736.
- (13) Dalapati, S.; Jin, E.; Addicoat, M.; Heine, T.; Jiang, D. Highly Emissive Covalent Organic Frameworks. *J. Am. Chem. Soc.* **2016**, *138*, 5797–5800.
- (14) Martínez-Abadía, M.; Stoppiello, C. T.; Strutyński, K.; Lerma-Berlanga, B.; Martí-Gastaldo, C.; Saeki, A.; Melle-Franco, M.; Khlobystov, A. N.; Mateo-Alonso, A. A Wavy Two-Dimensional Covalent Organic Framework from Core-Twisted Polycyclic Aromatic Hydrocarbons. *J. Am. Chem. Soc.* **2019**, *141*, 14403–14410.

- (15) Salonen, L. M.; Medina, D. D.; Carbó-Argibay, E.; Goesten, M. G.; Mafra, L.; Guldris, N.; Rotter, J. M.; Stroppa, D. G.; Rodríguez-Abreu, C. A supramolecular strategy based on molecular dipole moments for high-quality covalent organic frameworks. *Chem. Commun.* **2016**, 52, 7986–7989.
- (16) Evans, A. M.; Castano, I.; Brumberg, A.; Parent, L. R.; Corcos, A. R.; Li, R. L.; Flanders, N. C.; Gosztola, D. J.; Gianneschi, N. C.; Schaller, R. D.; et al. Emissive Single-Crystalline Boroxine-Linked Colloidal Covalent Organic Frameworks. *J. Am. Chem. Soc.* **2019**, 141, 19728–19735.
- (17) Frey, L.; Jarju, J. J.; Salonen, L. M.; Medina, D. D. Boronic-acid-derived covalent organic frameworks: from synthesis to applications. *New J. Chem.* **2021**, 45, 14879–14907.
- (18) Jackson, K. T.; Reich, T. E.; El-Kaderi, H. M. Targeted synthesis of a porous borazine-linked covalent organic framework. *Chem. Commun.* **2012**, 48, 8823–8825.
- (19) Keller, N.; Sick, T.; Bach, N. N.; Koszalkowski, A.; Rotter, J. M.; Medina, D. D.; Bein, T. Dibenzochrysenes enable tightly controlled docking and stabilize photoexcited states in dual-pore covalent organic frameworks. *Nanoscale* **2019**, 11, 23338–23345.
- (20) Bessinger, D.; Muggli, K.; Beetz, M.; Auras, F.; Bein, T. Fast-Switching Vis–IR Electrochromic Covalent Organic Frameworks. *J. Am. Chem. Soc.* **2021**, 143, 7351–7357.
- (21) Rotter, J. M.; Guntermann, R.; Auth, M.; Mähringer, A.; Sperlich, A.; Dyakonov, V.; Medina, D. D.; Bein, T. Highly conducting Wurster-type twisted covalent organic frameworks. *Chem. Sci.* **2020**, 11, 12843–12853.
- (22) Haase, F.; Troschke, E.; Savasci, G.; Banerjee, T.; Duppel, V.; Dörfler, S.; Grundei, M. M. J.; Burow, A. M.; Ochsenfeld, C.; Kaskel, S.; et al. Topochemical conversion of an imine- into a thiazole-linked covalent organic framework enabling real structure analysis. *Nat. Commun.* **2018**, 9, 2600.
- (23) Yang, Y.; He, X.; Zhang, P.; Andaloussi, Y. H.; Zhang, H.; Jiang, Z.; Chen, Y.; Ma, S.; Cheng, P.; Zhang, Z. Combined Intrinsic and Extrinsic Proton Conduction in Robust Covalent Organic Frameworks for Hydrogen Fuel Cell Applications. *Angew. Chem. Int. Ed.* **2020**, 59, 3678–3684.
- (24) Acharjya, A.; Pachfule, P.; Roeser, J.; Schmitt, F.-J.; Thomas, A. Vinylene-Linked Covalent Organic Frameworks by Base-Catalyzed Aldol Condensation. *Angew. Chem. Int. Ed.* **2019**, 58, 14865–14870.
- (25) Bi, S.; Thiruvengadam, P.; Wei, S.; Zhang, W.; Zhang, F.; Gao, L.; Xu, J.; Wu, D.; Chen, J.-S. Vinylene-Bridged Two-Dimensional Covalent Organic Frameworks via Knoevenagel Condensation of Tricyanomesitylene. *J. Am. Chem. Soc.* **2020**, 142, 11893–11900.
- (26) Jadhav, T.; Fang, Y.; Patterson, W.; Liu, C.-H.; Hamzehpoor, E.; Perepichka, D. F. 2D Poly(arylene vinylene) Covalent Organic Frameworks via Aldol Condensation of Trimethyltriazine. *Angew. Chem. Int. Ed.* **2019**, 58, 13753–13757.
- (27) Lyu, H.; Diercks, C. S.; Zhu, C.; Yaghi, O. M. Porous Crystalline Olefin-Linked Covalent Organic Frameworks. *J. Am. Chem. Soc.* **2019**, 141, 6848–6852.
- (28) Xu, S.; Richter, M.; Feng, X. Vinylene-Linked Two-Dimensional Covalent Organic Frameworks: Synthesis and Functions. *Acc. Mater. Res.* **2021**, 2, 252–265.
- (29) Xu, S.; Sun, H.; Addicoat, M.; Biswal, B. P.; He, F.; Park, S.; Paasch, S.; Zhang, T.; Sheng, W.; Brunner, E.; et al. Thiophene-Bridged Donor–Acceptor sp²-Carbon-Linked 2D Conjugated Polymers as Photocathodes for Water Reduction. *Adv. Mater.* **2021**, 33, 2006274.

- (30) Zhao, Y.; Liu, H.; Wu, C.; Zhang, Z.; Pan, Q.; Hu, F.; Wang, R.; Li, P.; Huang, X.; Li, Z. Fully Conjugated Two-Dimensional sp^2 -Carbon Covalent Organic Frameworks as Artificial Photosystem I with High Efficiency. *Angew. Chem. Int. Ed.* **2019**, *58*, 5376–5381.
- (31) Keller, N.; Bein, T. Optoelectronic processes in covalent organic frameworks. *Chem. Soc. Rev.* **2021**, *50*, 1813–1845.

2. Characterization Methods

2.1 X-ray Diffraction (XRD)

The main concerns for characterizing COFs include structural order, atomic connectivity and morphology. So far, the method of choice for the analysis of COFs is powder X-ray diffraction (PXRD). With this method, the crystallinity and structure of powders, films and single crystals of a big variety of different compounds can be assessed and additionally, the phase composition can be characterized. PXRD is a very important characterization method that has been used to address many issues concerning the crystal structure of solids, like e.g., lattice constants, geometry, orientation of single crystals or defects. In 1895, Wilhelm Conrad Röntgen discovered electromagnetic radiation with typical wavelengths ranging from 5 pm to 100 pm, called X-Rays. In principle, these X-rays can be generated, when accelerated, focused electrons hit a metal target. A hole in the inner shell of the atom is generated by an impinging electron which is subsequently filled by an electron from an outer shell. The energy difference between these two energy states is emitted as X-ray photon whereas the wavelength and the intensity of the X-rays depend on the specimen that was used as a metal target. These differences can be attributed to the differences in electron shells of different target materials, described by *Moseley's law*: $\frac{1}{\lambda} = \frac{K}{(Z-\sigma)^2}$. With this, the relationship between the atomic number Z and the wavelength is described, whereas K and σ are constants for a given spectral line. Different metal filters and a collimator are used to isolate an intense part of the spectrum, which is usually K_{α} radiation. When a collimated beam of X-ray hits a specimen, it is diffracted by the crystalline phases in the specimen according to *Bragg's law*:

$$\lambda = 2d \sin \theta \quad (2.1)$$

d is the spacing between the atomic planes in the crystalline phase, λ is the X-ray wavelength (for Cu- K_{α} 1.540562 Å) and θ the diffraction angle. This relation is also depicted in **Figure 2.1**.

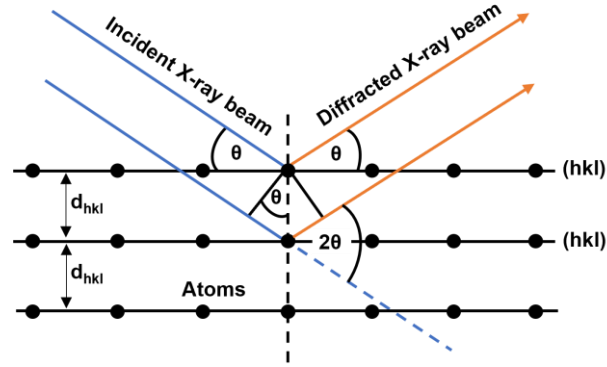


Figure 2.1. Schematic illustration of *Bragg's relation* at constructive interference. Diffraction of incident X-ray beams at the crystallographic planes (hkl) with distances d_{hkl} and under the angle θ .

This technique is based on the principle that X-rays are scattered at crystallite lattice planes having a similar spacing as the X-ray wavelength. Depending on the angle under which X-rays impinge, different scattering events can happen, meaning that scattered X-rays can interfere either constructively or destructively. Thereby, with *Bragg's law* the circumstances can be described at which constructive interference can be observed. Thus, the obtained pattern of constructive interference can be transformed into a plot of the intensity versus the diffraction angle 2θ , a so-called diffraction pattern, which contains information about the atomic arrangement in the crystal. In this one-dimensional diffraction pattern, the constructive interference of reflected X-rays can be observed as peak, a so-called reflection, with the measured intensities being mostly dependent on the lattice atoms and their spatial positions. The size of the crystalline domains also influences the diffraction pattern. For instance, smaller crystalline domains would lead to a broadening of the reflection peaks compared to larger domains. By using Scherrer's formula (eqn. 2.2), the crystallite size D can be estimated from the peak width.³

$$D = \frac{k\lambda}{B \cos \theta_B} \quad (2.2)$$

λ is the X-ray wavelength, B is the full width at half maximum (FWHM) of a diffraction peak, θ_B is the diffraction angle and k is the Scherrer's constant of the order unity for a usual crystal.⁴

During all the projects, this method was used to determine the crystallinity of the samples and their crystal structure. The XRD measurements were performed using a Bruker D8 Discover with Ni-filtered Cu- K_{α} -radiation and a position-sensitive semiconductor detector (LynxEye).

2.2 Grazing-Incidence Wide-Angle X-ray Scattering (GIWAXS)

To analyze crystalline surfaces such as oriented thin COF films, grazing-incidence X-ray scattering is the method of choice. Thereby, by illuminating a planar sample at grazing angle of incidence thin films or surfaces can be characterized which would otherwise not be possible using general X-ray geometries due to the low sample thickness. In this measurement, the angle of the incident beam is below the critical angle of the substrate. Schematically, the geometry of such X-ray measurements is shown in **Figure 2.2**.^{5,6}

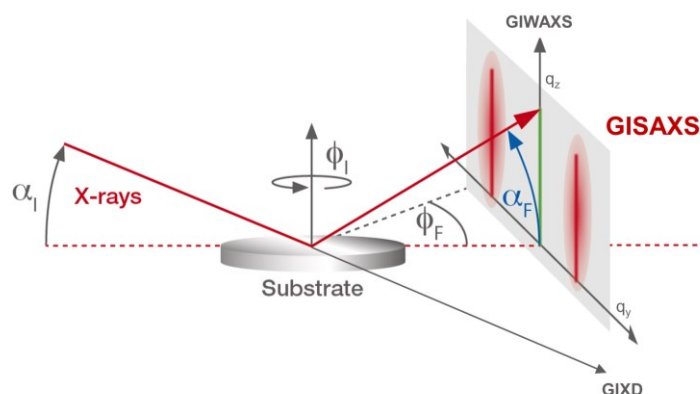


Figure 2.2. Schematic illustration of the GISAXS geometry.⁵

As can be seen in **Figure 2.2** a monochromatic X-ray beam is focused on a sample surface at a small incident angle α_i . Subsequently, the X-rays are scattered and measured by a 2D area detector along α_F and ϕ_F . While most devices are operated at large sample-detector distances (> 2 m; grazing incidence small angle X-ray scattering (GISAXS)), with reduced distances, recording of X-ray scattering at wide angles is enabled (GIWAXS). The positions of the detected reflection peaks are measured as the wavelength-independent scattering vector q . The q -values obtained by these measurements are connected to 2θ angles by equation 2.3.^{5,6}

$$q = \frac{4\pi}{\lambda} \sin \frac{2\theta}{2} \quad (2.3)$$

GIWAXS is a suitable technique, for studying the structure and orientation of thin layers of organic materials, such as covalent organic frameworks (COFs) on any substrate. Thereby, a preferential orientation of COF thin films can be seen as distinct scattering spots in the 2D GIWAXS pattern, while non-oriented materials lead to the appearance of Debye-Scherrer rings with a homogeneous intensity distribution.^{5,6}

Two-dimensional grazing-incidence wide angle X-ray scattering (2D GIWAXS) patterns were measured using an Anton-Paar SAXSpace system equipped with a Cu K α microfocus source operated at 50 kV and 1 mA and an Eiger Dectris R 1M 2D detector.

2.3 Gas Sorption

For the characterization of COFs, the determination of the specific surface area and the pore size distribution are fundamental parameters. Both these properties can be easily investigated using the physisorption technique. This characterization method relies on the fact that gaseous adsorptives can reversibly bind onto the surface of a material (adsorbent) and thereby valuable information about the underlying structure and porosity of the analyzed material can be obtained. Exposure of a material to nitrogen gas at 77 K will lead to an enrichment of the gas on the surface of the solid due to weak van-der-Waals forces. This process is known as physical adsorption or physisorption. The reversible adsorption of the nitrogen gas will lead to the coverage of the specimen surface and the formation of several layers. During the measurement, the amount of adsorbed gas molecules with increasing partial pressure is determined at a constant temperature. Accordingly, the relative pressure of the adsorbate p/p_0 can be plotted against the amount of substance n that was adsorbed at standard pressure and constant temperature. Hence, typical isotherm diagrams can be obtained.⁷

There are two different ways of determining the adsorption isotherm. It can either be measured gravimetrically or volumetrically. Both variants are based on the step-wise increase of the gas pressure in the reaction chamber. As soon as equilibrium is reached, the gas pressure is not changed for a defined period of time and subsequently, either the adsorbed gas volume (volumetric) or the mass gain (gravimetric) is determined. When a relative pressure close to $p/p_0 = 1$ is obtained, the desorption isotherm can be recorded by the removal of defined gas volumes from the specimen container and detection of the equilibrium pressures for every step. With nitrogen sorption measurements, different characteristic isotherm shapes and hysteresis types can be obtained depending on the porosity of the material. **Figure 2.3** shows the classification of the different gas physisorption isotherms.

In total there are eight different isotherms that were classified by the International Union of Pure and Applied Chemistry (IUPAC).⁸ Pores with a diameter of 2 nm or lower are defined as micropores, a width between 2 and 50 nm corresponds to mesopores and macropores exceed a diameter of 50 nm.

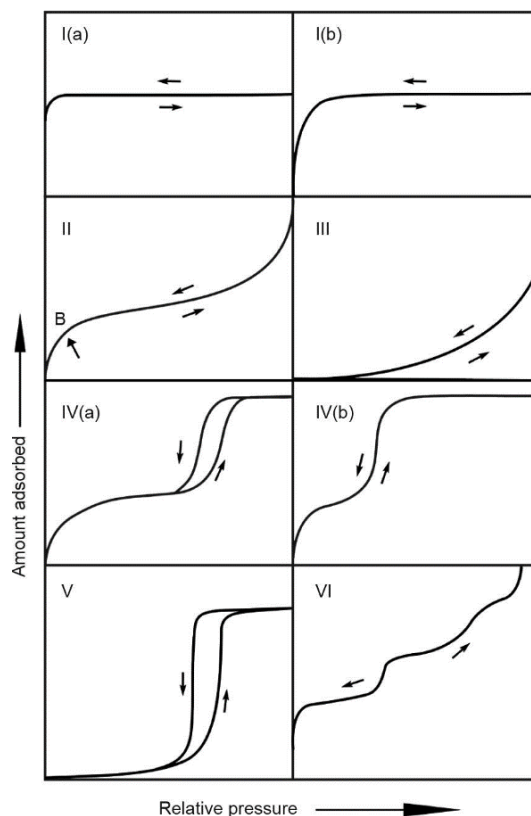


Figure 2.3. Classification of the isotherms according to IUPAC.⁸

Type I, or also called the *Langmuir*-isotherm is commonly present for microporous systems with small external surfaces. The steep increase of the adsorbed quantity at low relative pressure indicates that the micropores are completely filled. Type I can be separated into two different isotherms, namely type I(a) and I(b), whereas type I(a) corresponds to micropore filling in mainly narrow micropores and type I(b) to wider micropores and narrow mesopores.⁸

A Type II isotherm shows the typical behavior of non-porous or macroporous material. Monolayer coverage is followed by multilayer adsorption at higher relative pressures whereas *B* marks the point in the isotherm where multilayer adsorption starts.⁸

Type III and V isotherms both indicate weak adsorbate-adsorbent interactions and are mostly associated with non-porous and mesoporous adsorbents, respectively.

Type IV isotherms are typical for mesoporous materials. Monolayer-multilayer adsorption can be observed comparable to a type II isotherm, whereas again *B* depicts the point where monolayer coverage is complete. The difference between Type II and IV isotherms is that for the latter one, a hysteresis loop is present within the curve which indicates capillary condensation taking place in the mesopores. This can be explained by the strength of adsorbate-adsorbent and adsorbate-adsorbate interactions. Type IV isotherms can be separated into two different isotherms, type IV(a) and type IV(b), whereas type IV(a)

corresponds to capillary condensation and hysteresis in mesoporous materials and type IV(b) to a reversible isotherm of mesoporous materials with a smaller pore width.

Type VI shows the process of a stepwise multilayer adsorption on non-porous, uniform surfaces with the height of the individual steps corresponding to the respective monolayer capacity for each adsorbed layer.

There are several different theories describing and interpreting adsorption isotherms whereas one of the most common ones is called the Brunauer-Emmett-Teller (BET) theory⁹. The BET-theory is based on three main assumptions: (1) Adsorption of gas molecules occurs in multilayers on the solid whereas the number of layers is infinite. (2) Each layer only interacts with the next adjacent adsorption layer (except for the first one) and (3) the Langmuir theory¹⁰, which covers monolayer to multilayer molecular adsorption, can be applied for each layer. Here, the adsorption enthalpy for each layer is the same besides the one for the first layer. Eqn. 2.4 shows the BET-equation.

$$\frac{\frac{p}{p_0}}{n(1 - \frac{p}{p_0})} = \frac{(C - 1)}{n_m C} \frac{p}{p_0} + \frac{1}{n_m C} \quad (2.4)$$

Where n_m is the adsorbed amount for the monolayer, C is the BET-constant, n the adsorbed amount at relative pressure p/p_0 , p the equilibrium pressure and p_0 the saturation pressure.

A true value of n_m can only be obtained for the linear part of the equation which is typically restricted to relative pressures in the range of around 0.05-0.30. Therefore, the total surface area a_s can be determined using the following equation:

$$a_s(BET) = n_m N_A \frac{\sigma_m}{m} \quad (2.5)$$

With N_A being the Avogadro constant, σ_m the molecular cross-sectional area and m the mass of the adsorbent.^{7,11}

2.4 Thermogravimetric Analysis (TGA)

Thermogravimetric Analysis (TGA) is a method that can be used to determine the thermal stability of a sample.¹² Thereby, the mass of a substance is monitored as a function of temperature or time while the sample is subjected to a temperature program in a controlled atmosphere. With this, temperature-dependant mass-changes can be clearly observed by changes in the shape of the TGA profile and

therefore attributed to solvent evaporation, dehydration, combustion, or decomposition of the investigated material. Typically, the sample to be analyzed is precisely weighed in a non-reactive crucible and heated with a linear heating rate under the desired atmosphere up to 900 °C, while simultaneously monitoring mass changes over time with a precision balance.

In this thesis, TGA was used to analyze the thermal stability of the synthesized COFs. Thereby, a NETZSCH TA 440 C TG/DSC was used (heating rate of 10 °C min⁻¹ in a stream of synthetic air or nitrogen of about 25 mL min⁻¹).

2.5 Electron Microscopy (EM)

Electron Microscopy (EM) is a powerful method that uses a beam of accelerated electrons and that can be used to reveal the structure and morphology of nanostructured materials. The advantage of EM over optical microscopy is that compared to optical microscopy, which is classically limited in resolution to approximately 200 nm (the Abbe limit, but note the advent of superresolution microscopy¹³), due to the use of electrons with a de-Broglie-wavelength in the range of a few picometers, EM can resolve objects down to the atomic level. Thereby, an electron microscope can be used to image the well-defined crystalline domains, their morphologies and pores of covalent organic frameworks. The electron microscope is operated under high vacuum to avoid scattering of the high energy electrons at residual gas molecules and to ensure the thermal and chemical stability of the electron gun. The electron beam is generated using a field emission gun (tungsten filament) or a thermal emitter (heated tungsten tip). Then the beam is focused onto the sample using an array of electromagnetic lenses.^{3,14}

2.5.1 Scanning Electron Microscopy (SEM)

To investigate the surface properties of the sample scanning electron microscopy (SEM) can be used. Thereby, a convergent electron beam at low acceleration voltages (1 – 30 kV) is used to scan the sample surface in a grid pattern. The signal that is detected after the interaction of the electron beam with the sample in combination with the beam's position can be used to generate an image. The image is thereby generated by scanning the sample point-by-point and line-by-line and here high resolutions (up to approximately 0.6 nm) can be obtained. The accelerated electrons penetrate the first layers of the sample and thereby cause the emission of further electrons and photons. Depending on the detection mode and acceleration voltage, different types of SEM imaging are possible by using either backscattered electrons (BSE), secondary electrons (SE) or characteristic X-Rays. Backscattered electrons (BSE) are primary electrons with high-energy that result from elastic scattering from the sample. Secondary electrons (SE) are lower in energy and result from inelastic scattering in less deep regions and are therefore surface sensitive.^{3,14}

2.5.2 Transmission Electron Microscopy (TEM)

A transmission electron microscope (TEM) can be used to get information about the internal structure of a specimen. Thereby, high resolutions far below 10 nm can be achieved using a TEM. Moreover, data can be obtained in reciprocal space by electron diffraction, making it a very powerful tool for the characterization of covalent organic frameworks. TEMs are typically operated at very high voltages between 60 kV and 400 kV and therefore robust samples are required to get high quality images. Less stable samples might degrade or decompose which therefore might lead to lower resolution and lower image quality.^{3,14}

In **Figure 2.4**, a schematic illustration of the imaging mode in a TEM is shown. Typically, a TEM consists of an electron gun (source), an electromagnetic condenser lens system, followed by a specimen stage with a specimen. Using an objective lens afterwards, an image of the specimen can be generated. The selected area aperture and objective aperture are used to enhance the contrast, followed by an intermediate and a projector lens, used to enlarge the image. The high energy electron image is converted into a visible image by electromagnetic lenses and detected using a fluorescent screen or is produced in an electronic image detector. Further, to maximize the mean free path of the electrons, the whole device is kept under high vacuum.^{3,14}

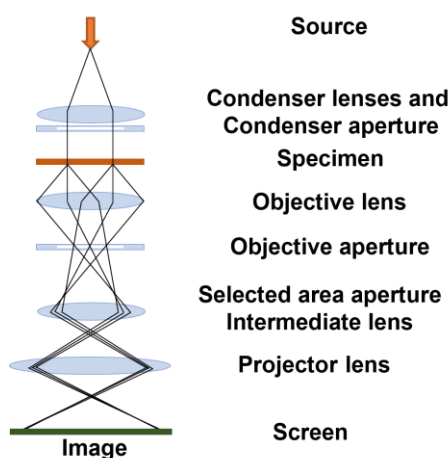


Figure 2.4. Schematic illustration of the imaging mode in a TEM.

The scanning electron microscopy images in this work were recorded on a Thermo Fischer FEI Helios G3 UC Dual Beam Microscope with an acceleration voltage of 1-30 kV. High Resolution Transmission Electron Microscopy (HRTEM) and Scanning Transmission Electron Microscopy in High Angle Annular Dark Field mode (STEM-HAADF) were performed using a FEI Titan Themis 60-300 equipped with a field emission gun operated at 300 kV.

2.6 Infrared Spectroscopy (IR)

Infrared spectroscopy (IR) is based on absorption spectra that are detected in the infrared range when the sample is placed in the path of a suitable infrared radiation source. Thereby, IR absorption spectra can be used to get information on the chemical bonding in the system. Normally, molecular vibrations and rotations are excited by electromagnetic radiation in the infrared region with a range between 4000 cm^{-1} and 400 cm^{-1} . The bonds of molecules can be thought of as springs which can be set into vibration with frequencies depending on the atomic weights and stiffness of the underlying bonds of the molecules. Thereby, many functional groups of organic molecules show characteristic vibrations corresponding to specific parts of the IR spectrum and thereby IR spectroscopy allows for identifying and distinguishing functional groups. In an infrared experiment, the intensity of the IR radiation is measured before and after the interaction with the sample whereby radiation is absorbed by the molecule to excite vibrations. The frequency of the absorbed IR radiation depends on the bond strength and the atomic masses whereby greater bond strength and lower atomic masses require more energy to excite these vibrations and thus results in higher vibrational frequencies. In IR spectroscopy there are different selection rules: (i) molecular vibrations of molecules with changing dipole moments occurring during the vibration process are called IR-active and can be excited; (ii) if a molecule with a centre of symmetry exhibits vibrations that are symmetric to the centre of symmetry, these molecular vibrations are called IR-inactive (forbidden). Using the Fourier transformed infrared (FT-IR) spectroscopy technique allows for fast and accurate measurements. Thereby, the molecules are excited using a beam that contains multiple wavelengths at once. Using a Michelson interferometer, this beam can be modified to contain a different combination of wavelengths. Thus, the absorption of each wavelength and thereby the IR spectrum can be calculated using a computer.³

IR measurements were conducted on a Perkin Elmer Spectrum BX FT-IR instrument in combination with an attenuated total reflection (ATR) accessory comprising an ATR diamond crystal.

2.7 Nuclear-Magnetic-Resonance Spectroscopy (NMR)

Nuclear magnetic resonance (NMR) spectroscopy has become an indispensable method for the characterization of chemical molecules. It allows molecular structure determination as well as the study of dynamics in organic, inorganic and biological systems. Moreover, the electronic periphery of magnetic isotopes in molecules and their interactions with surrounding atoms can be analyzed. The molecular structure can be determined, since the interaction of an oscillating radio-frequency electromagnetic field with a collection of nuclei immersed in a strong external magnetic field can be measured. Depending on their chemical environment, atoms with a nuclear spin will show characteristic

behaviour in an external magnetic field. With NMR spectroscopy only nuclei can be measured that reveal an intrinsic spin and therefore, the investigated nuclei need to have an odd number of protons, neutrons or both such as *e.g.* ^1H , ^{13}C or ^{19}F . This nuclear spin goes along with a spin angular momentum \vec{S} whereas the two are connected *via* the gyromagnetic ratio γ . This relation can be seen in eqn. 2.6.

$$\vec{\mu} = \gamma \vec{S} \quad (2.6)$$

When atoms are exposed to an external magnetic field, the possible orientations of their magnetic momentum are limited. Only certain quantum states are allowed, which are determined by the spin quantum number I . For each spin quantum number $2I+1$ orientations exist. These spin states are not degenerate in an external magnetic field and thus split into certain energy levels. Absorption of electromagnetic radiation in the radio frequency range will lead to a transition between these states, when the following equations (eqn. 2.7 and 2.8) are fulfilled.

$$\nu = \frac{\gamma B_0}{2\pi} \quad (2.7)$$

$$\nu = \gamma B_{loc} = \gamma(B_0 + B_{int}) \quad (2.8)$$

ν is the resonance frequency, B_0 the external magnetic field, B_{loc} the local magnetic field, B_{int} the internal magnetic field and γ the gyromagnetic ratio.

The different electronic surroundings of the atoms will lead to a difference between the external and the local magnetic field which will subsequently cause a difference in resonance frequency. This difference can be measured and can thus give valuable information about the electronic structure and chemical environment.¹⁵⁻¹⁷ NMR measurements were conducted on a 400 MHz Bruker Avance III HD spectrometer.

2.8 Mass Spectrometry

Mass spectrometry can be used to identify a compound from the molecular or atomic mass(es) of its constituents. With this information, identification of elements and determination of the molecular formula of the analyzed molecule becomes possible. The basic principle of mass spectrometry is the generation of ions of the sample that is to be analyzed. These ions are then separated and quantitatively detected, whereby separation of the ions happens according to their different mass to charge (m/z) ratios.

In principle, a small amount of a compound is evaporated, and leaked into the ionization chamber where it is ionized by the use of an electron beam. These positively charged ions are then forced out of the ionization chamber by inducing a small positive charge and are then accelerated by an electrostatic field before entering the analyzer. Within the analyzer, separation of the ions takes place. A strong magnetic field is applied perpendicular to the motional direction of the ions which leads the ions to follow a circular trajectory due to the Lorentz acceleration, whereas the radius is dependent on the mass to charge ratio (m/z) of the ions. After passing the exit-slit, the ions collide on a collector-electrode where the resulting current is amplified and registered as a function of the magnetic-field force or the accelerating voltage.

During all the projects, the molecules were analyzed using electron ionization (EI), also called electron impact ionization or simply electron impact. This ionization method is the oldest and most characterized one and offers the advantage that it can be applied to virtually all volatile compounds.¹⁸⁻²⁰

2.9 Ultraviolet-Visible Spectroscopy (UV-vis)

UV-vis spectroscopy is an important characterization method that can be used to determine the absorption properties of a certain molecule in solution, as solids or as a thin film. For this purpose, light in the range of the ultraviolet (UV), visible (VIS) and near-infrared (NIR) spectrum is used to irradiate the sample. This radiation will lead to a transition of valence electrons from the ground state to various excited states. Thereby, the energy of the absorbed photon needs to match the energy difference between the highest occupied molecular orbital (HOMO) and the lowest unoccupied molecular orbital (LUMO). Further, an excitation into higher vibrational levels is also possible when using an excitation source providing more energy than the bandgap.

The *Lambert-Beer law* (eqn. 2.9)) describes the relationship between the measured intensity of transmitted light, the concentration of the absorbing sample and the path length.

$$A = -\log_{10} \frac{I}{I_0} = \epsilon c L \quad (2.9)$$

Where A is the absorbance of the analyzed sample, I_0 the intensity of the incoming light, I the intensity of the transmitted light, ϵ the extinction coefficient, c the concentration of the absorbing species and L the path length (pathway of the absorbing species).

The absorbance A of a sample can then be used to calculate the optical bandgap using a Tauc plot (eqn. 2.10). Thereby, α is the absorption coefficient or absolute absorbance, ν the frequency of light, E_g the

bandgap, h Planck's constant and A a proportionality constant. Depending on the type of transition, r can vary between 0.5, 1.5, 2 and 3, where 0.5 stands for direct allowed, 1.5 for direct forbidden, 2 indirect allowed and 3 for indirect forbidden transitions. In all the projects described in this thesis $r = 0.5$ was used, assuming a direct bandgap transition for the different studied COFs and molecules.²¹

$$(\alpha hv)^{\frac{1}{r}} = A(hv - E_g) \quad (2.10)$$

For COFs, it is often necessary to study their absorption properties on solid (powder) materials. Here, the Kubelka-Munk (KM) theory can be used. Thereby, this theory is based on two assumptions: (1) scattering is more likely than absorption and (2) reflection on the surface is negligible. The diffuse reflectance of the sample to be analyzed is measured and referenced to barium sulfate as white standard. Using the Kubelka-Munk equation (eqn. 2.11), the experimental data can then be converted into spectra that approximate the absorption behavior of the analyzed solids.²²

$$KM = \frac{(1 - R)^2}{2R} \quad (2.11)$$

During this thesis, UV-Vis-NIR spectra were recorded on a Perkin-Elmer Lambda 1050 spectrometer equipped with a 150 mm integrating sphere and photomultiplier tube (PMT) and InGaAs detectors. Diffuse reflectance spectra were measured with a Praying Mantis (Harrick) accessory and were referenced to barium sulfate powder as white standard.

2.10 Photoluminescence Spectroscopy (PL)

For further characterizing the photophysical properties of the synthesized building blocks or the resulting frameworks, photoluminescence spectroscopy was used. The physical principle of photoluminescence spectroscopy (PL) can easily be described using the *Jablonski*-diagram, depicted in **Figure 2.5**. When a photon of a particular energy ($h\nu_{ex}$) supplied by an external source, such as a laser, hits a fluorophore and gets absorbed, an excited singlet state (S_1) is created. Immediately after excitation, the molecule will return to the rotational and vibrational ground state of the excited singlet state. The excited state only exists for a finite time. To return back to the ground state there are several different processes that can occur. The electron can either return to the ground state S_0 radiatively *via* fluorescence emission or non-radiatively *via* one of these three processes: internal conversion (IC), collisional quenching (CQ) or intersystem crossing to a triplet excited state T_1 (ISC) that lies at lower energy relative to S_1 . From this triplet state, relaxation to the ground state can either occur *via* the emission of a photon by phosphorescence or *via* deactivation through internal conversion to S_0 . Since, however, a transition

from T_1 to S_0 is formally spin-forbidden and the triplet states tend to be long-lasting, phosphorescence shows a delayed photon emission.²³

The difference of photoluminescence spectroscopy (PL) compared to UV-Vis measurements is that, detection of photons emitted by the relaxation from an excited state to the ground state of a molecule is possible. Thereby, one has to distinguish two types of photoluminescence, namely fluorescence and phosphorescence. While fluorescence emission occurs within a few nanoseconds after photoexcitation, phosphorescence emission can last much longer, up to several hours.²⁴

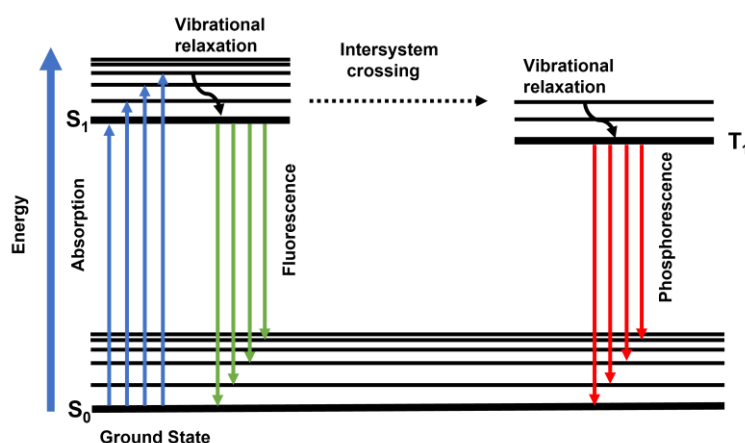


Figure 2.5. Jablonski-diagram showing possible transitions between the ground state and excited states.

Steady-state PL measurements were conducted on the same setup as the Time-Correlated Single Photon-Counting (TCSPC) measurements (FluoTime 300, PicoQuant GmbH). The PL was measured using a high-resolution monochromator and photomultiplier detector assembly (PMA-C 192-N-M, PicoQuant GmbH).

2.11 Time-Correlated Single Photon Counting (TCSPC)

Using Time-Correlated Single Photon Counting (TCSPC), the lifetime of excited states can be measured. Thereby, in contrast to steady-state photoluminescence measurements, TCSPC looks at the time-resolved kinetics of the photoemission of a sample. The lifetime of a fluorescent sample describes the average time a sample spends in an excited state. In principle, using a pulsed laser, the sample can be excited and subsequently a single photon can be emitted. Thereby, single photon events are detected, and time delay between excitation and emission is measured using ultra-fast electronics. **Figure 2.6** shows a schematic illustration of the measurement of start-stop times in a time-resolved TCSPC measurement. As shown in this figure, the process is repeated many times to gather sufficient information on the fluorescence lifetimes of the samples. As a single photon sensitive detector

Photomultiplier Tube (PMT), a Micro Channel Plate (MCP), a Single Photon Avalanche Diode (SPAD) or a Hybrid PMT can be used. For the measurement of multiple cycles of excitation, a pulsed laser with repeat frequencies in the range of 100 kHz to 80 MHz is used. The resulting histogram displays the exponential excitation decay and the corresponding lifetimes (**Figure 2.7**). Using bi- or multi-exponential functions, the lifetimes of the different species and the respective contributions to the sum of all decay dynamics can be calculated.²⁵

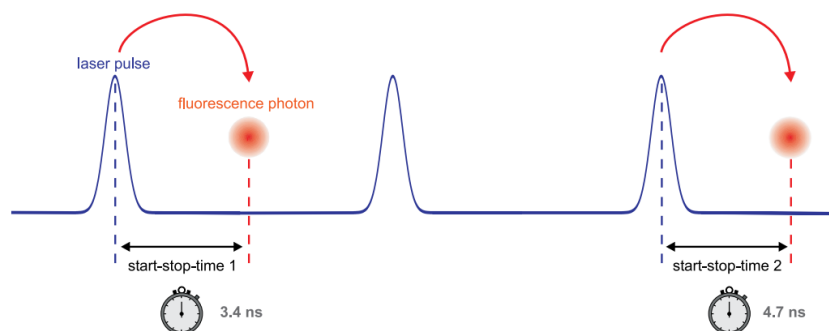


Figure 2.6. Measurement of start-stop times in time-resolved fluorescence measurements with TCSPC.²⁵

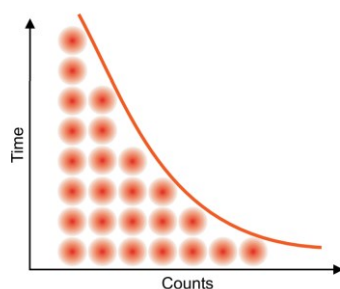


Figure 2.7. Histogram of start-stop times in time-resolved fluorescence measurements with TCSPC.²⁵

Time-resolved PL measurements were conducted using a time-correlated single photon counting (TCSPC) setup (FluoTime 300, PicoQuant GmbH). The samples were photo-excited using a 378 nm laser (LDH-P-C-375) pulsed at 500 kHz with a pulse duration of ~ 100 ps and fluence of ~ 300 nJ cm⁻² / pulse.

2.12 Atomic Force Microscopy (AFM)

Using an atomic force microscope (AFM), morphologies and nanoscale surface structures can be analyzed. Thereby, with this technique distinct forces, mainly van-der-Waals and Coulomb forces between a very sharp tip connected to a flexible cantilever and the sample surface are measured. This way, the topography, roughness and height distribution of samples such as COF thin films can be

analyzed. Depending on the force between tip and surface, the cantilever is either bent towards the surface or away from it, whereas the bending is detected by a laser beam that is reflected from the back of the cantilever onto a detector, which converts the deflection and motion of the cantilever into an electric signal (**Figure 2.8**). There are three different imaging modes, depending on different interactions between tip and sample surface: contact mode, tapping mode or non-contact mode. In contact-mode, the tip is in direct contact with the sample surface, measuring the repulsive forces by maintaining a constant bending of the cantilever and thereby resulting in a topographic image of the surface. In tapping mode, a constant oscillation amplitude of the cantilever is set, thus maintaining a fixed tip-sample interaction. Thereby, the cantilever oscillates at its resonance frequency and slightly touches the sample surface. This way, an image of the surface can be obtained. In non-contact mode, the cantilever oscillates with a fixed amplitude above the sample with no contact to the surface and van-der-Waals forces are measured. By this, the surface topography can be mapped.¹⁴

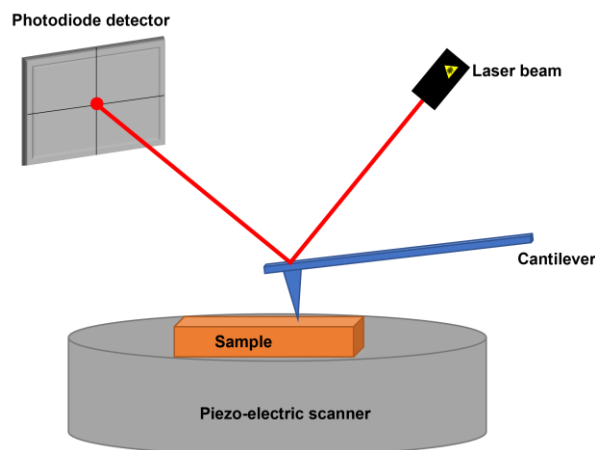


Figure 2.8 Schematic illustration of an atomic force microscope. The tip is screening the sample surface in xy -direction. Thereby, an incident laser beam is reflected from the back of a cantilever and detected a position sensitive quadrant photodiode detector.

Conductive atomic force microscopy (C-AFM) is a mode in AFM where the topography of a material and the electric current flow at the contact point of the tip can be measured simultaneously. Thereby, as described above, the topography is measured by detecting the deflection of a cantilever using a laser. Further, the current in C-AFM can be detected using a current-to-voltage preamplifier.

The conductive AFM (C-AFM) measurements were performed by collaboration partners from the Georg-August-University Göttingen using a Jupiter XR AFM by Oxford Instruments using SCM-PIT conductive AFM tips with PtIr5 coating. The COF films for this analysis were grown on glass substrates covered by a thin gold layer.

2.13 References

- (1) L. R. B. Elton; D. F. Jackson. X-Ray Diffraction and the Bragg Law. *Am. J. Phys.* **1966**, 1036.
- (2) Y. Waseda; E. Matsubara; K. Shinoda. *X-Ray Diffraction Crystallography*; Springer-Verlag Berlin Heidelberg, **2011**.
- (3) G. Cao; Y. Wang. *Nanostructures and Nanomaterials*, 2nd ed.; World Scientific Publishing Co Pte Ltd, **2010**.
- (4) P. Scherrer. *Nachrichten von der Gesellschaft der Wissenschaften zu Göttingen*, Mathematisch-Physikalische Klasse **1918**.
- (5) <https://wiki.anton-paar.com/de-de/roentgenkleinwinkelstreuung-unter-streifendem-einfall-gisaxs/> (accessed January 18, 2022).
- (6) Müller-Buschbaum, P. A Basic Introduction to Grazing Incidence Small-Angle X-Ray Scattering. In *Applications of Synchrotron Light to Scattering and Diffraction in Materials and Life Sciences*; Gomez, Marian and Nogales, Aurora and Garcia-Gutierrez, Mari Cruz and Ezquerra, T.A., Ed.; Springer Berlin Heidelberg: Berlin, Heidelberg, **2009**; pp 61–89.
- (7) K. S. W. Sing, D. H. Everett, R. A. W. Haul, L. Moscou, R. A. Pierotti, F. Rouquerol, T. Siemieniowska. *Pure Appl. Chem.* **1985**, 603–619.
- (8) Katie A. Cychosz; Matthias Thommes. Progress in the Physisorption Characterization of Nanoporous Gas Storage Materials. *Engineering* **2018**, 4, 559–566.
- (9) Brunauer, S.; Emmett, P. H.; Teller, E. Adsorption of Gases in Multimolecular Layers. *J. Am. Chem. Soc.* **1938**, 60, 309–319.
- (10) Langmuir, I. The constitution and fundamental properties of solid and liquids part I. solids. *J. Am. Chem. Soc.* **1916**, 38, 2221–2295.
- (11) Thommes, M.; Kaneko, K.; Neimark, A. V.; Olivier, J. P.; Rodriguez-Reinoso, F.; Rouquerol, J.; Sing, K. S.W. Physisorption of gases, with special reference to the evaluation of surface area and pore size distribution (IUPAC Technical Report). *Pure Appl. Chem.* **2015**, 87, 1051–1069.
- (12) Coats, A. W.; Redfern, J. P. Thermogravimetric analysis. A review. *Analyst* **1963**, 88, 906–924.
- (13) J Vangindertael; R Camacho; W Sempels; H Mizuno; P Dedecker; K P F Janssen. An introduction to optical super-resolution microscopy for the adventurous biologist. *Methods and Applications in Fluorescence* **2018**, 6, 22003.
- (14) John Wiley & Sons, Ed. *Microstructural Characterization of Materials*: D. Brandon; D. W. Kaplan, 2nd ed., **2008**.
- (15) C. Evans, R. Brundle, S. Wilson. *Encyclopedia of Material Characterization*. Maning Publications Co. **1992**.
- (16) Wiley-VCH, Ed. *Ein- und zweidimensionale NMR-Spektroskopie: Eine Einführung*, 5th ed.; Wiley-VCH: Weinheim, **2013**.

- (17) M. Hesse, M. Herbert, B. Zeech. *Spektroskopische Methoden in der organischen Chemie*. Thieme: Stuttgart **2005**, 468.
- (18) J. H. Gross. *Mass Spectrometry*. Springer **2011**.
- (19) P. M. van Galen, M. C. Feiters. *Mass Spectrometry* **2016**.
- (20) W. M. A. Niessen, D. Falck. *Analyzing Biomolecular Interactions by Mass Spectrometry*. Wiley-VCH Verlag GmbH & Co. KGaA **2015**.
- (21) Springer: Berlin, H., Ed. *UV-VIS Spectroscopy and Its Applications*, 1st ed., **2013**.
- (22) Hecht, H. G. The Interpretation of Diffuse Reflectance Spectra. *J Res Natl Bur Stand A Phys Chem* **1976**, 80A, 567–583.
- (23) Springer US: Baltimore, Ed. *Principles of Fluorescence Spectroscopy*, 3rd ed., **2007**.
- (24) Oxford University Press, Ed. *Atkins' Physical Chemistry*, 10th ed., **2014**.
- (25) M. Wahl. *Time-Correlated Single Photon Counting*. Technical Note PicoQuant GmbH.

3. A Post-synthetic Modification Strategy for the Synthesis of Pyrene-fused Azaacene COFs

This chapter is based on the following article:

A post-synthetic modification strategy for the synthesis of pyrene-fused azaacene covalent organic frameworks

published as: S. P.S. Fernandes,^{‡[a,b]} L. Frey,^{‡[c]} K. M. Cid-Seara,^[a,d] O. Oliveira,^[a] N. Guldris,^[a] E. Carbó-Argibay,^[a] C. Rodríguez-Abreu,^[c] Y. V. Kolen'ko,^[a] A. M.S. Silva,^[b] D. D. Medina,^{*[c]} and Laura M. Salonen^{*[a]} *Micropor. Mesopor. Mat.* **2022**, 112162.

^[a] International Iberian Nanotechnology Laboratory (INL), Avenida Mestre José Veiga, 4715-330, Braga, Portugal
E-mail: laura.salonen@inl.int

^[b] Associate Laboratory for Green Chemistry-Network of Chemistry and Technology (LAQV-REQUIMTE), Department of Chemistry, University of Aveiro, Campus Universitário de Santiago, 3810-193, Aveiro, Portugal

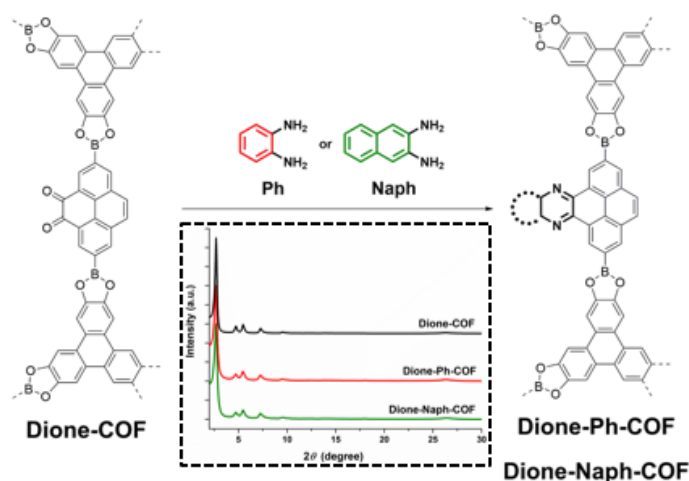
^[c] Department of Chemistry and Center for Nanoscience (CeNS), Ludwig-Maximilians University Munich (LMU), Butenandtstr. 5-11, D-81377, Munich, Germany, E-mail: dmepc@cup.uni-muenchen.de

^[d] Department of Inorganic Chemistry, University of Vigo, Campus Universitário, As Lagoas-Marcosende, 36310, Vigo, Spain

^[e] Institute of Advanced Chemistry of Catalonia, Spanish National Research Council (IQAC-CSIC) and Networking Research Center on Bioengineering, Biomaterials and Nanomedicine (CIBER-BBN), Jordi Girona 18-26, 08034 Barcelona, Spain

* Corresponding Authors.

‡ These authors contributed equally.



3.1 Abstract

Post-synthetic modification strategy is presented to extend the π -system in covalent organic framework (COF) backbones, giving access to boronic-ester-based pyrene-fused azaacene COFs. Optimized catalyst-free reaction conditions yield COFs post-synthetically modified with up to 33% conversion and corresponding intriguing optical properties. The presented chemistry is expected to find application in post-synthetic tailoring of the optical properties of COFs.

3.2 Introduction

In the last years, two-dimensional covalent organic frameworks (2D COFs) have been increasingly explored for a wide range of applications from catalysis,¹⁻⁴ optoelectronics,^{5,6} and energy storage⁷⁻⁹ to water treatment.¹⁰⁻¹³ Crystalline nanoporous 2D COFs are formed by condensation polymerization of purely organic building blocks forming molecular stacks and a layered structure of 2D sheets, giving access to versatile materials with long-range order and permanent porosity.¹⁴⁻¹⁶ In general, the structural features of COFs are determined by pre-functionalized monomers through a so-called bottom-up approach.¹⁴⁻¹⁶ However, this strategy is hampered by the possible incompatibility of the functional groups decorating the building blocks with the COF synthesis conditions, sterically demanding side groups, or low solubility of the building blocks, which may prevent the formation of a crystalline material. To overcome these barriers, post-synthetic-modification (PSM) has been established as a straightforward and elegant approach to tailor the COF structure without compromising its crystalline nature.^{17,18} In this manner, the introduction of functional groups into the pore wall of COFs has been achieved, allowing for structural and chemical fine-tuning of COF properties while maintaining crystallinity of the material. In addition, this strategy can be used to render the reversible COF linkages, such as imine, non-reversible, thus giving access to crystalline material of which hydrolysis is prevented.¹⁹⁻²⁴

Pyrazaacenes, compounds featuring a pyrazine ring accompanied by fused aromatic rings, have excellent electronic properties,^{25,26} rendering them of high interest for application *e.g.* in organic light emitting diodes,^{27,28} organic field effect transistors,^{29,30} and solar cells.^{31,32} Specifically, pyrene-fused pyrazaacenes³³ are highly stable compounds, which feature interesting properties for organic electronic applications.^{34,35} Herein, we report a simple catalyst-free cyclocondensation PSM reaction of boronic-ester-based Dione-COF, previously reported by our group,³⁶ to afford pyrene-fused pyrazaacene COFs. The presented PSM strategy allows for the expansion of π -conjugation of the COF backbone, which provides an interesting opportunity to tailor the photophysical properties of these COF materials.

3.3 Results and Discussion

First, we carried out the envisioned modification to pyrene-fused pyrazaacenes on the single molecule pyrene 4,5-dione-building block **1** (**Figure 3.1A**). Boronic-acid-bearing pyrene 4,5-dione **1** was prepared from pyrene modifying our previously described synthesis (for more details see **section 3.5.2**, in the appendix).³⁶ Direct condensation of building block **1** with *o*-phenylenediamine and 2,3-diaminonaphthalene at 100 °C for 8 days in DMSO gave model organic compounds **2** and **3** in 50% and 67% yield, respectively (**Figure 3.1A**, for more details see **section 3.5.2** in the appendix). To verify the impact of the extension of π -conjugation on the photophysical properties of pyrene 4,5-dione building block **1**, UV-vis measurements were conducted. The absorption spectrum of pristine pyrene-dione building block **1** shows an absorption maximum in the blue spectral region at 418 nm (**Figure 3.1B**, black). Upon modification, pyrazaacene compound **2** exhibits two absorption band maxima at 422 and 442 nm (**Figure 3.1B**, red). These maxima are further red shifted to 453 and 477 nm (**Figure 3.1B**, green) for pyrazaacene **3**, followed by a clear red-shift of the absorption onset compared with pristine pyrene-dione building block **1**. Similar trend was observed in the photoluminescence (PL) spectra (**Figure 3.1C**), where a significant red-shift in the PL emission spectra from 440 nm of pristine pyrene-dione building block **1** (**Figure 3.1C**, black) to 500 and 535 nm for pyrazaacenes **2** (**Figure 3.1C**, red) and **3** (**Figure 3.1C**, green), respectively, was observed. These observations indicate that the photophysical properties of boronic-acid-bearing pyrene-4,5-dione building block **1** can be systematically modified by azaacene formation inducing an extension of the π -system.

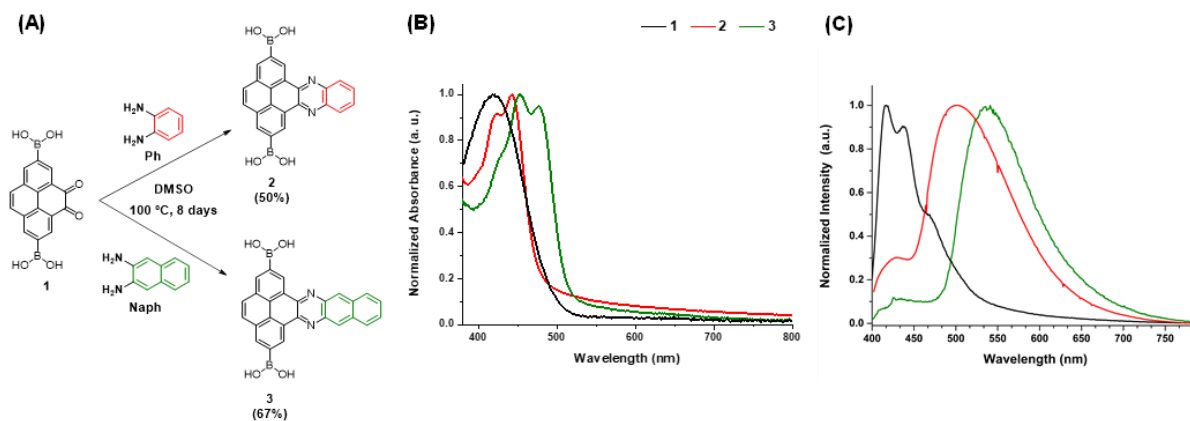


Figure 3.1 (A) Synthesis of model organic compounds **2** and **3** from reaction of boronic acid-based pyrene-4,5-dione building block **1** with *o*-phenylenediamine (Ph) and 2,3-diaminonaphthalene (Naph), respectively, in DMSO, at 100 °C, for 8 days. (B) UV-vis spectra of building block **1** (black), and model organic compounds **2** (red) and **3** (green). (C) Steady-state photoluminescence (PL) spectra of building block **1** (black), and model organic compounds **2** (red) and **3** (green).

Next, to probe the reaction on a COF, we prepared Dione-COF, following our previous report,³⁶ by reacting boronic-acid-bearing pyrene-4,5-dione building block **1** with 2,3,6,7,10,11-hexahydroxytriphenylene (HHTP) under solvothermal conditions in a mixture of 1:1 mesitylene and *n*-

BuOH at 120 °C for 7 days (for more details see **section 3.5.2**, in the appendix). As assessed by powder X-ray diffraction (PXRD), a highly crystalline precipitate was obtained (**Figure 3.3A**, black), with six main reflections at $2\theta = 2.71^\circ$, 4.77° , 5.48° , 7.29° , 9.56° , and 26.1° , in good agreement with the reported data (for further characterization of Dione-COF, see **sections 3.5.4-3.5.9** in the appendix).³⁶ The nitrogen sorption measurement at 77 K showed a type IV isotherm, and the Brunauer-Emmett-Teller (BET) surface area was found to be $1050 \text{ m}^2 \text{ g}^{-1}$, slightly lower to that found previously,³⁶ which could be due to the modified drying procedure used (**Figure 3.3B**, **Figures 3.20-3.21**).

The PSM conditions were optimized using *o*-phenylenediamine as the counterpart (**Figure 3.2**). Anhydrous aprotic solvents were chosen for the reaction due to the hydrolytic instability of boronic-ester-based COFs. To this end, Dione COF was reacted with 2.1 equivalents of *o*-phenylenediamine under reflux conditions for 3 days in CHCl_3 , CCl_4 , 1,4-dioxane, and CH_2Cl_2 (**Table 3.1**, entries 1-4). After the reaction time had elapsed, the COF materials were carefully washed with anhydrous acetone to remove unreacted diamine. Anhydrous acetone, as opposed to water as in the case of the model compounds **2** and **3**, was used as washing solvent due to the low hydrolytic stability of the boronic ester linkages of Dione-COF in water. To determine the degree of conversion of the dione moieties to azaacenes in the post-synthetically modified COFs, the materials were suspended in $\text{DMSO-}d_6$ and hydrolyzed to the respective building blocks by addition of D_2O (**Figure 3.2**). Subsequently, the obtained solutions were analyzed by $^1\text{H-NMR}$ spectroscopy to verify the extent of the conversion by comparing integration between signals corresponding to proton H-3 of the cleaved pyrene-fused pyrazaacenes **2** and **3** and proton H-2 or H-3 of the pyrene-4,5-dione building block **1**, respectively (for more details, see caption of **Scheme 3.2** in the appendix).

The highest conversion of 30% was obtained in 1,4-dioxane and CH_2Cl_2 (**Table 3.1**, entries 3 and 4, respectively). However, $^1\text{H-NMR}$ spectroscopy indicated that the purity of the material from CH_2Cl_2 was higher than that obtained in 1,4-dioxane, and therefore, CH_2Cl_2 was chosen as the optimal solvent. Next, the influence of the reaction time was evaluated using CH_2Cl_2 , and with 7 days of reaction time (**Table 3.1**, entry 5) the conversion increased to 33% with an increase in purity as compared to the reaction time of 3 days (**Table 3.1**, entry 4). Increasing the amount of *o*-phenylenediamine from 2.1 to 6.0 equivalents (**Table 3.1**, entry 6) resulted in reduction in the conversion to 25%. Therefore, the optimum conditions were determined as 2.1 equivalents of diamine in CH_2Cl_2 at 50 °C for 7 days, resulting in the PSM of Dione-COF to form Dione-Ph-COF with 33% conversion of dione moieties to azaacenes (**Figure 3.2**). Using the same conditions, we also tested the PSM reaction of Dione-COF using 2,3-diaminonaphthalene (**Figure 3.2A**), giving access to Dione-Naph-COF with 19% of the diones converted to azaacenes, as assessed by $^1\text{H-NMR}$ spectroscopy (**Figure 3.12**).

Table 3.1 Experimental conditions tested for PSM of Dione-COF with *o*-phenylenediamine. All experiments were performed in a nitrogen-filled 15 mL pressure tube using anhydrous solvents. Conversion of dione moieties to the azaacene was determined from ^1H NMR spectra prepared in $\text{DMSO-}d_6$ with the addition of 3 drops of D_2O to hydrolyze the COF.

Entry	Ph (equiv.)	Solvent	T (°C)	t (days)	Yield (%)
1	2.1	CHCl_3	65	3	20 ^[a]
2	2.1	CCl_4	80	3	25 ^[a]
3	2.1	1,4-Dioxane	100	3	30 ^[a]
4	2.1	CH_2Cl_2	50	3	30
5	2.1	CH_2Cl_2	50	7	33
6	6.0	CH_2Cl_2	50	3	25 ^[a]

[a] The presence of impurities was seen in the ^1H NMR spectrum.

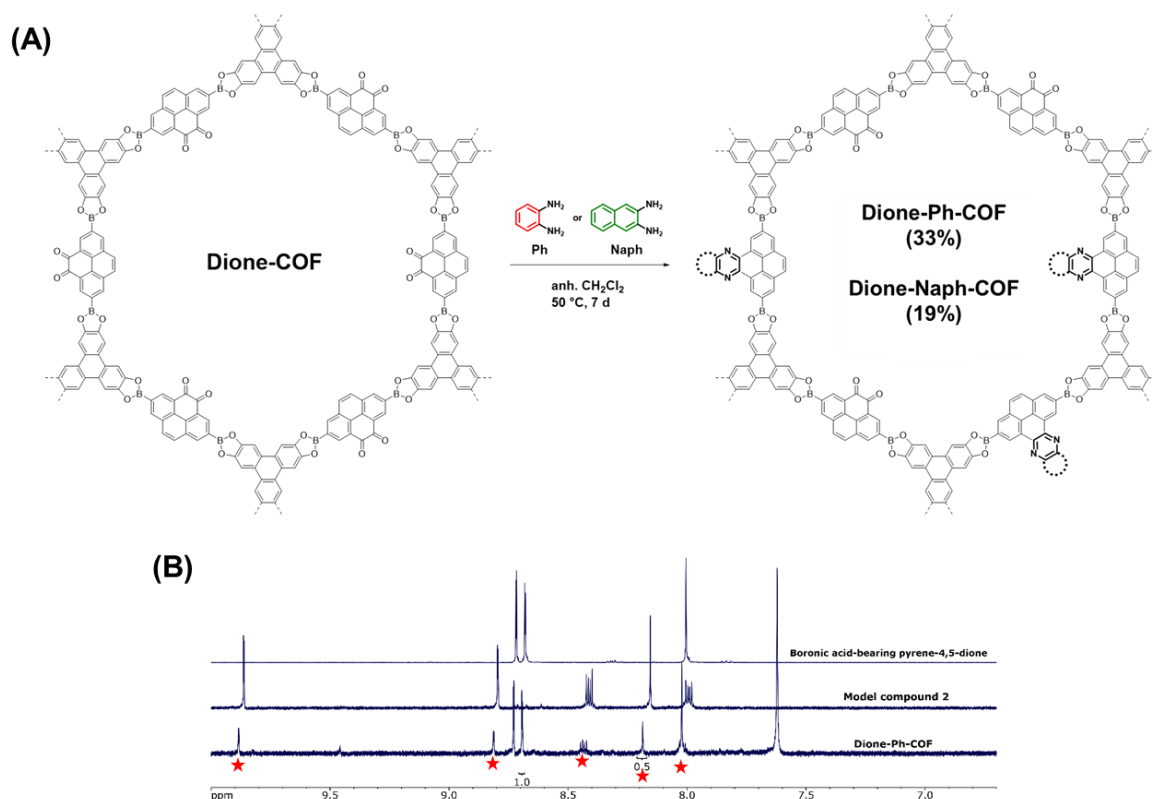


Figure 3.2. (A) Post-synthetic modification of Dione-COF to Dione-Ph-COF and Dione-Naph-COF by reaction with *o*-phenylenediamine (Ph) and 2,3-diaminonaphthalene (Naph), respectively; (B) ^1H NMR spectrum of Dione-Ph-COF overlaid with boronic acid-bearing pyrene-4,5-dione building block **1** and model compound **2** measured at 400 MHz in $(\text{CD}_3)_2\text{SO}+\text{D}_2\text{O}$.

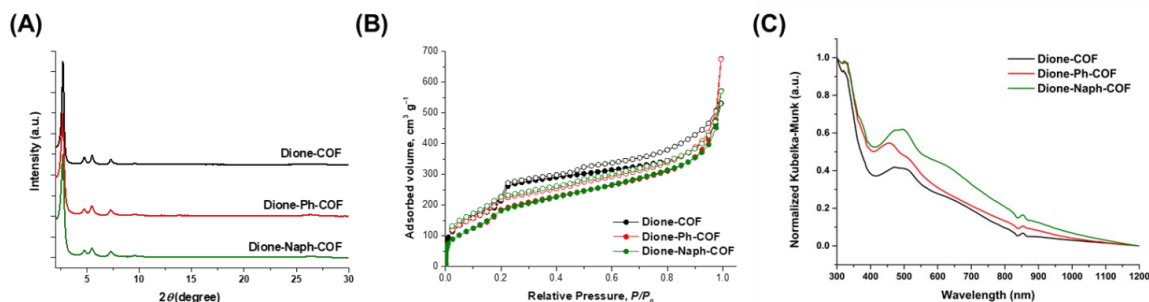


Figure 3.3 (A) Powder X-ray diffraction patterns; (B) nitrogen adsorption (filled spheres) and desorption (hollow spheres) isotherm profiles measured at 77 K; and (C) normalized UV-vis spectra of Dione-COF (black), Dione-Ph-COF (red), and Dione-Naph-COF (green).

To determine the success of the PSM strategy, the long-range order of the obtained powders was examined by PXRD. Impressively, despite the use of nucleophilic aromatic amines for the PSM, the crystallinity of Dione-COF was preserved upon functionalization (**Figure 3.3A**, red), demonstrating the formation of Dione-Ph-COF with the main reflections at $2\theta = 2.7^\circ$, 4.72° , 5.47° , 7.24° , 9.51° , and 26.3° , in agreement with the simulated PXRD pattern (**Figure 3.16**). Dione-Naph-COF showed a similar diffraction pattern (**Figure 3.3A**, green), with reflections at $2\theta = 2.71^\circ$, 4.72° , 5.48° , 7.24° , 9.51° , and 26.3° , in agreement with the simulated PXRD pattern (**Figure 3.18**).

Accessible surface area of the obtained COFs was examined by nitrogen sorption measurement at 77 K, evidencing a type IV isotherm (**Figure 3.3B**) typical of mesoporous materials, with a sharp nitrogen uptake at low partial pressure attributed to capillary condensation. As expected, the BET surface area of Dione-Ph-COF was found to be $800 \text{ m}^2 \text{ g}^{-1}$ (**Figure 3.22**), lower than that obtained for pristine Dione-COF, whereas Dione-Naph-COF showed a slightly higher surface area of $900 \text{ m}^2 \text{ g}^{-1}$ (**Figure 3.24**), in agreement with the lower degree of functionalization. Pore size distribution calculated using the QSDFT model for cylindrical pores (adsorption branch) showed a maximum at 3.0 nm (**Figure 3.23**) and 2.9 nm (**Figure 3.25**) for Dione-Ph-COF and Dione-Naph-COF, respectively, slightly lower than that obtained for Dione-COF.

The success of the cyclocondensation reaction was also supported by Fourier-transform infrared (FTIR) spectroscopy, where a significant decrease in the band for carbonyl group stretching at 1668 cm^{-1} was observed for both COFs (**Figure 3.26**). In addition, similarities in the FTIR spectrum of model compounds with those obtained from Dione-Ph-COF and Dione-Naph-COF indicated a successful PSM reaction (**Figures 3.27** and **3.28**, respectively). The post-synthetically modified COF materials were found to feature similar high thermal stability up to 400°C as Dione-COF (**Figure 3.29-3.31**) and

scanning electron microscopy (SEM) images showed the wire-like morphology of Dione-COF³⁶ to remain conserved for both post-synthetically modified COFs (**Figure 3.32, 3.33**).

Next, the effect of PSM on the photophysical properties of the resulting COFs was analyzed using UV-vis spectroscopy. The absorbance of the modified COFs was measured and compared to that of pristine Dione-COF (**Figure 3.3C**). Broad absorption bands reaching the near-infrared region were observed in all studied COFs and attributed to the presence of redox-active dione moieties. Upon PSM, the absorption onset was red-shifted for Dione-Ph-COF and even further red-shifted for Dione-Naph-COF as compared to Dione-COF, attributed to the extension of the π -conjugation of part of the dione moieties and providing further confirmation of the success of the PSM. Interestingly, Dione-COF and its derivatives were not found to be PL active. This could be the result of aggregation-quenched fluorescence, internal charge-transfer between the pyrene-4,5-dione and HHTP building blocks, or non-radiative relaxation processes. To shed light on this aspect, the PL spectra of the dione building block and a physical mixture of dione and HHTP in powder form were recorded (**Figure 3.34**). The pyrene-4,5-dione building block **1** shows a broad PL emission profile with a maximum at 680 nm, strongly red-shifted compared to the PL emission in solution. In stark contrast, the spectrum of the mixed powders shows only residual PL related with the dione building block. This points to an internal charge-transfer between the two building blocks, where boronate-ester serves as junction.³⁷

3.4 Conclusion

In summary, we have developed a simple, catalyst-free cyclocondensation PSM for reactive boronic-ester-based COFs to form pyrene-fused pyrazaacene moieties, which show interesting photophysical properties. Dione-Ph-COF and Dione-Naph-COF derivatives were modified in up to 33% conversion of the dione moieties with retention of their high crystallinity and surface area. Clear modification of their photophysical properties was evidenced in the UV-vis spectra. Quenching of PL in the resulting COFs was attributed to internal charge transfer, and further studies are underway in our laboratories for the optimal combination of building blocks to allow for the exploitation of the electronic properties of the pyrene-fused azaacenes in COFs.

3.5 References

- (1) S. M. J. Rogge, A. Bavykina, J. Hajek, H. Garcia, A. I. Olivos-Suarez, A. Sepúlveda Escribano, A. Vimont, G. Clet, P. Bazin, F. Kapteijn, M. Daturi, E. V. Ramos-Fernandez, F. X. Llabrés i Xamena, V. Van Speybroeck and J. Gascon, *Chem. Soc. Rev.* **2017**, *46*, 3134–3184.
- (2) Y. Zhi, Z. Wang, H. L. Zhang, Q. Zhang, *Small* **2020**, 2001070.

- (3) L. P. L. Gonçalves, D. B. Christensen, M. Meledina, L. M. Salonen, D. Y. Petrovykh, E. Carbó-Argibay, J. P. S. Sousa, O. S. G. P. Soares, M. F. R. Pereira, S. Kegnæs, et al., *Catal. Sci. Technol.* **2020**, *10*, 1991–1995.
- (4) J. Guo and D. Jiang, *ACS Cent. Sci.* **2020**, *6*, 869–879.
- (5) D. D. Medina, T. Sick, T. Bein, *Adv. Energy Mater.* **2017**, *7*, 1700387.
- (6) N. Keller, T. Bein, *Chem. Soc. Rev.* **2021**, *50*, 1813–1845.
- (7) A. K. Mandal, J. Mahmood, J. B. Baek, *ChemNanoMat* **2017**, *3*, 373–391.
- (8) Y. Zhang, S. N. Riduan, J. Wang, *Chem. - A Eur. J.* **2017**, *23*, 16419–16431.
- (9) T. Sun, J. Xie, W. Guo, D. Li, Q. Zhang, *Adv. Energy Mater.* **2020**, *10*, 1904199.
- (10) S. P. S. Fernandes, P. Kovář, M. Pšenička, A. M. S. Silva, L. M. Salonen, B. Espiña, *ACS Appl. Mater. Interfaces* **2021**, *13*, 15053–15063.
- (11) S. P. S. Fernandes, V. Romero, B. Espiña, L. M. Salonen, *Chem. Eur. J.* **2019**, *25*, 6461–6473.
- (12) Z. Wang, S. Zhang, Y. Chen, Z. Zhang, S. Ma, *Chem. Soc. Rev.* **2020**, *49*, 708–735.
- (13) A. Mellah, S. P. S. Fernandes, R. Rodríguez, J. Otero, J. Paz, J. Cruces, D. D. Medina, H. Djamil, B. Espiña, L. M. Salonen, *Chem. Eur. J.* **2018**, *24*, 10601–10605.
- (14) S. Kandambeth, K. Dey, R. Banerjee, *J. Am. Chem. Soc.* **2019**, *141*, 1807–1822.
- (15) K. Geng, T. He, R. Liu, K. T. Tan, Z. Li, S. Tao, Y. Gong, Q. Jiang, D. Jiang, *Chem. Rev.*, **2020**, *120*, 8814–8933.
- (16) Z. Li, T. He, Y. Gong, D. Jiang, *Acc. Chem. Res.* **2020**, *53*, 1672–1685.
- (17) J. L. Segura, S. Royuela, M. Mar Ramos, *Chem. Soc. Rev.* **2019**, *48*, 3903–3945.
- (18) Y. Yusran, X. Guan, H. Li, Q. Fang, S. Qiu, *Natl. Sci. Rev.* **2020**, *7*, 170–190.
- (19) X. Li, C. Zhang, S. Cai, X. Lei, V. Altoe, F. Hong, J. J. Urban, J. Ciston, E. M. Chan, Y. Liu, *Nat. Commun.* **2018**, *9*, 2998.
- (20) F. Haase, E. Troschke, G. Savasci, T. Banerjee, V. Duppel, S. Dörfler, M. M. J. Grundei, A. M. Burow, C. Ochsenfeld, S. Kaskel, et al., *Nat. Commun.* **2018**, *9*, 2600.
- (21) P. J. Waller, Y. S. Alfaraj, C. S. Diercks, N. N. Jarenwattananon, O. M. Yaghi, *J. Am. Chem. Soc.* **2018**, *140*, 9099–9103.
- (22) L. Cusin, H. Peng, A. Ciesielski and P. Samor, *Angew. Chem. Int. Ed.* **2021**, *60*, 14236–14250.
- (23) H. Qian, F. Meng, C. Yang, X. Yan, *Angew. Chemie Int. Ed.* **2020**, *59*, 17607–17613.
- (24) Z. Yang, P. Chen, W. Hao, Z. Xie, Y. Feng, G. Xing, L. Chen, *Chem. Eur. J.* **2021**, *27*, 3817–3822.
- (25) Z. Zhang and Q. Zhang, *Mater. Chem. Front.* **2020**, *4*, 3419–3432.

- (26) J. Merz, M. Dietz, Y. Vonhausen, F. Wöber, A. Friedrich, D. Sieh, I. Krummenacher, H. Braunschweig, M. Moos, M. Holzapfel, et al., *Chem. Eur. J.* **2020**, *26*, 438–453.
- (27) D. B. Lindner, Y. Zhang, S. Hofle, N. Berger, C. Teusch, M. Jesper, K. I. Hardcastle, X. Qian, U. Lemmer, A. Colsmann, et al., *J. Mater. Chem. C* **2013**, *1*, 5718–5724.
- (28) D. Cortizo-Lacalle, A. Pertegás, M. Melle-Franco, H. Bolink, A. Mateo-Alonso, *Org. Chem. Front.* **2017**, *4*, 876–881.
- (29) L. Huang, Q. Yan, F. Hu, H. Zhang, Q. Zhang, *Appl. Mater. Interfaces* **2012**, *4*, 1883–1886.
- (30) Z. Wu, W. Sun, H. Tian, Z. Yu, R. Guo, X. Shao, H.-L. Zhang, *Adv. Electron. Mater.* **2019**, *5*, 1800598.
- (31) P. Gu, N. Wang, A. Wu, Z. Wang, M. Tian, *Chem. Asian J.* **2016**, *11*, 2135–2138.
- (32) P. Gu, N. Wang, C. Wang, Y. Zhou, G. Long, M. Tian, W. Chen, X. W. Sun, M. G. Kanatzidis, Q. Zhang, *J. Mater. Chem. A* **2017**, *5*, 7339–7344.
- (33) A. Mateo-Alonso, *Chem. Soc. Rev.* **2014**, *43*, 6311–24.
- (34) T. M. Figueira-duarte, M. Klaus, *Chem. Rev.* **2011**, *111*, 7260–7314.
- (35) J. Li, S. Chen, Z. Wang, Q. Zhang, *Chem. Rec.* **2016**, *16*, 1518–1530.
- (36) L. M. Salonen, D. D. Medina, E. Carbó-Argibay, M. G. Goesten, L. Mafra, N. Guldris, J. M. Rotter, D. G. Stroppa, C. Rodríguez-Abreu, *Chem. Commun.* **2016**, *52*, 7986–7989.
- (37) M. Calik, F. Auras, L. M. Salonen, K. Bader, I. Grill, M. Handloser, D. D. Medina, M. Dogru, F. Löbermann, D. Trauner, A. Hartschuh and T. Bein, *J. Am. Chem. Soc.* **2014**, *136*, 17802–17807.

3.6 Appendix

3.6.1 Materials and Methods

Commercial reagents and solvents were obtained from diverse suppliers and used as received, with exception of pyrene, which was recrystallized prior to use from a mixture of CH_2Cl_2 /hexane. Reaction progresses were monitored by analytical thin-layer chromatography (TLC) on ALUGRAM® Xtra SIL G/UV₂₅₄ aluminium sheets from Macherey Nagel. TLC plates were rendered visible by exposure to ultraviolet light. All purifications were carried out under flash-chromatographic conditions on silica gel (60 Å, 40–63 µm, 230–400 mesh, Macherey Nagel).

Proton nuclear magnetic resonance (¹H NMR) spectra were recorded on 400 MHz Bruker Avance II spectrometer at the NMR service of University of Minho in Braga, Portugal. Chemical shifts are given in ppm (δ) and calibrated using residual undeuterated solvent peak as internal reference (CDCl_3 : δ 7.26; $(\text{CD}_3)_2\text{SO}$: 2.5; CD_2Cl_2 : 5.32). Multiplicities are reported as follow: s (singlet), d (doublet), t (triplet), m (multiplet), or combinations thereof. Coupling constants J are given in Hz.

Powder X-ray diffraction (PXRD) measurements were performed using a Bruker D8 Discover with Ni-filtered $\text{Cu K}\alpha$ radiation and a LynxEye position-sensitive detector.

Small-angle X-ray scattering (SAXS) measurements were performed in an Anton Paar SAXSess mc2 instrument operating at 40 kV and 50 mA. Data were collected with an image plate detector. Samples were placed into a holder with Mylar windows for the measurement. Data are background corrected.

Nitrogen sorption measurements were carried out on a Quantachrome Autosorb IQ2 automated analyser. Prior to the measurements, samples were outgassed by heating to 120 °C (heating rate: 5 °C min⁻¹, dwelling time: 720 min). Surface areas of the obtained powders were estimated by the multipoint Brunauer–Emmett–Teller (BET) method using ASIQuin™ software. Pore size distribution were assessed using quenched-solid density functional theory (QSDFT) for cylindrical pores (N_2 at 77 K on carbon, adsorption branch).

Infrared (IR) spectra were recorded on a Bruker VERTEX 80v FT-IR spectrometer in ATR mode. IR data is background corrected and reported in frequency of adsorption (cm⁻¹).

Thermogravimetric analysis (TGA) were performed on a TGA/DSC 1 STAR[®] system (Mettler Toledo). The samples were heated from 303.15 to 1173.15 K at 283.15 K min⁻¹ under a continuous flow of argon of 20 mL min⁻¹.

Scanning electron microscopy (SEM) studies were performed using a Quanta 650 field-emission scanning electron microscope operating at 3 kV and employing an Everhardt-Thornley secondary electrons detector, with a working distance of ca. 10 mm. The samples were prepared by adhesion of the sample powder directly on a conductive double-sided copper tape attached to SEM pin stub.

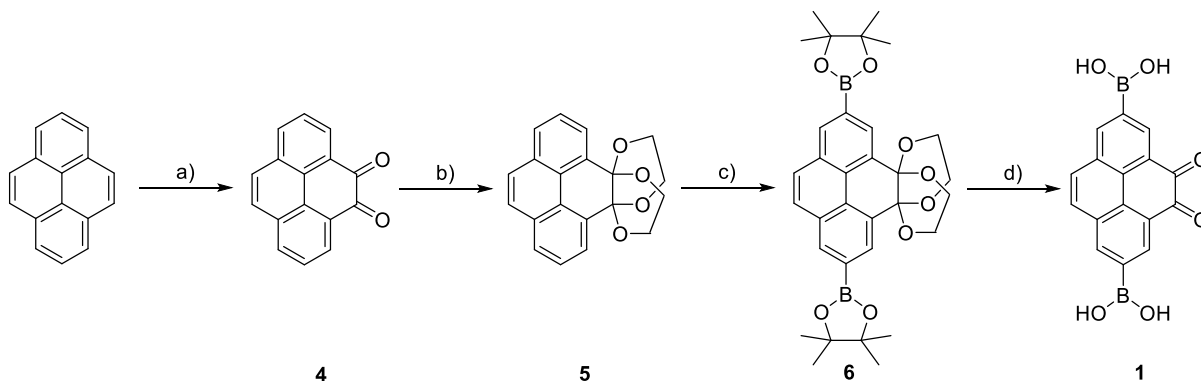
UV-vis-infrared absorption spectra were recorded on a Perkin-Elmer Lambda 1050 spectrometer equipped with a 150 mm integration sphere. The spectral feature at 860 nm corresponds to a detector change of our setup.

Photoluminescence (PL) data were processed with a FluoTime 300 from PicoQuant GmbH. Samples were excited using a 378 nm laser source.

3.6.2 Synthetic Procedures

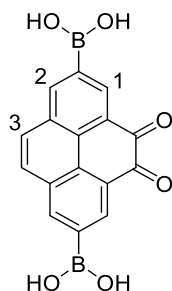
Synthesis of Boronic-acid-bearing Pyrene-4,5-dione Building Block 1

Starting point of synthetic route of boronic acid-bearing pyrene-4,5-dione building block **1** is the selective ruthenium catalyzed oxidation of pyrene in its 4 - and 5- positions, to afford pyrene-4,5-dione (**4**).¹ The following protection of ketone groups using ethylene glycol gave **5** in 43% yield.² Up next, iridium-catalyzed C-H borylation takes place at the 2,7-positions to afford **6** in 49% yield.² Finally, deprotection of both protecting groups at room temperature with NaIO₄ under acidic conditions² gave boronic acid-bearing pyrene-4,5-dione building block **1** in 88% yield.³



Scheme 3.1. Synthetic route of boronic acid-bearing pyrene-4,5-dione building block **1**. a) CH₂Cl₂, THF, RuCl₃ · 2H₂O, N-methylimidazole, H₂O, NaIO₄, 2.5 h, 50%; b) ethylene glycol, PTSA, toluene, 125 °C, 20 h, 43%; c) bis(pinacolato)diboron, [Ir(OMe)COD]₂, 4,4'-di-tert-butyl-2,2'-bipyridine, MTBE, 80 °C, 20 h, 49%; d) NaIO₄, TFA, THF, H₂O, air, RT, 3 d, 88 %.

(7-Borono-4,5-dioxo-pyren-2-yl)boronic acid (boronic acid-bearing pyrene-4,5-dione)³ (**1**)

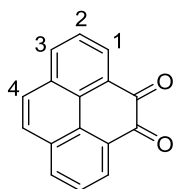


The procedure was adapted from literature procedures.^{2,3} In a round-bottom flask, **6** (522 mg, 0.91 mmol, 1 eq.) was dissolved in a mixture of THF/H₂O (41/12 mL). NaIO₄ (1.65 g, 7.71 mmol, 8.5 eq.) was added, and the mixture was stirred at room temperature for 30 min. Then, TFA (85 mL) was added dropwise and the reaction mixture was stirred for 3 days at room temperature while bubbling air through

the solution. An orange solid precipitated and the suspension was diluted with CH₂Cl₂ and H₂O. The aqueous phase was extracted with CH₂Cl₂, and the organic phase was filtered. The collected solid was combined with the aqueous phase and centrifuged (15 min, 4400 rpm). The orange solid was suspended in water and centrifugation repeated. This last washing step was repeated four times in total. The solid was dried under high vacuum to give boronic acid-bearing pyrene-4,5-dione building block **1** (255 mg, 88%) as an orange solid.

¹H NMR (400 MHz, DMSO-d₆+D₂O): δ = 8.72 (d, *J* = 1.3 Hz, 2H; H-C(1)), 8.68 (d, *J* = 1.3 Hz, 2H; H-C(2)), 8.01 (s, 2H; H-C(3)).

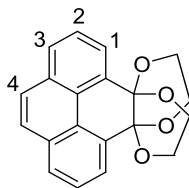
Pyrene-4,5-dione¹ (**4**)



In a round-bottom flask, pyrene crystals (9.7 g, 47.9 mmol, 1 eq.) were dissolved in a mixture of CH₂Cl₂ and THF (240/240 mL). To the yellow solution were added RuCl₃•2H₂O (0.99 g, 4.79 mmol, 0.1 eq.), N-methylimidazole (190.5 μL, 2.39 mmol, 0.05 eq.) and water (240 mL). Then, over a period of 20 min, sodium periodate (46.1 g, 215.4 mmol, 4.5 eq.) was added in small portions, and the mixture was stirred at RT for 2.5 h. Organic solvents were removed under reduced pressure, and the aqueous phase was extracted with CH₂Cl₂. Collected organic phase was washed with water, dried with anhydrous Na₂SO₄, and concentrated under reduced pressure to afford a dark-orange solid. Purification by column chromatography (SiO₂; CH₂Cl₂) gave **4** (5.5 g, 23.7 mmol, 50%) as a bright-orange solid.

R_f = 0.3 (CH₂Cl₂);

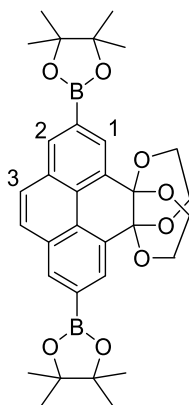
¹H NMR (400 MHz, CDCl₃): δ = 8.44 (dd, *J* = 7.4 Hz, *J* = 1.3 Hz, 2H, H-C(1) or H-C(3)), 8.13 (dd, *J* = 7.9 Hz, *J* = 1.3 Hz, 2H, H-C(1) or H-C(3)), 7.80 (s, 2H, H-C(4)), 7.72 (dd, *J* = 7.9 Hz, *J* = 7.5 Hz, 2H, H-C(2)).

Pyrene-4,5-di(ethyleneglycol)ketal² (5)

To a suspension of pyrene-4,5-dione (**4**) (2.99 g, 12.9 mmol, 1 eq.) in toluene (150 mL) were added ethylene glycol (90 mL, 1.61 mol, 125 eq.) and *p*-toluenesulfonic acid (1.11 g, 5.81 mmol, 0.45 eq.). The obtained orange reaction mixture was refluxed at 125 °C for 20 h. Reaction mixture was cooled down and toluene was removed under reduced pressure. Then, 200 mL of water was added and a light brown solid precipitated, which was collected by filtration and washed with water. Purification by flash chromatography (SiO₂; cyclohexane/ethyl acetate 9:1) gave **5** (1.80 g, 5.54 mmol, 43%) as white solid.

R_f = 0.29 (cyhex/EtOAc 9:1);

¹H NMR (400 MHz, CD₂Cl₂): δ = 7.94 (dd, *J* = 7.6 Hz, *J* = 1.2 Hz, 4H; H-C(1) or H-C(3)), 7.80 (s, 2H; H-C(4)), 7.70 (t, *J* = 7.6 Hz, 2H; H-C(2)), 4.27 (br, 4H), 3.73 (br, 4H).

2,7-Bis(Bpin)-4,5-di(ethyleneglycol)ketal-pyrene² (6)

In an nitrogen-filled 100 mL pressure tube (ACE glass, bushing type back seal, 17.8 cm x 38.1 mm) were added pyrene-4,5-di(ethyleneglycol)ketal (**5**) (0.89 g, 2.76 mmol, 1 eq.), bis(pinacolato)diboron (1.41 g, 5.52 mmol, 2 eq.), [Ir(OMe)COD]₂ (0.09 g, 0.14 mmol, 0.05 eq.), 4,4'-di-*tert*-butyl-2,2'-bipyridine (0.07 g, 0.28 mmol, 0.1 eq.), and *tert*-butyl methyl ether (18 mL). Reaction mixture was stirred at 80 °C for 20 h, cooled down and passed through a pad of silica using toluene as the eluent. The solvent was removed under reduced pressure and the product was purified by flash chromatography (SiO₂; cyclohexane/ethyl acetate 9:1 → 8:2 → 7:3), as off-white solid (0.77 g, 0.95 mmol, 49%).

$R_f = 0.2$ (cyhex/EtOAc 9:1);

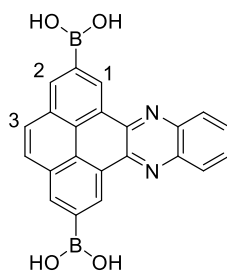
$^1\text{H NMR}$ (400 MHz, CD_2Cl_2): $\delta = 8.36$ (d, $J = 1.2$ Hz, 2H; H-C(1) or H-C(2)), 8.24 (d, $J = 1.2$ Hz, 2H; H-C(1) or H-C(2)), 7.81 (s, 2H; H-C(3)), 4.28 (br, 4H), 3.71 (br, 4H), 1.37 (s, 24H).

Synthesis of Model Organic Compounds

General procedure

In a 15 mL pressure tube (ACE glass, bushing type back seal, 10.2 cm x 25.4 mm), boronic acid-bearing pyrene-4,5-dione building block and *ortho*-diamine derivatives (1 equiv., *o*-phenylenediamine or 2,3-diaminonaphthalene) were dissolved in DMSO. The reaction mixture was stirred at 100 °C for 8 days. The precipitate was collected by centrifugation at 4400 rpm for 15 min and washed with H_2O for four times. The solid was dried under vacuum to give correspondent model organic compound **2** and **3**.

Model organic compound **2**

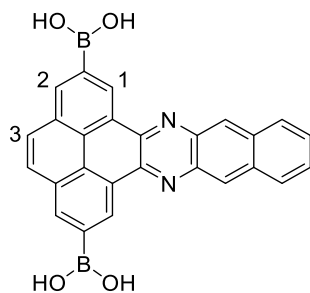


Boronic acid-bearing pyrene-4,5-dione building block **1** (12 mg, 0.04 mmol); *o*-phenylenediamine (4 mg, 0.04 mmol); DMSO (1 mL); brown model organic compound **2** (9 mg, 0.02 mmol, 50%).

$^1\text{H NMR}$ (400 MHz, $(\text{CD}_3)_2\text{SO}+\text{D}_2\text{O}$): $\delta = 9.86$ (d, $J = 1.2$ Hz, 2H; H-C(1) or H-C(2)), 8.79 (d, $J = 1.2$ Hz, 2H; H-C(1) or H-C(2)), 8.41 (dd, $J_1 = 3.4$ Hz, $J_2 = 6.5$ Hz, 2H; H-Ph), 8.15 (s, 2H; H-3), 7.99 (dd, $J_1 = 3.4$ Hz, $J_2 = 6.5$ Hz, 2H; H-Ph).

$^{13}\text{C NMR}$ (100 MHz, $(\text{CD}_3)_2\text{SO}+\text{D}_2\text{O}$): 143.4, 142.1, 135.9 (CH-1 or CH-2), 131.1 (CH-Ph), 130.9, 129.5 (CH-Ph or CH-1 or CH-2), 129.5 (CH-Ph or CH-1 or CH-2), 128.3, 127.8 (CH-3), 126.7 ppm.

IR (ATR): 3448, 3415, 1662, 1610, 1520, 1468, 1416, 1352, 1275, 1174, 1140, 1099, 891, 806, 744, 669, 563, 523.

Model organic compound 3

Boronic acid-bearing pyrene-4,5-dione building block **1** (11 mg, 0.03 mmol); 2,3-diaminonaphthalene (5.5 mg, 0.03 mmol); DMSO (1 mL); brown model organic compound **3** (10 mg, 0.02 mmol, 67%).

¹H NMR (400 MHz, (CD₃)₂SO+D₂O): δ= 9.74 (d, *J* = 1.0 Hz, 2H; H-C(1) or H-C(2)), 8.91 (bs, 2H; H-C(1) or H-C(2)), 8.70 (d, *J* = 1.2 Hz, 2H; H-Naph), 8.67 (d, *J* = 1.2 Hz, 1H; H-Naph), 8.62 (d, *J* = 1.2 Hz, 1H, H-Naph), 8.08 (s, 2H; H-C(3)), 7.96 (s, 2H, H-Naph).

¹³C NMR (100 MHz, (CD₃)₂SO+D₂O): 144.7, 142.0 (CH-Naph), 138.8, 136.8 (CH-Naph), 134.7, 134.3 (CH-Naph), 131.8, 131.3, 130.1 (CH-1 or CH-2), 128.5, 127.7 (CH-3 or CH-Naph), 127.1 ppm.

IR (ATR): 3379, 1674, 1614, 1520, 1338, 1265, 1157, 1099, 874, 800, 723, 673, 625, 580.

Synthesis of Dione-COF

Dione-COF was synthesized according to our previous report,³ in a 10 mL ampoule (Wheaton, prescored, borosilicate, 19 x 107 mm) flushed with argon. To the boronic acid-bearing pyrene-4,5-dione building block **1** (30 mg, 0.10 mmol, 1 eq.) with 2,3,6,7,10,11 hexahydroxytriphenylene (HHTP) hydrate (20 mg, 0.06 mmol, 0.64 eq.) were added a mixture of 1:1 mesitylene and n-butanol (3.5 mL), previously degassed by three cycles of freeze-pump-thaw. The reaction mixture was sonicated for 5 min. The ampoule was immersed in a bath of liquid N₂, sealed under vacuum, and heated in the oven at 120 °C, for 7 days. The precipitate was collected by centrifugation, washed with anhydrous acetone for four times, and dried under nitrogen at 90 °C, to give 45 mg of Dione-COF as brown solid.

Post-synthetic Modification of Dione-COF**General procedure**

In a nitrogen-filled 15 mL pressure tube (ACE glass, bushing type back seal, 10.2 cm x 25.4 mm) Dione-COF was added. In a separate vial, *o*-phenylenediamine (Ph) or 2,3-diaminonaphthalene (Naph) (2.1

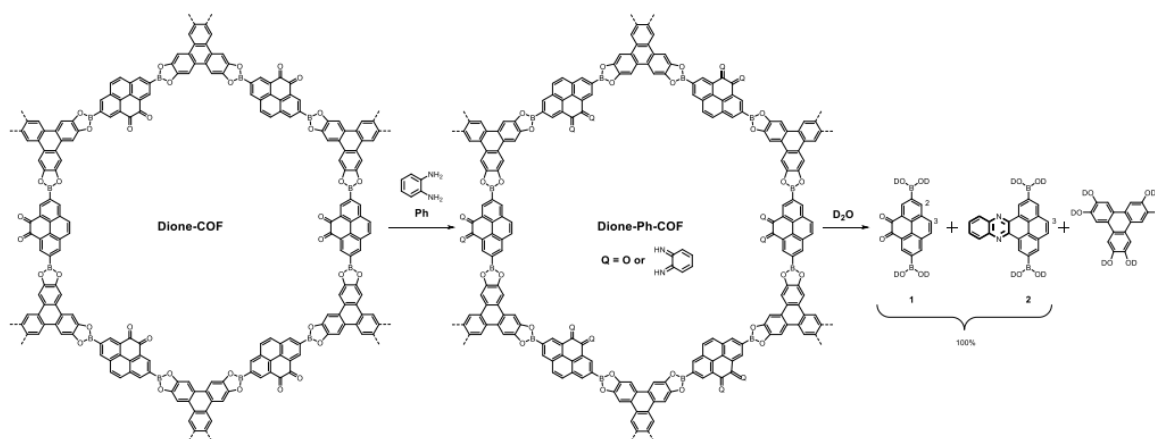
equiv.) was dissolved in anhydrous dichloromethane (3 mL), and the clear solution was poured into the pressure tube containing Dione-COF. The reaction mixture was heated at 50 °C for 7 days. The precipitate was collected by centrifugation, washed four times with anhydrous acetone, and dried under N₂ at 90 °C, to afford Dione Ph COF and Dione-Naph-COF.

Dione-Ph-COF synthesis

Dione-COF (60 mg, 0.26 mmol). *o*-Phenylenediamine (59 mg, 0.54 mmol, 2.1 eq.). Dione-Ph-COF (50 mg, 33% yield of functionalization).

Dione-Naph-COF synthesis

Dione-COF (60 mg, 0.26 mmol). 2,3-Diaminonaphthalene (86 mg, 0.54 mmol, 2.1 eq.). Dione-Naph-COF (55 mg, 19% yield of functionalization).



Scheme 3.2 Hydrolysis of Dione-Ph-COF by D₂O to the respective building blocks for the determination of the yield of the PSM. The yield was calculated by ¹H NMR spectroscopy by comparison of the signal intensities between the proton H-3 of the cleaved pyrene-fused pyrazaacene **2** and proton H-2 of pyrene-4,5-dione building block **1**. The yield of the reaction was calculated by dividing the integrated intensity of the pyrazaacene proton signal with the sum of the intensities of the pyrazaacene proton signal and that of the pyrene-4,5-dione building block **1**.

The yield for Dione-Naph-COF was calculated in a similar manner but using the proton H-3 of pyrene-4,5-dione building block **1** due to signal overlap.

3.6.3 NMR Spectra

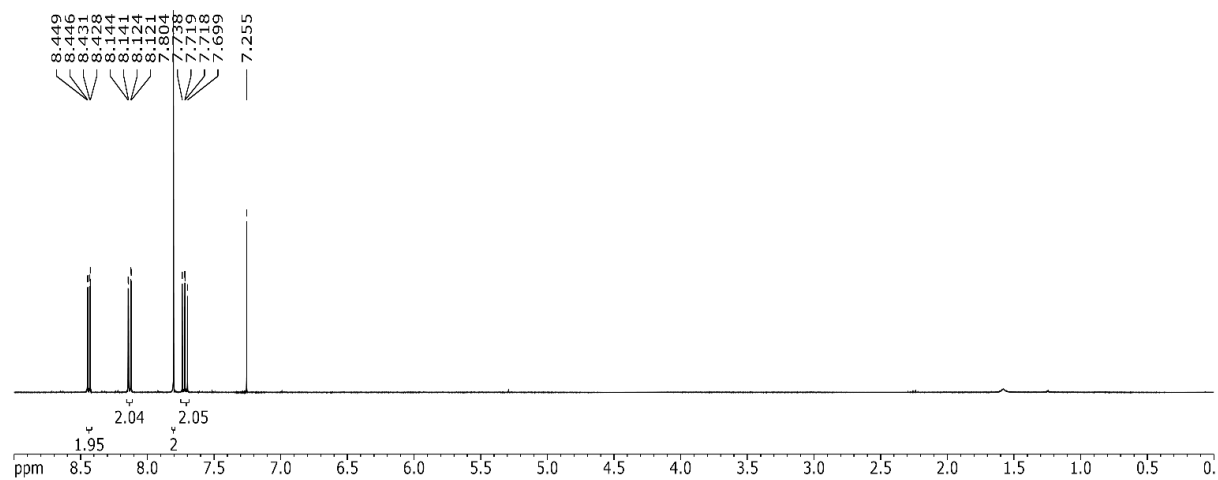


Figure 3. 3.4. ¹H NMR spectrum of pyrene-4,5-dione (**4**) measured at 400 MHz, in CDCl₃.

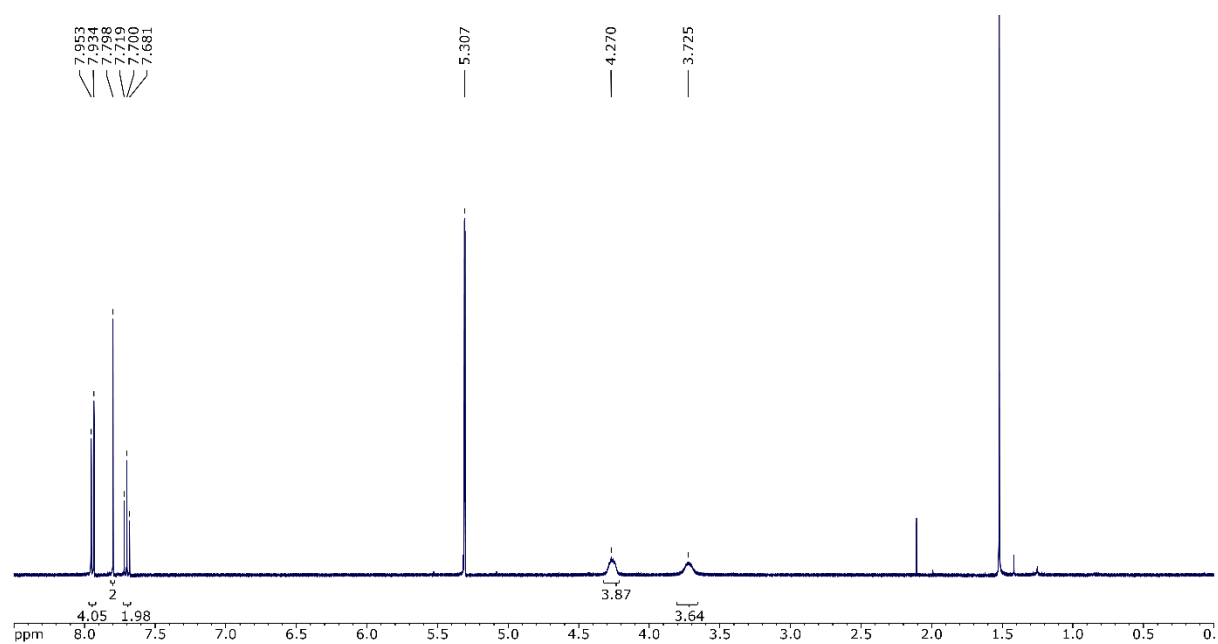


Figure 3.5. ¹H NMR spectrum of pyrene-4,5-di(ethyleneglycol)ketal (**5**), measured at 400 MHz, in CD₂Cl₂.

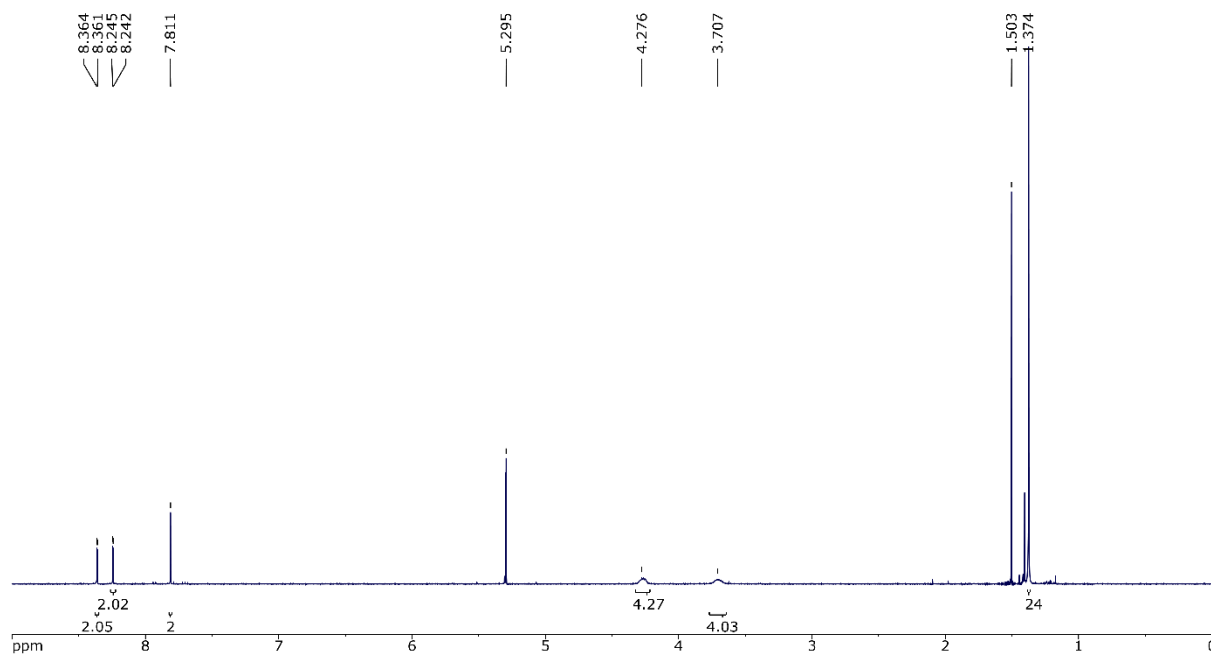


Figure 3.6. ^1H NMR spectrum of 2,7-bis(Bpin)-4,5-di(ethyleneglycol)ketal-pyrene (**6**), measured at 400 MHz, in CD_2Cl_2 .

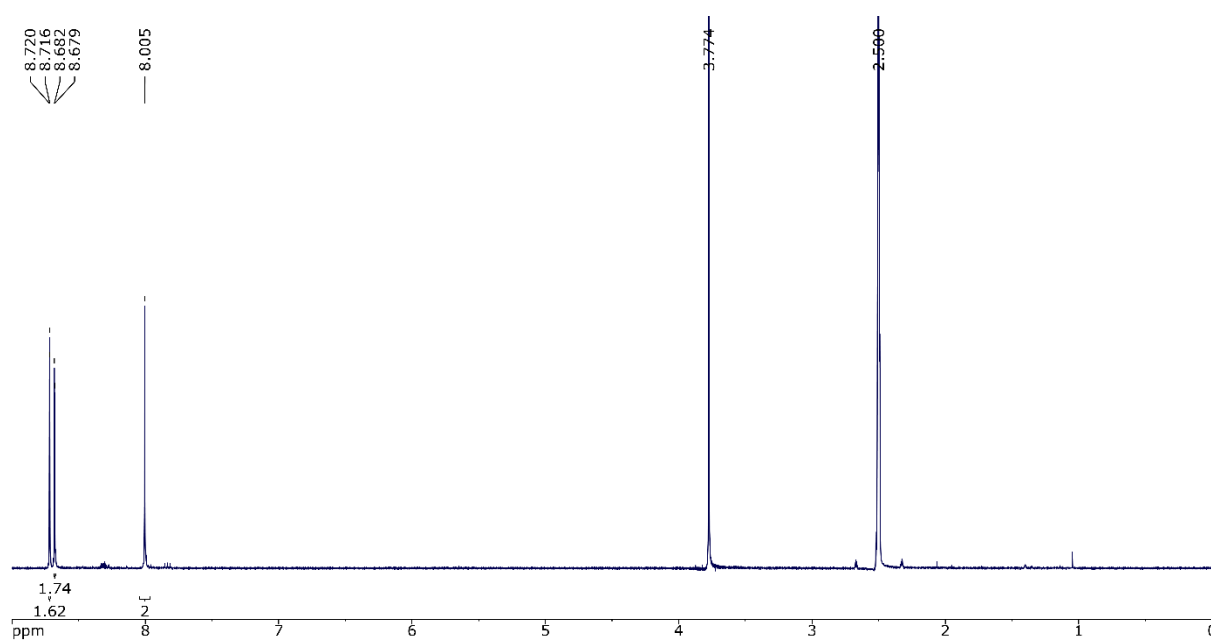


Figure 3.7. ^1H NMR spectrum of (7-borono-4,5-dioxo-pyren-2-yl)boronic acid (pyrene-4,5-dione building block **1**) measured at 400 MHz, in $(\text{CD}_3)_2\text{SO}+\text{D}_2\text{O}$.

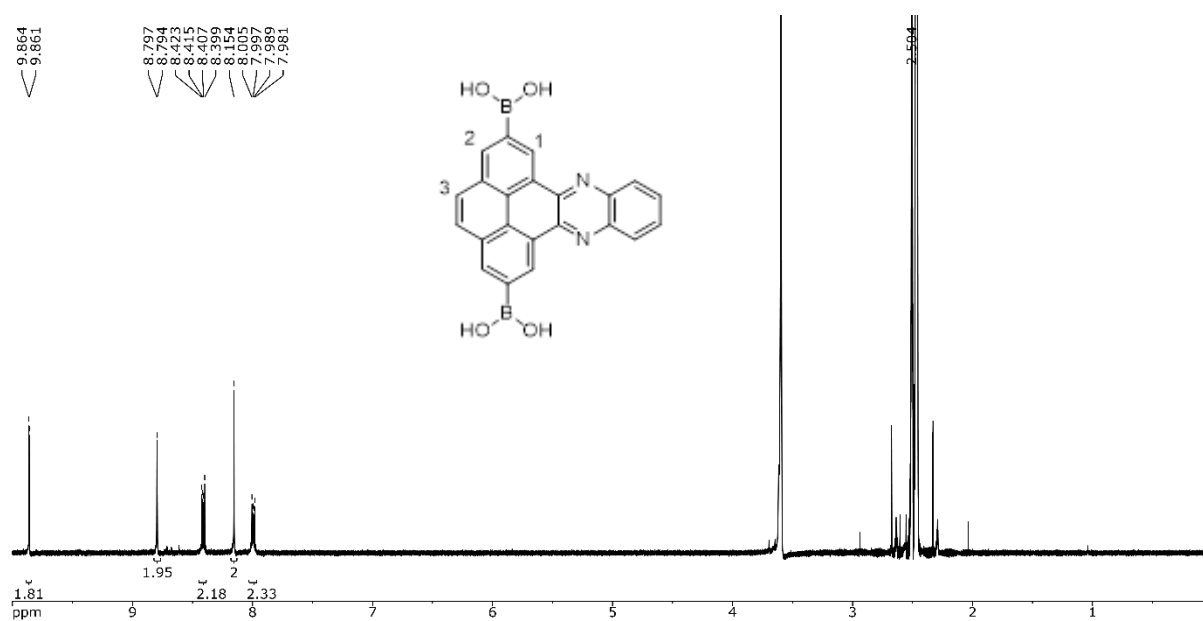


Figure 3.8. ¹H NMR spectrum of model compound 2, measured at 400 MHz, in (CD₃)₂SO+D₂O.

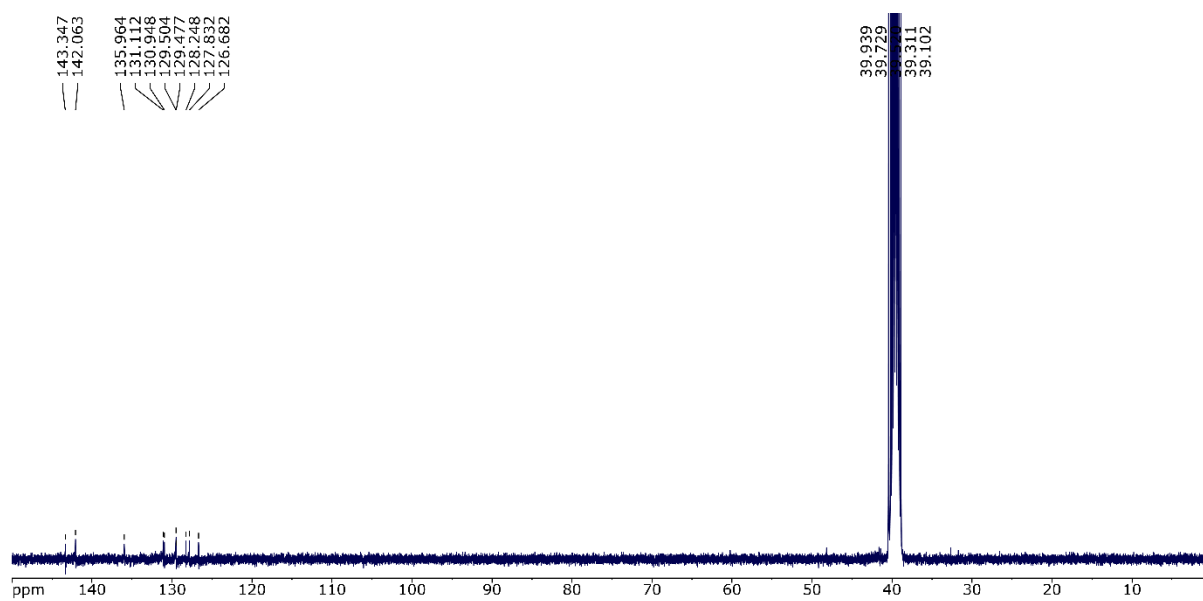


Figure 3.9. ¹³C NMR spectrum of model compound 2, measured at 100 MHz, in (CD₃)₂SO+D₂O.

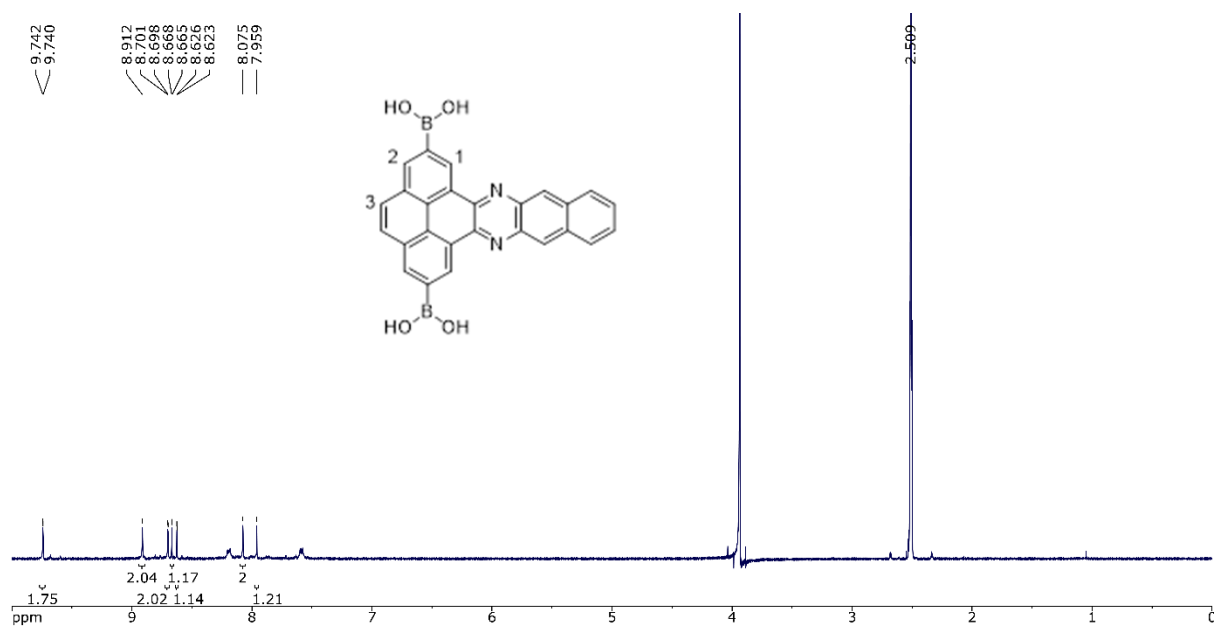


Figure 3.10. ^1H NMR spectrum of model compound **3**, measured at 400 MHz, in $(\text{CD}_3)_2\text{SO}+\text{D}_2\text{O}$.

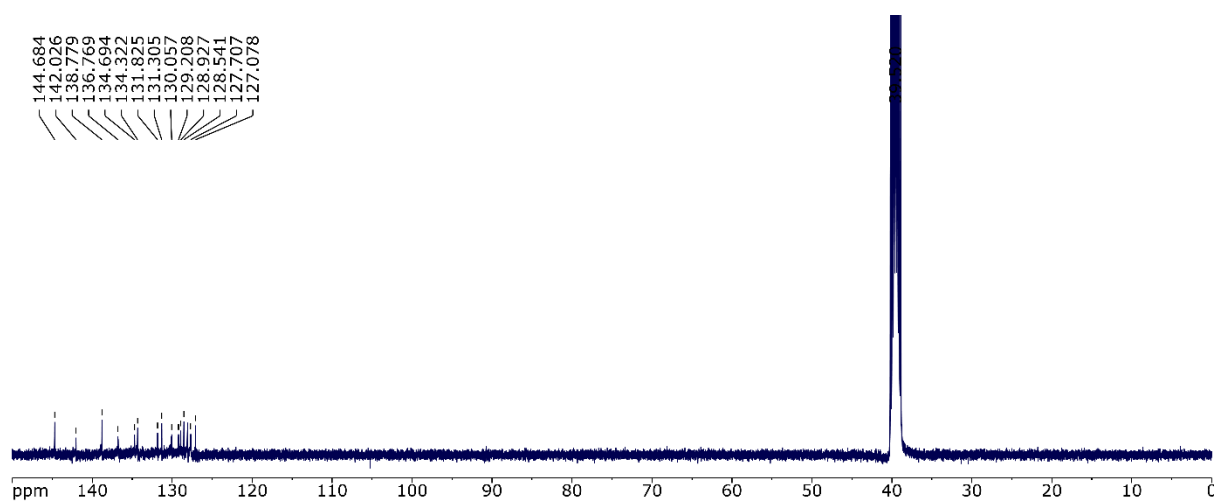


Figure 3.11. ^{13}C NMR spectrum of model compound **3**, measured at 100 MHz, in $(\text{CD}_3)_2\text{SO}+\text{D}_2\text{O}$.

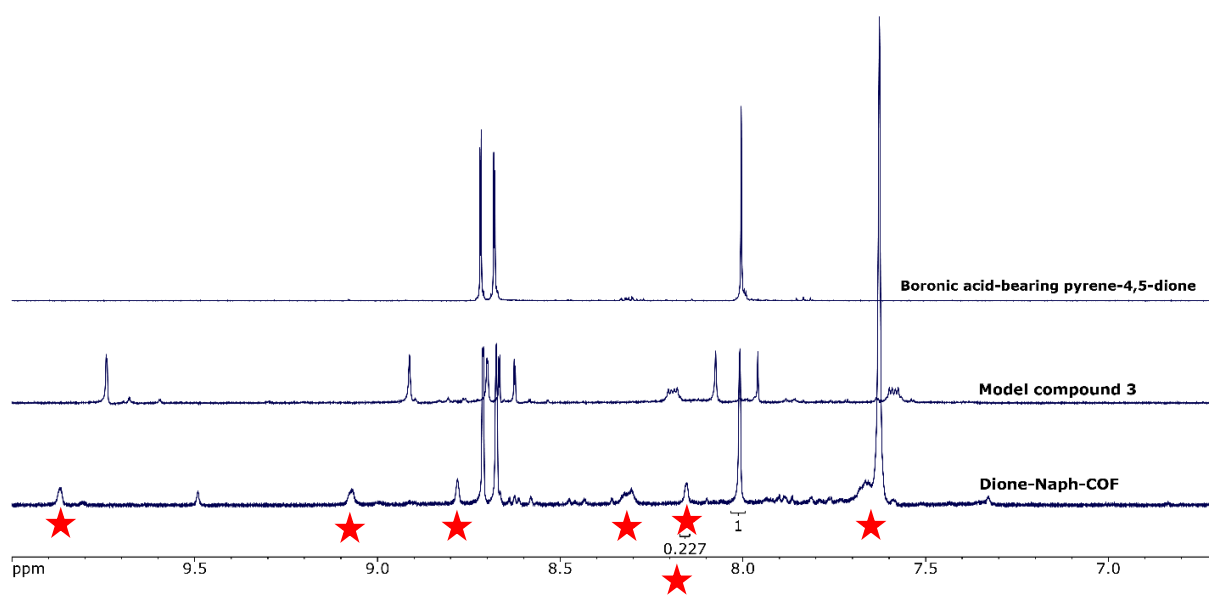


Figure 3.12. ¹H NMR spectrum of Dione-Naph-COF overlaid with boronic acid-bearing pyrene-4,5-dione building block **1** and model organic compound **3**, measured at 400 MHz, in (CD₃)₂SO+D₂O.

3.6.4 Crystal Structure Simulation

The simulated unit cell of Dione-Ph-COF and Dione-Naph-COF were constructed with the visualization environment of Materials Studio and the geometry optimized using force field methods. The simulated diffraction pattern corresponds well with the experimental powder X-ray diffraction (PXRD) data.

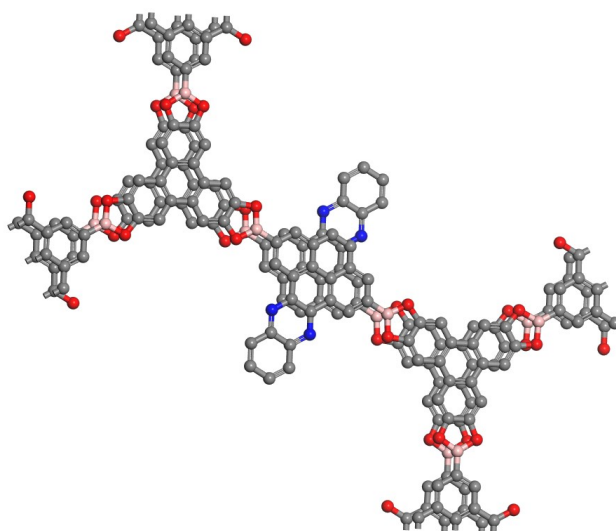


Figure 3.13. Simulation of the crystal unit cell of Dione-Ph-COF. View on *ab*-plane.

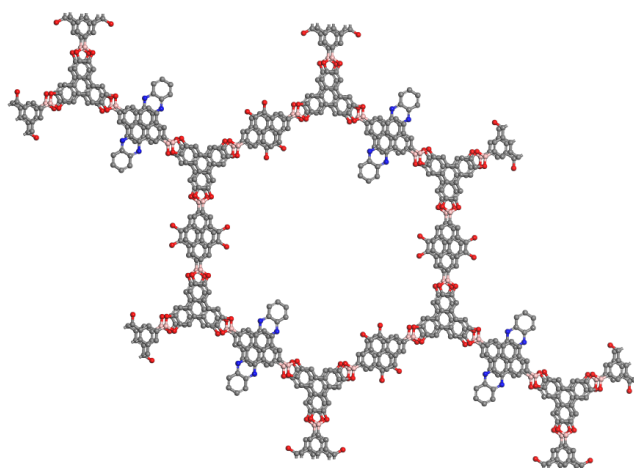


Figure 3.14. View of four unit cells constructing the Dione-Ph-COF pore.

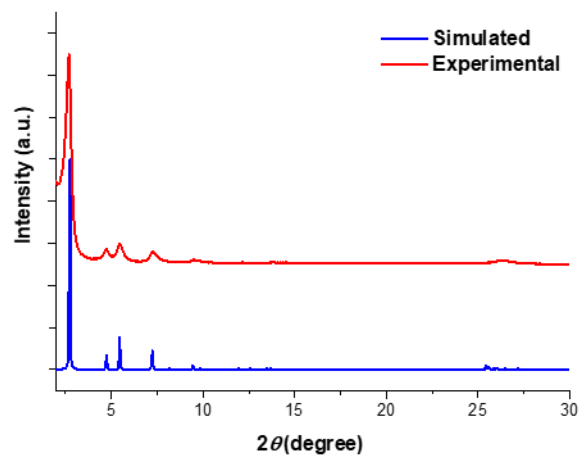


Figure 3.15. Experimentally obtained PXRD pattern (red) of Dione-Ph-COF and its simulated PXRD pattern (blue) obtained in Material Studio.

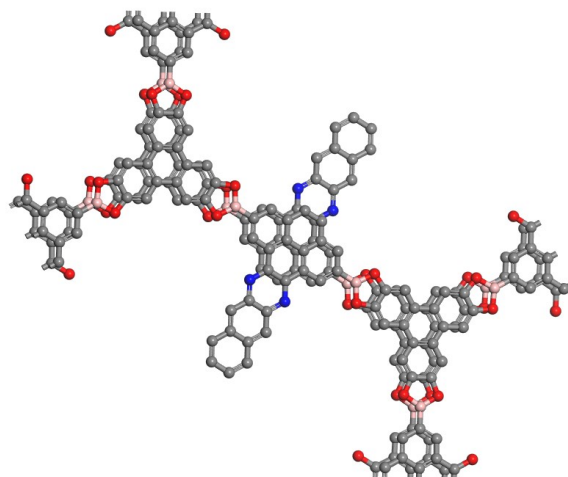


Figure 3.16. Simulation of the crystal unit cell of Dione-Naph-COF. View on *ab*-plane.

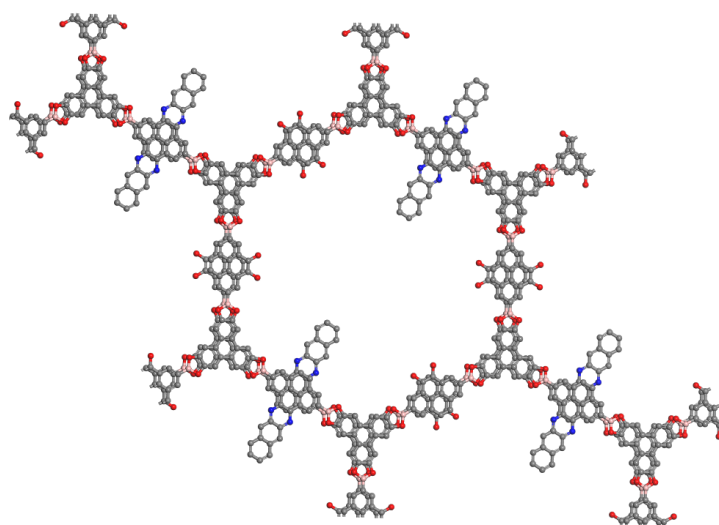


Figure 3.17. View of four unit cells constructing the Dione-Naph-COF pore.

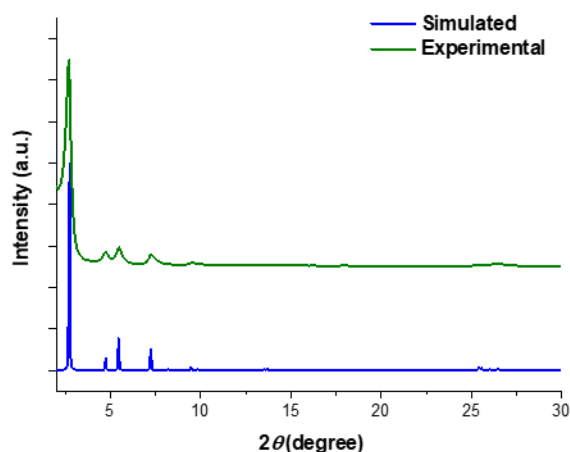


Figure 3.18. Experimentally obtained PXRD pattern (green) of Dione-Naph-COF and its simulated PXRD pattern (blue) obtained in Material Studio.

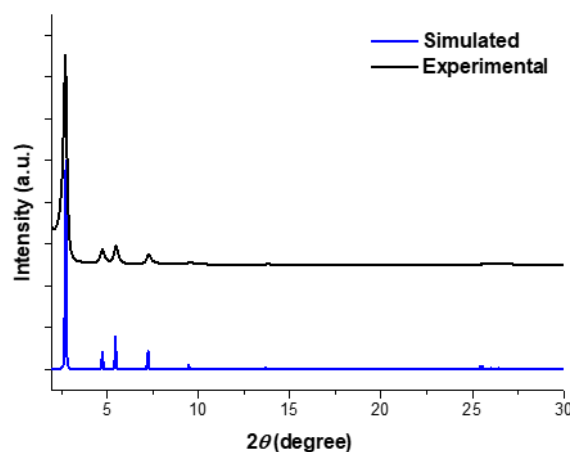


Figure 3.19. Experimentally obtained PXRD pattern (black) of Dione-COF and its simulated PXRD pattern (blue) obtained in Material Studio.

Unit cell parameters (*P1*) and atomic coordinates for Dione-Ph-COF

$$a = b = 37.3, c = 7.0 \text{ \AA}$$

$$\alpha = \beta = 90^\circ, \gamma = 120^\circ$$

Atom	a/x	b/y	c/z
C1	0.62880	0.29532	0.24348
C2	0.66715	0.29562	0.24348
C3	0.59137	0.25721	0.24348
C4	0.59266	0.22067	0.24348
C5	0.62952	0.22090	0.24348
C6	0.66708	0.25777	0.24348
O7	0.55864	0.18124	0.24348
B8	0.57934	0.15673	0.24348
O9	0.62455	0.18158	0.24348
C10	0.55521	0.10874	0.24348
C11	0.51208	0.08777	0.24348

C12	0.48943	0.04455	0.24348
C13	0.51044	0.02188	0.24349
C14	0.55420	0.04339	0.24348
C15	0.57624	0.08658	0.24348
C16	0.44385	0.02269	0.24348
C17	0.57555	0.02158	0.24348
O18	0.42116	0.04538	0.24348
C19	0.30771	0.35309	0.74348
C20	0.30771	0.28502	0.74348
C21	0.70468	0.33348	0.24348
C22	0.70438	0.37153	0.24348
C23	0.74279	0.33416	0.24348
C24	0.77933	0.37199	0.24348
C25	0.77910	0.40862	0.24348
C26	0.74223	0.40931	0.24348
O27	0.81876	0.37740	0.24348
B28	0.84327	0.42261	0.24348
O29	0.81842	0.44297	0.24348
C30	0.89126	0.44647	0.24348
C31	0.91223	0.42431	0.24348
C32	0.95545	0.44488	0.24348
C33	0.97812	0.48856	0.24349
C34	0.95661	0.51081	0.24348
C35	0.91342	0.48966	0.24348
C36	0.97731	0.42116	0.24348
C37	0.97842	0.55397	0.24348
O38	0.95462	0.37578	0.24348
C39	0.66652	0.37120	0.24348
C40	0.62847	0.33285	0.24348
C41	0.66584	0.40863	0.24348
C42	0.62801	0.40734	0.24348
C43	0.59138	0.37048	0.24348
C44	0.59069	0.33292	0.24348
O45	0.62260	0.44136	0.24348
B46	0.57739	0.42066	0.24348
O47	0.55703	0.37545	0.24348
C48	0.55353	0.44479	0.24348
C49	0.57569	0.48792	0.24348
C50	0.55512	0.51057	0.24348
C51	0.51144	0.48956	0.24349
C52	0.48919	0.44580	0.24348
C53	0.51034	0.42376	0.24348
C54	0.57884	0.55615	0.24348
C55	0.44603	0.42445	0.24348
N56	0.62422	0.57884	0.24348
C57	0.64691	0.62422	0.24348
C58	0.37120	0.70468	0.74348
C59	0.33285	0.70438	0.74348
C60	0.40863	0.74279	0.74348
C61	0.40734	0.77933	0.74348
C62	0.37048	0.77910	0.74348
C63	0.33292	0.74223	0.74348
O64	0.44136	0.81876	0.74348
B65	0.42066	0.84327	0.74348
O66	0.37545	0.81842	0.74348
C67	0.44479	0.89126	0.74348
C68	0.48792	0.91223	0.74348
C69	0.51057	0.95545	0.74348

A Post-synthetic Modification Strategy for the Synthesis of Pyrene-fused Azaacene COFs

C70	0.48956	0.97812	0.74349
C71	0.44580	0.95661	0.74348
C72	0.42376	0.91342	0.74348
C73	0.55615	0.97731	0.74348
C74	0.42445	0.97842	0.74348
O75	0.57884	0.95462	0.74348
C76	0.69229	0.64691	0.24348
C77	0.69229	0.71498	0.24348
C78	0.29532	0.66652	0.74348
C79	0.29562	0.62847	0.74348
C80	0.25721	0.66584	0.74348
C81	0.22067	0.62801	0.74348
C82	0.22090	0.59138	0.74348
C83	0.25777	0.59069	0.74348
O84	0.18124	0.62260	0.74348
B85	0.15673	0.57739	0.74348
O86	0.18158	0.55703	0.74348
C87	0.10874	0.55353	0.74348
C88	0.08777	0.57569	0.74348
C89	0.04455	0.55512	0.74348
C90	0.02188	0.51144	0.74349
C91	0.04339	0.48919	0.74348
C92	0.08658	0.51034	0.74348
C93	0.02269	0.57884	0.74348
C94	0.02158	0.44603	0.74348
O95	0.04538	0.62422	0.74348
C96	0.33348	0.62880	0.74348
C97	0.37153	0.66715	0.74348
C98	0.33416	0.59137	0.74348
C99	0.37199	0.59266	0.74348
C100	0.40862	0.62952	0.74348
C101	0.40931	0.66708	0.74348
O102	0.37740	0.55864	0.74348
B103	0.42261	0.57934	0.74348
O104	0.44297	0.62455	0.74348
C105	0.44647	0.55521	0.74348
C106	0.42431	0.51208	0.74348
C107	0.44488	0.48943	0.74348
C108	0.48856	0.51044	0.74349
C109	0.51081	0.55420	0.74348
C110	0.48966	0.57624	0.74348
C111	0.42116	0.44385	0.74348
C112	0.55397	0.57555	0.74348
N113	0.37578	0.42116	0.74348
C114	0.35309	0.37578	0.74348
C115	0.70468	0.37120	0.74348
C116	0.70438	0.33285	0.74348
C117	0.74279	0.40863	0.74348
C118	0.77933	0.40734	0.74348
C119	0.77910	0.37048	0.74348
C120	0.74223	0.33292	0.74348
O121	0.81876	0.44136	0.74348
B122	0.84327	0.42066	0.74348
O123	0.81842	0.37545	0.74348
C124	0.89126	0.44479	0.74348
C125	0.91223	0.48792	0.74348
C126	0.95545	0.51057	0.74348
C127	0.97812	0.48956	0.74349

A Post-synthetic Modification Strategy for the Synthesis of Pyrene-fused Azaacene COFs

C128	0.95661	0.44580	0.74348
C129	0.91342	0.42376	0.74348
C130	0.97731	0.55615	0.74348
C131	0.97842	0.42445	0.74348
O132	0.95462	0.57884	0.74348
C133	0.64691	0.69229	0.24348
C134	0.71498	0.69229	0.24348
C135	0.66652	0.29532	0.74348
C136	0.62847	0.29562	0.74348
C137	0.66584	0.25721	0.74348
C138	0.62801	0.22067	0.74348
C139	0.59138	0.22090	0.74348
C140	0.59069	0.25777	0.74348
O141	0.62260	0.18124	0.74348
B142	0.57739	0.15673	0.74348
O143	0.55703	0.18158	0.74348
C144	0.55353	0.10874	0.74348
C145	0.57569	0.08777	0.74348
C146	0.55512	0.04455	0.74348
C147	0.51144	0.02188	0.74349
C148	0.48919	0.04339	0.74348
C149	0.51034	0.08658	0.74348
C150	0.57884	0.02269	0.74348
C151	0.44603	0.02158	0.74348
O152	0.62422	0.04538	0.74348
C153	0.62880	0.33348	0.74348
C154	0.66715	0.37153	0.74348
C155	0.59137	0.33416	0.74348
C156	0.59266	0.37199	0.74348
C157	0.62952	0.40862	0.74348
C158	0.66708	0.40931	0.74348
O159	0.55864	0.37740	0.74348
B160	0.57934	0.42261	0.74348
O161	0.62455	0.44297	0.74348
C162	0.55521	0.44647	0.74348
C163	0.51208	0.42431	0.74348
C164	0.48943	0.44488	0.74348
C165	0.51044	0.48856	0.74349
C166	0.55420	0.51081	0.74348
C167	0.57624	0.48966	0.74348
C168	0.44385	0.42116	0.74348
C169	0.57555	0.55397	0.74348
N170	0.42116	0.37578	0.74348
C171	0.37578	0.35309	0.74348
C172	0.29532	0.62880	0.24348
C173	0.29562	0.66715	0.24348
C174	0.25721	0.59137	0.24348
C175	0.22067	0.59266	0.24348
C176	0.22090	0.62952	0.24348
C177	0.25777	0.66708	0.24348
O178	0.18124	0.55864	0.24348
B179	0.15673	0.57934	0.24348
O180	0.18158	0.62455	0.24348
C181	0.10874	0.55521	0.24348
C182	0.08777	0.51208	0.24348
C183	0.04455	0.48943	0.24348
C184	0.02188	0.51044	0.24349
C185	0.04339	0.55420	0.24348

A Post-synthetic Modification Strategy for the Synthesis of Pyrene-fused Azaacene COFs

C186	0.08658	0.57624	0.24348
C187	0.02269	0.44385	0.24348
C188	0.02158	0.57555	0.24348
O189	0.04538	0.42116	0.24348
C190	0.35309	0.30771	0.74348
C191	0.28502	0.30771	0.74348
C192	0.33348	0.70468	0.24348
C193	0.37153	0.70438	0.24348
C194	0.33416	0.74279	0.24348
C195	0.37199	0.77933	0.24348
C196	0.40862	0.77910	0.24348
C197	0.40931	0.74223	0.24348
O198	0.37740	0.81876	0.24348
B199	0.42261	0.84327	0.24348
O200	0.44297	0.81842	0.24348
C201	0.44647	0.89126	0.24348
C202	0.42431	0.91223	0.24348
C203	0.44488	0.95545	0.24348
C204	0.48856	0.97812	0.24349
C205	0.51081	0.95661	0.24348
C206	0.48966	0.91342	0.24348
C207	0.42116	0.97731	0.24348
C208	0.55397	0.97842	0.24348
O209	0.37578	0.95462	0.24348
C210	0.37120	0.66652	0.24348
C211	0.33285	0.62847	0.24348
C212	0.40863	0.66584	0.24348
C213	0.40734	0.62801	0.24348
C214	0.37048	0.59138	0.24348
C215	0.33292	0.59069	0.24348
O216	0.44136	0.62260	0.24348
B217	0.42066	0.57739	0.24348
O218	0.37545	0.55703	0.24348
C219	0.44479	0.55353	0.24348
C220	0.48792	0.57569	0.24348
C221	0.51057	0.55512	0.24348
C222	0.48956	0.51144	0.24349
C223	0.44580	0.48919	0.24348
C224	0.42376	0.51034	0.24348
C225	0.55615	0.57884	0.24348
C226	0.42445	0.44603	0.24348
N227	0.57884	0.62422	0.24348
C228	0.62422	0.64691	0.24348

Unit cell parameters (P1) and atomic coordinates for Dione-Naph-COF

$$a = b = 37.3, c = 7.0 \text{ \AA}$$

$$\alpha = \beta = 90^\circ, \gamma = 120^\circ$$

Atom	a/x	b/y	c/z
C1	0.62880	0.29532	0.24348
C2	0.66715	0.29562	0.24348
C3	0.59137	0.25721	0.24348
C4	0.59266	0.22067	0.24348
C5	0.62952	0.22090	0.24348
C6	0.66708	0.25777	0.24348
O7	0.55864	0.18124	0.24348
B8	0.57934	0.15673	0.24348
O9	0.62455	0.18158	0.24348
C10	0.55521	0.10874	0.24348
C11	0.51208	0.08777	0.24348
C12	0.48943	0.04455	0.24348
C13	0.51044	0.02188	0.24349
C14	0.55420	0.04339	0.24348
C15	0.57624	0.08658	0.24348
C16	0.44385	0.02269	0.24348
C17	0.57555	0.02158	0.24348
O18	0.42116	0.04538	0.24348
C19	0.30771	0.35309	0.74348
C20	0.30771	0.28502	0.74348
C21	0.70468	0.33348	0.24348
C22	0.70438	0.37153	0.24348
C23	0.74279	0.33416	0.24348
C24	0.77933	0.37199	0.24348
C25	0.77910	0.40862	0.24348
C26	0.74223	0.40931	0.24348
O27	0.81876	0.37740	0.24348
B28	0.84327	0.42261	0.24348
O29	0.81842	0.44297	0.24348
C30	0.89126	0.44647	0.24348
C31	0.91223	0.42431	0.24348
C32	0.95545	0.44488	0.24348
C33	0.97812	0.48856	0.24349
C34	0.95661	0.51081	0.24348
C35	0.91342	0.48966	0.24348
C36	0.97731	0.42116	0.24348
C37	0.97842	0.55397	0.24348
O38	0.95462	0.37578	0.24348
C39	0.66652	0.37120	0.24348
C40	0.62847	0.33285	0.24348
C41	0.66584	0.40863	0.24348
C42	0.62801	0.40734	0.24348
C43	0.59138	0.37048	0.24348
C44	0.59069	0.33292	0.24348
O45	0.62260	0.44136	0.24348
B46	0.57739	0.42066	0.24348

A Post-synthetic Modification Strategy for the Synthesis of Pyrene-fused Azaacene COFs

O47	0.55703	0.37545	0.24348
C48	0.55353	0.44479	0.24348
C49	0.57569	0.48792	0.24348
C50	0.55512	0.51057	0.24348
C51	0.51144	0.48956	0.24349
C52	0.48919	0.44580	0.24348
C53	0.51034	0.42376	0.24348
C54	0.57884	0.55615	0.24348
C55	0.44603	0.42445	0.24348
N56	0.62422	0.57884	0.24348
C57	0.64691	0.62422	0.24348
C58	0.37120	0.70468	0.74348
C59	0.33285	0.70438	0.74348
C60	0.40863	0.74279	0.74348
C61	0.40734	0.77933	0.74348
C62	0.37048	0.77910	0.74348
C63	0.33292	0.74223	0.74348
O64	0.44136	0.81876	0.74348
B65	0.42066	0.84327	0.74348
O66	0.37545	0.81842	0.74348
C67	0.44479	0.89126	0.74348
C68	0.48792	0.91223	0.74348
C69	0.51057	0.95545	0.74348
C70	0.48956	0.97812	0.74349
C71	0.44580	0.95661	0.74348
C72	0.42376	0.91342	0.74348
C73	0.55615	0.97731	0.74348
C74	0.42445	0.97842	0.74348
O75	0.57884	0.95462	0.74348
C76	0.69229	0.64691	0.24348
C77	0.69229	0.71498	0.24348
C78	0.29532	0.66652	0.74348
C79	0.29562	0.62847	0.74348
C80	0.25721	0.66584	0.74348
C81	0.22067	0.62801	0.74348
C82	0.22090	0.59138	0.74348
C83	0.25777	0.59069	0.74348
O84	0.18124	0.62260	0.74348
B85	0.15673	0.57739	0.74348
O86	0.18158	0.55703	0.74348
C87	0.10874	0.55353	0.74348
C88	0.08777	0.57569	0.74348
C89	0.04455	0.55512	0.74348
C90	0.02188	0.51144	0.74349
C91	0.04339	0.48919	0.74348
C92	0.08658	0.51034	0.74348
C93	0.02269	0.57884	0.74348
C94	0.02158	0.44603	0.74348
O95	0.04538	0.62422	0.74348
C96	0.33348	0.62880	0.74348
C97	0.37153	0.66715	0.74348
C98	0.33416	0.59137	0.74348
C99	0.37199	0.59266	0.74348
C100	0.40862	0.62952	0.74348
C101	0.40931	0.66708	0.74348

A Post-synthetic Modification Strategy for the Synthesis of Pyrene-fused Azaacene COFs

O102	0.37740	0.55864	0.74348
B103	0.42261	0.57934	0.74348
O104	0.44297	0.62455	0.74348
C105	0.44647	0.55521	0.74348
C106	0.42431	0.51208	0.74348
C107	0.44488	0.48943	0.74348
C108	0.48856	0.51044	0.74349
C109	0.51081	0.55420	0.74348
C110	0.48966	0.57624	0.74348
C111	0.42116	0.44385	0.74348
C112	0.55397	0.57555	0.74348
N113	0.37578	0.42116	0.74348
C114	0.35309	0.37578	0.74348
C115	0.70468	0.37120	0.74348
C116	0.70438	0.33285	0.74348
C117	0.74279	0.40863	0.74348
C118	0.77933	0.40734	0.74348
C119	0.77910	0.37048	0.74348
C120	0.74223	0.33292	0.74348
O121	0.81876	0.44136	0.74348
B122	0.84327	0.42066	0.74348
O123	0.81842	0.37545	0.74348
C124	0.89126	0.44479	0.74348
C125	0.91223	0.48792	0.74348
C126	0.95545	0.51057	0.74348
C127	0.97812	0.48956	0.74349
C128	0.95661	0.44580	0.74348
C129	0.91342	0.42376	0.74348
C130	0.97731	0.55615	0.74348
C131	0.97842	0.42445	0.74348
O132	0.95462	0.57884	0.74348
C133	0.64691	0.69229	0.24348
C134	0.71498	0.69229	0.24348
C135	0.66652	0.29532	0.74348
C136	0.62847	0.29562	0.74348
C137	0.66584	0.25721	0.74348
C138	0.62801	0.22067	0.74348
C139	0.59138	0.22090	0.74348
C140	0.59069	0.25777	0.74348
O141	0.62260	0.18124	0.74348
B142	0.57739	0.15673	0.74348
O143	0.55703	0.18158	0.74348
C144	0.55353	0.10874	0.74348
C145	0.57569	0.08777	0.74348
C146	0.55512	0.04455	0.74348
C147	0.51144	0.02188	0.74349
C148	0.48919	0.04339	0.74348
C149	0.51034	0.08658	0.74348
C150	0.57884	0.02269	0.74348
C151	0.44603	0.02158	0.74348
O152	0.62422	0.04538	0.74348
C153	0.62880	0.33348	0.74348
C154	0.66715	0.37153	0.74348
C155	0.59137	0.33416	0.74348
C156	0.59266	0.37199	0.74348

A Post-synthetic Modification Strategy for the Synthesis of Pyrene-fused Azaacene COFs

C157	0.62952	0.40862	0.74348
C158	0.66708	0.40931	0.74348
O159	0.55864	0.37740	0.74348
B160	0.57934	0.42261	0.74348
O161	0.62455	0.44297	0.74348
C162	0.55521	0.44647	0.74348
C163	0.51208	0.42431	0.74348
C164	0.48943	0.44488	0.74348
C165	0.51044	0.48856	0.74349
C166	0.55420	0.51081	0.74348
C167	0.57624	0.48966	0.74348
C168	0.44385	0.42116	0.74348
C169	0.57555	0.55397	0.74348
N170	0.42116	0.37578	0.74348
C171	0.37578	0.35309	0.74348
C172	0.29532	0.62880	0.24348
C173	0.29562	0.66715	0.24348
C174	0.25721	0.59137	0.24348
C175	0.22067	0.59266	0.24348
C176	0.22090	0.62952	0.24348
C177	0.25777	0.66708	0.24348
O178	0.18124	0.55864	0.24348
B179	0.15673	0.57934	0.24348
O180	0.18158	0.62455	0.24348
C181	0.10874	0.55521	0.24348
C182	0.08777	0.51208	0.24348
C183	0.04455	0.48943	0.24348
C184	0.02188	0.51044	0.24349
C185	0.04339	0.55420	0.24348
C186	0.08658	0.57624	0.24348
C187	0.02269	0.44385	0.24348
C188	0.02158	0.57555	0.24348
O189	0.04538	0.42116	0.24348
C190	0.35309	0.30771	0.74348
C191	0.28502	0.30771	0.74348
C192	0.33348	0.70468	0.24348
C193	0.37153	0.70438	0.24348
C194	0.33416	0.74279	0.24348
C195	0.37199	0.77933	0.24348
C196	0.40862	0.77910	0.24348
C197	0.40931	0.74223	0.24348
O198	0.37740	0.81876	0.24348
B199	0.42261	0.84327	0.24348
O200	0.44297	0.81842	0.24348
C201	0.44647	0.89126	0.24348
C202	0.42431	0.91223	0.24348
C203	0.44488	0.95545	0.24348
C204	0.48856	0.97812	0.24349
C205	0.51081	0.95661	0.24348
C206	0.48966	0.91342	0.24348
C207	0.42116	0.97731	0.24348
C208	0.55397	0.97842	0.24348
O209	0.37578	0.95462	0.24348
C210	0.37120	0.66652	0.24348
C211	0.33285	0.62847	0.24348

A Post-synthetic Modification Strategy for the Synthesis of Pyrene-fused Azaacene COFs

C212	0.40863	0.66584	0.24348
C213	0.40734	0.62801	0.24348
C214	0.37048	0.59138	0.24348
C215	0.33292	0.59069	0.24348
O216	0.44136	0.62260	0.24348
B217	0.42066	0.57739	0.24348
O218	0.37545	0.55703	0.24348
C219	0.44479	0.55353	0.24348
C220	0.48792	0.57569	0.24348
C221	0.51057	0.55512	0.24348
C222	0.48956	0.51144	0.24349
C223	0.44580	0.48919	0.24348
C224	0.42376	0.51034	0.24348
C225	0.55615	0.57884	0.24348
C226	0.42445	0.44603	0.24348
N227	0.57884	0.62422	0.24348
C228	0.62422	0.64691	0.24348
C229	0.71498	0.76036	0.24348
C230	0.76036	0.78305	0.24348
C231	0.78305	0.76036	0.24348
C232	0.76036	0.71498	0.24348
C233	0.28502	0.23964	0.74348
C234	0.23964	0.21695	0.74348
C235	0.21695	0.23964	0.74348
C236	0.23964	0.28502	0.74348

3.6.5 N₂ Physisorption

Dione-COF

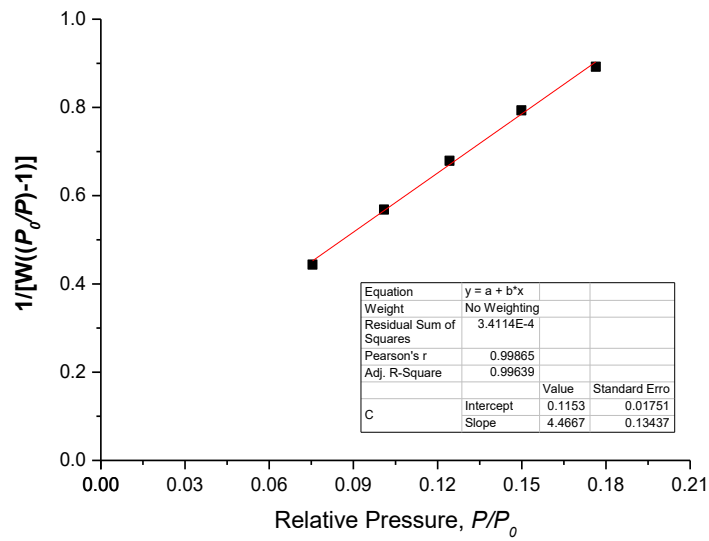


Figure 3.20. Multi-point BET plot and linear fit.

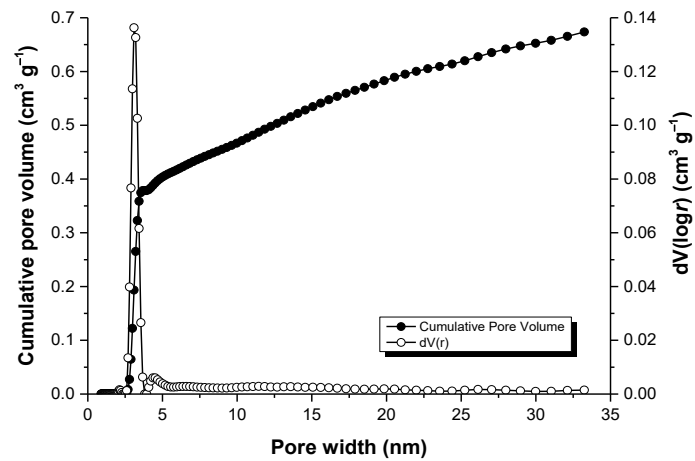


Figure 3.21. Pore size distribution (hollow spheres) and cumulative pore volume (filled spheres) profiles.

Dione-Ph-COF

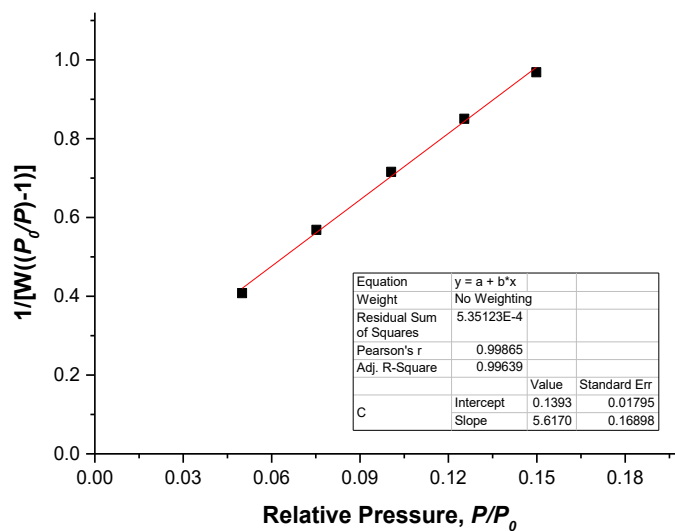


Figure 3.22. Multi-point BET plot and linear fit.

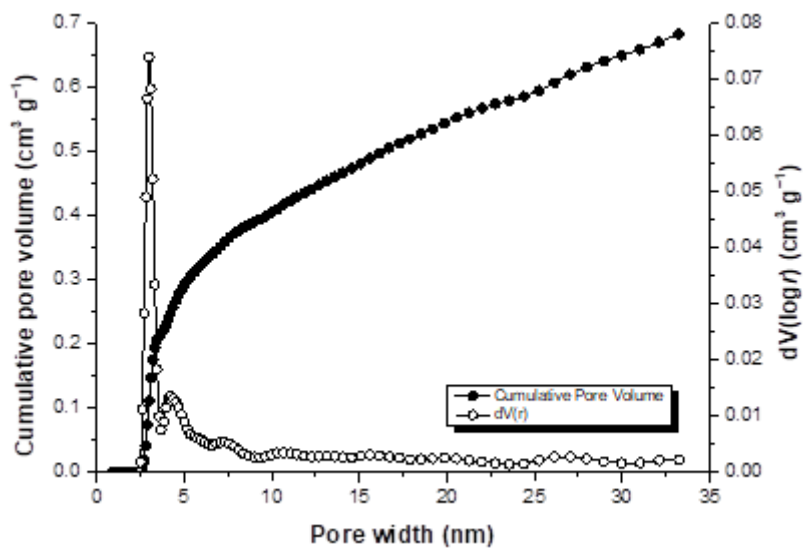


Figure 3.23. Pore size distribution (hollow spheres) and cumulative pore volume (filled spheres) profiles.

Dione-Naph-COF

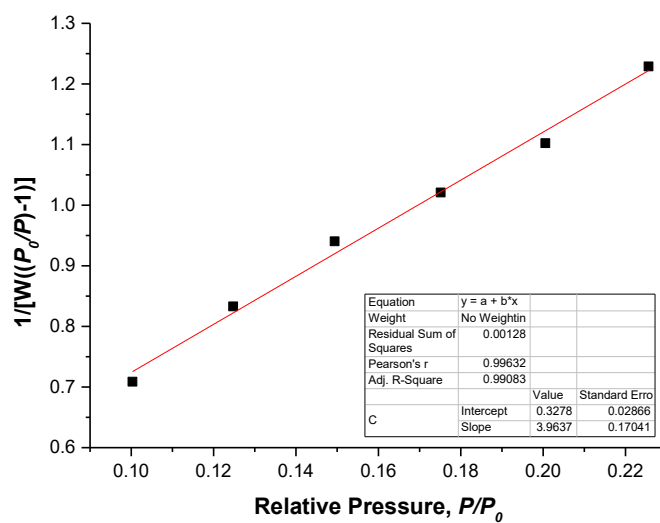


Figure 3.24. Multi-point BET plot and linear fit.

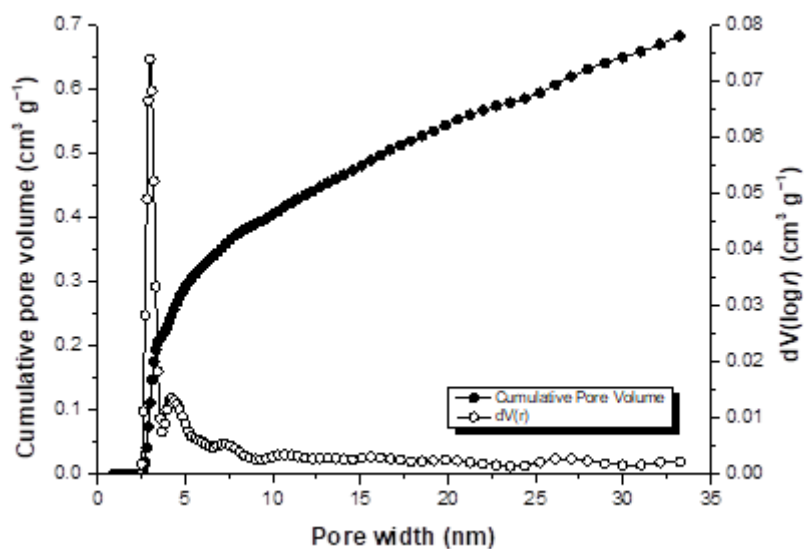


Figure 3.25. Pore size distribuion (hollow spheres) and cumulative pore volume (filled spheres) profiles.

3.6.6 Fourier-transform Infrared (FT-IR) Spectroscopy

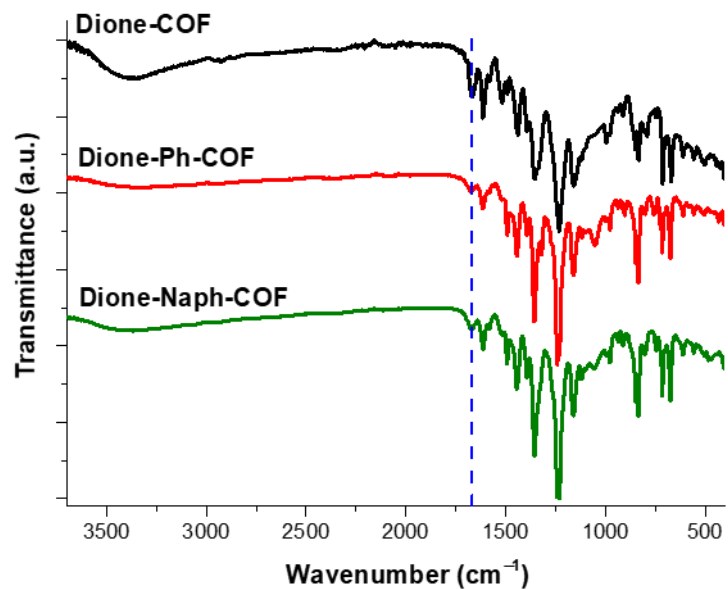


Figure 3.26. FT-IR spectrum of Dione-COF, Dione-Ph-COF and Dione-Naph-COF.

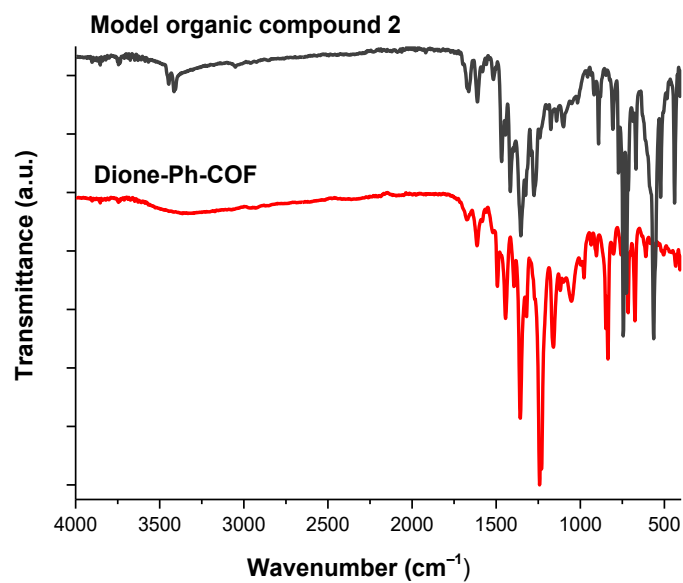


Figure 3.27. FT-IR spectrum of model organic compound 2 and Dione-Ph-COF.

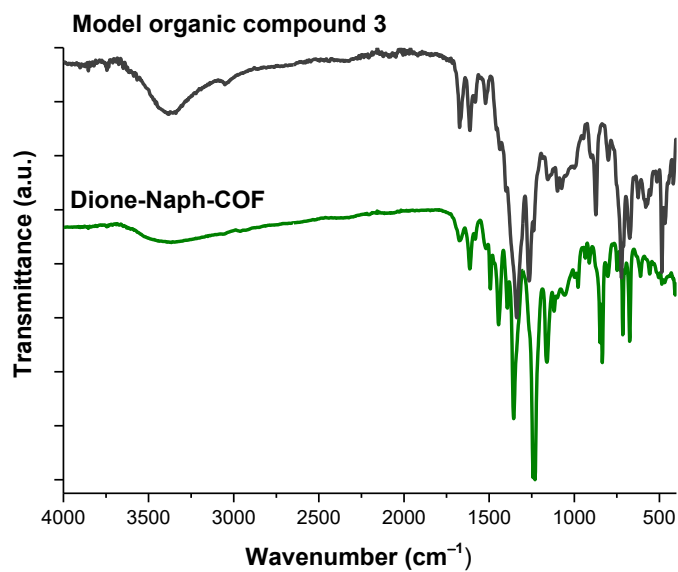


Figure 3.28. FT-IR spectrum of model organic compound **3** and Dione-Naph-COF.

3.6.7 Thermogravimetric Analysis (TGA)

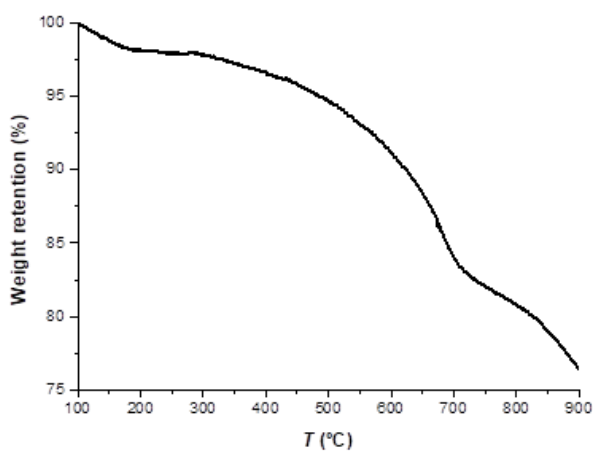


Figure 3.29. TGA profile of Dione-COF.

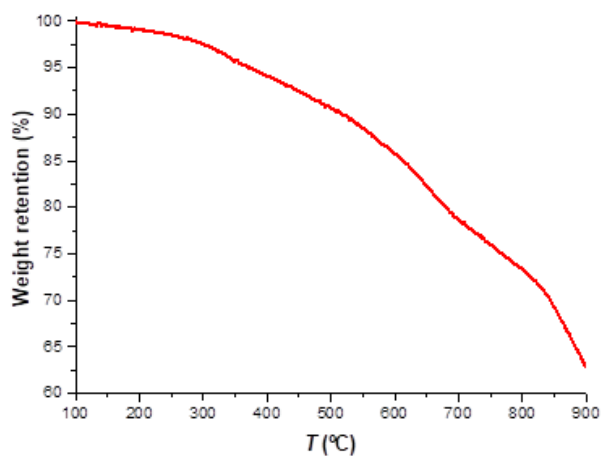


Figure 3.30. TGA profile of Dione-Ph-COF.

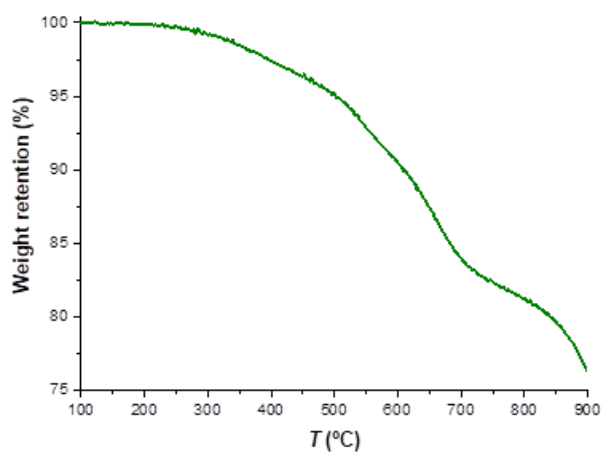


Figure 3.31. TGA profile of Dione-Naph-COF.

3.6.8 Scanning Electron Microscopy (SEM)

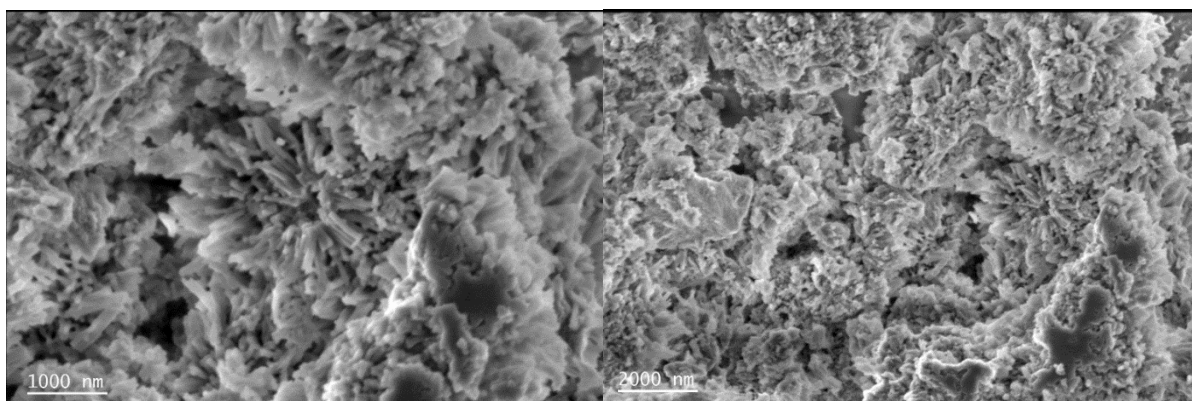


Figure 3.32. SEM image of Dione-Ph-COF.

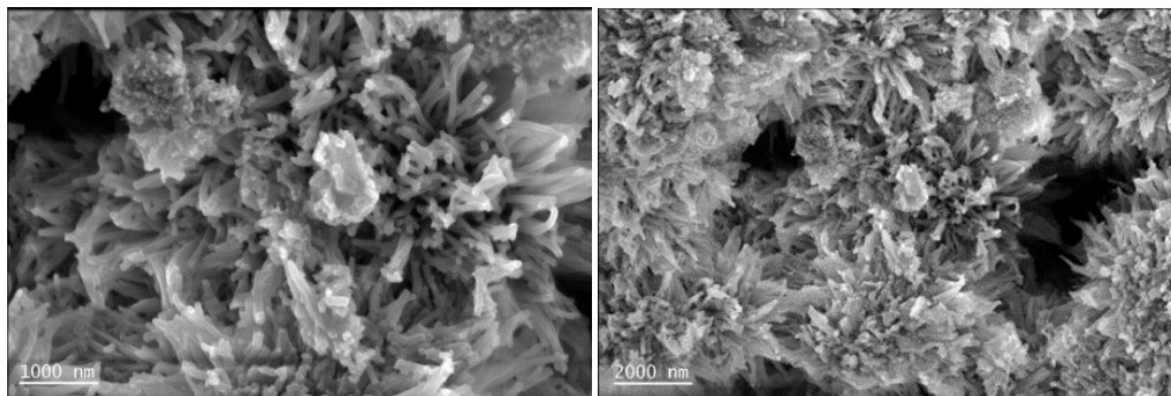


Figure 3.33. SEM image of Dione-Naph-COF

3.6.9 Optical Properties of the Dione Building Block

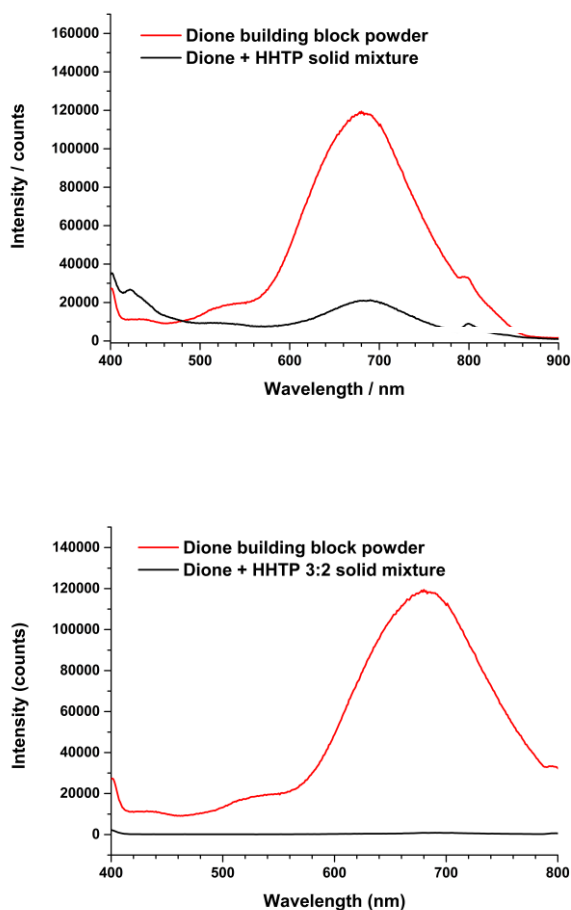


Figure 3.34. Top: PL spectra of dione building block 1 as powder (red), and a physical mixture of 1 and HHTP as powder (black). Bottom: PL spectra of dione building block 1 as powder (red), and a dropcasted mixture of 1 and HHTP as 2:3 slurry (black).

3.6.10 References

- (1) K. M. Williams, D. Lungerich, G. J. Bodwell, *Eur. J. Org. Chem.* **2016**, 5933–5936.
- (2) J. Merz, M. Dietz, Y. Vonhausen, F. Wöber, A. Friedrich, D. Sieh, I. Krummenacher, H. Braunschweig, M. Moos, M. Holzapfel, C. Lambert, T. B. Marder, *Chem. Eur. J.* **2020**, *26*, 438–453.
- (3) L. M. Salonen, D. D. Medina, E. Carbó-Argibay, M. G. Goesten, L. Mafra, N. Guldris, J. M. Rotter, D. G. Stroppa, C. Rodríguez-Abreu, *Chem. Commun.* **2016**, *52*, 7986–7989.

4. Building Blocks and COFs formed *in chorus*

This chapter is based on the following article:

Building Blocks and COFs formed *in chorus* – Three-component Synthesis of Pyrene-fused Azaacene Covalent Organic Framework Bulk and Films

Laura Frey,^{[a]‡} Orlando Oliveira,^{[b]‡} Soraia P. S. Fernandes,^[b,c] Krystal M. Cid-Seara,^[b,d] Roman Guntermann,^[a] Laura M. Salonen^{*[b,e]} and Dana D. Medina^{*[a]} *Manuscript in preparation.*

^[a] Department of Chemistry and Center for Nanoscience (CeNS), Ludwig-Maximilians University Munich (LMU), Butenandtstr. 5-11, D-81377, Munich, Germany, E-mail: dmepc@cup.uni-muenchen.de

^[b] International Iberian Nanotechnology Laboratory (INL), Avenida Mestre José Veiga, 4715-330, Braga, Portugal, E-mail: laura.salonen@inl.int

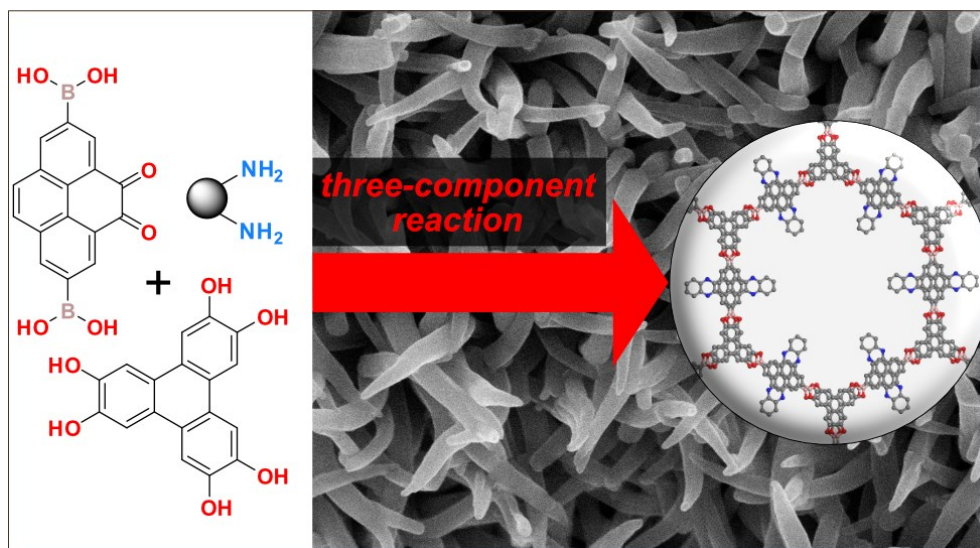
^[c] Associate Laboratory for Green Chemistry-Network of Chemistry and Technology (LAQV-REQUIMTE), Department of Chemistry, University of Aveiro, Campus Universitário de Santiago, 3810-193, Aveiro, Portugal

^[d] Department of Inorganic Chemistry, University of Vigo, Campus Universitário, As Lagoas-Marcosende, 36310, Vigo, Spain

^[e] CINBIO, Universidade de Vigo, Department of Organic Chemistry, 36310 Vigo, Spain.

‡ These authors contributed equally.

* Corresponding Authors.



4.1 Abstract

Covalent Organic Frameworks (COFs) are crystalline, highly ordered, porous polymers that are formed by the condensation of purely organic molecular building blocks. Typically, the functionalities of the resulting COF structures are pre-determined by the design and synthesis of functionalized monomers. The development of new synthetic methods is of high interest to advance progress in the field of COFs. Here, a simple one-step methodology for the functionalization of COFs, a three-component approach, is described where large fused aromatic systems could be formed starting from small components. Using the well-known Dione-COF, modification of the dione moieties with different amines forming pyrene fused azaacenes was possible with up to 100 % conversion yield. In this case, framework formation and functionalization happen simultaneously by adding the respective amines directly to the reaction mixture of the COF formation reaction. Moreover, using the non-epitaxy *in situ* approach, functional COF thin films featuring nanostructured surfaces were grown on different substrates. Strikingly, this methodology was applicable to the rather labile boronate-ester based COF, whereby framework formation was not hindered despite the use of strong nucleophiles. Using the three-component approach, gradual modification of the photophysical properties of Dione-COF was possible. Thereby, the main absorption maxima are red-shifted, with Aza-2Ph-COF exhibiting the absorption maximum with the shortest wavelength at around 420 nm, followed by Aza-Ph-COF at around 450 nm and lastly Aza-Naph-COF with an absorption maximum at around 480 nm, which was attributed to the extension of the π -conjugation.

4.2 Introduction

In the last years, covalent organic frameworks (COFs) have been explored as crystalline, highly ordered, porous polymers. COFs are formed mostly by reversible condensation reactions of organic building blocks, which allows for structural faults to be corrected throughout the process of framework formation and therefore, highly structurally defined products are within reach.^{1,2} During an in-plane polymerization process, two-dimensional polymers are assembled by weak π - π interactions (2D COFs) to form defined molecular stacks.³ In the case of a spatial polymerization process in 3D, covalently linked three-dimensional polymers (3D COFs) are accessible.⁴

COF materials are solely composed of organic building blocks thus, alternation of the frameworks' chemical and physical character is mainly achieved by using the diverse organic chemistry toolbox to make COFs talented agents tailored for a specific task. To design COFs, two main synthesis strategies are considered: (i) modification of building blocks, where the desired functional groups are installed at specific positions onto the building block prior to the COF assembly. Alternatively, (ii) applying a post-

synthetic modification (PSM) reaction scheme, where assembled frameworks bearing anchor groups react with chemical components to form a desired functional product.⁵⁻¹⁰ To select the most suitable strategy for realizing the framework, several factors are of critical importance. In a building block modification, solubility, shape and packing of the building blocks are vital aspects that synergistically contribute to the successful formation of a COF, whereas in a post-synthetic modification scheme, the frameworks' stability under the employed conditions and the target yield of functionalization are among the major aspects to be considered.

Considering advanced thin film applications, the synthesis of functional COFs as thin films is of high interest to enable their utilization for certain applications, such as sensing¹¹⁻¹³, separation^{14,15} and optoelectronics.^{16,17} For the latter, the mode of assembly of 2D COFs onto (semi)-conductive electrodes has been extensively investigated as means to control the alignment of electro-(photo)-active molecular segments onto a substrate. In this respect, several methods for thin film assembly with oriented COF crystallites have been introduced, i.e., the solvothermal *in situ* growth,¹⁸ interfacial syntheses,^{19,20} and continuous-flow synthesis²¹. Because these synthesis approaches are based on solution processing of bulk COF materials, they are subjected to the same limitations mentioned above.

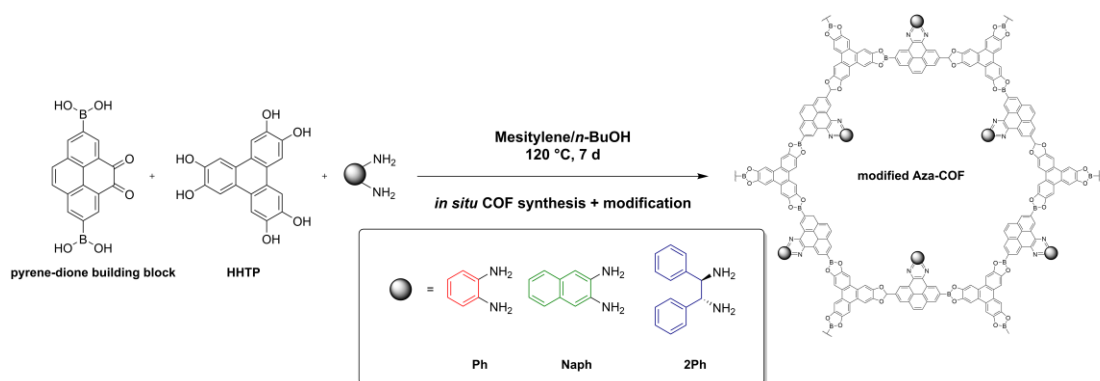
Linear acenes consisting of laterally fused benzenoid rings have been extensively studied owing to their intriguing properties related to energy conversion and optoelectronic applications. The most prominent of the latter are pentacene dimers which feature an efficient singlet fission process.²⁵ However, acenes are rather unstable materials, largely insoluble and their performance is highly dependent on their assembly. To address these issues, bulky side groups are typically installed on the molecular acene backbone endowing pentacene with a greater stability, solubility and largely directing their assembly. Substitutional nitrogen-doped acenes, termed azaacenes, are robust acene analogs featuring intriguing photophysical properties. Similar to pentacene, their use, processing and assembly is governed by their solubility. Therefore, the development of strategies where fused aromatics are assembled orderly as powders and films is of critical importance for their further characterization and utilization.²²⁻²⁶

Very recently, we demonstrated a PSM approach to form pyrene-fused azaacene assembled stacks, using two-dimensional Dione-COF as precursor to place these aromatic slabs in ordered stacks, with up to 33% conversion yield.²⁷ To boost the yield of the reaction and to expand the paradigm of COF synthesis, we now introduce a three-component synthesis approach where the framework and functionalities are forming simultaneously. This way, challenges such as solubility of the building block or compromising the COFs' order are overcome.²⁸ To take this one step further, the synthesis of COF films using such a simultaneous approach allows for the realization of functional frameworks as thin films which are challenging to be obtained with the available methodologies to date.

Using the chemistry of the well-known boronate ester Dione-COF²⁹, the pyrene-dione building block was reacted to form the respective azaacenes using different amines, namely *o*-phenylenediamine (Ph), 2,3-diaminonaphthalene (Naph) or (1*R*,2*R*)-(+)-1,2-diphenyl-ethylenediamine (2Ph) in the course of the COF formation. The resulting COF powders termed Aza-Ph-, Aza-Naph- and Aza-2Ph-COF feature large surface areas reaching up to 2390 m² g⁻¹ for Aza-Ph-COF and long-range order illustrated by nitrogen physisorption and PXRD analysis, respectively. Strikingly, the extent of the dione moiety conversion to respective azaacenes was assessed by liquid ¹H-NMR to be 100%. Scanning electron microscopy (SEM) revealed a wire-like morphology in the case of Aza-Ph- and Aza-Naph-COF and spherical morphology for Aza-2Ph-COF, and transmission electron microscopy (TEM) further confirmed the high crystallinity of the obtained Aza-COFs showing high order diffraction lines in the obtained electron diffraction patterns. All three COFs showed light absorption in the visible range up to the near infrared (NIR) region. Two photoluminescence (PL) emission bands were observed for Aza-Ph- and -Naph-COF, i.e., at 540 and 685 nm for Aza-Ph- and at 570 and 690 nm in case of Aza-Naph-COF, whereas Aza-2Ph-COF exhibits one emission band at 555 nm. Next, the synthesis of fused aromatic azaacene COF films was carried out. Here, highly oriented, thin films were successfully grown on different substrates for all three COFs with thicknesses ranging between 200-400 nm. Interestingly, SEM cross-sectional and top-view images showed nanostructured surfaces for the Aza-COFs. The crystallite orientation of the thin Aza-COF films was indicated by grazing-incidence diffraction (GID) analyses. UV-vis spectroscopy showed light absorption in the 300-500 nm wavelength range and only weak photoluminescence emission bands similar to the COF bulk powders.

4.3 Results and Discussion

4.3.1 Synthesis



Scheme 4.1. Schematic illustration of the three-component synthesis of modified Aza-COFs using *o*-phenylenediamine (Ph, red), 2,3-diaminonaphthalene (Naph, green) or (1*R*,2*R*)-(+)-1,2-diphenyl-ethylenediamine (2Ph, blue) as amines.

The dione building block and Dione-COF were synthesized following a previously reported procedure.²⁹ The three-component COFs synthesis was carried out under solvothermal conditions. Briefly, in a 6 mL culture tube dione and HHTP building blocks were suspended in mesitylene and *n*-butanol 1:1 v/v along with 2.1 equivalents of the respective amines (either *o*-phenylenediamine (Ph), 2,3-diaminonaphthalene (Naph) or (1*R*,2*R*)-(+)-1,2-diphenylethylenediamine (2Ph)). The culture tube was sealed and placed in a preheated oven for 7 days at 120 °C. After the given reaction time, a dark brown precipitate was obtained in all three cases. The powders were isolated by filtration and washed with anhydrous acetone (for further information see **Scheme 4.1** and appendix **section 4.2**).

The obtained powders were first analyzed by powder X-ray diffraction (PXRD). Notably, despite of the use of nucleophilic amines in the synthesis mixture, in all three cases highly crystalline boronate ester frameworks with a high degree of order were obtained indicating that the two condensation reactions namely boronate-ester and azaacene formation are orthogonal reactions (**Figure 4.1a**). The PXRD patterns reveal prominent reflections at $2\theta = 2.7^\circ, 4.7^\circ, 5.4^\circ, 7.1^\circ, 9.5^\circ$ and $26.1\text{--}26.6^\circ$, corresponding to *hkl* (100), (110), (200), (210), (220), and (001) in agreement with the simulated PXRD patterns and the previously reported reflections for Dione-COF.²⁹ For Dione-COF a reflection associated with the interlayer distance at $26.3^\circ 2\theta$ was observed, corresponding to a π -stacking distance of about 3.4 Å. For the modified Aza-COFs reflections at 26.1, 26.2 and $26.6^\circ 2\theta$ were obtained for Aza-Ph, Aza-Naph- and Aza-2Ph-COF, respectively, corresponding to π -stacking distances of 3.4 Å in the case of Aza-Ph- and Aza-Naph-COF and 3.3 Å for Aza-2Ph-COF.

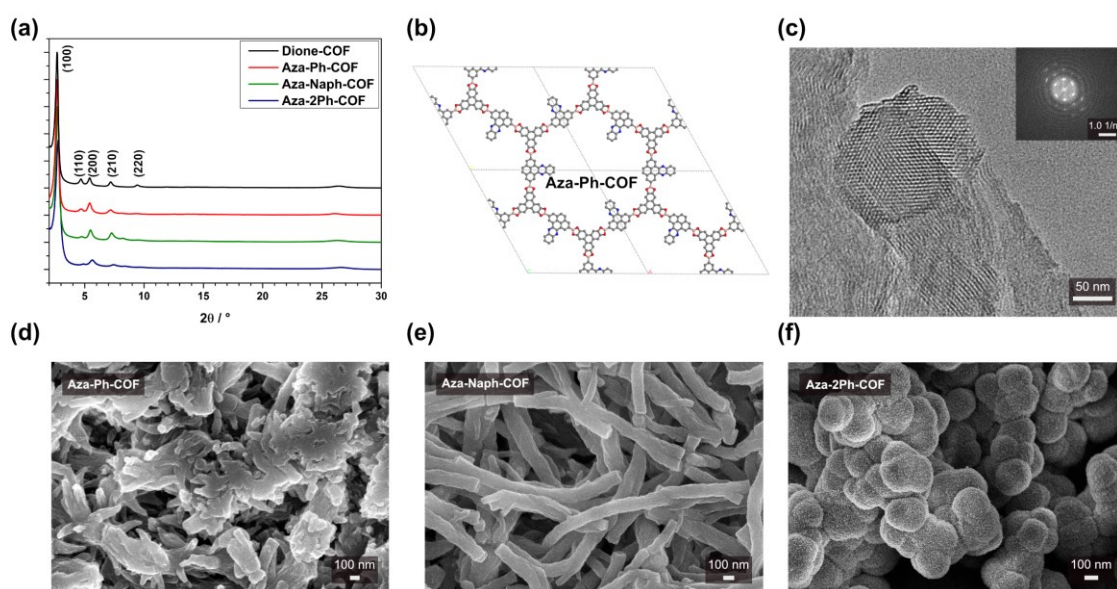


Figure 4.1. (a) PXRD patterns of Dione-COF, Aza-Ph-, Aza-Naph-COF and Aza-2Ph-COF. (b) Schematic representation of one layer of fully converted Aza-Ph-COF-. (c) TEM image of Aza-Ph-COF. The inset shows an electron diffraction pattern. (d), (e) and (f) SEM images of Aza-Ph-COF, Aza-Naph- and Aza-2Ph-COF powders, respectively.

A close look at the diffraction patterns revealed several interesting differences between the Dione-COF and the Aza-COFs. Primarily, the relative reflection intensity corresponding to the (110) and (200) Miller-planes changes upon the lateral extension of pyrene dione's aromatic system. For the non-modified Dione-COF, (110) and (200) show similar scattering intensities. Upon lateral expansion of pyrene dione with Ph, Naph or 2Ph, the intensity of hkl (110) is largely diminished compared to hkl (200). This is attributed to the introduction of scattering elements into the pore along the 200 plane (Figure 4.10). Such pore filling can be related to a successful conversion of dione moieties to their azaacene derivatives.³⁰ Additionally, the broad and weak reflection at around $26^\circ 2\theta$, corresponding to the 001 plane and associated with the interlayer distance, is slightly shifted in the different Aza-COF diffraction patterns. Interestingly, the position of the 001 reflection of the more sterically demanding azaacene COF, Aza-2Ph-COF, occurs at higher diffraction angles.

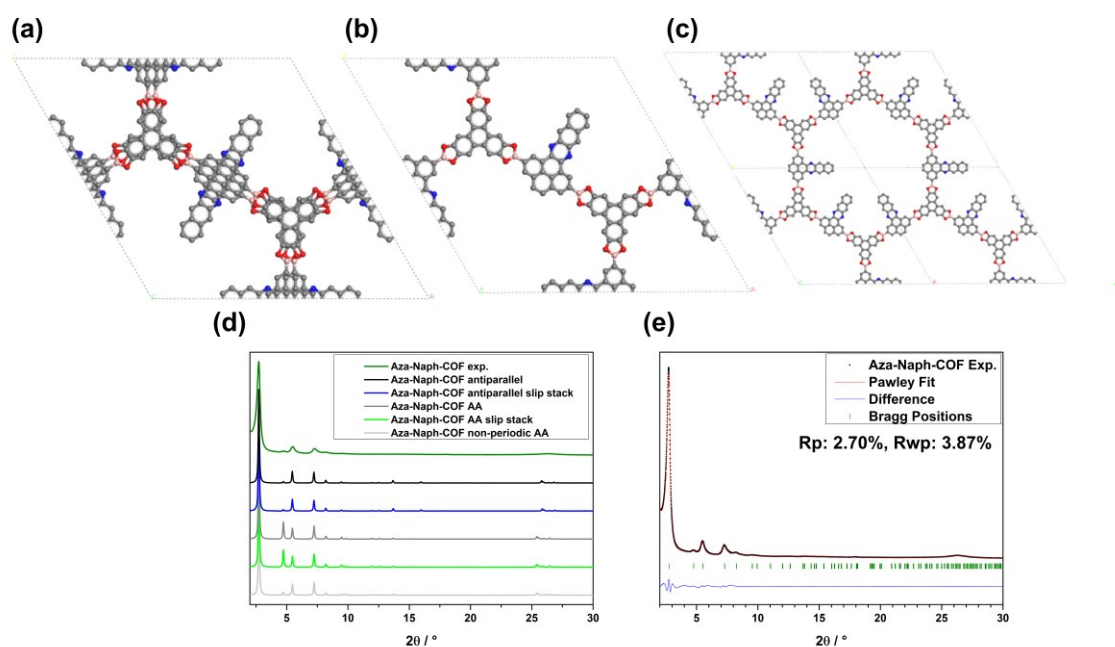


Figure 4.2. (a) and (b) View of one unit cell for an AA and antiparallel layer arrangement using high symmetries for Aza-Naph-COF, respectively. (c) View of four unit cells for a non-periodic AA arrangement for Aza-Naph-COF using $P1$ symmetry. (d) Experimentally obtained and the simulated PXRD patterns for different layer arrangements for Aza-Naph-COF. (e) Experimental PXRD pattern (black dots) of Aza-Naph-COF. Pawley refinement (red line), difference plot between the experimental data and the Pawley refined PXRD pattern (blue line), Bragg positions are indicated by green ticks.

To relate these observations to a COF layer packing and ultimately to shed light on the overall COF structure, we turned to COF structure and PXRD modeling. Using the Materials Studio software package (Accelrys Inc.), the structure simulations and geometry optimization were carried out using the Forcite module employing the universal force field. In the case of asymmetric building blocks such as pyrene-dione or -azaacenes, there are three general modes of building block arrangement in successive layers i.e., (i) fully overlapped building blocks, AA, (ii) antiparallel, AP, where the moieties alternate between successive layers, and (iii) random distribution, namely a mixture of AA and AP structures. To shed

light on the COF layer arrangements, two structure models for each COF were simulated corresponding to possible packing scenarios (**Figure 4.2** and **Figure 4.11-4.12**). For fully overlapping and antiparallel planar Aza-Ph- and -Naph-COFs, $P-6_2m$ and $P6_3cm$ space groups of the hexagonal crystal system were employed, respectively.^[27] To simulate an AA layer arrangement for Aza-2Ph-COF, $P1$ was found to be suitable to describe the rotating phenyl groups out of plane. The calculated PXRD patterns obtained for the respective COFs were compared to those obtained experimentally (**Figure 4.2** for Aza-Naph-COF and **Figure 4.11-4.12** for Aza-Ph- and Aza-2Ph-COF, respectively). In both assembly models, the calculated PXRD reproduces the observed diffraction pattern regarding reflection positions at low angles (**Figure 4.2**, **Figure 4.11-4.12**). Interestingly, the different models indicate different relative reflection intensities of the 110 and 200 planes. Here, the AP model for all COFs corresponds well with the weakening of the 110 reflection upon pore occupancy, particularly for Aza-2Ph- and Aza-Naph-COFs. Employing hexagonal symmetry space groups for AA models results in a systematic and even distribution of the azaacene moieties pointing to neighboring pores. Thereby, every pore consists of three azaacene moieties. To simulate a different distribution of the azaacene in the pores, COF structures with AA layer assembly where pores consist of three adjacent moieties were simulated (**Figure 4.2e**). Here, the resulting calculated PXRD patterns reproduce well the relative reflection intensity obtained in the experimental pattern, particularly in the case of Aza-2Ph- and Aza-Ph-COFs. Other distribution schemes failed to reproduce the experimentally obtained diffraction pattern.

At higher angles, the different models of Aza-2Ph-COF show different positions of the rather weak reflection related to interlayer distance. Here, the AA model indicates interlayer distances of 3.5, 3.5 and 3.7 Å, whereas the AP model corresponds to shorter interlayer distances of about 3.4, 3.4 and 3.3 Å, for Aza-Ph-, Aza-Naph- and Aza-2Ph-COF, respectively, in good agreement with the experimental PXRD patterns. The AP model allows for compromising between favorable dispersive interaction and electrostatic repulsion. Accordingly, these observations indicate that the probable average structure of the Aza-COF consists of mainly antiparallel pyrene azaacenes guided by the asymmetry of the pyrene dione precursor. Notably, at the level of theory employed here, small deviations from these models in the form of slipped layers or unidirectional assembly cannot be accounted for. Therefore, for further characterization of the COFs we utilized the antiparallel structure model of high symmetry. In the next step, the obtained unit cell parameters were refined using the Pawley method according to the observed PXRD (**Figure 4.14**). Thereby, unit cell parameters of $a = b = 37.0$ Å, $c = 7.0$ Å, $\alpha = \beta = 90^\circ$ and $\gamma = 120^\circ$ were obtained for Aza-Ph- and Aza-Naph-COF and $a = b = 36.8$ Å, $c = 7.0$ Å, $\alpha = \beta = 90^\circ$ and $\gamma = 120^\circ$ for Aza-2Ph-COF, which agrees well with the unit cell parameters of Dione-COF.

To confirm the extent of the conversion of the dione moiety to the respective azaacene, the COFs were hydrolyzed to the building blocks in DMSO- d_6 by addition of 3 drops of D₂O and analyzed by ¹H NMR spectroscopy (**Figure 4.5-4.7**). After hydrolysis in all three cases, the complete absence of the two

doublets at 8.73 and 8.69 ppm and the singlet at 8.02 ppm from the dione building block evidence the complete reaction with the respective amines. The relation between the integration of the singlet at 7.63 ppm, corresponding to the aromatic C–H of the HHTP building block, and the signals attributed to the different azaacene moieties, indicates a ratio of 2:3 of the HHTP building block and the different azaacene moieties, respectively, as is expected for hexagonal frameworks.

Importantly, in all three cases we found complete conversion of the dione moiety, showing that the formation of large area aromatics is possible simultaneously with the formation of the backbone. In the case of Aza-Ph- and Aza-Naph-COF, the dione moieties were fully converted to the respective azaacenes. In the case of Aza-2Ph-COF, a mixture of products was evident from the ^1H NMR spectrum. To gain insight into the obtained products, the model system of the Aza-2Ph moiety was prepared by reacting the dione building block with 2Ph in DMSO at 100 °C for 7 days. The resulting precipitate was a mixture of products, as evident from the ^1H NMR spectrum (**Figure 4.9**).

To shed light on the reactivity of the dione moiety, we studied the reaction of the dione building block with *o*-phenylenediamine in the presence of catechol as a mimic of HHTP in a mixture of deuterated mesitylene and deuterated *n*-butanol (1:1 *v/v*) (**Figure 4.8**). Interestingly, no reaction was seen at room temperature when catechol (4 equiv.) was added to dione building block (**Figure 4.8, middle**). However, after subsequent addition of *o*-phenylenediamine (2.2 equiv.) at room temperature, the ^1H NMR spectrum evidenced direct conversion of the dione to the corresponding azaacene in ~34% yield (**Figure 4.8, bottom**). The high reaction rate even at room temperature suggests that in the case of the three-component COF synthesis, the azaacene formation occurs more quickly than the formation of the COF, which indicates that mainly azaacene compounds are involved in the COF assembly rather than the dione building block.

The success of the condensation reaction was further analyzed using Fourier-transform infrared (FTIR) spectroscopy. For Dione-COF, an absorption band is clearly observed at $\sim 1668\text{ cm}^{-1}$ corresponding to the carbonyl group stretching (**Figure 4.15**). In contrast, this band is not present in the spectra of Aza-Ph-, Aza-Naph- and Aza-2Ph-COF, further supporting a full conversion of the dione moieties to the respective pyrazaacenes. Thermogravimetric analysis (TGA) under synthetic air flow showed that all three modified Aza-COFs are thermally stable at temperatures up to 500 °C. At 500 °C a significant weight loss was observed corresponding to a structural degradation of the COF materials (**Figure 4.18**).

Scanning electron microscopy (SEM) analysis of the COF powders revealed that Dione-COF features a wire-like morphology²⁹ which is maintained upon modification of the framework in the case of Aza-Ph- and Aza-Naph-COF (**Figure 4.1d,e**). Only in the case of Aza-2Ph-COF the morphology changes to sphere-like crystallites (**Figure 4.1f**). Transmission electron microscopy (TEM) analysis of the COFs further supports the highly crystalline nature of the COFs (**Figure 4.1c, 4.19**). Projections along the *c*-

axis reveal the expected honeycomb structure of the COFs in all cases. Moreover, electron diffraction patterns of the obtained images confirm the formation of highly crystalline COFs, whereas high order diffraction lines for a single crystallite are visible (**Figure 4.1c, 4.19**).

The impact of the modification on the pore accessibility of the frameworks was analyzed using nitrogen sorption at 77K (**Figure 4.16**). Thereby, for Aza-Ph-COF a type IV isotherm (**Figure 4.16**, red curve) was obtained which is characteristic for mesoporous materials with two steep and well-defined nitrogen uptakes at relatively low partial pressure ($p/p_0 < 0.16$ and up to $567 \text{ cm}^3 \text{ g}^{-1}$). For Aza-Naph- and Aza-2Ph-COF, type I sorption profiles are obtained which are characteristic for microporous materials (**Figure 4.16**, green and blue curve, respectively). In the isotherms, sharp nitrogen uptakes at low partial pressure are obtained ($p/p_0 < 0.12$ and up to $366 \text{ cm}^3 \text{ g}^{-1}$ for Aza-Naph- and $p/p_0 < 0.11$ and up to $195 \text{ cm}^3 \text{ g}^{-1}$ for Aza-2Ph-COF, respectively). BET surface areas of $2197 \text{ m}^2 \text{ g}^{-1}$, $1375 \text{ m}^2 \text{ g}^{-1}$ and $804 \text{ m}^2 \text{ g}^{-1}$ were obtained for Aza-Ph-, Naph-Aza- and Aza-2Ph-COF, respectively. As expected, the BET surface area of Aza-Ph-COF is larger than the ones obtained for Aza-Naph- and Aza-2Ph-COF, in agreement with the size of the linker. Pore size distributions were calculated using the QSDFT model for cylindrical pores (adsorption branch). Thereby, pore sizes of 2.7 nm, 2.0 nm and 2.2 nm were obtained for Aza-Ph-, Aza-Naph- and Aza-2Ph-COF, respectively which are in good agreement with the simulations (**Figure 4.17**).

4.3.2 Oriented Thin Films of Fully Modified Aza COFs

To study the photophysical properties, oriented COF thin films of Dione-COF as well as the derived Aza-COFs were synthesized on various substrates. The synthesis was carried out in glass vessels equipped with a Teflon-substrate holder using the non-epitaxy *in situ* approach and the solvothermal synthesis protocol for the Dione-COF and the newly developed three-component synthesis to obtain the Aza-COFs. To this end, the substrates were positioned and immersed horizontally using the Teflon substrate holder into the reaction vessel, charged with the appropriate reactive precursor solution (including 2.1 equivalents of the respective diamine for the synthesis of the derived Aza-COF thin films). Subsequently, the reaction vessel was heated to $120 \text{ }^\circ\text{C}$ for 6 days. After removal from the reaction mixture, the substrate was thoroughly washed with anhydrous acetone and dried under a stream of nitrogen. Thereby, homogeneous and shimmering layers (**Figure 4.3d-f, insets**) were obtained on top of the substrates. SEM cross-section and top-view images showed that a homogeneous coverage of the substrate was obtained with nanostructured surfaces consisting of individual, rod-shaped crystallites preferentially oriented orthogonally to the surface (**Figure 4.3d-i, 4.20**). The crystallinity and crystal orientation were further confirmed using grazing incidence wide-angle X-ray scattering (GIWAXS) (**Figure 4.3a-c, 4.20**). For all three modified COF thin films and the Dione-COF thin film, strong distinct reflections at $q_y = 1.9, 3.4, 3.9, 5.1, 6.8 \text{ nm}^{-1}$ and $q_z = 18.6 \text{ nm}^{-1}$ were obtained corresponding to *hkl* (100), (110), (200), (210), (220), and (001). The q values obtained by data-reduction to 1D-plots match those obtained for the bulk powder XRD patterns. The GIWAXS data of all the studied COFs confirm the

preferential orientation of COF crystallites on the substrate with the [001] axis being oriented orthogonally to the substrate (**Figure 4.3a-c**). Importantly, the obtained 1D plots of the Aza-COF films show similar intensity ratios of the (110) and (200) planes upon modification, strongly indicative of the successful azaacene formation.

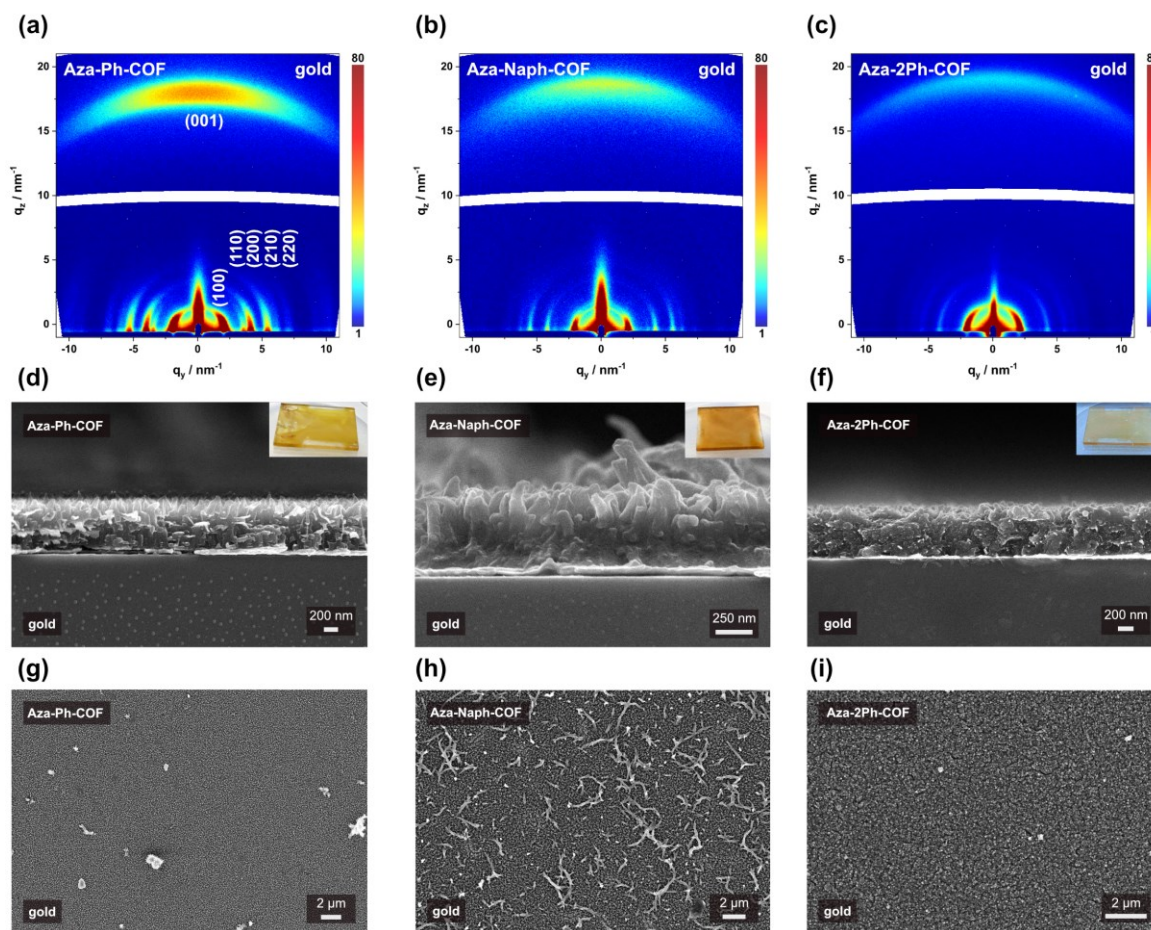


Figure 4.3. (a), (b) and (c) GIWAXS 2D patterns of Aza-Ph-COF, Aza-Naph- and Aza-2Ph-COF thin films grown on gold-coated glass substrates, respectively. (d,g), (e,h) and (f,i) SEM cross-section and top-view images of Aza-Ph-COF, Aza-Naph- and Aza-2Ph-COF thin films grown on gold-coated glass substrates, respectively. The insets show macroscopic photographs of Aza-Ph-, Aza-Naph- and Aza-2Ph-COF thin films on quartz substrates.

4.3.3 Photophysical Properties

The effect of the functionalization on the photophysical properties of the respective COF bulk powders and thin films was analyzed using UV-vis and photoluminescence (PL) spectroscopies. The main absorption bands are located in the UV and blue spectral regions for Aza-Ph-, Aza-Naph- and Aza-2Ph-COF bulk powders (**Figure 4.4**). Further, for Aza-2Ph-COF a second very broad absorption band is observed reaching the near-infrared region. The main absorption maxima are red-shifted with respect to each other with Aza-2Ph-COF exhibiting the absorption maximum with the shortest wavelength at around 420 nm, followed by Aza-Ph-COF at around 450 nm and lastly Aza-Naph-COF with an absorption maximum at around 480 nm. This red-shift in the absorption maxima is attributed to the

extension of the π -conjugation in this series of COFs. A similar trend was observed for the absorbance measurements of the respective thin films on quartz substrates (**Figure 4.21**) indicating a successful conversion of the dione-moieties in thin films using the newly developed three-component approach.

Steady-state PL was measured for the three different COFs at an excitation wavelength of 378 nm. Aza-Ph- and Aza-Naph-COF feature two emission bands which are red-shifted respectively, in agreement with the extension of the π -conjugation and the absorption profile. In contrast to the planar Aza-COFs (Aza-Ph- and Aza-Naph-COF), in the case of Aza-2Ph-COF, one distinct emission band at around 555 nm was observed. Furthermore, a drastic change in PL intensity is evident for the different COFs where Aza-Ph- exhibits the highest intensity and Aza-2Ph-COF features the weakest PL emission. These findings are particularly interesting because the pristine Dione-COF and the partially converted Dione-COF obtained by PSM are not PL active (**Figure 4.22**). However, in the case of fully converted Aza-COFs PL is observed.

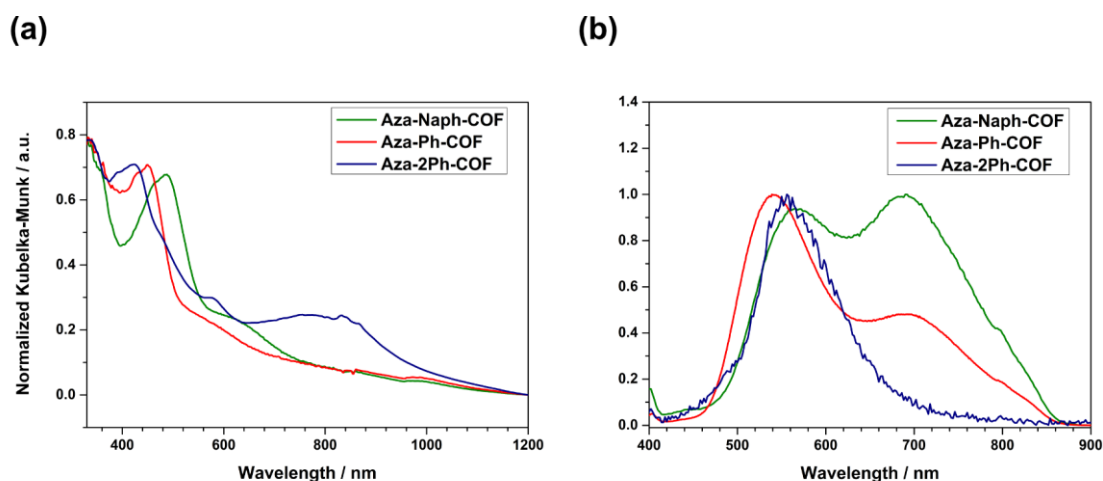


Figure 4.4. (a) Normalized Kubelka-Munk absorption spectra of Aza-Ph-COF (red), Aza-Naph- (green) and Aza-2Ph-COF (blue). (b) Normalized PL emission spectra of Aza-Ph- (red), Aza-Naph-COF (green) and Aza-2Ph-COF (blue).

4.4 Conclusion

Summarizing, a one-pot, three-component methodology for the functionalization of covalent organic framework bulk and thin films has been discovered. Here, small-sized building blocks are included in the reaction mixture which react exclusively at particular sites to form large building blocks and frameworks within a similar time frame. Using the well-known di-boronic acid pyrene dione, linear amines and catechol building blocks, COFs exclusively built up from pyrene azaacenes corresponding to a 100 % conversion yield of dione moieties, termed Aza-COFs, are formed. Upon the inclusion of amines in the reaction mixture, an extension of the aromatic system of the pyrene dione building block

is obtained, where aromatization is considered to be one of the driving forces for amines to react exclusively with diones in the three-component reaction. Remarkably, this methodology is suitable to construct the fragile boronate-ester based COFs, where catecholes and boronic acids react undisturbed despite the presence of strong competing amine nucleophiles. Generally, the way COF building blocks interact between successive layers is one of the most urgent matters to achieve a fundamental understanding of charge carrier dynamics in such systems. Here, the pyrene dione building block yields asymmetric pyrene azaacenes where fully overlapped or anti parallel stacking scenarios are considered. Powder X-ray diffraction analysis of the obtained COFs implies that Aza-COFs comprise mainly antiparallel-aligned pyrene azaacenes in the successive layers. Furthermore, the newly developed methodology was implemented to direct thin film synthesis where preferentially oriented and crystalline Aza-COF thin films are obtained by the one-pot three-component synthesis. The photophysical properties of the Aza-COFs were determined. In line with the extension of the π -conjugation, for Aza-2Ph- to Aza-Ph- and Aza-Naph-COF a gradual red-shift of the absorption maximum is evident. In conclusion, the above approach represents a versatile addition to the toolkit of COF bulk and thin film synthesis methodologies.

4.5 References

- (1) Côté, A. P.; Benin, A. I.; Ockwig, N. W.; O’Keeffe, M.; Matzger, A. J.; Yaghi, O. M. Porous, Crystalline, Covalent Organic Frameworks. *Science* **2005**, *310*, 1166–1170.
- (2) Frey, L.; Jarju, J. J.; Salonen, L. M.; Medina, D. D. Boronic-acid-derived covalent organic frameworks: from synthesis to applications. *New J. Chem.* **2021**, *45*, 14879–14907.
- (3) Mähringer, A.; Medina, D. D. Taking stock of stacking. *Nature Chemistry* **2020**, *12*, 985–987.
- (4) El-Kaderi, H. M.; Hunt, J. R.; Mendoza-Cortés, J. L.; Côté, A. P.; Taylor, R. E.; O’Keeffe, M.; Yaghi, O. M. Designed Synthesis of 3D Covalent Organic Frameworks. *Science* **2007**, *316*, 268–272.
- (5) Zhang, X.; Li, G.; Di Wu; Zhang, B.; Hu, N.; Wang, H.; Liu, J.; Wu, Y. Recent advances in the construction of functionalized covalent organic frameworks and their applications to sensing. *Biosens. Bioelectron* **2019**, *145*, 111699.
- (6) Segura, J. L.; Royuela, S.; Mar Ramos, M. Post-synthetic modification of covalent organic frameworks. *Chem. Soc. Rev.* **2019**, *48*, 3903–3945.
- (7) Huang, N.; Krishna, R.; Jiang, D. Tailor-Made Pore Surface Engineering in Covalent Organic Frameworks: Systematic Functionalization for Performance Screening. *J. Am. Chem. Soc.* **2015**, *137*, 7079–7082.
- (8) Tian, Y.; Cheng, J.; Han, X.; Li, Y.; Yang, T.; Chen, M.-L.; Ma, J.; Wang, J.-H. Novel thiol-functionalized covalent organic framework-enabled ICP-MS measurement of ultra-trace metals in complex matrices. *J. Anal. At. Spectrom.* **2022**, *37*, 157–164.

- (9) Wang, H.; Zhao, L.; Tang, X.; Lv, L.-P.; Sun, W.; Wang, Y. Functionalized Graphene Quantum Dots Modified Dioxin-Linked Covalent Organic Frameworks for Superior Lithium Storage. *Chem. Eur. J.* **2022**, *28*, e202103901.
- (10) Kandambeth, S.; Dey, K.; Banerjee, R. Covalent Organic Frameworks: Chemistry beyond the Structure. *J. Am. Chem. Soc.* **2019**, *141*, 1807–1822.
- (11) Ascherl, L.; Evans, E. W.; Gorman, J.; Orsborne, S.; Bessinger, D.; Bein, T.; Friend, R. H.; Auras, F. Perylene-Based Covalent Organic Frameworks for Acid Vapor Sensing. *J. Am. Chem. Soc.* **2019**, *141*, 15693–15699.
- (12) Jhulki, S.; Evans, A. M.; Hao, X.-L.; Cooper, M. W.; Feriante, C. H.; Leisen, J.; Li, H.; Lam, D.; Hersam, M. C.; Barlow, S.; *et al.* Humidity Sensing through Reversible Isomerization of a Covalent Organic Framework. *J. Am. Chem. Soc.* **2020**, *142*, 783–791.
- (13) Wang, Y.; Zhao, Z.; Li, G.; Yan, Y.; Hao, C. A 2D covalent organic framework as a sensor for detecting formaldehyde. *J. Mol. Model.* **2018**, *24*, 153.
- (14) Cui, W.-R.; Zhang, C.-R.; Jiang, W.; Li, F.-F.; Liang, R.-P.; Liu, J.; Qiu, J.-D. Regenerable and stable sp² carbon-conjugated covalent organic frameworks for selective detection and extraction of uranium. *Nat. Commun.* **2020**, *11*, 436.
- (15) Khan, N. A.; Zhang, R.; Wu, H.; Shen, J.; Yuan, J.; Fan, C.; Cao, L.; Olson, M. A.; Jiang, Z. Solid–Vapor Interface Engineered Covalent Organic Framework Membranes for Molecular Separation. *J. Am. Chem. Soc.* **2020**, *142*, 13450–13458.
- (16) Calik, M.; Auras, F.; Salonen, L. M.; Bader, K.; Grill, I.; Handloser, M.; Medina, D. D.; Dogru, M.; Löbermann, F.; Trauner, D.; *et al.* Extraction of photogenerated electrons and holes from a covalent organic framework integrated heterojunction. *J. Am. Chem. Soc.* **2014**, *136*, 17802–17807.
- (17) Guo, J.; Xu, Y.; Jin, S.; Chen, L.; Kaji, T.; Honsho, Y.; Addicoat, M. A.; Kim, J.; Saeki, A.; Ihee, H.; *et al.* Conjugated organic framework with three-dimensionally ordered stable structure and delocalized π clouds. *Nat. Commun.* **2013**, *4*, 2736.
- (18) Medina, D. D.; Werner, V.; Auras, F.; Tautz, R.; Dogru, M.; Schuster, J.; Linke, S.; Döblinger, M.; Feldmann, J.; Knochel, P.; *et al.* Oriented Thin Films of a Benzodithiophene Covalent Organic Framework. *ACS Nano* **2014**, *8*, 4042–4052.
- (19) Zhang, B.; Song, X.; Li, Y.; Li, Y.; Peng, Z.; Ye, L.; Chen, L. 2D covalent organic framework thin films via interfacial self-polycondensation of an A₂B₂ type monomer. *Chem. Commun.* **2020**, *56*, 3253–3256.
- (20) Park, S.; Liao, Z.; Ibarlucea, B.; Qi, H.; Lin, H.-H.; Becker, D.; Melidonie, J.; Zhang, T.; Sahabudeen, H.; Baraban, L.; *et al.* Two-Dimensional Boronate Ester Covalent Organic Framework Thin Films with Large Single Crystalline Domains for a Neuromorphic Memory Device. *Angew. Chem. Int. Ed.* **2020**, *59*, 8218–8224.
- (21) Bisbey, R. P.; DeBlase, C. R.; Smith, B. J.; Dichtel, W. R. Two-dimensional Covalent Organic Framework Thin Films Grown in Flow. *Journal of the American Chemical Society* **2016**, *138*, 11433–11436.
- (22) Ahrens, L.; Butscher, J.; Brosius, V.; Rominger, F.; Freudenberg, J.; Vaynzof, Y.; Bunz, U. H. F. Azaacene Dimers: Acceptor Materials with a Twist. *Chem. Eur. J.* **2020**, *26*, 412–418.

- (23) Feng, X.; Iwanaga, F.; Hu, J.-Y.; Tomiyasu, H.; Nakano, M.; Redshaw, C.; Elsegood, M. R. J.; Yamato, T. An Efficient Approach to the Synthesis of Novel Pyrene-Fused Azaacenes. *Organic Letters* **2013**, *15*, 3594–3597.
- (24) Wang, Q.; Gao, W.; Chen, Y.; Wang, X.; Zeng, J.; Liu, Y.; Ran, H.; Hu, Z.; Bai, J.; Feng, X.; *et al.* Pyrene-fused Dibenzoozatetracenes: Synthesis, Crystal Structures, Photophysical Properties and their Morphologies. *Asian J. Org. Chem.* **2021**, *10*, 233–240.
- (25) Li, Z.; Feng, X.; Zou, Y.; Zhang, Y.; Xia, H.; Liu, X.; Mu, Y. A 2D azine-linked covalent organic framework for gas storage applications. *Chem. Commun.* **2014**, *50*, 13825–13828.
- (26) Yazdani, H.; Hooshmand, S. E.; Varma, R. S. Covalent organic frameworks and multicomponent reactions: an endearing give-and-take relationship. *Org. Chem. Front.* **2022**, *9*, 4178–4191.
- (27) Fernandes, S. P.S.; Frey, L.; Cid-Seara, K. M.; Oliveira, O.; Guldris, N.; Carbó-Argibay, E.; Rodríguez-Abreu, C.; Kolen'ko, Y. V.; Silva, A. M.S.; Medina, D. D.; *et al.* A post-synthetic modification strategy for the synthesis of pyrene-fused azaacene covalent organic frameworks. *Micropor. Mesopor. Mat.* **2022**, 112162.
- (28) Li, X.-T.; Zou, J.; Wang, T.-H.; Ma, H.-C.; Chen, G.-J.; Dong, Y.-B. Construction of Covalent Organic Frameworks via Three-Component One-Pot Strecker and Povarov Reactions. *J. Am. Chem. Soc.* **2020**, *142*, 6521–6526.
- (29) Salonen, L. M.; Medina, D. D.; Carbó-Argibay, E.; Goesten, M. G.; Mafra, L.; Guldris, N.; Rotter, J. M.; Stroppa, D. G.; Rodríguez-Abreu, C. A supramolecular strategy based on molecular dipole moments for high-quality covalent organic frameworks. *Chem. Commun.* **2016**, *52*, 7986–7989.
- (30) Lohse, M. S.; Rotter, J. M.; Margraf, J. T.; Werner, V.; Becker, M.; Herbert, S.; Knochel, P.; Clark, T.; Bein, T.; Medina, D. D. From benzodithiophene to diethoxy-benzodithiophene covalent organic frameworks – structural investigations. *CrystEngComm* **2016**, *18*, 4295–4302.

4.6 Appendix

4.6.1 Materials and Methods

General: Commercial reagents and solvents were obtained from diverse suppliers and used as received, with exception of pyrene, which was recrystallized prior to use from a mixture of CH₂Cl₂/hexane. Reaction progresses were monitored by analytical thin-layer chromatography (TLC) on ALUGRAM® Xtra SIL G/UV254 aluminium sheets from Macherey Nagel. TLC plates were rendered visible by exposure to ultraviolet light. All purifications were carried out under flash-chromatographic conditions on silica gel (60 Å, 40-63 µm, 230-400 mesh, Macherey Nagel).

Nuclear magnetic resonance (NMR) spectra were recorded using Bruker AV 400 and AV 400 TR spectrometers. Chemical shifts are expressed in parts per million (δ scale) and are calibrated using residual (undeuterated) solvent peaks as an internal reference (¹H-NMR: CDCl₃: 7.26, DMSO-d₆: 2.50; ¹³C-NMR: CDCl₃: 77.16, DMSO-d₆: 39.52). Data for ¹H NMR spectra are reported in the following way: chemical shift (δ ppm) (multiplicity, coupling constant/ Hz, integration). Multiplicities are reported as follows: s = singlet, d = doublet, t = triplet, q = quartet, m = multiplet, or combinations thereof.

Powder X-ray diffraction (PXRD) patterns were measured on a Bruker D8 Advance diffractometer in Bragg-Brentano geometry equipped with a Cu K α source (0.1 mm divergence slit, knife edge air scatter screen) and a LynxEye detector. K β radiation was attenuated with a 0.0125 mm Ni filter.

The **structure models of the COFs** were constructed using the Accelrys Materials Studio software package. For each COF the highest possible symmetry was applied. Structure refinements using the Pawley method were carried out as implemented in the Reflex module of the Materials Studio software.

2D grazing-incidence wide angle X-ray scattering (GIWAXS) data were recorded with an Anton Paar SAXSpoint 2.0 system equipped with a Primux 100 microCu K α source and a Dectris EIGER R 1M 2D detector. The COF films were positioned at a sample-detector distance of 140 mm and were measured with an incidence angle of 0.2°.

Nitrogen sorption isotherms were recorded with Quantachrome Autosorb 1 and Autosorb iQ instruments at 77 K. The samples were outgassed for 24 h at 120 °C under high vacuum prior to the measurements. Surface areas of the obtained powders were estimated by the multipoint Brunauer-Emmett-Teller (BET) method using ASIQwin™ software. Pore size distributions were calculated using quenched solid density functional theory (QSDFT) model with a carbon kernel for cylindrical pores (N₂ at 77 K on carbon, adsorption branch).

Infrared (IR) spectra were recorded on a Bruker VERTEX 80v FT-IR spectrometer in ATR mode. IR data were background corrected and reported in wavenumbers (cm^{-1}).

Thermogravimetric analysis (TGA) measurements were performed on a Netzsch Jupiter ST 499 C instrument equipped with a Netzsch TASC 414/4 controller. The samples were heated from room temperature to $900\text{ }^{\circ}\text{C}$ under a synthetic air flow (25 ml min^{-1}) at a heating rate of 10 K min^{-1} .

Scanning electron microscopy (SEM) images were recorded with a FEI Helios NanoLab G3 UC scanning electron microscope equipped with a field emission gun operated at 3-5 kV.

Transmission electron microscopy (TEM) was performed on an FEI Titan Themis instrument equipped with a field emission gun operated at 300 kV.

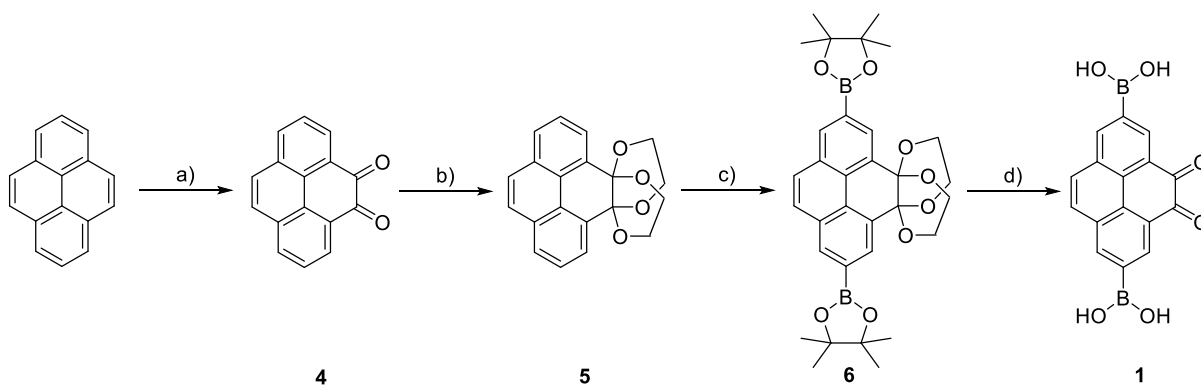
UV-VIS-NIR spectra were recorded on a Perkin-Elmer Lambda 1050 spectrometer equipped with a 150 mm InGaAs integrating sphere. **Diffuse reflectance spectra** were collected with a Praying Mantis (Harrick) accessory and were referenced to barium sulfate powder as white standard. The specular reflection of the sample surface was removed from the signal using apertures that allow only light scattered at angles $> 20^{\circ}$ to pass.

Photoluminescence (PL) measurements were performed using a PicoQuant FluoTime300 time-correlated single photon counting setup. The steady-state spectrum was recorded using a 378 nm laser (PicoQuant LDH-P-C-375).

4.6.2 Synthetic Procedures

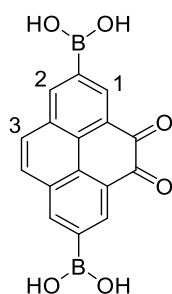
4.6.2.1 Synthesis of Boronic acid-bearing Pyrene-4,5-dione Building Block

Starting point of synthetic route of boronic acid-bearing pyrene-4,5-dione building block **1** is the selective ruthenium catalyzed oxidation of pyrene in its 4- and 5-positions, to afford pyrene-4,5-dione (**4**).¹ The following protection of ketone groups using ethylene glycol gave **5** in 43% yield.² Up next, iridium-catalyzed C-H borylation takes place at the 2,7-positions to afford **6** in 49% yield.² Finally, deprotection of both protecting groups at room temperature with NaIO₄ under acidic conditions² gave boronic acid-bearing pyrene-4,5-dione building block **1** in 88% yield.³



Scheme 4.2. Synthetic route of boronic acid-bearing pyrene-4,5-dione building block **1**. a) CH₂Cl₂, THF, RuCl₃ · 2H₂O, N-methylimidazole, H₂O, NaIO₄, 2.5 h, 50%; b) ethylene glycol, PTSA, toluene, 125 °C, 20 h, 43%; c) bis(pinacolato)diboron, [Ir(OMe)COD]₂, 4,4'-di-tert-butyl-2,2'-bipyridine, MTBE, 80 °C, 20 h, 49%; d) NaIO₄, TFA, THF, H₂O, air, RT, 3 d, 88 %.

(7-Borono-4,5-dioxo-pyren-2-yl)boronic acid (boronic acid-bearing pyrene-4,5-dione)³ (**1**)

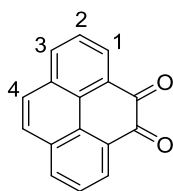


The procedure was adapted from literature procedures.^{2,3} In a round-bottom flask, **6** (522 mg, 0.91 mmol, 1 eq.) was dissolved in a mixture of THF/H₂O (41/12 mL). NaIO₄ (1.65 g, 7.71 mmol, 8.5 eq.) was added, and the mixture was stirred at room temperature for 30 min. Then, TFA (85 mL) was added dropwise and the reaction mixture was stirred for 3 days at room temperature while bubbling air through the solution. An orange solid precipitated and the suspension was diluted with CH₂Cl₂ and H₂O. The aqueous phase was extracted with CH₂Cl₂, and the organic phase was filtered. The collected solid was

combined with the aqueous phase and centrifuged (15 min, 4400 rpm). The orange solid was suspended in water and centrifugation repeated. This last washing step was repeated four times in total. The solid was dried under high vacuum to give boronic acid-bearing pyrene-4,5-dione building block **1** (255 mg, 88%) as an orange solid.

¹H NMR (400 MHz, DMSO-*d*₆+D₂O): δ = 8.72 (d, J = 1.3 Hz, 2H; H-C(1)), 8.68 (d, J = 1.3 Hz, 2H; H-C(2)), 8.01 (s, 2H; H-C(3)).

Pyrene-4,5-dione¹ (**4**)

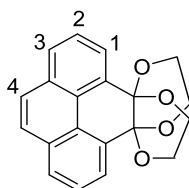


In a round-bottom flask, pyrene crystals (9.7 g, 47.9 mmol, 1 eq.) were dissolved in a mixture of CH₂Cl₂ and THF (240/240 mL). To the yellow solution were added RuCl₃•2H₂O (0.99 g, 4.79 mmol, 0.1 eq.), N-methylimidazole (190.5 μ L, 2.39 mmol, 0.05 eq.) and water (240 mL). Then, over a period of 20 min, sodium periodate (46.1 g, 215.4 mmol, 4.5 eq.) was added in small portions, and the mixture was stirred at RT for 2.5 h. Organic solvents were removed under reduced pressure, and the aqueous phase was extracted with CH₂Cl₂. Collected organic phase was washed with water, dried with anhydrous Na₂SO₄, and concentrated under reduced pressure to afford a dark-orange solid. Purification by column chromatography (SiO₂; CH₂Cl₂) gave **4** (5.5 g, 23.7 mmol, 50%) as a bright-orange solid.

R_f = 0.3 (CH₂Cl₂);

¹H NMR (400 MHz, CDCl₃): δ = 8.44 (dd, J = 7.4 Hz, J = 1.3 Hz, 2H, H-C(1) or H-C(3)), 8.13 (dd, J = 7.9 Hz, J = 1.3 Hz, 2H, H-C(1) or H-C(3)), 7.80 (s, 2H, H-C(4)), 7.72 (dd, J = 7.9 Hz, J = 7.5 Hz, 2H, H-C(2)).

Pyrene-4,5-di(ethyleneglycol)ketal² (**5**)



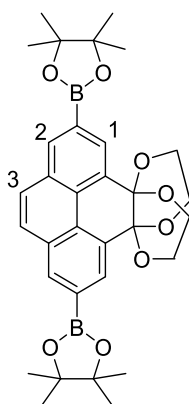
To a suspension of pyrene-4,5-dione (**4**) (2.99 g, 12.9 mmol, 1 eq.) in toluene (150 mL) were added ethylene glycol (90 mL, 1.61 mol, 125 eq.) and *p*-toluenesulfonic acid (1.11 g, 5.81 mmol, 0.45 eq.).

The obtained orange reaction mixture was refluxed at 125 °C for 20 h. Reaction mixture was cooled down and toluene was removed under reduced pressure. Then, 200 mL of water was added and a light brown solid precipitated, which was collected by filtration and washed with water. Purification by flash chromatography (SiO₂; cyclohexane/ethyl acetate 9:1) gave **5** (1.80 g, 5.54 mmol, 43%) as white solid.

$R_f = 0.29$ (cyhex/EtOAc 9:1);

¹H NMR (400 MHz, CD₂Cl₂): $\delta = 7.94$ (dd, $J = 7.6$ Hz, $J = 1.2$ Hz, 4H; H-C(1) or H-C(3)), 7.80 (s, 2H; H-C(4)), 7.70 (t, $J = 7.6$ Hz, 2H; H-C(2)), 4.27 (br, 4H), 3.73 (br, 4H).

2,7-Bis(Bpin)-4,5-di(ethyleneglycol)ketal-pyrene² (**6**)



In a nitrogen-filled 100 mL pressure tube (ACE glass, bushing type back seal, 17.8 cm x 38.1 mm) were added pyrene-4,5-di(ethyleneglycol)ketal (**5**) (0.89 g, 2.76 mmol, 1 eq.), bis(pinacolato)diboron (1.41 g, 5.52 mmol, 2 eq.), [Ir(OMe)COD]₂ (0.09 g, 0.14 mmol, 0.05 eq.), 4,4'-di-*tert*-butyl-2,2'-bipyridine (0.07 g, 0.28 mmol, 0.1 eq.), and *tert*-butyl methyl ether (18 mL). The reaction mixture was stirred at 80 °C for 20 h, cooled down and passed through a pad of silica using toluene as the eluent. The solvent was removed under reduced pressure and the product was purified by flash chromatography (SiO₂; cyclohexane/ethyl acetate 9:1 → 8:2 → 7:3), as off-white solid (0.77 g, 0.95 mmol, 49%).

$R_f = 0.2$ (cyhex/EtOAc 9:1);

¹H NMR (400 MHz, CD₂Cl₂): $\delta = 8.36$ (d, $J = 1.2$ Hz, 2H; H-C(1) or H-C(2)), 8.24 (d, $J = 1.2$ Hz, 2H; H-C(1) or H-C(2)), 7.81 (s, 2H; H-C(3)), 4.28 (br, 4H), 3.71 (br, 4H), 1.37 (s, 24H).

4.6.2.2 Synthesis of Dione-COF

Dione-COF was synthesized according to our previous report³, in a 10 mL ampoule (Wheaton, prescored, borosilicate, 19 x 107 mm) flushed with argon. To the boronic acid-bearing pyrene-4,5-dione building block (30 mg, 0.10 mmol, 1 equiv.) with 2,3,6,7,10,11-hexahydroxytriphenylene (HHTP) hydrate (20 mg, 0.06 mmol, 0.64 equiv.) were added a mixture of 1:1 mesitylene and *n*-butanol (3.5 mL), previously degassed by three cycles of freeze-pump-thaw. The reaction mixture was sonicated for 5 min. The ampoule was immersed in a bath of liquid N₂, sealed under vacuum, and heated in the oven at 120 °C, for 7 days. The precipitate was collected by centrifugation, washed with anhydrous acetone for four times, and dried under nitrogen at 90 °C, to give 45 mg of Dione COF as brown solid.

4.6.2.3 Three-component Reactions

General procedure

In a 6 mL culture tube the boronic acid-bearing pyrene-4,5-dione building block (8.57 mg, 28.6 μmol, 1 equiv.), 2,3,6,7,10,11-hexahydroxytriphenylene (HHTP) hydrate (5.71 mg, 17.1 μmol, 0.64 equiv.) and 2.1 equiv. of the respective amine (*o*-phenylenediamine (Ph), 2,3-diaminonaphthalene (Naph) or (1*R*,2*R*)-(+)-1,2-diphenyl-ethylenediamine (2Ph)) were suspended in a 1:1 mixture of mesitylene and *n*-butanol (2 mL). The reaction mixture was heated at 120 °C for 7 days. The precipitate was collected by filtration and washed four times with anhydrous acetone to afford Aza-Ph-COF, Aza-Naph-COF and Aza-2Ph-COF.

Aza-Ph-COF synthesis

o-Phenylenediamine (6.49 mg, 0.06 mmol, 2.1 equiv.). Aza-Ph-COF (up to 100% conversion of dione moieties).

Aza-Naph-COF synthesis

2,3-Diaminonaphthalene (9.50 mg, 0.06 mmol, 2.1 equiv.). Aza-Naph-COF (up to 100% conversion of dione moieties).

Aza-2Ph-COF synthesis

(1*R*,2*R*)-(+)-1,2-Diphenyl-ethylenediamine (6.49 mg, 0.06 mmol, 2.1 equiv.). Aza-2Ph-COF (up to 100% conversion of dione moieties).

4.6.2.4 Thin Film Synthesis

General procedure

The thin films were synthesized using a face-down approach. A 100 mL Schott Duran glass bottle equipped with a teflon liner and a substrate was charged with the boronic acid-bearing pyrene-4,5-dione building block (8.57 mg, 28.6 μmol, 1 equiv.), 2,3,6,7,10,11-hexahydroxytriphenylene (HHTP) hydrate (5.71 mg, 17.1 μmol, 0.64 equiv.) and in case of the full conversion films 2.1 equiv. (0.06 mmol) of the

respective amine (*o*-phenylenediamine (Ph), 2,3-diaminonaphthalene (Naph) or (1*R*,2*R*)-(+)-1,2-diphenyl-ethylenediamine (2Ph). Next a mixture of mesitylene and *n*-butanol (2000 μ L, v: v 1:1) was added. The glass bottle was sealed and heated at 120 °C for 6 d. After cooling to room temperature, the COF film was rinsed with anhydrous acetone and dried under a stream of nitrogen.

4.6.3 NMR Spectra

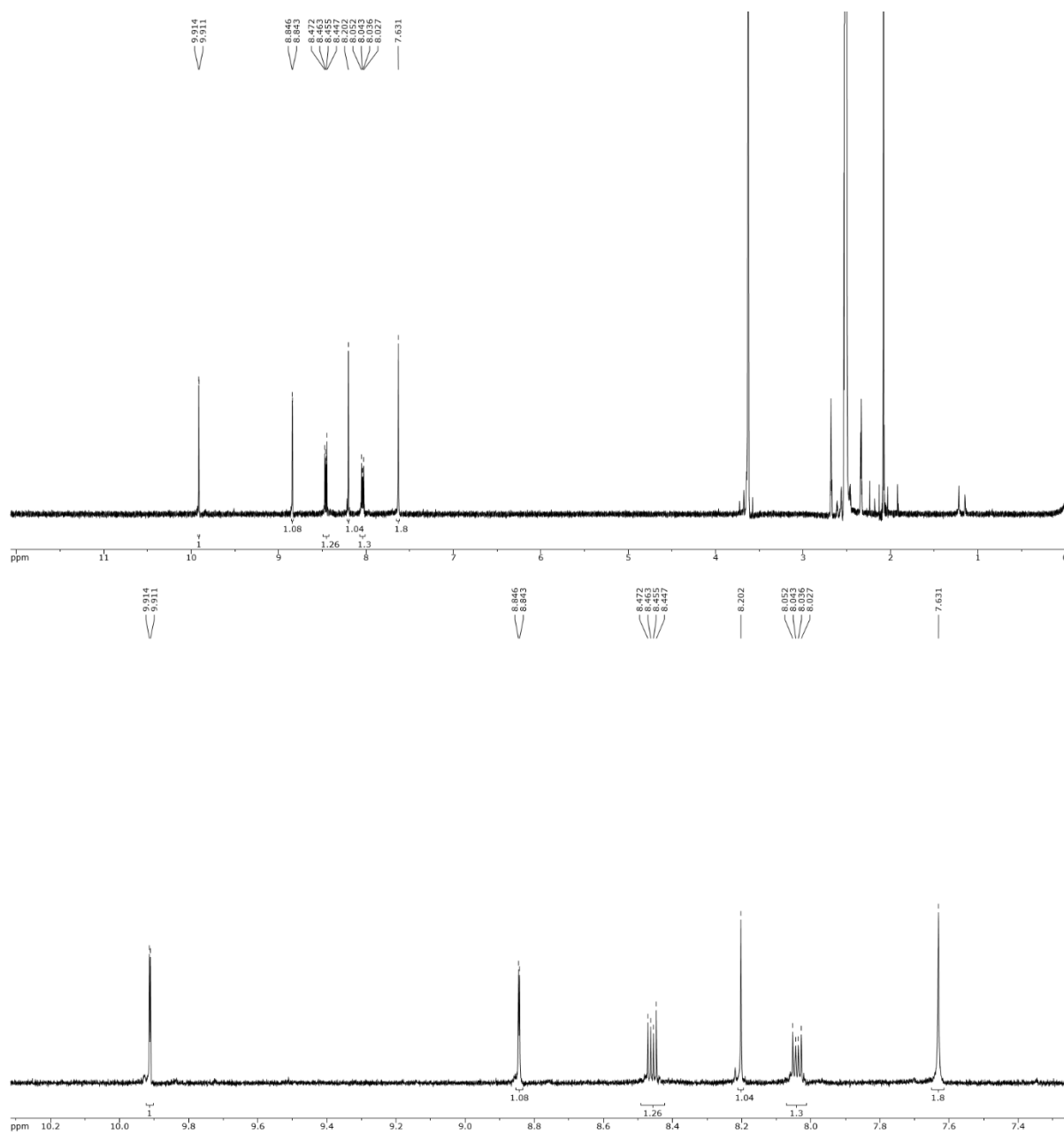


Figure 4.5. ^1H NMR spectrum of Aza-Ph-COF, measured at 400 MHz, in $(\text{CD}_3)_2\text{SO}+\text{D}_2\text{O}$.

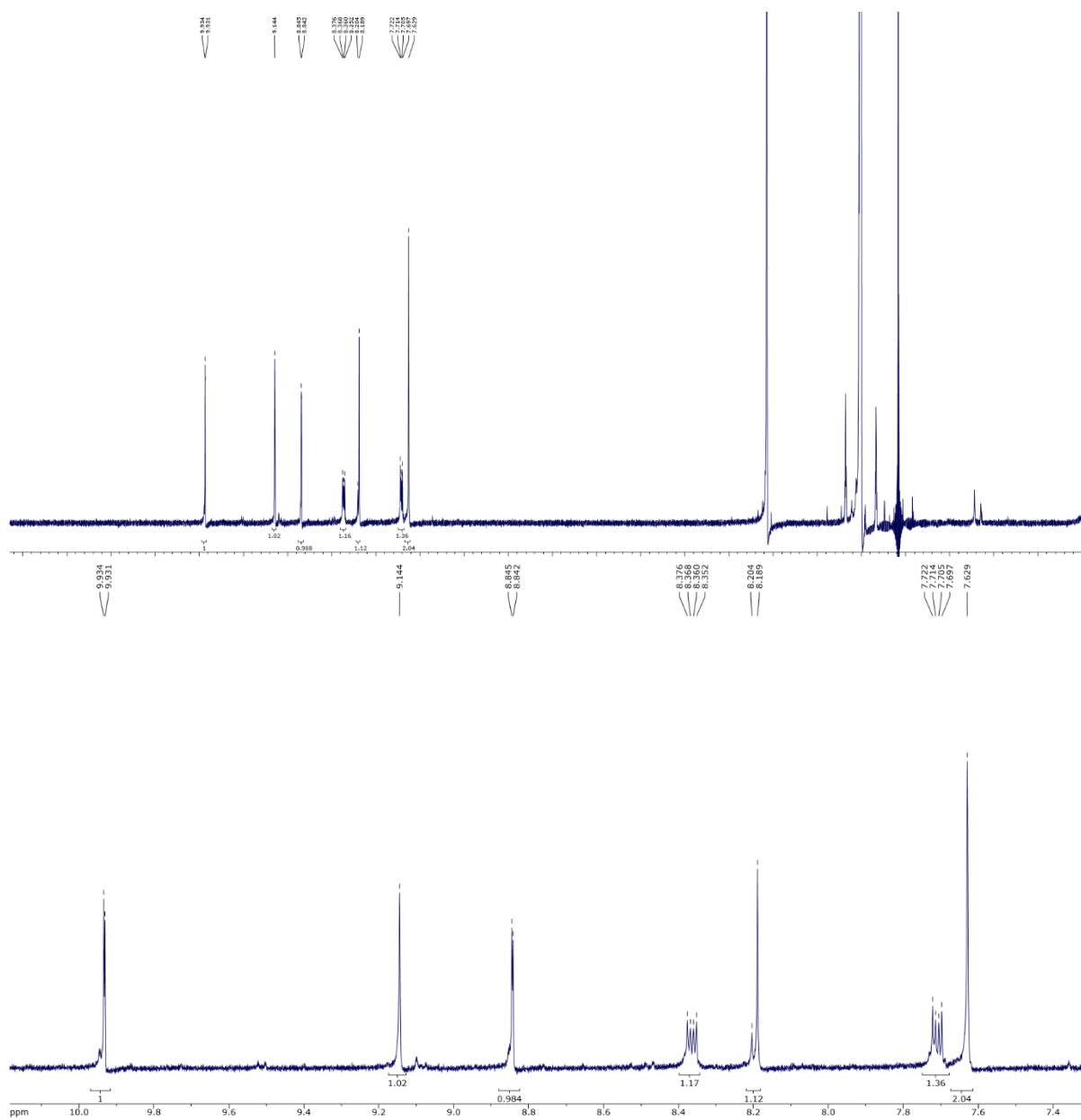


Figure 4.6. ^1H NMR spectrum of Aza-Naph-COF, measured at 400 MHz, in $(\text{CD}_3)_2\text{SO}+\text{D}_2\text{O}$.

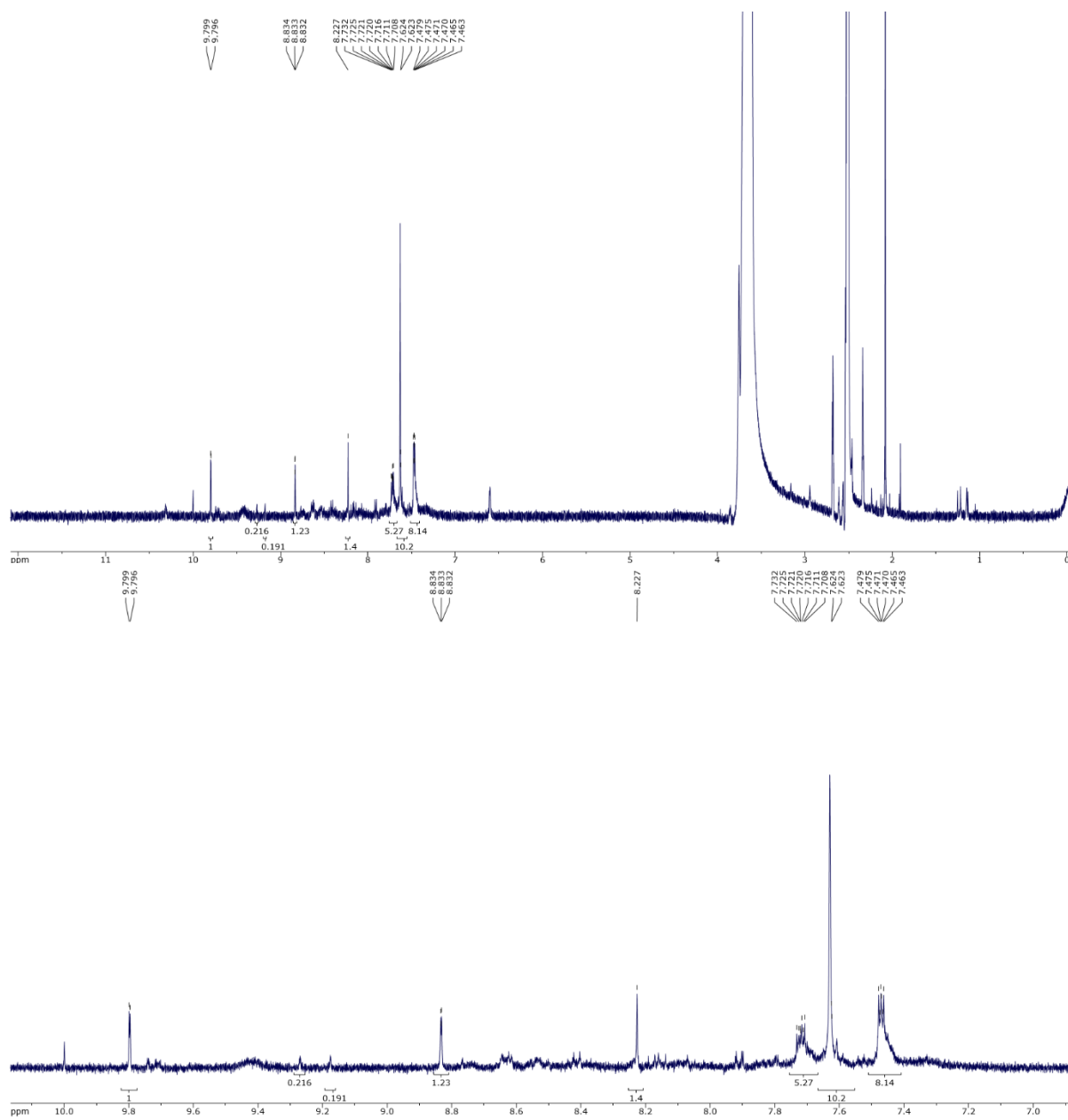


Figure 4.7. ¹H NMR spectrum of Aza-2Ph-COF, measured at 400 MHz, in (CD₃)₂SO+D₂O.

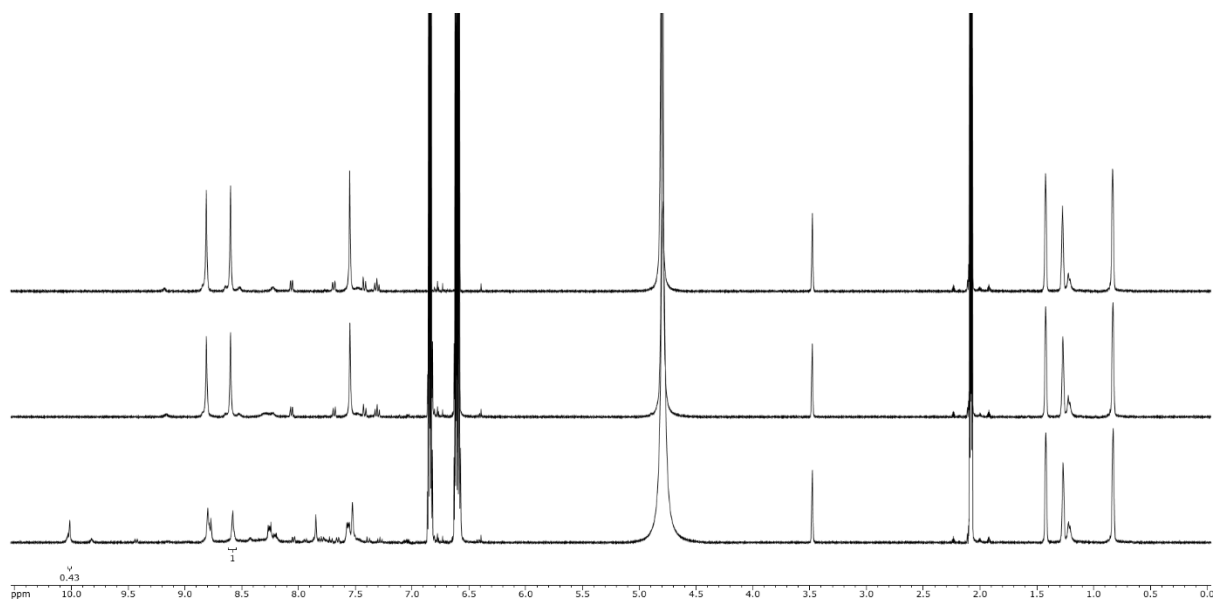


Figure 4.8. ¹H NMR spectrum overlay of pyrene-dione building block after addition of excess catechol and *o*-phenylenediamine respectively, measured at 400 MHz, in deuterated mesitylene and *n*-butanol (1:1 v/v).

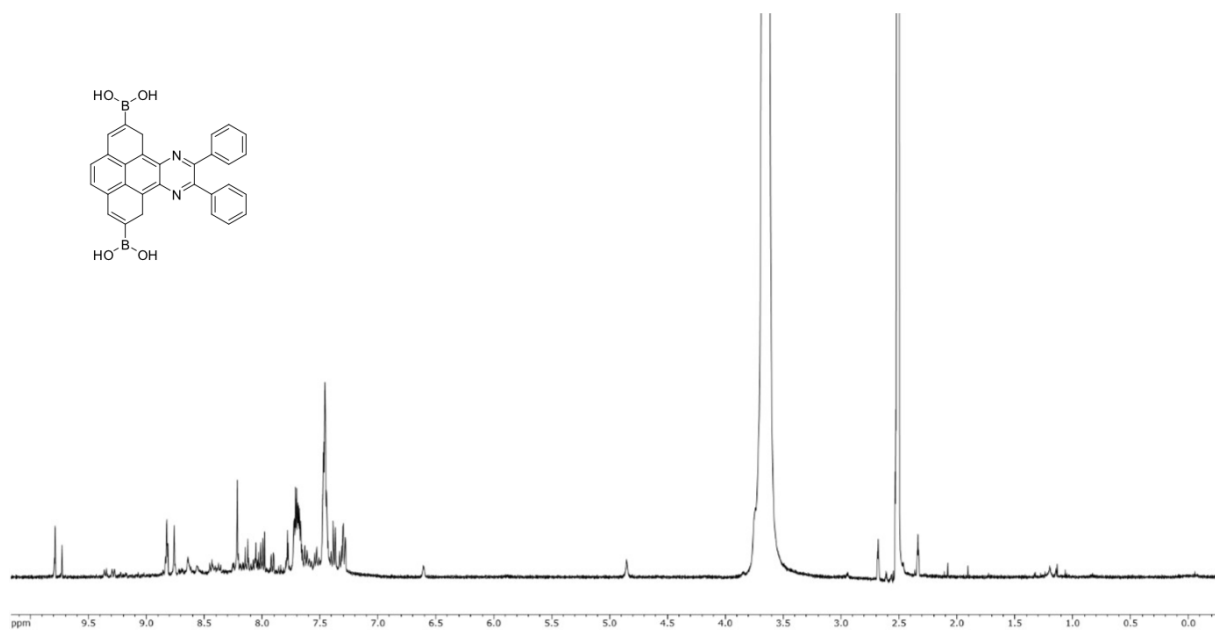


Figure 4.9. ¹H NMR spectrum of 2Ph model system, measured at 400 MHz, in (CD₃)₂SO+D₂O.

4.6.4 Structural Analysis

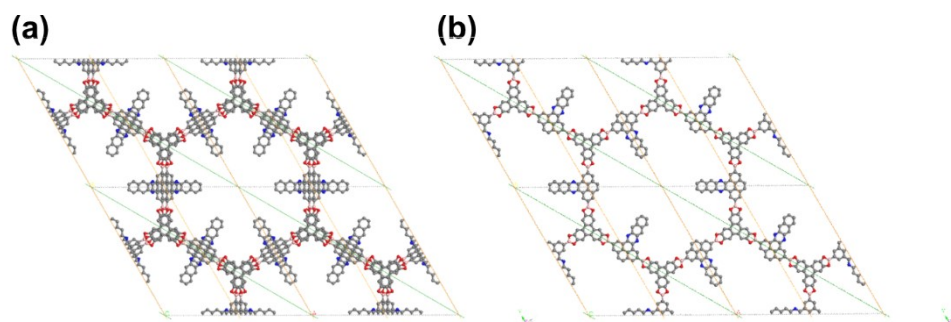


Figure 4.10. Simulated structures of an antiparallel (a) and AA layer arrangement (b) of Aza-Naph-COF with the Miller planes (110) and (200) highlighted by green and orange lines, respectively.

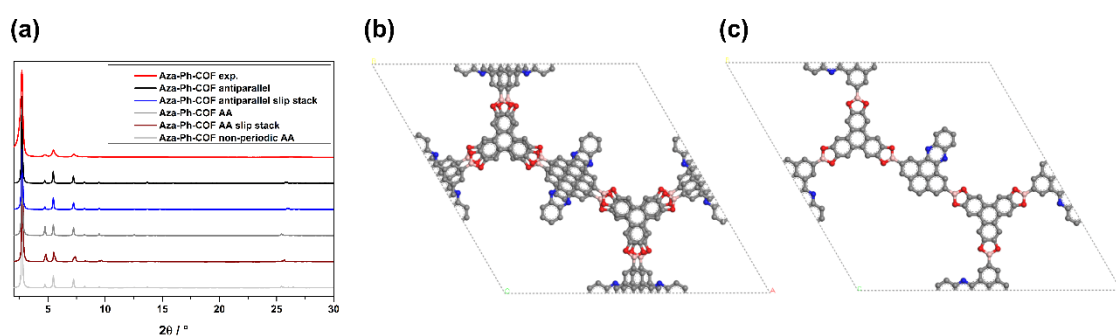


Figure 4.11. (a) Experimentally obtained and simulated PXRD patterns for an AA and antiparallel layer arrangement of Aza-Ph-COF. (b) and (c) View of one unit cell for an AA and antiparallel layer arrangement, respectively.

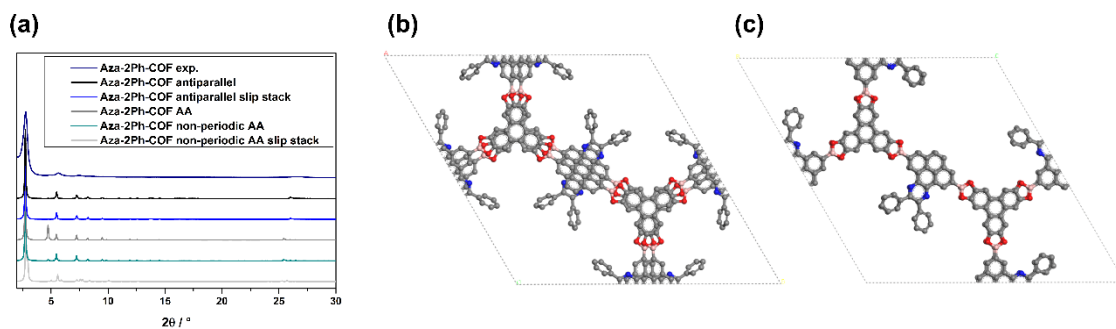


Figure 4.12. (a) Experimentally obtained and simulated PXRD patterns for an AA and antiparallel layer arrangement of Aza-2Ph-COF. (b) and (c) View of one unit cell for an AA and antiparallel layer arrangement, respectively.

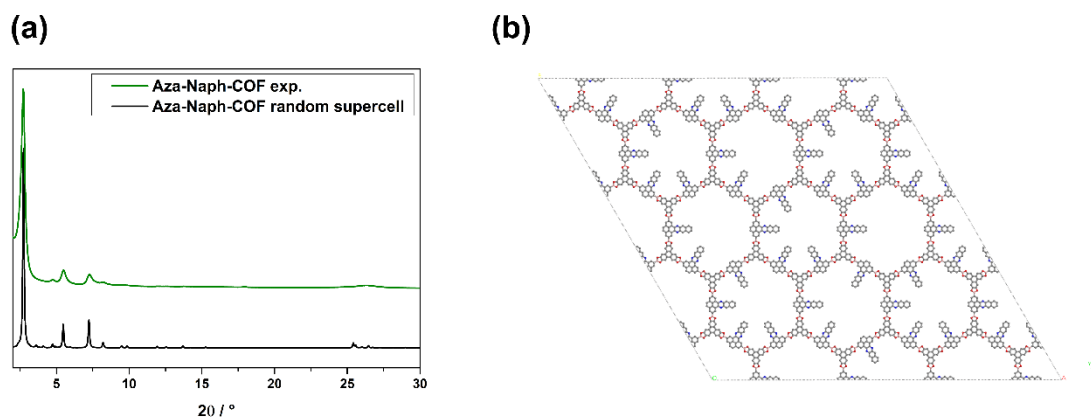


Figure 4.13. (a) Experimentally obtained and simulated PXRD pattern for a supercell with random layer arrangement of Aza-Naph-COF. (b) View of one unit cell for the random layer arrangement, respectively.

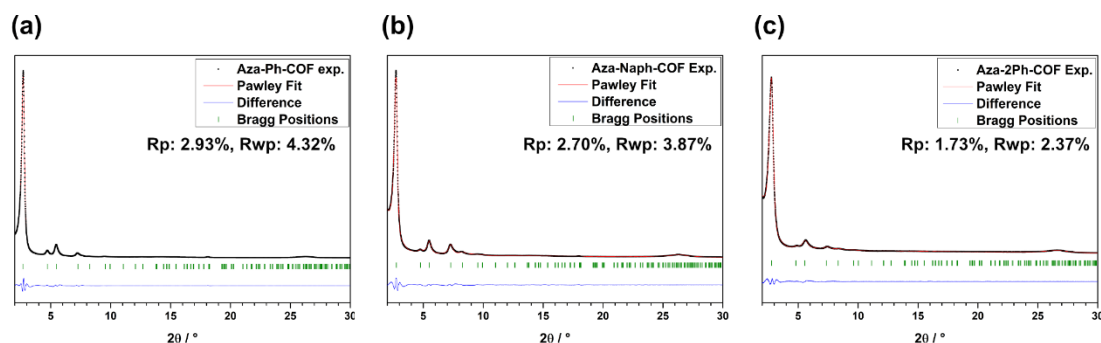


Figure 4.14. (a), (b) and (c) Experimental PXRD patterns (black dots) of Aza-Ph-, Aza-Naph- and Aza-2Ph-COF using antiparallel alignment of the layers, respectively. Pawley refinement (red line), difference plot between the experimental data and the Pawley-refined PXRD pattern (blue line), Bragg positions are indicated by green ticks.

Unit cell parameters (*P*-63cm) and atomic coordinates for Aza-Ph-COF

$$a = b = 37.0, c = 7.0 \text{ \AA}$$

$$\alpha = \beta = 90^\circ, \gamma = 120^\circ$$

Atom	a/x	b/y	c/z
C1	0.62880	0.29532	0.24348
C2	0.66715	0.29562	0.24348
C3	0.59137	0.25721	0.24348
C4	0.59266	0.22067	0.24348
C5	0.62952	0.22090	0.24348
C6	0.66708	0.25777	0.24348
O7	0.55864	0.18124	0.24348
B8	0.57934	0.15673	0.24348

O9	0.62455	0.18158	0.24348
C10	0.55521	0.10874	0.24348
C11	0.51208	0.08777	0.24348
C12	0.48943	0.04455	0.24348
C13	0.51044	0.02188	0.24349
C14	0.55420	0.04339	0.24348
C15	0.57624	0.08658	0.24348
C16	0.44385	0.02269	0.24348
C17	0.57555	0.02158	0.24348
N18	0.42116	1.04538	0.24348
C19	0.37578	1.02269	0.24348
C20	0.30771	0.35309	0.74348
C21	0.30771	0.28502	0.74348

Unit cell parameters (*P*-63cm) and atomic coordinates for Aza-Naph-COF

$$a = b = 37.0, c = 7.0 \text{ \AA}$$

$$\alpha = \beta = 90^\circ, \gamma = 120^\circ$$

Atom	a/x	b/y	c/z
C1	0.62880	0.29532	0.24348
C2	0.66715	0.29562	0.24348
C3	0.59137	0.25721	0.24348
C4	0.59266	0.22067	0.24348
C5	0.62952	0.22090	0.24348
C6	0.66708	0.25777	0.24348
O7	0.55864	0.18124	0.24348
B8	0.57934	0.15673	0.24348
O9	0.62455	0.18158	0.24348
C10	0.55521	0.10874	0.24348
C11	0.51208	0.08777	0.24348
C12	0.48943	0.04455	0.24348
C13	0.51044	0.02188	0.24349
C14	0.55420	0.04339	0.24348

C15	0.57624	0.08658	0.24348
C16	0.44385	0.02269	0.24348
C17	0.57555	0.02158	0.24348
N18	0.42116	1.04538	0.24348
C19	0.37578	1.02269	0.24348
C20	0.30771	0.35309	0.74348
C21	0.30771	0.28502	0.74348
C22	0.76036	0.71498	0.24348
C23	0.78305	0.76036	0.24348

Unit cell parameters (*P*-63cm) and atomic coordinates for Aza-2Ph-COF

$$a = b = 36.8, c = 7.0 \text{ \AA}$$

$$\alpha = \beta = 90^\circ, \gamma = 120^\circ$$

Atom	a/x	b/y	c/z
C1	0.63010	0.29424	0.20418
C2	0.66956	0.29693	0.20426
C3	0.59399	0.25513	0.20282
C4	0.59766	0.21997	0.20184
C5	0.63556	0.22240	0.20234
C6	0.67192	0.26036	0.20340
O7	0.56508	0.17987	0.19859
B8	0.58785	0.15742	0.19719
O9	0.63284	0.18403	0.19985
C10	0.56538	0.10972	0.18994
C11	0.52247	0.08828	0.17995
C12	0.50086	0.04534	0.17280
C13	0.52232	0.02303	0.17731
C14	0.56575	0.04494	0.18724
C15	0.58703	0.08820	0.19292
C16	0.45584	0.02296	0.15445
C17	0.59078	0.02371	0.19648
N18	0.43242	1.03637	0.20851

C19	0.39566	1.02381	0.26315
C20	0.33203	0.38451	0.85591
C21	0.29920	0.34373	0.85980
C22	0.26143	0.33410	0.94326
C23	0.25602	0.36543	1.02213
C24	0.28832	0.40636	1.01660
C25	0.32601	0.41584	0.93303

4.6.5 Fourier-transform Infrared (FT-IR) Spectra

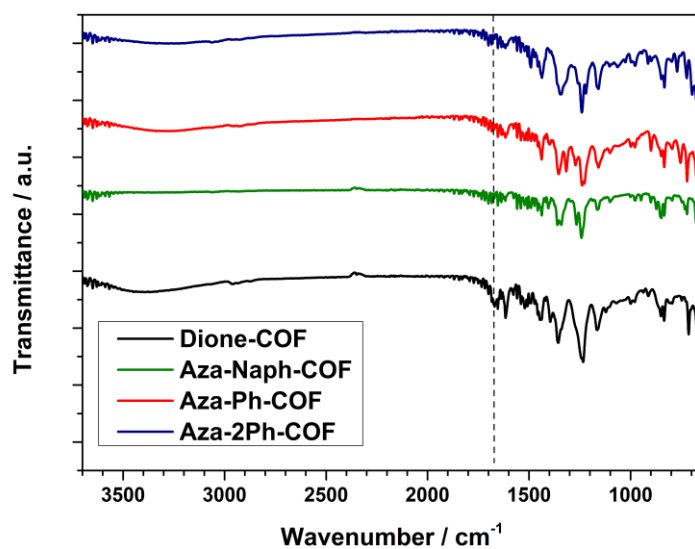


Figure 4.15. FT-IR spectrum of Dione-COF (black), Aza-Ph-COF (red), Aza-Naph-COF (green) and Aza-2Ph-COF (blue).

4.6.6 N₂ Physisorption

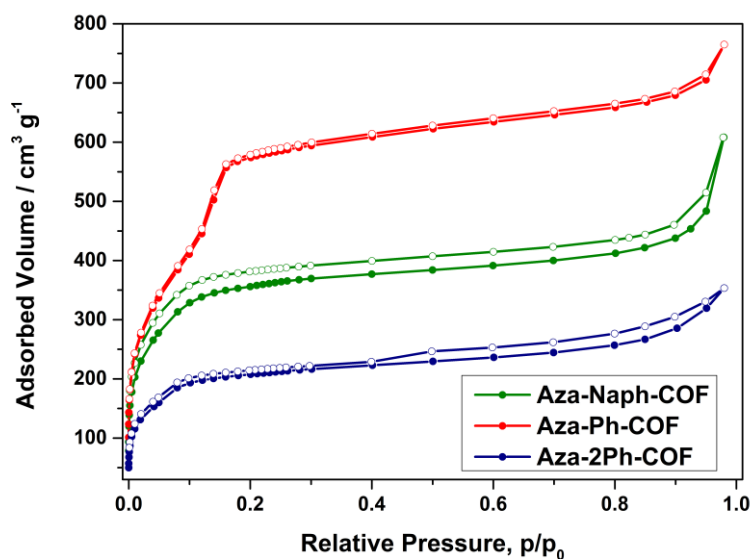


Figure 4.16. Nitrogen adsorption (filled spheres) and desorption (hollow spheres) isotherm profiles measured at 77 K for Aza-Ph- (red), Aza-Naph- (green) and Aza-2Ph-COF (blue).

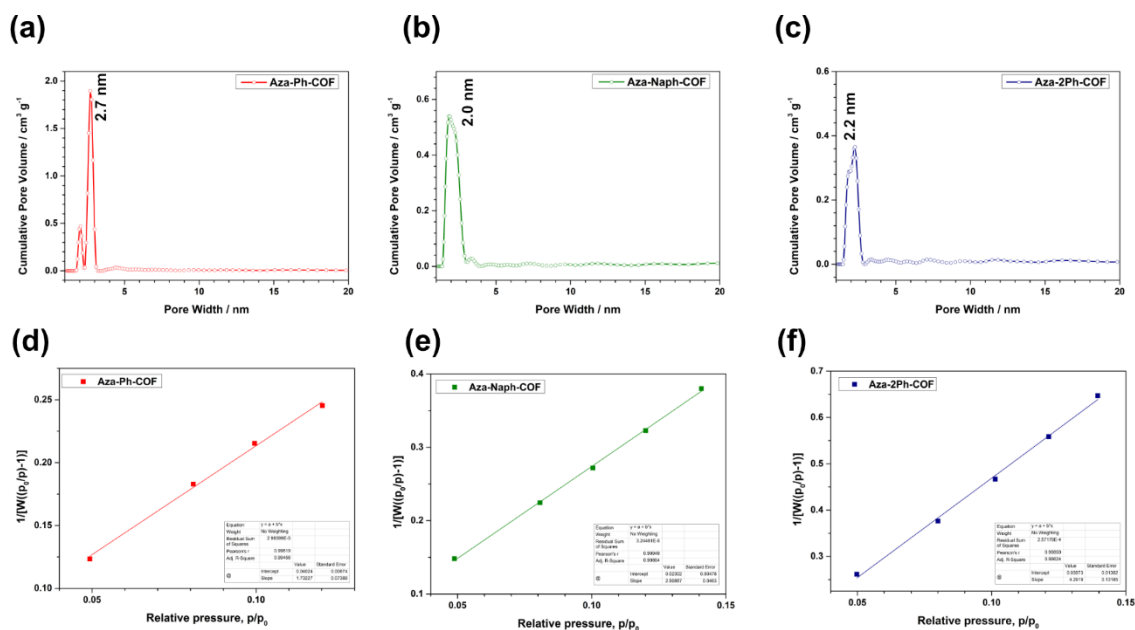


Figure 4.17. Pore size distributions of Aza-Ph- (a), Aza-Naph- (b) and Aza-2Ph-COF (c). Multi-point BET plots of Aza-Ph- (d), Aza-Naph- (e) and Aza-2Ph-COF (f).

4.6.7 Thermogravimetric Analysis (TGA)

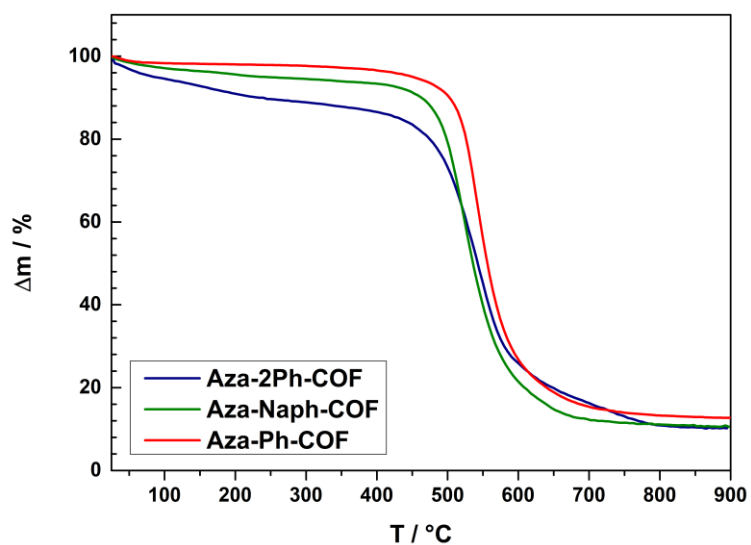


Figure 4.18. Thermogravimetric analysis (TGA) of Aza-Ph- (red), Aza-Naph- (green) and Aza-2Ph-COF (blue) measured for bulk materials.

4.6.8 Transmission Electron Microscopy (TEM)

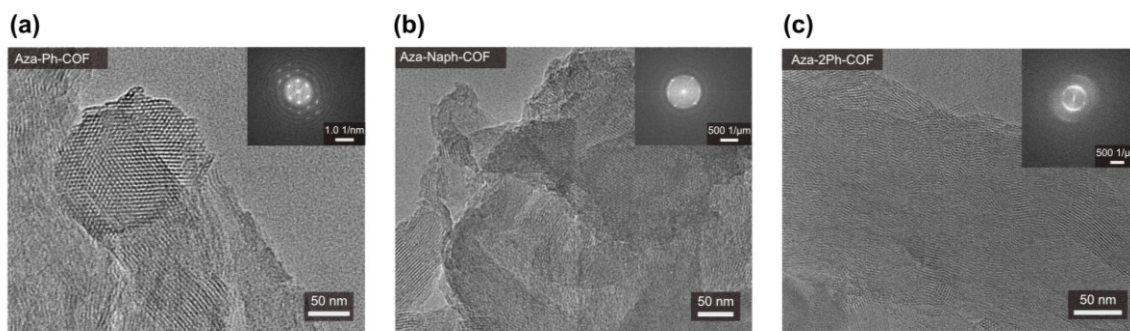


Figure 4.19. Transmission electron microscopy images of (a) Aza-Ph-COF, (b) Aza-Naph-COF, (c) Aza-2Ph-COF and the respective electron diffraction images as insets.

4.6.9 Thin Film Analysis

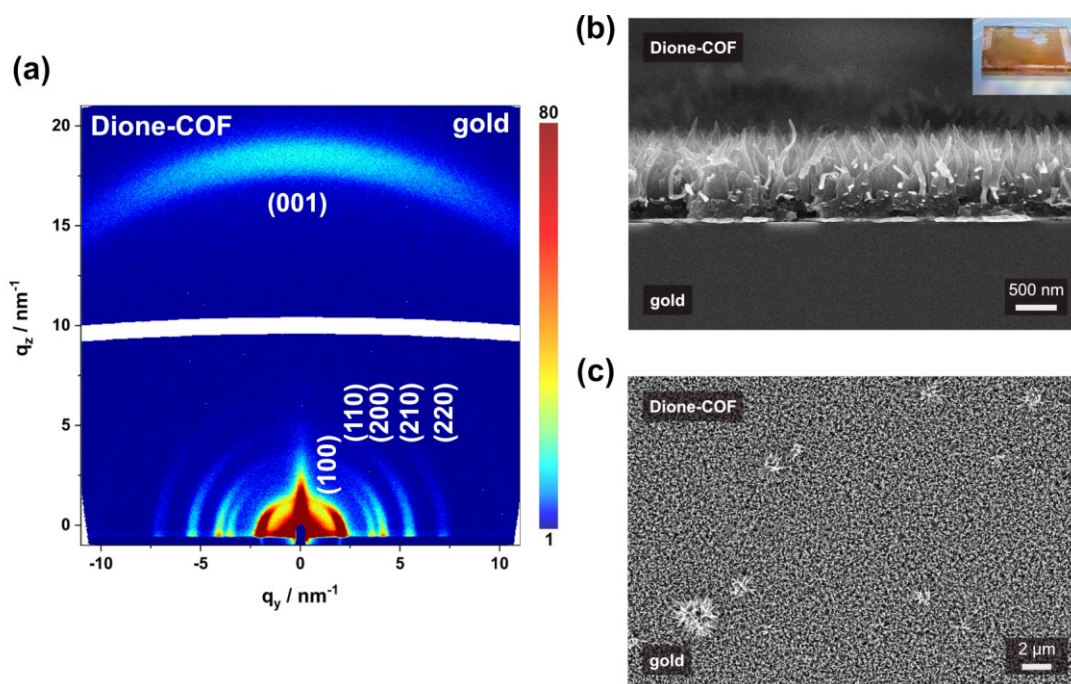


Figure 4.20 (a) GIWAXS 2D patterns of Dione COF thin film grown on gold coated glass substrates. (b) and (c) SEM cross-section and top-view images of Dione COF thin film grown on a gold coated glass substrate. The inset shows a macroscopic photograph of a Dione COF thin film grown on a glass substrate.

4.6.10 Photophysical Properties

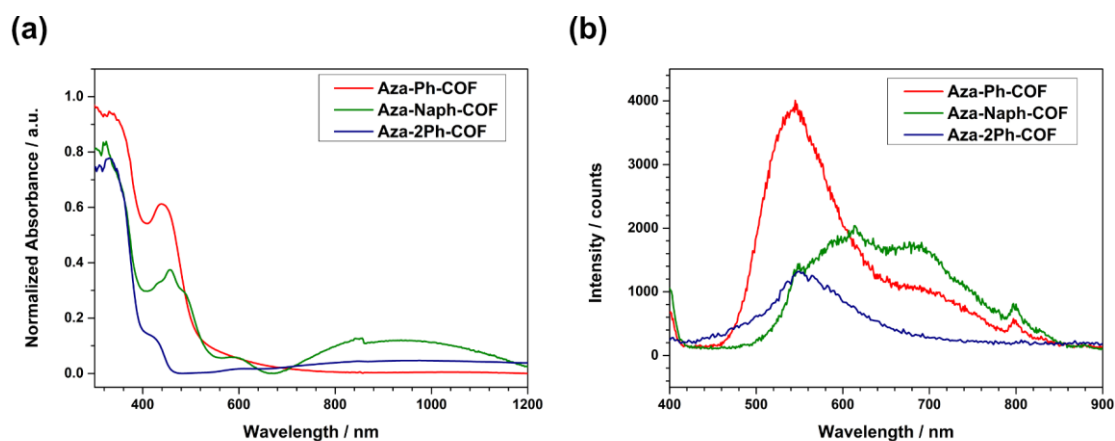


Figure 4.21. (a) Normalized absorption spectra of Aza-Ph-COF (red), Aza-Naph- (green) and Aza-2Ph-COF (blue) thin films on quartz substrates. (b) Normalized PL emission spectra of Aza-Ph- (red), Aza-Naph-COF (green) and Aza-2Ph-COF (blue) thin films on quartz substrates.

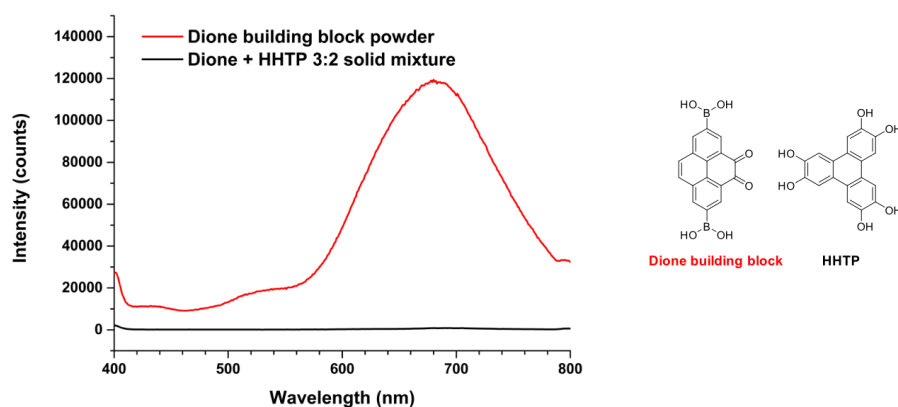


Figure 4.22. PL spectra of dione building block 1 as powder (red), and a dropcast mixture of Dione building block (1) and HHTP as 2:3 slurry (black).

4.6.11 References

- (1) Walsh, J. C.; Williams, K.-L. M.; Lungerich, D.; Bodwell, G. J. Synthesis of Pyrene-4,5-dione on a 15 g Scale. *Eur. J. Org. Chem.* **2016**, 2016, 5933–5936.
- (2) Merz, J.; Dietz, M.; Vonhausen, Y.; Wöber, F.; Friedrich, A.; Sieh, D.; Krummenacher, I.; Braunschweig, H.; Moos, M.; Holzapfel, M.; *et al.* Synthesis, Photophysical and Electronic Properties of New Red-to-NIR Emitting Donor–Acceptor Pyrene Derivatives. *Chem. Eur. J.* **2020**, 26, 438–453.
- (3) Salonen, L. M.; Medina, D. D.; Carbó-Argibay, E.; Goesten, M. G.; Mafra, L.; Guldris, N.; Rotter, J. M.; Stroppa, D. G.; Rodríguez-Abreu, C. A supramolecular strategy based on molecular dipole moments for high-quality covalent organic frameworks. *Chem. Commun.* **2016**, 52, 7986–7989

5. Thiophene-based Vinylene-Linked COF Films

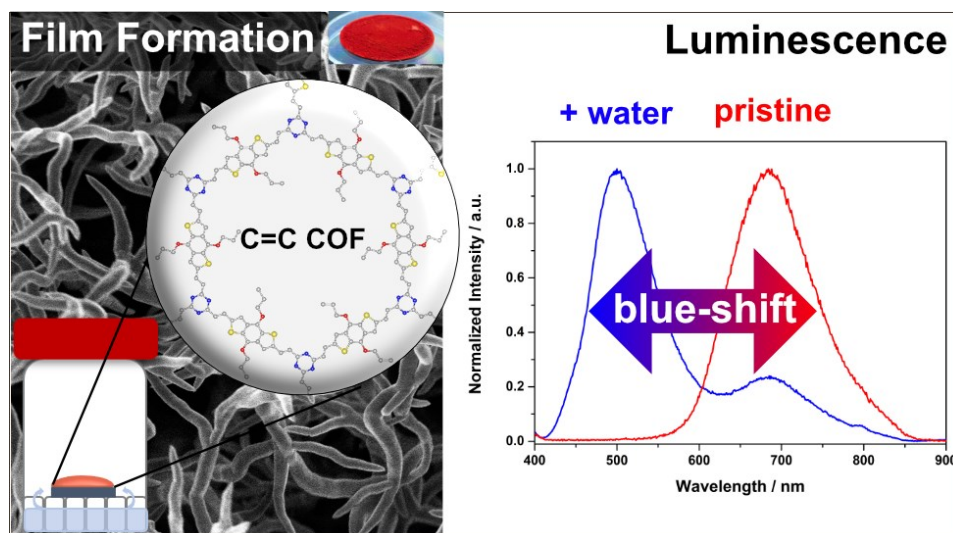
This chapter is based on the following article:

Thiophene-based Vinylene-Linked Covalent Organic Framework Films

Laura Frey,[†] Alexander Biewald,[†] Achim Hartschuh,[†] and Dana D. Medina^{†*} *Manuscript in preparation.*

[†] Department of Chemistry and Center for Nanoscience (CeNS), Ludwig-Maximilians University (LMU), Butenandtstraße 11 (E), 81377 Munich, Germany

* Corresponding Author.



5.1 Abstract

Covalent Organic Frameworks (COFs) are crystalline, highly ordered, porous materials. Diverse linkage chemistries have already been used for constructing these materials, such as boronate-ester bonds, boroxine or imine-bonds. However, these COFs although thermally stable can be much less stable in aqueous/ acidic media or towards moisture, depending on the specific structure. Here, we show the synthesis of two new highly crystalline, porous, luminescent and stable vinylene-linked COFs, namely TMT BDTOEt and TMT BDTOPr which were synthesized using a Knoevenagel polycondensation reaction with trimethyltriazine (TMT) and differently functionalized benzodithiophene (BDT) aldehydes as building blocks. Subsequently, the frameworks were grown successfully as porous and highly crystalline films on different substrates using the vapor-assisted conversion (VAC) method that was already established in our group for boronate-ester based COFs but has not yet been shown for vinylene-linked COFs. The resulting films show interesting photophysical properties upon interaction with different solvents. The addition of a droplet of ethanol or water led to a drastic blue-shift in the photon emission maximum of up to 200 nm, changing from 690 nm for the pristine TMT COF to 480 nm upon interaction with ethanol. Further, the lifetimes of the excited states also changed upon interaction with solvents, increasing from 0.7 ns (pristine TMT BDTOPr COF) to 9.97 ns (addition of water) for the largest contributions.

5.2 Introduction

Covalent Organic Frameworks (COFs) are crystalline, highly ordered, porous materials that are formed by condensation reactions of a large variety of organic building blocks.¹ The frameworks feature long-range order, large surface areas and well-defined pore systems. Using the principles of reticular chemistry and the great variety of organic building blocks allows for constructing tailor-made COFs where key properties such as framework dimension, so-called 2D or 3D structures, pore shape, optical properties and electronic coupling between the individual monomers can be modified by fine-tuning of the chemical structure and geometry of the respective building blocks. Further, owing to the great variety of structures, COFs can be used for many different applications such as gas storage^{2,3}, sensing⁴⁻⁶, catalysis^{7,8}, separation^{9,10} and optoelectronics^{11,12}. Since the reactions used for the formation of COFs are slightly reversible, “proof-reading” related to building block assembly faults can be ensured, thus allowing for the formation of highly structurally defined products. Diverse chemical linkages have been demonstrated to be suitable so far for constructing COFs, particularly, based on the reversible formation of B–O^{1,13-17}, B–N¹⁸ and C–N¹⁹⁻²¹ bonds. However, these COFs although being thermally stable are often prone to hydrolysis in aqueous/ acidic media or moisture which can be critical for the implementation of such structures for certain applications.²² To obtain robust and stable COFs, various

synthesis strategies such as keto-enol-tautomerization²³ or post-synthetic modifications²² have been employed. In the past years, vinylene-linked COFs^{24–30} (sp²-carbon linked COFs), which are synthesized using a Knoevenagel polycondensation reaction, have emerged. These frameworks feature greater stability towards hydrolysis compared to imine- or boronate ester-linked COFs²⁴ in combination with non-polar in-plane π -conjugation.²⁸ However, the synthesis of new vinylene-linked COF structures with control over crystallinity and porosity is a great challenge mainly due to the poor reversibility of the water elimination step creating the desired C=C bonds under the employed solvothermal conditions. This hampers the self-healing process and often leads to a reduced structural order. Even though the elementary construction principles of vinylene-linked COFs have been illustrated, the development of synthesis approaches and optimized reactions conditions under which ordered vinylene-linked COFs are obtained are highly desired targets. In this context, very recently an elegant synthesis approach using a solvent mixture of benzoic anhydride and benzoic acid was published.³¹ In that report, a self-catalyzed benzoylation of the used pyridine-based monomer was used to activate the aryl α -carbon atoms for the Knoevenagel polycondensation reaction at the pyridylmethyl carbon atoms, resulting in a highly crystalline COF.

In the literature, the formation of vinylene-linked COFs by Knoevenagel condensation reaction has been demonstrated using either acidic or basic catalytic conditions. For example, Thomas *et al.*²⁴ reported that the synthesis of a vinylene-linked COF which was published by Yaghi *et al.*²⁷ was only possible using acidic conditions and could not be reproduced employing basic conditions, illustrating that the choice of the exact reaction conditions can be crucial for obtaining highly crystalline COFs. Another important aspect is expanding the variety of possible linkers suitable for the condensation reaction and framework formation. Particularly, highly ordered two dimensional vinylene-linked COFs which feature thiophene-based building blocks have not yet been reported.²⁹

In addition to the widely used solvothermal synthesis, the vapor-assisted conversion synthesis (VAC) approach has emerged as suitable to form highly crystalline framework materials directly on top of a substrate. It was pioneered for the synthesis of framework materials and illustrated for boronate ester- and boroxine-linked 2D COFs³² showing that highly crystalline and porous COF deposits can be synthesized at room temperature rather than at elevated temperatures. Later, VAC was developed as a powerful methodology to form metal-organic-framework films with control over film thickness and crystal orientation.³³

Herein, we report the synthesis of two novel highly crystalline and porous thiophene-based vinylene-linked COF structures which were synthesized using trimethyltriazine (TMT) and two different alkoxy-functionalized benzodithiophene-based aldehydes, 4,8-diethoxybenzo[1,2-b;4,5-b']dithiophene-2,6-dicarbaldehyde (BDTOEt) or 4,8-dipropoxybenzo[1,2-b;4,5-b']dithiophene-2,6-dicarbaldehyde (BDTOPr), yielding TMT BDTOEt and TMT BDTOPr, under two distinct reaction schemes, namely

solvothermal and vapor-assisted conversion (VAC). Through a solvothermal reaction scheme and under basic conditions, highly crystalline COF bulk materials were obtained. In addition, we report, for the first time, the synthesis of highly crystalline and porous vinylene-linked COF films at moderate temperatures and reaction conditions employing the VAC synthesis approach. For the latter, different reaction conditions such as temperature, reaction time and solvent vapor sources were assessed and their impact on the film crystallinity was studied by X-ray diffraction analyses. Strikingly, under VAC conditions, thiophene containing vinylene-linked COFs are formed at very mild conditions such as moderate temperatures as low as 40 °C, and short reaction times of 30 minutes. Moreover, UV-vis spectroscopy of TMT BDTOEt and TMT BDTOPr reveals light absorption in the 300-610 nm wavelength range and band gaps of around 2 eV assuming a direct transition for both COFs. Photoluminescence (PL) spectroscopy revealed intense photon emission at 690 nm for both COFs with short lifetimes of 0.70 ns (69 %) for the largest contribution measured by time-correlated single photon counting (TCSPC); remarkably, in contact with polar solvent such as water or ethanol the PL emission is strongly blue-shifted to 480 nm which might be due to a solvatochromic effect of the COF.

5.3 Results and Discussion

5.3.1 Synthesis

The thiophene-based vinylene-linked covalent organic frameworks (COFs) TMT BDTOEt and TMT BDTOPr were synthesized employing a Knoevenagel condensation under basic solvothermal reaction conditions. Briefly, trimethyltriazine (TMT) and alkoxy-functionalized benzodithiophene-based aldehydes, namely 4,8-diethoxybenzo[1,2-b;4,5-b']dithiophene-2,6-dicarbaldehyde (BDTOEt) or 4,8-dipropoxybenzo[1,2-b;4,5-b']dithiophene-2,6-dicarbaldehyde (BDTOPr) were added into a solvent mixture of 8:1 v:v methanol and mesitylene in the presence of solid NaOH as base catalyst. (**Figure 5.1a**) In a sealed stainless-steel autoclave, the mixture was transferred into a pre heated oven at 180 °C for 3 days. After the given reaction time, the resulting bright red COF powders were purified using Soxhlet extraction in methanol and subsequently dried under high vacuum (for further information on the synthesis of the building blocks as well as the new structures see appendix **Section 5.6.2**).

5.3.2 Structural Investigations

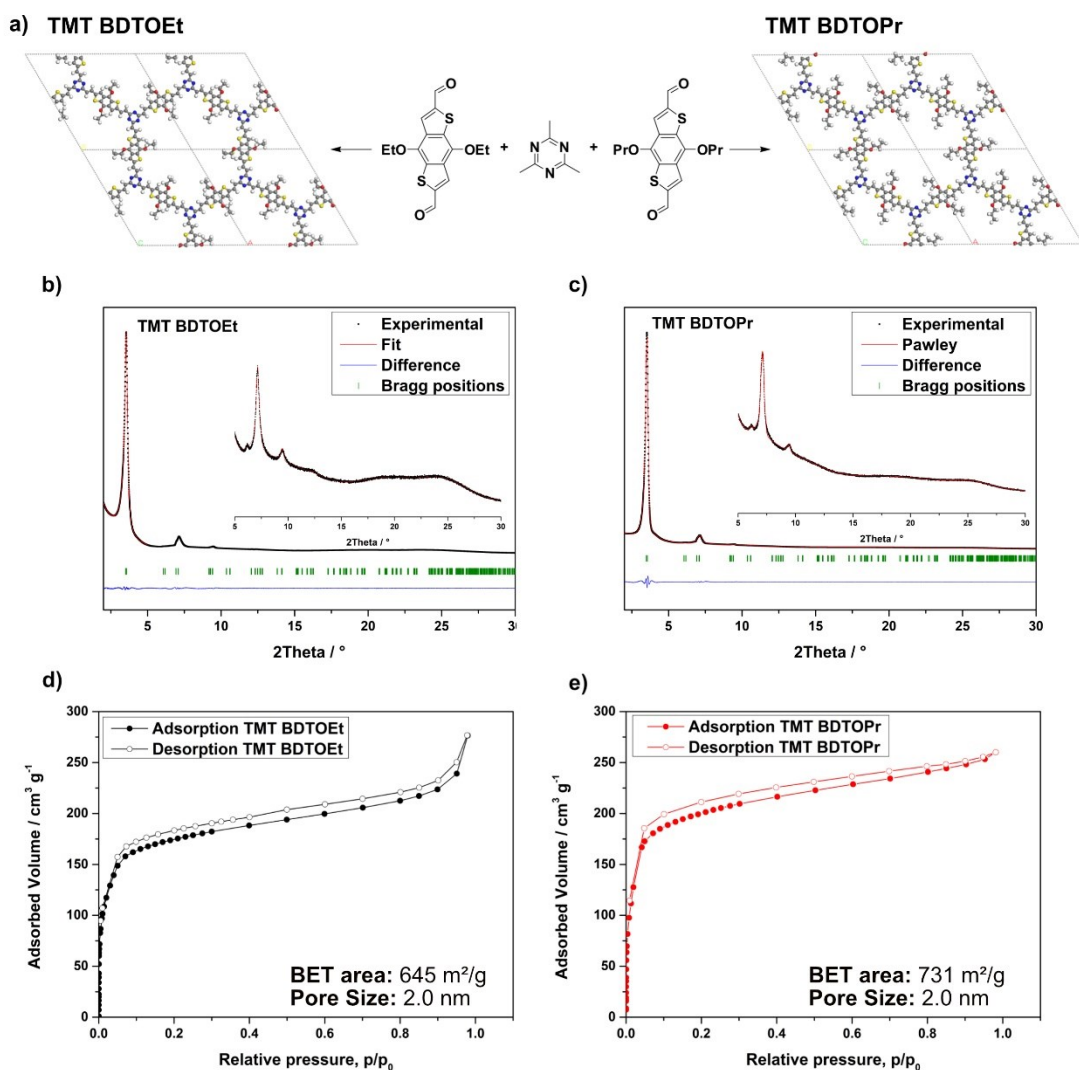


Figure 5.1 (a) Schematic representation of the synthesis of TMT BDTOEt and TMT BDTOPr from the molecular building blocks. (b) and (c) Experimental PXRD pattern (black dots) of TMT BDTOEt and TMT BDTOPr COF, respectively. Pawley refinement (red line), difference plot between the experimental data and the Pawley-refined PXRD pattern (blue line), Bragg positions are indicated by green ticks. The insets in both XRD patterns show a magnified view of $2\theta > 5^\circ$. (d) and (e) Nitrogen physisorption isotherms at 77 K of TMT BDTOEt and TMT BDTOPr, respectively.

The obtained powders were analyzed using powder X-ray diffraction to confirm the formation of a crystalline material (PXRD) (Figure 5.1b and c). The PXRD diffractograms of both COFs feature sharp and narrow reflections at small diffraction angles of $2\theta = 3.6^\circ, 7.2^\circ, 9.5^\circ$ and $2\theta = 3.5^\circ, 7.1^\circ, 9.4^\circ$ for TMT BDTOEt and TMT BDTOPr, respectively, (Figure 5.1b and c). According to the symmetry of the employed building blocks, simulations of the possible crystal structures were carried out using the Forcite module of Materials Studio software package (Accelrys Inc.) with the universal force field. For both COFs, assuming an AA model layer arrangement (Figure 5.1a) and using *P1* symmetry, layers with the presence of hexagonally shaped porous structures emerged. The obtained simulated cells were refined using the Reflex module in the Materials Studio software applying the Pawley method for

powder refinement according to the experimentally obtained PXRD patterns (**Figure 5.1b** and **c**). In the simulations, unit cell parameters of $a = 29.3 \text{ \AA}$, $b = 29.5 \text{ \AA}$, $c = 3.7 \text{ \AA}$, $\alpha = \beta = 90^\circ$, $\gamma = 120^\circ$ for TMT BDTOEt and $a = 29.5 \text{ \AA}$, $b = 29.5 \text{ \AA}$, $c = 3.7 \text{ \AA}$, $\alpha = \beta = 90^\circ$, $\gamma = 120^\circ$ for TMT BDTOPr were obtained. Additionally, the observed reflections in the PXRD patterns were indexed and attributed to the corresponding hkl planes. For TMT BDTOEt, hkl (100), (200), (210) correspond to $3.6, 7.2, 9.5^\circ 2\theta$ and for TMT BDTOPr hkl (100), (200), (210) correspond to $3.5, 7.1, 9.4^\circ 2\theta$, indicating the high crystallinity of the formed vinylene-linked COF structures.

To analyze the surface area of the two different structures, nitrogen gas physisorption measurements were conducted at 77 K. The COFs exhibit a type I isotherm with a steep nitrogen uptake at low partial pressures ($p/p_0 < 0.06$ and up to $160 \text{ cm}^3 \text{ g}^{-1}$ for TMT BDTOEt and $p/p_0 < 0.05$ and up to $170 \text{ cm}^3 \text{ g}^{-1}$ for TMT BDTOPr) indicating the presence of a microporous system for both vinylene-linked COFs (**Figure 5.1** and **e**). Additionally, in both cases, the adsorption isotherms are fully reversible showing nearly no hysteresis. For the analysis of the pore sizes the quenched solid density functional theory (QSDFT) model for 1D cylindrical pores and carbon surfaces was used. Pore sizes (**Figure 5.6**) of 2.0 nm, at the intersection of microporosity and mesoporosity, in both cases were calculated and show good agreement with the structurally modeled pore sizes (2.2 and 2.3 nm for TMT BDTOEt and TMT BDTOPr, respectively). Both COFs revealed high calculated Brunauer, Emmett, Teller (BET) surface areas of 645 and $731 \text{ m}^2 \text{ g}^{-1}$ for TMT BDTOEt and TMT BDTOPr, respectively. Thermogravimetric analysis under synthetic air flow revealed that both TMT COFs are thermally stable. Significant weight loss at around 350°C is detected indicating structural degradation, and the termination of the degradation process is evident at 550°C associated with a complete weight loss (**Figure 5.7**).

Further, to confirm the successful condensation reaction and the formation of C=C double bonds, IR-measurements of the resulting powders as well as the precursors were conducted. Here, in the absorption spectrum of the BDTOEt and BDTOPr building blocks, a clear peak at 1660 cm^{-1} referring to the aldehyde functional groups is visible. Upon condensation, this peak attenuated, and a new peak appears at around 1616 cm^{-1} in both cases, corresponding to the C=C bond stretching (**Figure 5.2a, b**). The morphology of the resulting vinylene-linked COF powders was analyzed using scanning electron microscopy (SEM) (**Figure 5.2**). For both COFs, an elongated and wavy wire-like morphology is observed. In the case of TMT BDTOEt the wavy wires are clockwise and anti-clockwise coiled up to form chiral corkscrew-like entities (**Figure 5.2c**). Transmission electron microscopy (TEM) and the respective electron diffraction patterns further support the formation of crystalline COFs (**Figure 5.2, f**).

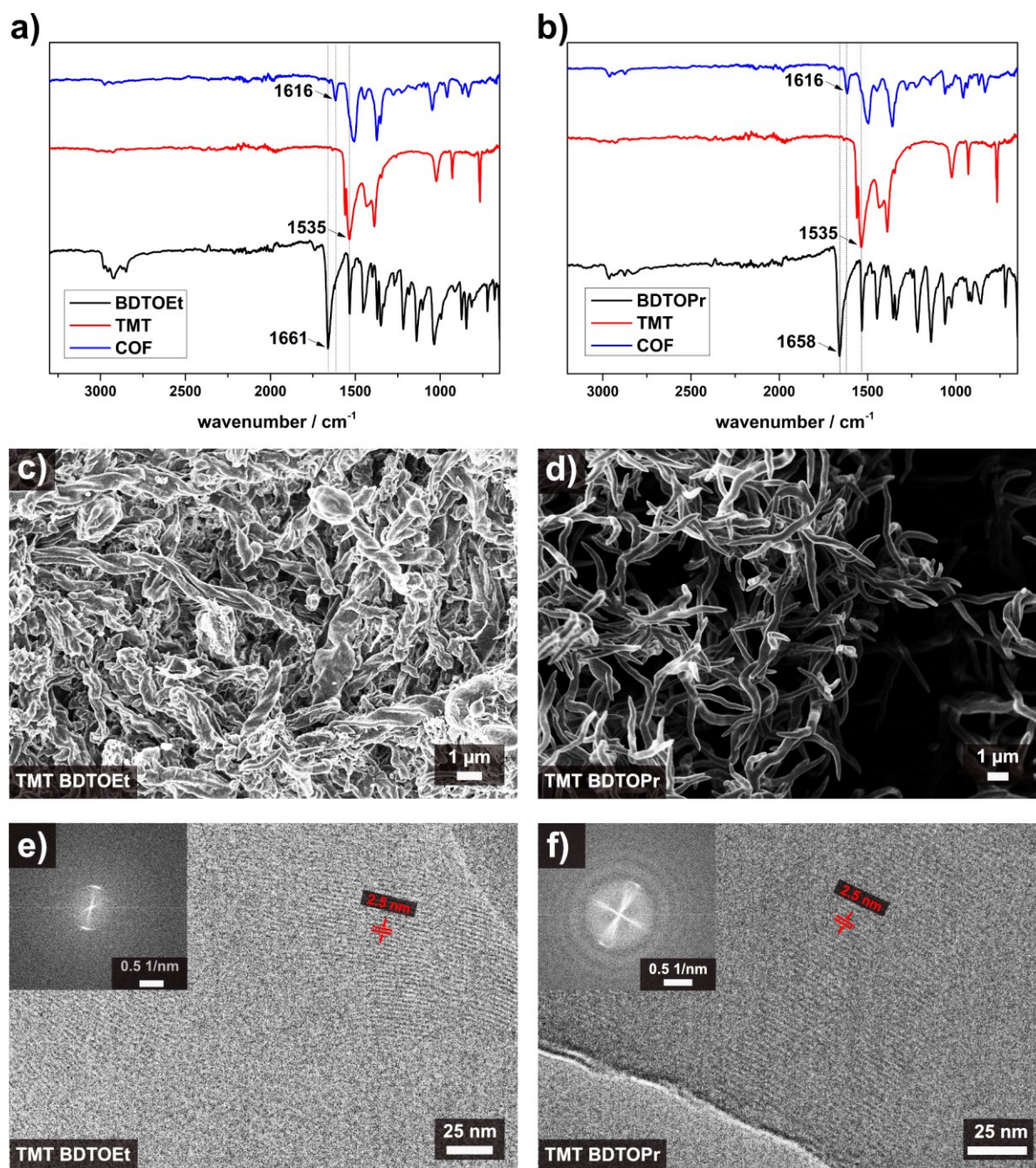


Figure 5.2. (a) and (b) IR spectra of TMT BDTOEt and TMT BDTOPr and the building blocks, respectively. (c) and (d) SEM images of TMT BDTOEt and TMT BDTOPr bulk powders. (e) and (f) TEM images of TMT BDTOEt and TMT BDTOPr, respectively.

5.3.3 Film Synthesis via Vapor-assisted Conversion

To enable the utilization and performance assessment of vinylene-linked COFs for applications, particularly as functional devices, the growth of thin vinylene-linked COF films with control over film thickness, morphology and crystallinity is highly desirable.

As the synthesis of the highly crystalline vinylene-linked COFs without an activation agent is a challenging task, the primary methodology of choice to obtain the on-surface growth was the well-established *in-situ* growth approach, namely the growth of film and powders simultaneously, employing the exact same conditions developed for the bulk synthesis. However, at elevated temperature and including a substrate in the reaction mixtures, the resulting COF films obtained from the reaction mixture exhibited poor coverage and crystallinity. Next, we turned to the vapor-assisted conversion approach which was developed for boronate ester- and boroxine-linked COFs³² as well as for metal-organic frameworks³³. In contrast to solvothermal approaches, VAC allows for the formation of highly crystalline frameworks as smooth and homogeneous films on top of a large variety of different substrates or films featuring textural porosity depending on the conversion scheme utilized (**Figure 5.3a**). For the VAC film synthesis of thiophene based vinylene-linked COFs, reaction parameter screening was employed where temperature and reaction times were the first parameters to study. For the synthesis, the reaction precursors were dissolved in a methanol/mesitylene 8:1 v:v solvent mixture and sonicated. After the addition of the respective amount of solid NaOH and subsequent sonication, the reactive solution was deposited on top of a glass substrate which was beforehand placed in a glass autoclave. On the bottom of the glass autoclave, spacers were placed as a platform for the glass substrate along with a methanol/ mesitylene 8:1 v:v solvent mixture which served as vapor source throughout the reaction. Subsequently, the glass autoclave was heated in an oven with temperatures ranging from 40 °C to 130 °C. After a designated reaction time of 24 h, the substrate was evenly covered with a bright, red-colored deposit layer. Subsequently, the coated glass substrate was removed from the reactor and dried under high vacuum.

Grazing-incidence wide-angle X-ray scattering analysis (GI-WAXS) and X-ray diffraction (XRD) were employed to study the long-range order of the obtained, red-colored deposits (**Figure 5.3d** and **Figure 5.8**). Strikingly, GI-WAXS measurements confirmed that for the first time, highly crystalline vinylene frameworks were formed on top of a substrate under mild reaction conditions, moderate temperatures and short reaction times using the VAC methodology (**Figure 5.3d**). The strong reflections at q_y 2.5 and 5.2 nm⁻¹ correspond to *hkl* (100), (200) and agree well with the corresponding bulk XRD patterns. This points to a crystalline deposit with random crystallite orientation. Further, powder X-ray diffraction (**Figure 5.3e**) showed the long-range order of the resulting deposits with the framework formation being completed after 6 h. Strikingly, under VAC conditions, these vinylene-linked frameworks nucleate and grow at a moderate temperature of 40 °C and a reaction time of 22 h (**Figure 5.9**). The crystallinity of the resulting deposits was assessed after 24 h at the different temperatures (ranging from 40-130°C). With this, an optimum temperature of 130 °C was found since this way, a highly crystalline COF deposit on top of the substrate was obtained. Moreover, the given reaction times were examined when using a fixed temperature of 130 °C. Under elevated temperature, first stages of framework formation are visible after a short reaction time of 30 minutes (**Figure 5.10**), and a successful formation of highly crystalline

frameworks was confirmed after 6 h reaction time. Finally, the vapor composition was examined. Here, altered ratios of a methanol/mesitylene solvent mixture ranging from only methanol to only mesitylene were employed. In the presence of solely mesitylene as vapor component, a poorly crystalline framework was obtained. Contrarily, using methanol as the sole vapor source, a crystalline framework was forming whereas COF deposits with a high degree in crystallinity were obtained when a methanol/mesitylene 8:1 v:v solvent mixture was used as vapor source (**Figure 5.11**). Summarizing, the optimal conditions for the synthesis of vinylene-linked TMT BDTOPr COF deposits were obtained at elevated temperature of 130 °C, a reaction time of 6 h and a methanol/mesitylene 8:1 v:v solvent mixture as vapor source (**Figure 5.3d and e**).

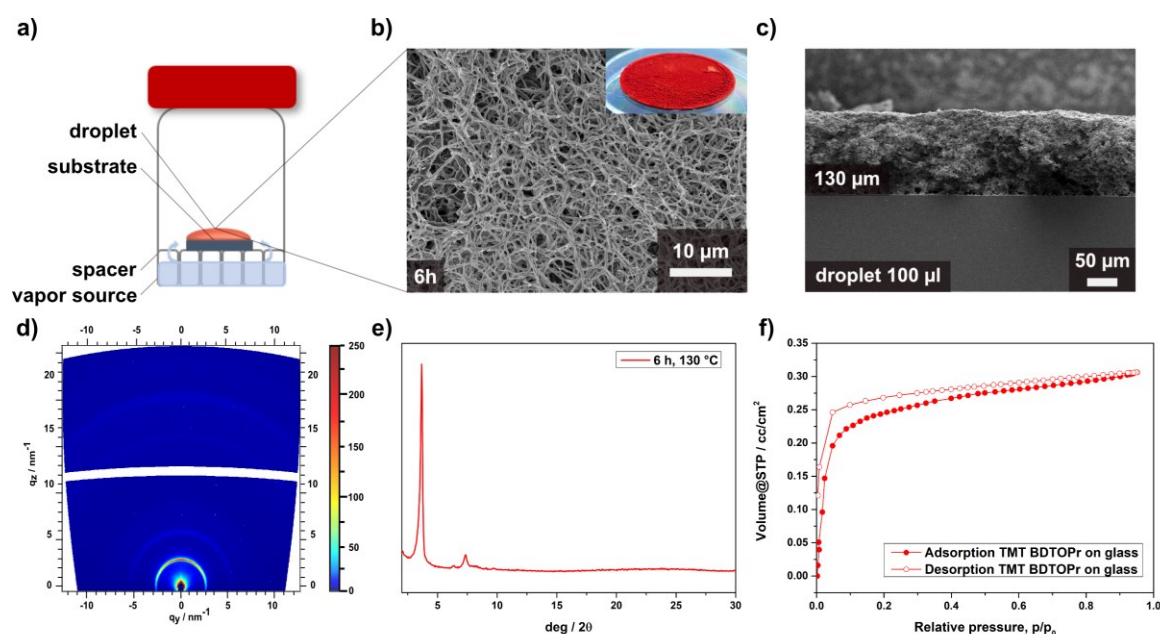


Figure 5.3 (a) Schematic representation of the film synthesis of TMT BDTOEt and TMT BDTOPr thin films using vapor-assisted conversion. (b) and (c) SEM top-view and cross-section images of a selected VAC film of TMT BDTOPr and a macroscopic photograph thereof as inset. (d) GIWAXS 2D pattern of TMT BDTOPr VAC thin film grown on glass. (e) Experimental PXRD pattern of TMT BDTOPr VAC thin film on glass. (f) Krypton physisorption isotherm of TMT BDTOPr COF films grown on glass substrates measured at 77.3 K.

SEM top-view images show that with VAC a homogeneous and even deposit is obtained on top of the surface consisting of small intergrown filaments which then form a continuous layer (see SEM top-view and cross section images **Figure 5.3b** and **c**). Depending on the droplet size (ranging from 50-100 μl on a 10x10 mm glass substrate), the thickness of the respective COF layer could be tuned, ranging from 80 to 130 μm in the case of TMT BDTOPr (for more information and SEM cross-section images see **Figure 5.15** and for additional data on TMT BDTOEt, see **Figure 5.13**). To further show the generality of this approach, the film formation was not only conducted on glass substrates but successfully expanded to substrates such as indium doped tin oxide (ITO) or gold-coated glass substrates (**Figure 5.12** and **Figure 5.14**). One of the important advantages of this method is that only a small amount of reactive precursors is needed for the formation of a large number of evenly covered substrates, e.g. using only 13 μmol of

the building blocks and a droplet size of 50 μl , 10 glass substrates (10 mm x 10 mm) can be evenly covered.

Using krypton sorption measurements at 77 K, the porosity of the prepared vinylene-linked COF films was analyzed. To obtain porosity, the films must be completely free of residual solvents or reactants. Therefore, the COF layers were grown on glass substrates and heated to 120 °C under vacuum prior to the sorption measurements. Thereby, a type I isotherm with one steep nitrogen uptake at low partial pressures ($p/p_0 < 0.07$ and up to $0.08 \text{ cm}^3 \text{ cm}^{-2}$ for TMT BDTOEt and $p/p_0 < 0.07$ and up to $0.21 \text{ cm}^3 \text{ cm}^{-2}$ for TMT BDTOPr) was obtained indicating a defined microporous structure as well as a narrow pore size distribution. Additionally, this corresponds well to the nitrogen sorption isotherms obtained for the bulk powders. Thus, the successful formation of vinylene-linked TMT COF films featuring additional textural porosity (as shown in the SEM images) was further confirmed (**Figure 5.3f** and **Figure 5.16**). The Brunauer-Emmett-Teller (BET) surface area was normalized to the geometric surface area and was calculated to be as high as $315 \text{ cm}^2/\text{cm}^2$ ($p/p_0 = 0.05\text{-}0.12$) for TMT BDTOEt and $680 \text{ cm}^2/\text{cm}^2$ ($p/p_0 = 0.05\text{-}0.30$) for TMT BDTOPr.

5.3.4 Photophysical Properties

Next, photophysical properties of the new vinylene-linked TMT COFs were investigated using UV-vis, PL and time-correlated single photon-counting (TCSPC) spectroscopies (**Figure 5.17** and **Figure 5.18**). Both COFs were found to be absorbing in the 300-610 nm spectral range. Thereby, both COFs feature an absorption onset at around 630 nm and an absorption maximum at around 500 nm (**Figure 5.18A**). Tauc plots were constructed to determine the optical band gaps of the two structures from the absorption spectra, yielding an optical bandgap of 2 eV for both COFs, assuming a direct band gap transition (**Figure 5.17B** and **C**). Steady-state photoluminescence (PL) of both TMT COFs was measured with an excitation wavelength of $\lambda_{\text{exc}} = 378 \text{ nm}$. Both COFs show similar rather narrow emission bands with a maximum at approximately 690 nm (**Figure 5.18A**). Furthermore, PL spectra of TMT COF films on glass grown by VAC show the same characteristics as the bulk powders. Using different droplet sizes for the film growth, the thickness of the resulting films was varied allowing for altered PL emission intensities where the intensity increases with increasing thickness of the COF layers (**Figure 5.19**). To study the excited state dynamics, time-correlated single photon counting (TCSPC) measurements were conducted. To this end, a 378 nm pulsed laser was used to excite the COF films and to obtain the decay profile of photoexcited singlet states that were generated in the respective COF bulk powders.

When fitting the data with a tri-exponential fit, lifetimes of 0.70 ns (69 %) and 0.69 ns (58 %) were obtained for the largest contributions for TMT BDTOEt and TMT BDTOPr, respectively. More information on the resulting TCSPC data can be found in the supporting information (**Figure 5.18B** and **C**).

Interestingly, the TMT COFs show a drastic change in their optical properties upon interaction with specific polar solvents (**Figure 5.4, Figure 5.21-5.22**). We found that while *n*-pentane or acetonitrile (MeCN) did not affect the PL properties of the TMT COFs, ethanol, water, and iso-propanol had a strong impact on it which might be attributed to a solvatochromic effect. In all cases, there was a change in fluorescence intensity and emission wavelength (**Figure 5.4a**), whereas ethanol showed the strongest effect with the emission wavelength changing from 690 nm for the pristine TMT BDTOPr COF to 480 nm after soaking the COF films with a droplet of ethanol. Importantly, the crystallinity of the TMT COFs was maintained throughout the solvent treatment, underscoring the robustness of these vinylene-linked COFs (**Figure 5.22**). Furthermore, the lifetimes of the excited states were examined upon interaction with the different solvents (**Figure 5.4b and c**). After addition of the solvents the lifetimes for the largest contributions changed from 0.69 ns (58%) to 8.16 ns (63%) and 9.97 ns (87%) upon interaction with ethanol and water, respectively. As control experiment, we dropcast a mixture of the respective building blocks on a glass substrate and measured photoluminescence. In this case, the photon emission was dominated by the strong emission of the BDTOPr building block with an emission wavelength of 650 nm and no effect could be measured upon addition of a droplet of ethanol or water, showing that the strong shift in PL emission can only be obtained upon interaction of the solvents with the respective frameworks (**Figure 5.20**). As a second control experiment, we tested whether the effect is also present when a suspension of TMT BDTOPr COF bulk powder in ethanol is measured. Thereby, the emission wavelength of 480 nm was obtained as for the VAC films and a strong decrease in intensity was noted upon ultrasonication of the suspension (**Figure 5.21**).

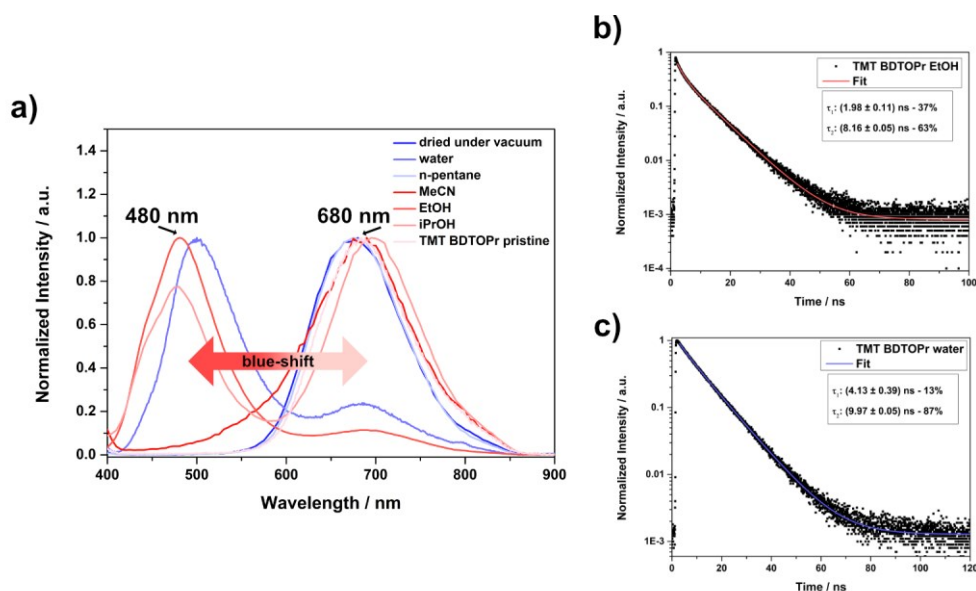


Figure 5.4 (a) Normalized PL ($\lambda_{\text{exc}} = 378 \text{ nm}$) spectra of pristine TMT BDTOPr COF film on a glass substrate and after addition of one droplet of the respective solvents. (b) and (c) Time-correlated single photon counting histograms of TMT BDTOPr COF film on a glass substrate after the addition of a droplet of ethanol and water, respectively.

To shed light on the possible solvatochromic effect, a model system was synthesized by reacting TMT with 4,8-diethoxybenzo[1,2-b;4,5-b']dithiophene-2-carbaldehyde (for details on the synthesis see appendix **section 5.6.2**). The resulting compound was dissolved in different solvents and the respective absorption and emission bands were measured. Thereby, a drastic blue-shift in absorption and emission wavelengths was observed when changing from solid material to dissolved (**Figure 5.23**) corresponding to differences in aggregation in the solid powder compared to the solutions. Moreover, changes in the emission absorption maxima were observed for the different solvents corresponding to different polarities of the applied solvents confirming that the model system exhibits a solvatochromic effect.

Furthermore, the PL emission profile of an amorphous polymer sample was measured. In this case, the strong blue shift in emission maxima was observed upon soaking the sample with water (**Figure 5.24**). Interestingly, the impact of solvents was more pronounced for the COFs given that the intensity changed more effectively for the frameworks upon interaction with solvents. This could be attributed to a textural effect since, the VAC films of the frameworks show high textural porosity and thereby, the uptake of solvents is effective compared to the non-crystalline polymer.

5.4 Conclusion

In summary, we showed the synthesis of two new highly crystalline thiophene-based vinylene-linked COF structures, namely TMT BDTOEt and TMT BDTOPr, which were formed *via* base-catalyzed Knoevenagel condensation reaction upon combination of trimethyl-triazine (TMT) and different functionalized benzo-dithiophene aldehydes. Moreover, the well-established VAC-method was used to form vinylene-linked COF films with good control over thickness and crystallinity. Thereby, different reaction conditions such as temperature, reaction time and vapor sources were assessed and their influence on the film crystallinity was probed using X-ray diffraction. Notably, we show, for the first time, that vinylene-linked COFs nucleate and grow under mild conditions, such as 40 °C or short reaction times of only 30 minutes. These novel vinylene-linked COFs feature interesting photophysical properties as bulk and films. They feature light absorption in the 300-610 nm wavelength range and a band gap of 2.0 eV, assuming a direct transition. Photoluminescence (PL) spectroscopy revealed strong photon emission at 690 nm for both COFs, which is strongly blue-shifted up to 480 nm upon interaction with different solvents such as water or ethanol, apparently resulting from a solvatochromic effect. Moreover, after addition of the solvents the lifetimes for the largest contributions changed from 0.69 ns (58%) to 8.16 ns (63%) and 9.97 ns (87%) upon interaction with ethanol and water, respectively.

5.5 References

- (1) Côté, A. P.; Benin, A. I.; Ockwig, N. W.; O’Keeffe, M.; Matzger, A. J.; Yaghi, O. M. Porous, Crystalline, Covalent Organic Frameworks. *Science* **2005**, *310*, 1166.
- (2) Li, Z.; Feng, X.; Zou, Y.; Zhang, Y.; Xia, H.; Liu, X.; Mu, Y. A 2D azine-linked covalent organic framework for gas storage applications. *Chem. Commun.* **2014**, *50*, 13825–13828.
- (3) Fan, H.; Mundstock, A.; Feldhoff, A.; Knebel, A.; Gu, J.; Meng, H.; Caro, J. Covalent Organic Framework–Covalent Organic Framework Bilayer Membranes for Highly Selective Gas Separation. *J. Am. Chem. Soc.* **2018**, *140*, 10094–10098.
- (4) Ascherl, L.; Evans, E. W.; Gorman, J.; Orsborne, S.; Bessinger, D.; Bein, T.; Friend, R. H.; Auras, F. Perylene-Based Covalent Organic Frameworks for Acid Vapor Sensing. *J. Am. Chem. Soc.* **2019**, *141*, 15693–15699.
- (5) Jhulki, S.; Evans, A. M.; Hao, X.-L.; Cooper, M. W.; Feriante, C. H.; Leisen, J.; Li, H.; Lam, D.; Hersam, M. C.; Barlow, S.; et al. Humidity Sensing through Reversible Isomerization of a Covalent Organic Framework. *J. Am. Chem. Soc.* **2020**, *142*, 783–791.
- (6) Wang, Y.; Zhao, Z.; Li, G.; Yan, Y.; Hao, C. A 2D covalent organic framework as a sensor for detecting formaldehyde. *J. Mol. Model.* **2018**, *24*, 153.
- (7) Wang, Y.; Liu, H.; Pan, Q.; Wu, C.; Hao, W.; Xu, J.; Chen, R.; Liu, J.; Li, Z.; Zhao, Y. Construction of Fully Conjugated Covalent Organic Frameworks via Facile Linkage Conversion for Efficient Photoenzymatic Catalysis. *J. Am. Chem. Soc.* **2020**, *142*, 5958–5963.
- (8) Shen, J.-C.; Jiang, W.-L.; Guo, W.-D.; Qi, Q.-Y.; Ma, D.-L.; Lou, X.; Shen, M.; Hu, B.; Yang, H.-B.; Zhao, X. A rings-in-pores net: crown ether-based covalent organic frameworks for phase-transfer catalysis. *Chem. Commun.* **2020**, *56*, 595–598.
- (9) Khan, N. A.; Zhang, R.; Wu, H.; Shen, J.; Yuan, J.; Fan, C.; Cao, L.; Olson, M. A.; Jiang, Z. Solid–Vapor Interface Engineered Covalent Organic Framework Membranes for Molecular Separation. *J. Am. Chem. Soc.* **2020**, *142*, 13450–13458.
- (10) Cui, W.-R.; Zhang, C.-R.; Jiang, W.; Li, F.-F.; Liang, R.-P.; Liu, J.; Qiu, J.-D. Regenerable and stable sp² carbon-conjugated covalent organic frameworks for selective detection and extraction of uranium. *Nat. Commun.* **2020**, *11*, 436.

- (11) Calik, M.; Auras, F.; Salonen, L. M.; Bader, K.; Grill, I.; Handloser, M.; Medina, D. D.; Dogru, M.; Löbermann, F.; Trauner, D.; et al. Extraction of Photogenerated Electrons and Holes from a Covalent Organic Framework Integrated Heterojunction. *J. Am. Chem. Soc.* **2014**, *136*, 17802–17807.
- (12) Guo, J.; Xu, Y.; Jin, S.; Chen, L.; Kaji, T.; Honsho, Y.; Addicoat, M. A.; Kim, J.; Saeki, A.; Ihee, H.; et al. Conjugated organic framework with three-dimensionally ordered stable structure and delocalized π clouds. *Nat. Commun.* **2013**, *4*, 2736.
- (13) Dalapati, S.; Jin, E.; Addicoat, M.; Heine, T.; Jiang, D. Highly Emissive Covalent Organic Frameworks. *J. Am. Chem. Soc.* **2016**, *138*, 5797–5800.
- (14) Martínez-Abadía, M.; Stoppiello, C. T.; Strutynski, K.; Lerma-Berlanga, B.; Martí-Gastaldo, C.; Saeki, A.; Melle-Franco, M.; Khlobystov, A. N.; Mateo-Alonso, A. A Wavy Two-Dimensional Covalent Organic Framework from Core-Twisted Polycyclic Aromatic Hydrocarbons. *J. Am. Chem. Soc.* **2019**, *141*, 14403–14410.
- (15) Salonen, L. M.; Medina, D. D.; Carbó-Argibay, E.; Goesten, M. G.; Mafra, L.; Guldris, N.; Rotter, J. M.; Stroppa, D. G.; Rodríguez-Abreu, C. A supramolecular strategy based on molecular dipole moments for high-quality covalent organic frameworks. *Chem. Commun.* **2016**, *52*, 7986–7989.
- (16) Evans, A. M.; Castano, I.; Brumberg, A.; Parent, L. R.; Corcos, A. R.; Li, R. L.; Flanders, N. C.; Gosztola, D. J.; Gianneschi, N. C.; Schaller, R. D.; et al. Emissive Single-Crystalline Boroxine-Linked Colloidal Covalent Organic Frameworks. *J. Am. Chem. Soc.* **2019**, *141*, 19728–19735.
- (17) Frey, L.; Jarju, J. J.; Salonen, L. M.; Medina, D. D. Boronic-acid-derived covalent organic frameworks: from synthesis to applications. *New J. Chem.* **2021**, *45*, 14879–14907.
- (18) Jackson, K. T.; Reich, T. E.; El-Kaderi, H. M. Targeted synthesis of a porous borazine-linked covalent organic framework. *Chem. Commun.* **2012**, *48*, 8823–8825.
- (19) Keller, N.; Sick, T.; Bach, N. N.; Koszalkowski, A.; Rotter, J. M.; Medina, D. D.; Bein, T. Dibenzochrysenes enables tightly controlled docking and stabilizes photoexcited states in dual-pore covalent organic frameworks. *Nanoscale* **2019**, *11*, 23338–23345.
- (20) Bessinger, D.; Muggli, K.; Beetz, M.; Auras, F.; Bein, T. Fast-Switching Vis-IR Electrochromic Covalent Organic Frameworks. *J. Am. Chem. Soc.* **2021**, *143*, 7351–7357.

- (21) Rotter, J. M.; Guntermann, R.; Auth, M.; Mähringer, A.; Sperlich, A.; Dyakonov, V.; Medina, D. D.; Bein, T. Highly conducting Wurster-type twisted covalent organic frameworks. *Chem. Sci.* **2020**, *11*, 12843–12853.
- (22) Haase, F.; Troschke, E.; Savasci, G.; Banerjee, T.; Duppel, V.; Dörfler, S.; Grundei, M. M. J.; Burow, A. M.; Ochsenfeld, C.; Kaskel, S.; et al. Topochemical conversion of an imine- into a thiazole-linked covalent organic framework enabling real structure analysis. *Nat. Commun.* **2018**, *9*, 2600.
- (23) Yang, Y.; He, X.; Zhang, P.; Andaloussi, Y. H.; Zhang, H.; Jiang, Z.; Chen, Y.; Ma, S.; Cheng, P.; Zhang, Z. Combined Intrinsic and Extrinsic Proton Conduction in Robust Covalent Organic Frameworks for Hydrogen Fuel Cell Applications. *Angew. Chem. Int. Ed.* **2020**, *59*, 3678–3684.
- (24) Acharjya, A.; Pachfule, P.; Roeser, J.; Schmitt, F.-J.; Thomas, A. Vinylene-Linked Covalent Organic Frameworks by Base-Catalyzed Aldol Condensation. *Angew. Chem. Int. Ed.* **2019**, *58*, 14865–14870.
- (25) Bi, S.; Thiruvengadam, P.; Wei, S.; Zhang, W.; Zhang, F.; Gao, L.; Xu, J.; Wu, D.; Chen, J.-S. Vinylene-Bridged Two-Dimensional Covalent Organic Frameworks via Knoevenagel Condensation of Tricyanomesitylene. *J. Am. Chem. Soc.* **2020**, *142*, 11893–11900.
- (26) Jadhav, T.; Fang, Y.; Patterson, W.; Liu, C.-H.; Hamzehpoor, E.; Perepichka, D. F. 2D Poly(arylene vinylene) Covalent Organic Frameworks via Aldol Condensation of Trimethyltriazine. *Angew. Chem. Int. Ed.* **2019**, *58*, 13753–13757.
- (27) Lyu, H.; Diercks, C. S.; Zhu, C.; Yaghi, O. M. Porous Crystalline Olefin-Linked Covalent Organic Frameworks. *J. Am. Chem. Soc.* **2019**, *141*, 6848–6852.
- (28) Xu, S.; Richter, M.; Feng, X. Vinylene-Linked Two-Dimensional Covalent Organic Frameworks: Synthesis and Functions. *Acc. Mater. Res.* **2021**, *2*, 252–265.
- (29) Xu, S.; Sun, H.; Addicoat, M.; Biswal, B. P.; He, F.; Park, S.; Paasch, S.; Zhang, T.; Sheng, W.; Brunner, E.; et al. Thiophene-Bridged Donor–Acceptor sp²-Carbon-Linked 2D Conjugated Polymers as Photocathodes for Water Reduction. *Adv. Mater.* **2021**, *33*, 2006274.
- (30) Zhao, Y.; Liu, H.; Wu, C.; Zhang, Z.; Pan, Q.; Hu, F.; Wang, R.; Li, P.; Huang, X.; Li, Z. Fully Conjugated Two-Dimensional sp²-Carbon Covalent Organic Frameworks as Artificial Photosystem I with High Efficiency. *Angew. Chem. Int. Ed.* **2019**, *58*, 5376–5381.

- (31) Bi, S.; Meng, F.; Wu, D.; Zhang, F. Synthesis of Vinylene-Linked Covalent Organic Frameworks by Monomer Self-Catalyzed Activation of Knoevenagel Condensation. *Journal of the American Chemical Society* **2022**, *144*, 3653–3659.
- (32) Medina, D. D.; Rotter, J. M.; Hu, Y.; Dogru, M.; Werner, V.; Auras, F.; Markiewicz, J. T.; Knochel, P.; Bein, T. Room Temperature Synthesis of Covalent–Organic Framework Films through Vapor-Assisted Conversion. *J. Am. Chem. Soc.* **2015**, *137*, 1016–1019.
- (33) Virmani, E.; Rotter, J. M.; Mähringer, A.; Zons, T. von; Godt, A.; Bein, T.; Wuttke, S.; Medina, D. D. On-Surface Synthesis of Highly Oriented Thin Metal–Organic Framework Films through Vapor-Assisted Conversion. *J. Am. Chem. Soc.* **2018**, *140*, 4812–4819.
- (31) Li, X. sp² carbon-conjugated covalent organic frameworks: synthesis, properties, and applications. *Mater. Chem. Front.* **2021**, *5*, 2931–2949.

5.6 Appendix

5.6.1 Methods

Nuclear magnetic resonance (NMR) spectra were recorded on Bruker AV 400 and AV 400 TR spectrometers. Chemical shifts are expressed in parts per million (δ scale) and are calibrated using residual (undeuterated) solvent peaks as an internal reference ($^1\text{H-NMR}$: CDCl_3 : 7.26, DMSO-d_6 : 2.50, DMF-d_7 : 8.03; $^{13}\text{C-NMR}$: CDCl_3 : 77.16, DMSO-d_6 : 39.52, DMF-d_7 : 163.15). Data for $^1\text{H NMR}$ spectra are reported in the following way: chemical shift (δ ppm) (multiplicity, coupling constant/ Hz, integration). Multiplicities are reported as follows: s= singlet, d= doublet, t= triplet, q= quartet, m= multiplet, or combinations of thereof.

High resolution electron ionization (EI) **mass spectra (MS)** were recorded with a Thermo Finnigan MAT 95 instrument.

Powder X-ray diffraction (PXRD) measurements were performed using a Bruker D8 Discover with Ni-filtered $\text{Cu K}\alpha$ radiation and a LynxEye position-sensitive detector.

The **structure models of the COFs** were constructed using the Accelrys Materials Studio soft-ware package. For each COF the highest possible symmetry was applied. Structure refinements using the Pawley method were carried out as implemented in the Reflex module of the Materials Studio software.

Nitrogen sorption isotherms were recorded with Quantachrome Autosorb 1 and Autosorb iQ instruments at 77 K. The samples were outgassed for 24h at 120 °C under high vacuum prior to the measurements. Pore size distributions were calculated using the QSDFT model with a carbon kernel for cylindrical pores.

Krypton sorption isotherms were performed with a Quantachrome Autosorb iQ (Quantachrome instruments, Florida, USA) at 77.3 K, assuming a saturation vapor pressure of $p_0 = 217$ Pa for Krypton. Prior to the measurements, the TMT COF films were activated under high vacuum at 120 °C overnight. For the measurement, the substrates which were evenly covered with COF material, were cut into small pieces and put into the measurement tube. The total surface area of the films was 15 cm^2 . Evaluation of the data was carried out with AsiQwin v.3.01 software.

Scanning electron microscopy (SEM) images were recorded with an FEI Helios NanoLab G3 UC scanning electron microscope equipped with a field emission gun operated at 3-5 kV.

UV-VIS-NIR spectra were recorded using a Perkin-Elmer Lambda 1050 spectrometer equipped with a 150 mm integrating sphere, photomultiplier tube (PMT) and InGaAs detectors. **Diffuse reflectance**

spectra were collected with a Praying Mantis (Harrick) accessory and were referenced to barium sulfate powder as white standard. The specular reflection of the sample surface was removed from the signal using apertures that allow only light scattered at angles $> 20^\circ$ to pass.

2D grazing-incidence wide angle X-ray scattering (GIWAXS) data were recorded with an Anton Paar SAXSpoint 2.0 system equipped with a Primux 100 microCu K_α source and a Dectris EIGER R 1M 2D detector. The COF films were positioned at a sample-detector distance of 140 mm and were measured with an incidence angle of 0.2° .

Photoluminescence (PL) and **time-correlated single photon counting (TCSPC)** data were processed with a FluoTime 300 from PicoQuant GmbH. The samples were photo-excited using a 378 nm laser, (LDH-P-C-375, from PicoQuant GmbH) pulsed at 500 kHz, with a pulse duration of ~ 100 ps and fluence of ~ 300 nJcm⁻²/pulse. The PL was collected using a high-resolution monochromator and photomultiplier detector assembly (PMA-C 192-N-M, PicoQuant GmbH).

Thermogravimetric analysis (TGA) measurements were performed on a Netzsch Jupiter ST 499 C instrument equipped with a Netzsch TASC 414/4 controller. The samples were heated from room temperature to 900°C under a synthetic air flow (25 ml min^{-1}) at a heating rate of 10 K min^{-1} .

A suspension of benzo[1,2-b:4,5-b']dithiophene-4,8-dione (2.29 g, 10.0 mmol, 1.0 eq.) in 40 mL 20% NaOH was heated to 90 °C. Zn dust (1.50 g, 22.9 mmol, 2.3 eq.) was added and the reaction mixture was stirred at 90 °C. After 1 h, ethyl-*p*-toluenesulfonate (5.95 g, 29.7 mmol, 2.97 eq.) or propyl-*p*-toluenesulfonate (6.36 g, 29.7 mmol, 2.97 eq.) was added and the resulting mixture was heated to 80 °C overnight. After completion, the solution was extracted with dichloromethane. The combined organic phases were dried over MgSO₄, the dried solution was filtered, and the filtrate was concentrated under reduced pressure. Purification *via* column chromatography (silica gel, CH₂Cl₂) afforded the compound as colorless solid in the case of the ethoxy-functionalization (1.56 g, 5.59 mmol, 56 %) and light yellow solid for 4,8-dipropoxybenzo[1,2-b:4,5-b']dithiophene (1.84 g, 6.0 mmol, 60 %).

4,8-diethoxybenzo[1,2-b:4,5-b']dithiophene (1.05 g, 3.76 mmol, 1.0 eq) was dissolved in 61 mL THF and cooled to -78 °C. *n*-BuLi (3.76 mL, 7.52 mmol, 2.1 eq) was slowly added and the solution was stirred at -78 °C for 1 h. After that, DMF (1.04 mL, 13.5 mmol, 3.6 eq.) was added, the solution was stirred at -78 °C and it was allowed to warm to room temperature overnight. After completion, 2M HCl was added and the mixture was extracted with CH₂Cl₂. The combined organic phases were dried over MgSO₄, the dried solution was filtered and the filtrate was concentrated under reduced pressure. Purification *via* column chromatography (silica gel, hexane/ EtOAc 5:1) afforded the compound as orange solid (1.05 g, 3.14 mmol, 84%).

4,8-dipropoxybenzo[1,2-b:4,5-b']dithiophene (1.0 g, 3.06 mmol, 1.0 eq) was dissolved in 51 mL THF and cooled to -78 °C. *n*-BuLi (3.06 mL, 6.12 mmol, 2.1 eq) was slowly added and the solution was stirred at -78 °C for 1 h. After that, DMF (0.85 mL, 11.02 mmol, 3.6 eq.) was added, the solution was stirred at -78 °C and it was allowed to warm to room temperature overnight. After completion, 2M HCl was added and the mixture was extracted with CH₂Cl₂. The combined organic phases were dried over MgSO₄, the dried solution was filtered and the filtrate was concentrated under reduced pressure. Purification *via* column chromatography (silica gel, hexane/ EtOAc 5:1) afforded the compound as orange solid (898 mg, 2.48 mmol, 81%).

BDTOEt

¹H NMR (400 MHz, CDCl₃) δ = 10.1 (s, 2H), 8.2 (s, 2H), 4.45 (q, *J* = 7.0 Hz, 4H), 1.53 (t, *J* = 7.0 Hz, 6H).

¹³C NMR (100 MHz, CDCl₃) δ = 186.4, 146.2, 143.9, 132.8, 132.7, 131.0, 70.3, 15.9.

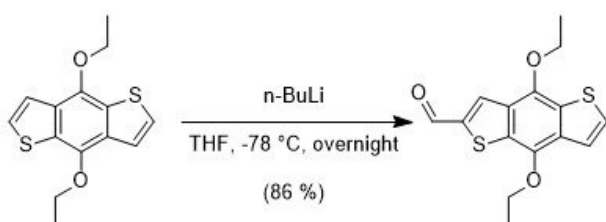
HRMS (EI) calcd for C₁₆H₁₄O₄S₂ [M]⁺: 334.03; found 334.03.

BDTOPr

$^1\text{H NMR}$ (400 MHz, $\text{DMSO-}d_6$) δ = 10.2 (s, 2H), 8.7 (s, 2H), 4.4 (t, J = 6.4 Hz, 4H), 1.8 – 1.9 (m, 4H), 1.1 (t, J = 7.4 Hz, 6H).

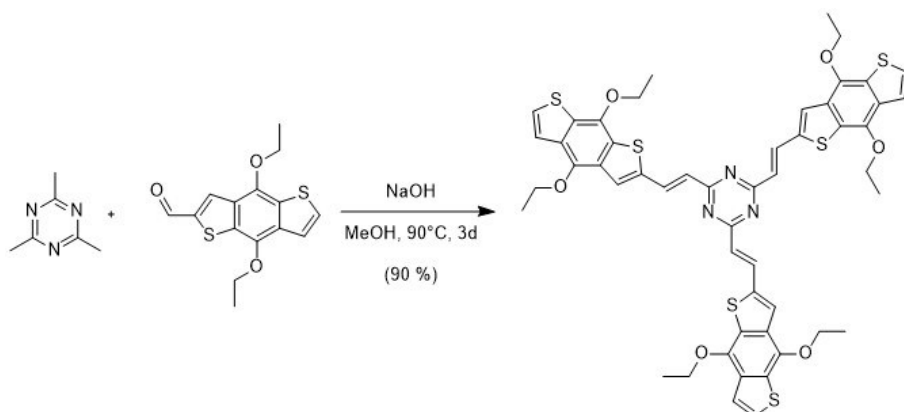
$^{13}\text{C NMR}$ (100 MHz, $\text{DMSO-}d_6$) δ = 186.4, 146.4, 143.9, 132.6, 132.5, 130.8, 76.0, 23.3, 10.4.

HRMS (EI) calcd for $\text{C}_{18}\text{H}_{18}\text{O}_4\text{S}_2$ $[\text{M}]^+$: 362.06; found 362.06.

4,8-diethoxybenzo[1,2-b;4,5-b']dithiophene-2-carbaldehyde

4,8-diethoxybenzo[1,2-b;4,5-b']dithiophene (835.2 mg, 3 mmol, 1.0 eq) was dissolved in 48 mL THF and cooled to $-78\text{ }^\circ\text{C}$. $n\text{-BuLi}$ (1.32 mL, 3.3 mmol, 1.1 eq) was slowly added and the solution was stirred at $-78\text{ }^\circ\text{C}$ for 1 h. After that, DMF (0.42 mL, 5.4 mmol, 1.8 eq.) was added, the solution was stirred at $-78\text{ }^\circ\text{C}$ and it was allowed to warm to room temperature overnight. After completion, the reaction mixture was poured onto ice water, filtered and the resulting orange powder was dried under high vacuum to afford the compound as orange solid (790 mg, 2.58 mmol, 86%).

$^1\text{H NMR}$ (400 MHz, CDCl_3) δ = 10.0 (s, 1H), 8.1 (s, 1H), 7.4 (d, J = 0.5 Hz, 2H), 4.45 (q, J = 7.0 Hz, 4H), 1.53 (t, J = 7.0 Hz, 6H).

Synthesis of TMT BDTOEt model system

TMT (12.3 mg, 0.1 mmol) and 4,8-diethoxybenzo[1,2-b;4,5-b']dithiophene-2-carbaldehyde (122 mg, 0.4 mmol) were dissolved in 10 mL methanol. 5 mL of a methanolic KOH solution (84 mg KOH in 5 mL) were added and the reaction mixture was refluxed at 90 °C for 3 days. After the reaction was complete, the resulting powder was filtered off and dried under high vacuum to give the model compound as red solid (88.9 mg, 0.09 mmol, 90%).

¹H NMR (400 MHz, DMSO-d₆) δ = 8.64 (d, *J* = 16.0 Hz, 3H), 8.1 (s, 3H), 7.81 (d, *J* = 5.6 Hz, 3H), 7.58 (d, *J* = 5.5 Hz, 3H), 6.94 (d, *J* = 15.6 Hz, 3H), 4.44-4.35 (m, 12H), 1.50-1.41 (m, 18H).

HRMS (EI) calcd for C₅₁H₄₅N₃O₆S₆ [M]⁺: 987.16; found 987.16.

Synthesis of TMT BDTOEt COF: acidic conditions

In a 6 mL culture tube, TMT (2.0 mg, 16.3 μ mol) and BDTOEt (8.36 mg, 25.0 μ mol) were suspended in a mixture of mesitylene and 1,4-dioxane (300 μ L, v: v 1:1). After adding 8.3 μ L of MeCN and 67 μ L of trifluoroacetic acid (conc.) the tube was sealed and heated at 150 °C for 72 h. The resulting precipitate was filtered and rinsed with methanol and acetone. After drying under reduced pressure, the final product was obtained as dark red powder.

Synthesis of TMT BDTOEt COF: basic conditions

In a stainless steel autoclave, TMT (6.4 mg, 52.2 μ mol) and BDTOEt (26.1 mg, 78.1 μ mol) were suspended in a mixture of mesitylene and methanol (4160 μ l, v:v 1:8). After adding solid sodium hydroxide (9.1 mg), the autoclave was sealed and heated to 180 °C for 72 h. The resulting precipitate was filtered and rinsed with methanol before Soxhlet extraction with methanol overnight. After drying under reduced pressure and supercritical CO₂ extraction, the final product was obtained as red powder.

Synthesis of TMT BDTOPr COF: acidic conditions

In a 6 mL culture tube, TMT (2.0 mg, 16.3 μ mol) and BDTOPr (9.06 mg, 25.0 μ mol) were suspended in a mixture of mesitylene and 1,4-dioxane (300 μ L, v: v 1:2). After adding 8.3 μ L of MeCN and 67 μ L of trifluoroacetic acid (conc.) the tube was sealed and heated at 150 °C for 72 h. The resulting precipitate was filtered and rinsed with methanol and acetone. After drying under reduced pressure, the final product was obtained as dark red powder.

Synthesis of TMT BDTOPr COF: basic conditions

In a stainless steel autoclave, TMT (6.4 mg, 52.2 μ mol) and BDTOPr (28.3 mg, 78.1 μ mol) were suspended in a mixture of mesitylene and methanol (4160 μ l, v:v 1:8). After adding solid sodium

hydroxide (9.1 mg), the autoclave was sealed and heated to 180 °C for 72 h. The resulting precipitate was filtered and rinsed with methanol before Soxhlet extraction with methanol overnight. After drying under reduced pressure and supercritical CO₂ extraction, the final product was obtained as red powder.

Vapor-assisted conversion (VAC) – Procedure

In a typical VAC-experiment, TMT (0.8 mg, 6.5 μmol) and BDTOPr (3.5 mg, 10.0 μmol) were dissolved in an 8:1 methanol/mesitylene solvent mixture (260 μl, v:v 8:1), sonicated and after addition of the respective amount of solid NaOH (1 mg) and successive sonication, the reactive solution was deposited onto a glass substrate placed in a glass autoclave. On the bottom of the glass autoclave (Schott Duran, borosilicate 3.3, ISO4796, 100 ml), spacers (14 Raschig rings, 10 x 10 mm, soda-lime glass) were placed as a base for the glass substrate along with 5 ml of an 8:1 methanol/ mesitylene solvent mixture which served as vapor source throughout the reaction. Subsequently, the glass autoclave was sealed and heated in an oven with temperatures ranging from 40°C to 130 °C for a designated reaction time. At the end of the framework formation, the glass substrate was evenly covered with a bright red-colored COF layer. The glass substrate with the resulting COF layer was removed without further purification and dried under high vacuum.

5.6.3 Vinylene-linked COFs – Acidic Conditions

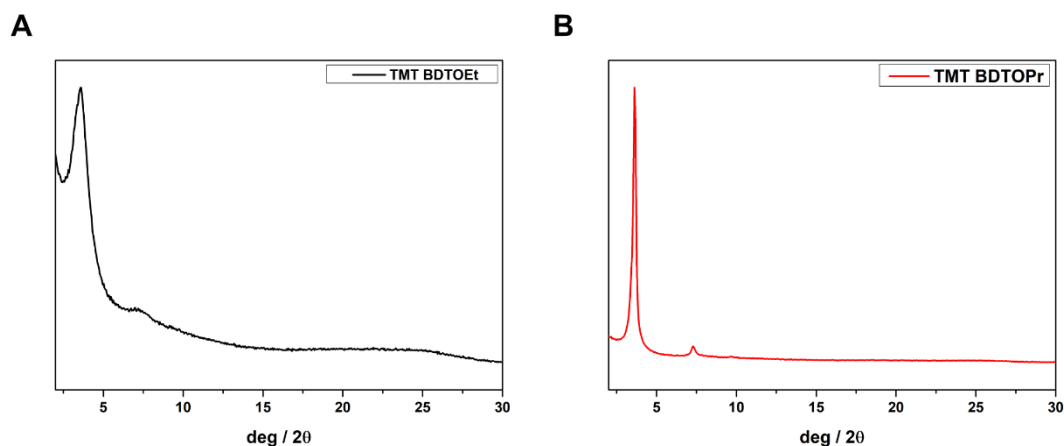


Figure 5.5 Powder X-ray diffraction patterns of vinylene-linked COF samples synthesized under acidic catalytic conditions. (A) TMT BDTOEt: Mesitylene/ Dioxane 1:1, MeCN, TFA, 150 °C, 3d. (B) TMT BDTOPr: Mesitylene/ Dioxane 1:2, MeCN, TFA, 150 °C, 3d.

5.6.4 Structural Analysis

Unit cell parameters (P1) and atomic coordinates for TMT BDTOEt

a = 29.3, b = 29.5, c = 3.7 Å

$\alpha = \beta = 90^\circ, \gamma = 120^\circ$

Atom	a/x	b/y	c/z
N1	0.29949	0.70493	0.53137
C2	0.26511	0.65284	0.53141
N3	0.28311	0.61858	0.53144
C4	0.33522	0.63631	0.53142
N5	0.36951	0.68855	0.53138
C6	0.35177	0.72291	0.53135
N7	0.59833	0.31925	0.53139
C8	0.61608	0.28490	0.53134
N9	0.66835	0.30289	0.53134
C10	0.70273	0.35498	0.53138
N11	0.68473	0.38923	0.53142
C12	0.63261	0.37149	0.53143
C13	0.57845	0.22876	0.53132
C14	0.43701	0.95680	0.53149
C15	0.48425	0.95715	0.53141
C16	0.53248	1.00378	0.53147
C17	0.53084	1.05101	0.53144
C18	0.48360	1.05065	0.53151
C19	0.43537	1.00402	0.53160
C20	0.39518	0.90668	0.53138
C21	0.41171	0.87060	0.53129
S22	0.47822	0.89658	0.53128
C23	0.57266	1.10113	0.53122
C24	0.55614	1.13720	0.53125
S25	0.48963	1.11122	0.53145
O26	0.38978	1.00822	0.53157
O27	0.57806	0.99958	0.53122
C28	0.34322	0.96436	0.53297
C29	0.62465	1.04347	0.53372
C30	0.37421	0.81443	0.53129
C31	0.38940	0.77904	0.53132
C32	0.48379	0.55083	0.53146

C33	0.43686	0.50365	0.53151
C34	0.43523	0.45542	0.53152
C35	0.48402	0.45694	0.53150
C36	0.53095	0.50413	0.53145
C37	0.53258	0.55236	0.53144
C38	0.47551	0.59264	0.53144
C39	0.42291	0.57621	0.53147
S40	0.38232	0.50976	0.53153
C41	0.49230	0.41514	0.53154
C42	0.54490	0.43157	0.53151
S43	0.58549	0.49802	0.53144
O44	0.58230	0.59789	0.53138
O45	0.38551	0.40989	0.53160
C46	0.58499	0.64823	0.53151
C47	0.38281	0.35957	0.53111
C48	0.40430	0.61377	0.53144
C49	0.56351	0.39401	0.53149
C50	0.61410	0.40912	0.53146
C51	0.35372	0.59867	0.53146
C52	1.03107	0.50415	0.53147
C53	1.03070	0.55100	0.53147
C54	0.98404	0.55257	0.53148
C55	0.93678	0.50367	0.53147
C56	0.93714	0.45682	0.53147
C57	0.98381	0.45527	0.53147
C58	1.08122	0.51249	0.53146
C59	1.11732	0.56508	0.53145
S60	1.09132	0.60556	0.53146
C61	0.88663	0.49535	0.53145
C62	0.85053	0.44276	0.53144
S63	0.87653	0.40227	0.53145
O64	0.97964	0.40552	0.53146
O65	0.98827	0.60237	0.53147
C66	1.02362	0.40294	0.53157
C67	0.94577	0.60497	0.53169
C68	0.79432	0.42407	0.53142
C69	0.75890	0.37350	0.53139

C70	0.59364	0.19338	0.53122
C71	0.30270	0.98275	0.53254
C73	0.66518	1.02509	0.53278
C75	0.63900	0.69341	0.53146
C77	0.32881	0.31439	0.53120
C79	0.95935	0.66391	0.53163
C81	1.02574	0.35193	0.53156
C83	1.17352	1.58376	0.53144
C84	1.20895	1.63433	0.53142

Unit cell parameters (P1) and atomic coordinates for TMT BDTOPr

a = 29.5, b = 29.5, c = 3.7 Å

$\alpha = \beta = 90^\circ$, $\gamma = 120^\circ$

Atom	a/x	b/y	c/z
N1	0.29969	0.70516	0.53148
C2	0.26521	0.65307	0.53148
N3	0.28314	0.61872	0.53146
C4	0.33533	0.63640	0.53148
N5	0.36975	0.68866	0.53149
C6	0.35203	0.72307	0.53148
N7	0.59809	0.31916	0.53149
C8	0.61581	0.28474	0.53148
N9	0.66816	0.30264	0.53148
C10	0.70263	0.35473	0.53148
N11	0.68469	0.38908	0.53146
C12	0.63252	0.37142	0.53148
C13	0.57810	0.22864	0.53146
C14	0.43696	0.95673	0.53147
C15	0.48436	0.95720	0.53146
C16	0.53262	1.00389	0.53147
C17	0.53086	1.05106	0.53147
C18	0.48346	1.05060	0.53146

C19	0.43521	1.00390	0.53147
C20	0.39515	0.90659	0.53150
C21	0.41185	0.87062	0.53148
S22	0.47849	0.89668	0.53149
C23	0.57265	1.10122	0.53150
C24	0.55596	1.13719	0.53149
S25	0.48932	1.11112	0.53149
O26	0.38945	1.00792	0.53153
O27	0.57837	0.99985	0.53152
C28	0.34125	0.96235	0.53150
C29	0.62659	1.04544	0.53150
C30	0.37438	0.81446	0.53145
C31	0.38972	0.77917	0.53146
C32	0.48388	0.55091	0.53147
C33	0.43681	0.50370	0.53147
C34	0.43512	0.45541	0.53148
C35	0.48396	0.45691	0.53147
C36	0.53102	0.50412	0.53146
C37	0.53273	0.55240	0.53147
C38	0.47563	0.59276	0.53149
C39	0.42295	0.57631	0.53148
S40	0.38221	0.50982	0.53148
C41	0.49217	0.41504	0.53148
C42	0.54485	0.43148	0.53148
S43	0.58561	0.49797	0.53149
O44	0.58256	0.59795	0.53149
O45	0.38528	0.40985	0.53152
C46	0.58537	0.64866	0.53149
C47	0.38250	0.35918	0.53150
C48	0.40441	0.61390	0.53146
C49	0.56343	0.39391	0.53146
C50	0.61409	0.40910	0.53148
C51	0.35376	0.59873	0.53147
C52	1.03115	0.50420	0.53148
C53	1.03071	0.55109	0.53149
C54	0.98394	0.55259	0.53148
C55	0.93668	0.50359	0.53148

C56	0.93712	0.45671	0.53149
C57	0.98390	0.45523	0.53148
C58	1.08139	0.51261	0.53146
C59	1.11743	0.56526	0.53147
S60	1.09135	0.60574	0.53147
C61	0.88644	0.49519	0.53146
C62	0.85040	0.44254	0.53147
S63	0.87648	0.40205	0.53147
O64	0.97984	0.40548	0.53143
O65	0.98803	0.60238	0.53144
C66	1.02444	0.40302	0.53145
C67	0.94492	0.60484	0.53147
C68	0.79416	0.42380	0.53150
C69	0.75881	0.37319	0.53148
C70	0.59344	0.19335	0.53145
C71	0.29969	0.97972	0.53147
C72	0.24785	0.93027	0.53144
C73	0.66815	1.02806	0.53147
C74	0.72002	1.07753	0.53145
C75	0.64111	0.69595	0.53148
C76	0.64344	0.75031	0.53147
C77	0.32676	0.31186	0.53148
C78	0.32446	0.25754	0.53146
C79	0.96055	0.66507	0.53148
C80	0.91319	0.66797	0.53151
C81	1.02495	0.35093	0.53148
C82	1.07449	0.35039	0.53151
C83	1.17367	1.58401	0.53149
C84	1.20901	1.63462	0.53148

5.6.5 Nitrogen Sorption

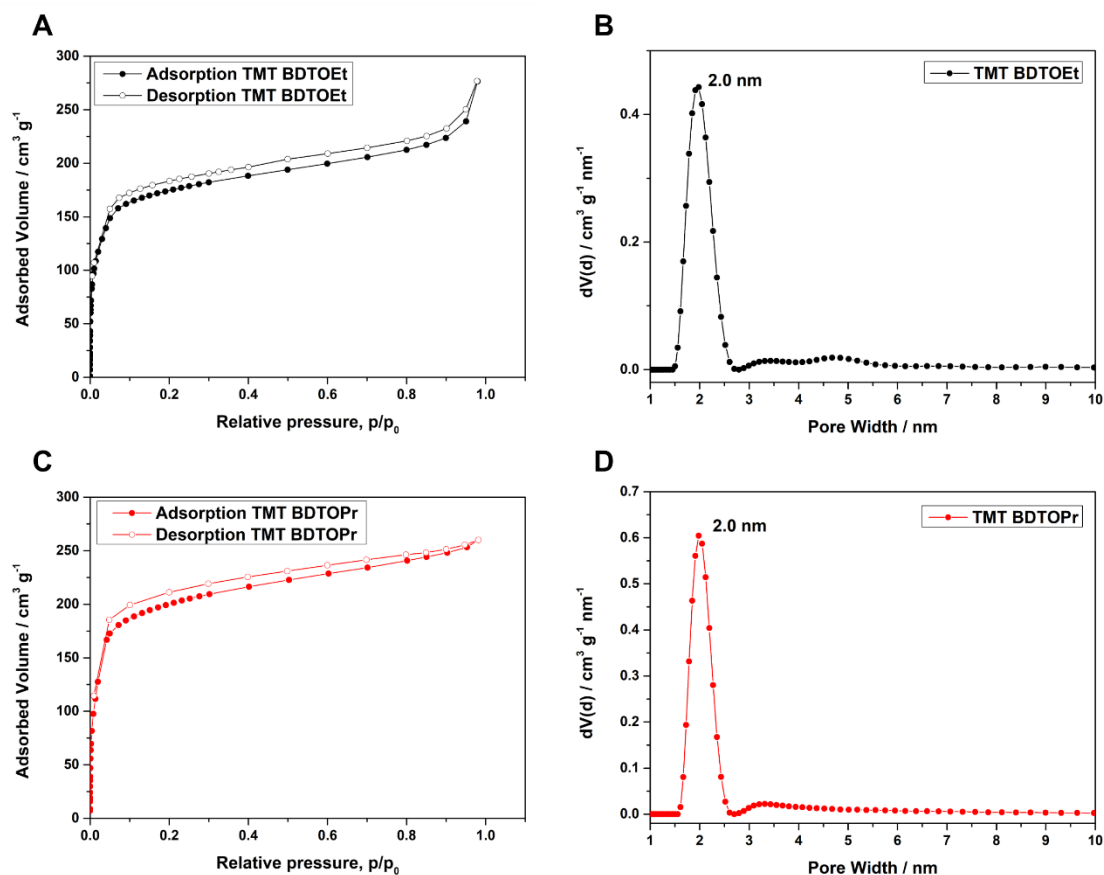


Figure 5.6 (A) Nitrogen adsorption and desorption isotherms of activated TMT BDTOEt measured at 77.3 K representing a Type I isotherm according to IUPAC. (B) The corresponding calculated pore size distribution obtained by DFT. (C) Nitrogen adsorption and desorption isotherms of activated TMT BDTOPr measured at 77.3 K representing a Type I isotherm according to IUPAC. (D) The corresponding calculated pore size distribution obtained by DFT.

5.6.6 Thermogravimetric Analysis

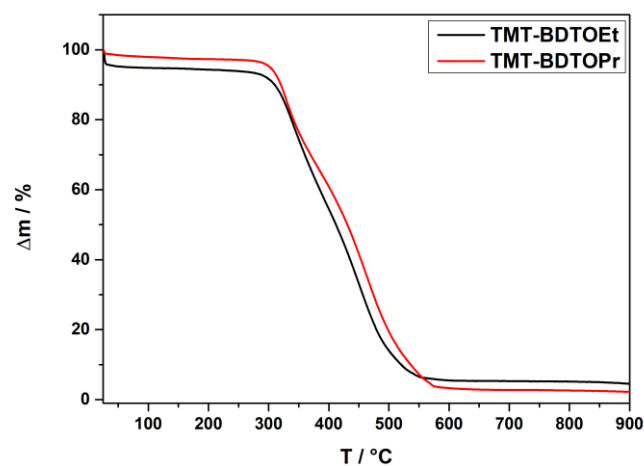


Figure 5.7 Thermogravimetric Analysis (TGA) of TMT BDTEt and TMT BDTPr measured as bulk materials.

5.6.7 Grazing-Incidence Wide-Angle X-ray Scattering – VAC Films

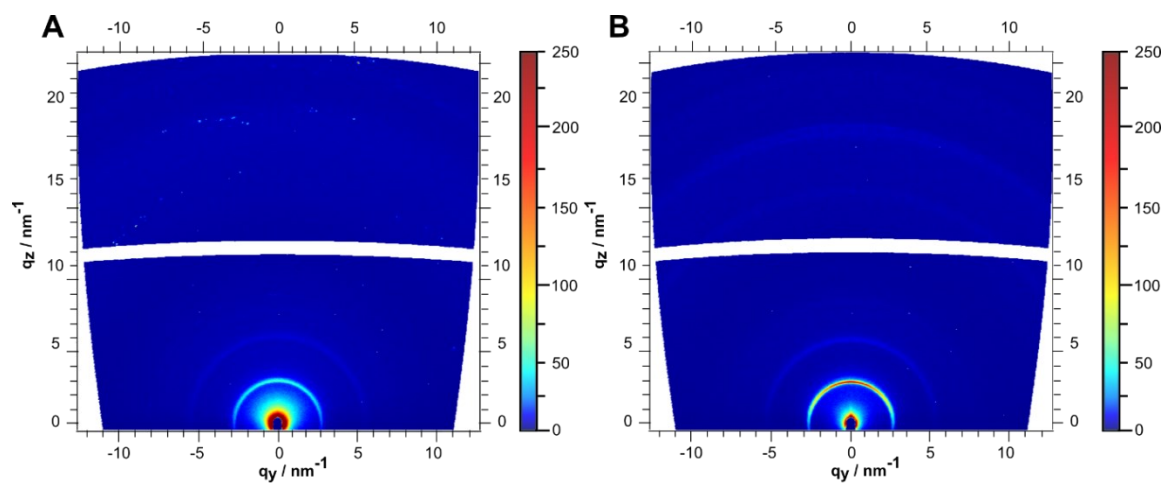


Figure 5.8 GIWAXS analysis of vinylene-linked TMT COF films grown by vapor-assisted conversion (VAC) on glass. (A) TMT-BDTEt, (B) TMT BDTPr.

5.6.8 SEM and X-Ray Diffraction Analysis – VAC Films

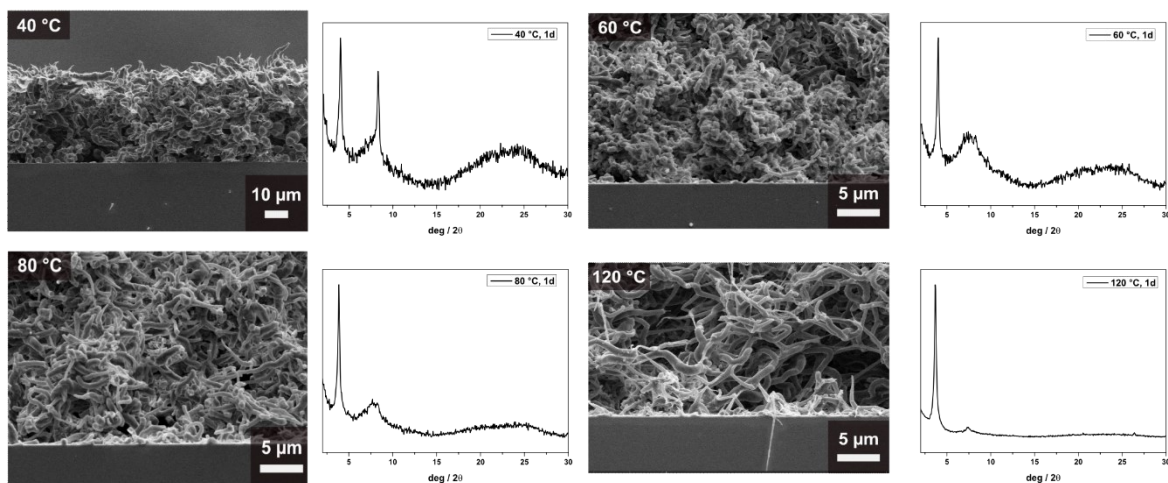


Figure 5.9 SEM cross-section images of thin films of vinylene-linked COF TMT BDTOPr grown by vapor-assisted conversion at different temperatures and the corresponding X-ray diffraction patterns. In all cases, the droplet size was 75 μL on a 10 x 10 mm glass substrate using the procedure as described in **section 6.6.2**.

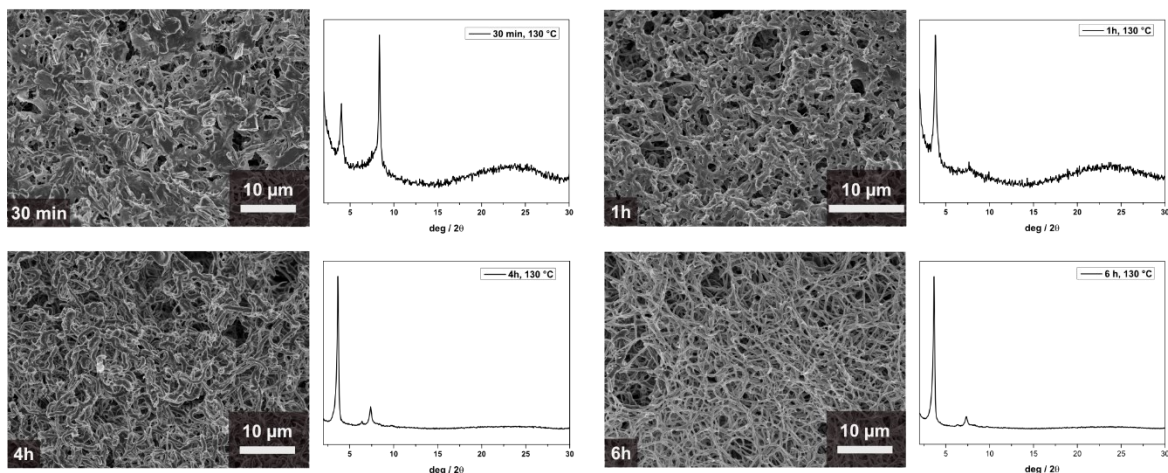


Figure 5.10 SEM top-view images of thin films of vinylene-linked COF TMT BDTOPr grown by vapor-assisted conversion using different reaction times and the corresponding X-ray diffraction patterns. In all cases, the droplet size was 75 μL on a 10 x 10 mm glass substrate using the procedure as described in **section 6.6.2**.

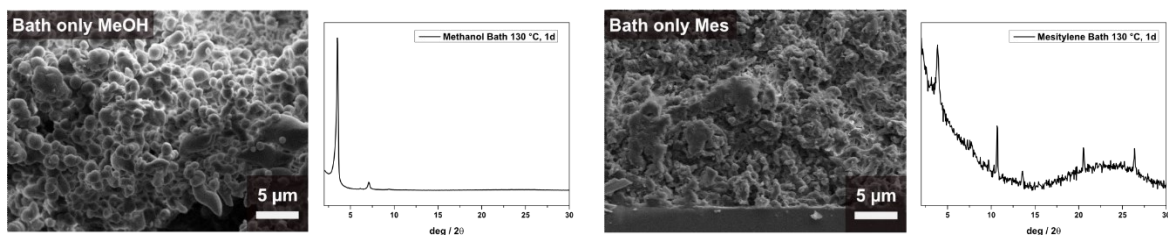


Figure 5.11 SEM cross-section images of thin films of vinylene-linked COF TMT BDTOPr grown by vapor-assisted conversion using different vapor sources and the corresponding X-ray diffraction patterns. In all cases, the droplet size was 75 μL on a 10 x 10 mm glass substrate using the procedure as described in **section 6.6.2**.

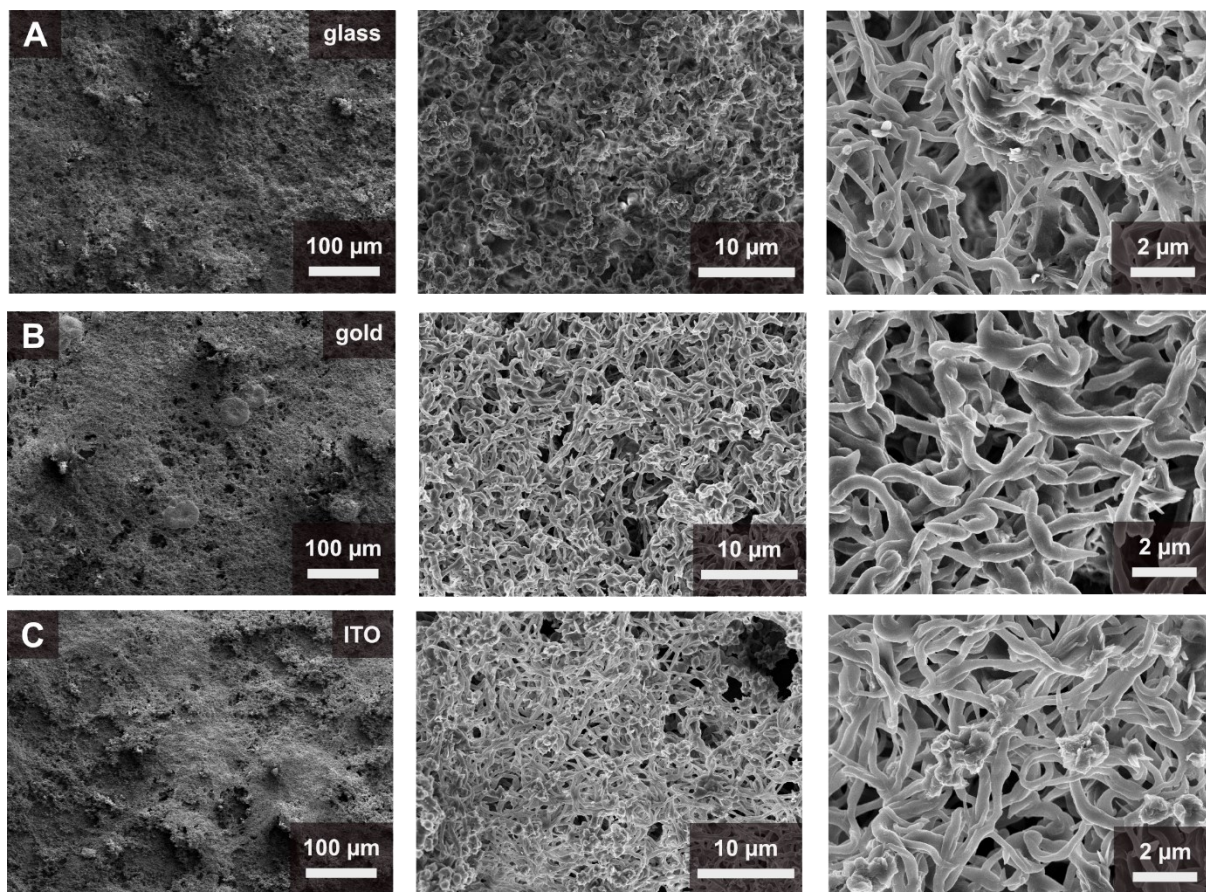


Figure 5.12 Additional SEM top-view images at different magnifications of TMT BDTOEt films on different substrates grown using VAC. In all cases the droplet size was 75 μL and the procedure was conducted as described in **section 6.6.2**. (A) glass substrates, (B) gold substrates, (C) indium-doped tin oxide (ITO) substrates.

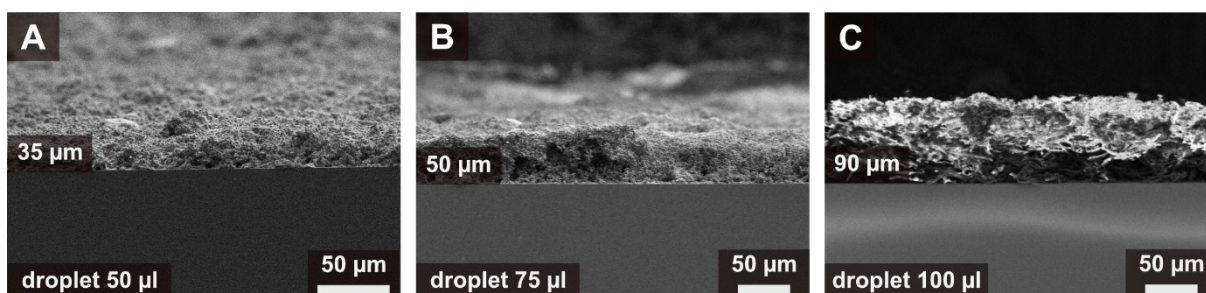


Figure 5.13 Additional cross-section images of TMT BDTOEt films grown using VAC at 130 $^{\circ}\text{C}$ and the procedure was conducted as described in **section 6.6.2**. Tunable thicknesses using different droplet sizes (pointed out in the inset) were achieved.

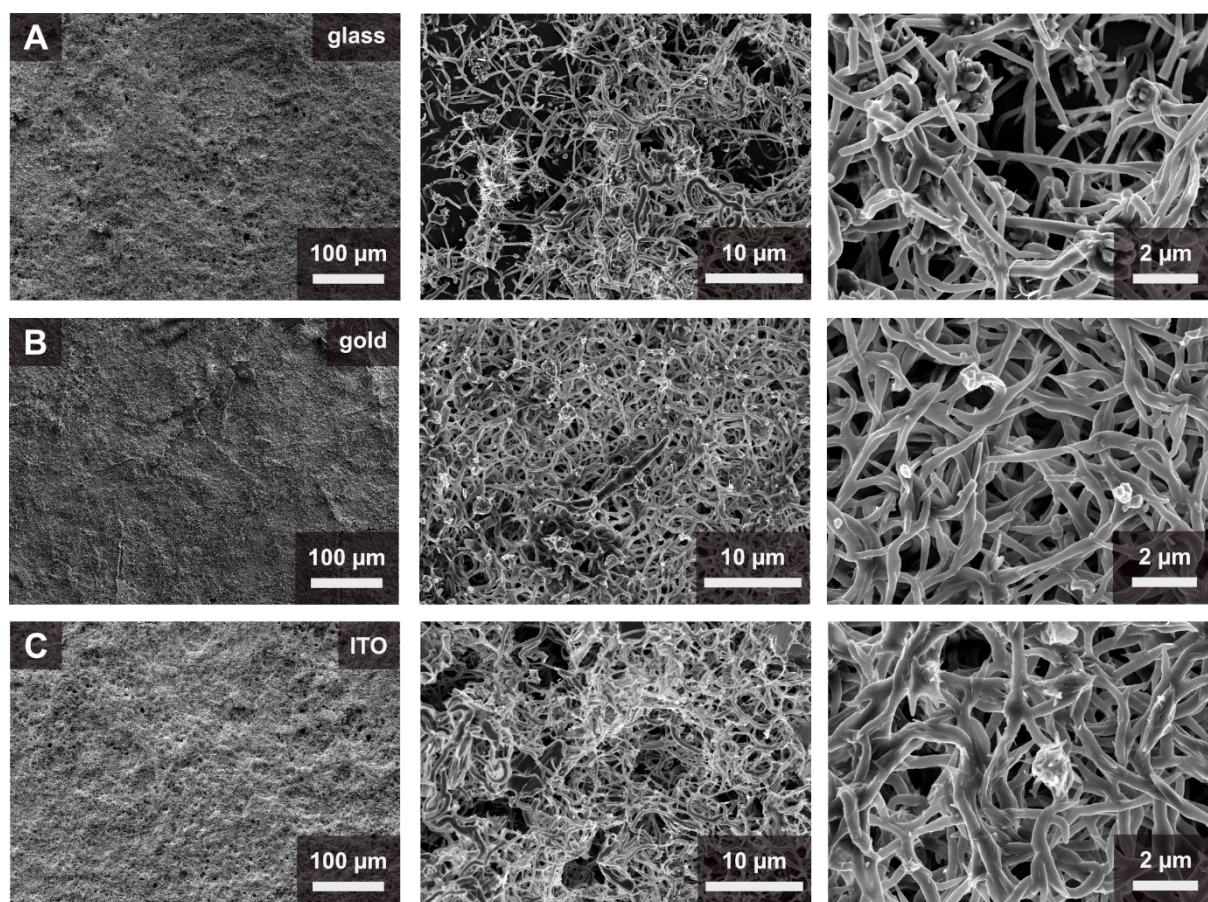


Figure 5.14. Additional SEM top-view images at different magnifications of TMT BDTOPr films on different substrates grown using VAC. In all cases the droplet size was 75 μL and the procedure was conducted as described in section 6.6.2. (A) glass substrates, (B) gold substrates, (C) indium-doped tin oxide (ITO) substrates.

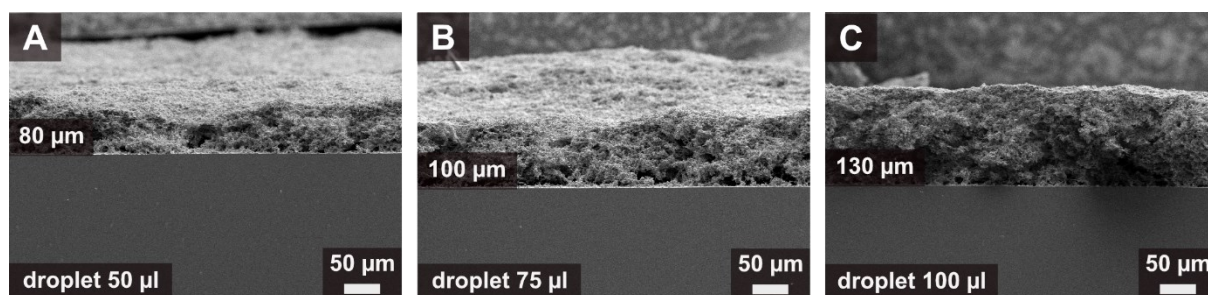


Figure 5.15 Additional cross-section images of TMT BDTOPr films grown using VAC at 130 $^{\circ}\text{C}$ and the procedure was conducted as described in section 6.6.2. Tunable thicknesses using different droplet sizes (pointed out in the inset) were achieved.

5.6.9 Krypton Sorption – VAC films

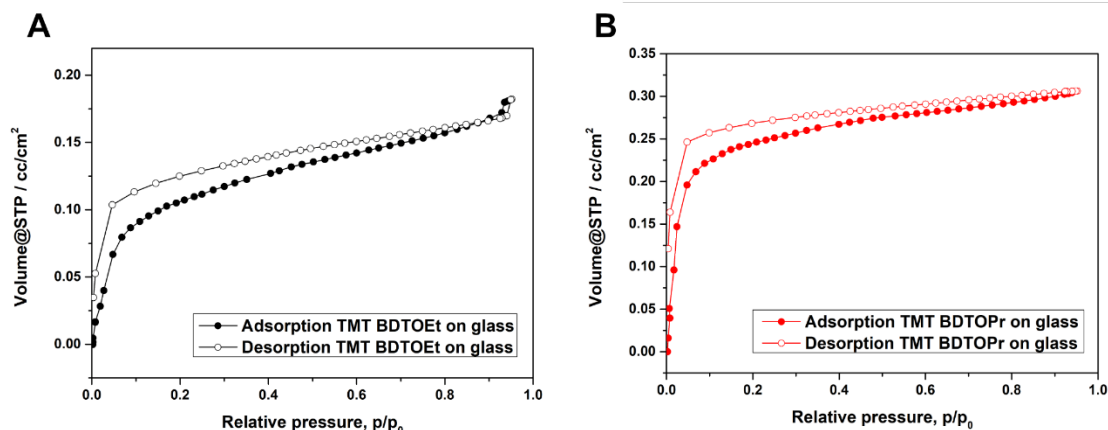


Figure 5.16 Krypton sorption isotherms of TMT BDTOEt (A) and TMT BDTOPr (B) films grown on glass using VAC.

5.6.10 Optical Characterization – Bulk and Films

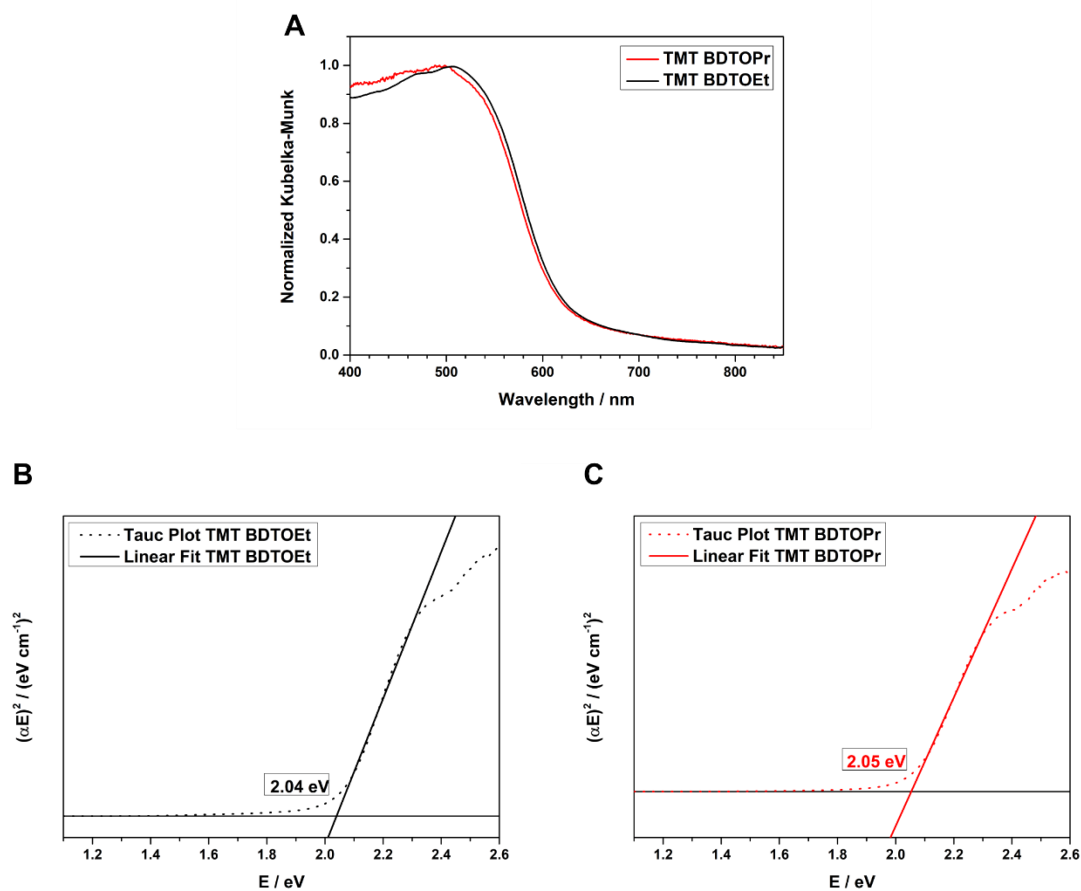


Figure 5.17 (A) UV-VIS spectra of TMT BDTOEt and TMT BDTOPr bulk powder and the respective calculated Tauc Plots assuming a direct bandgap. (B) TMT BDTOEt, (C) TMT BDTOPr.

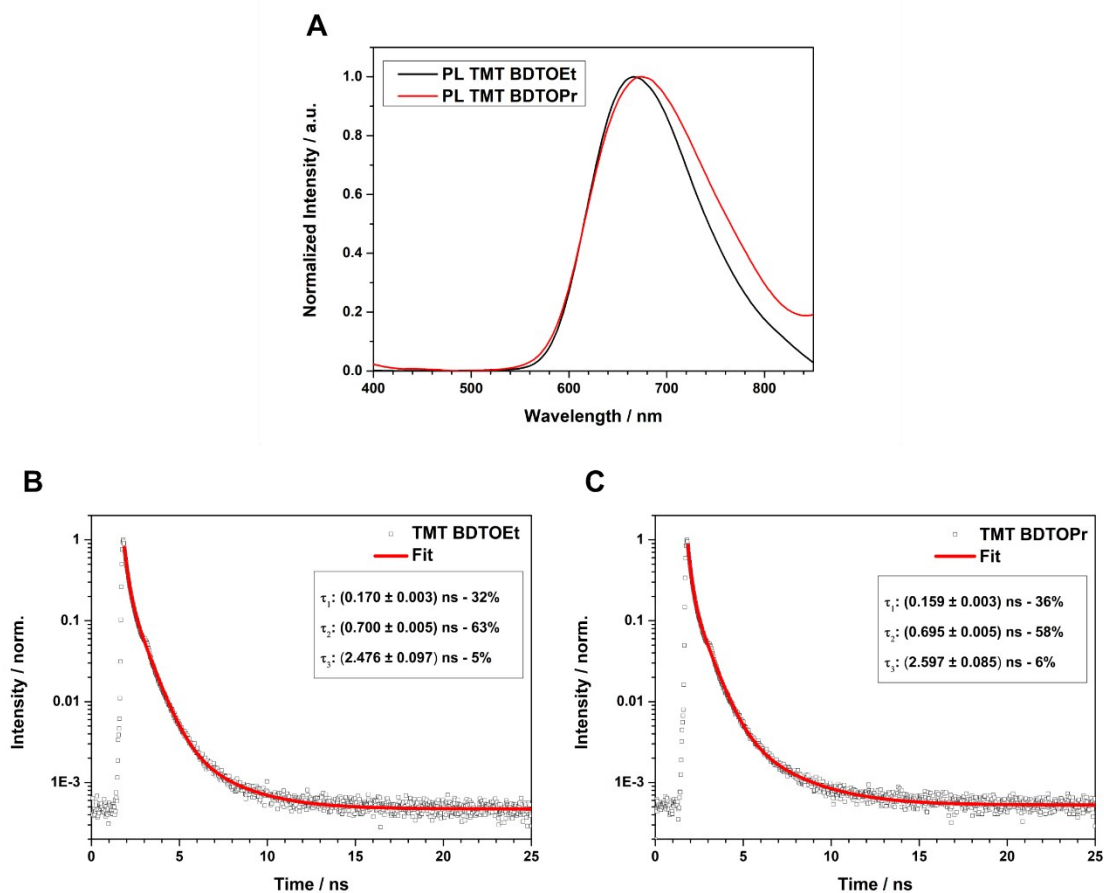


Figure 5.18 (A) PL spectra of TMT BDTOEt and TMT BDTOPr bulk powder and the respective time-correlated single photon counting measurements. (B) TMT BDTOEt, (C) TMT BDTOPr.

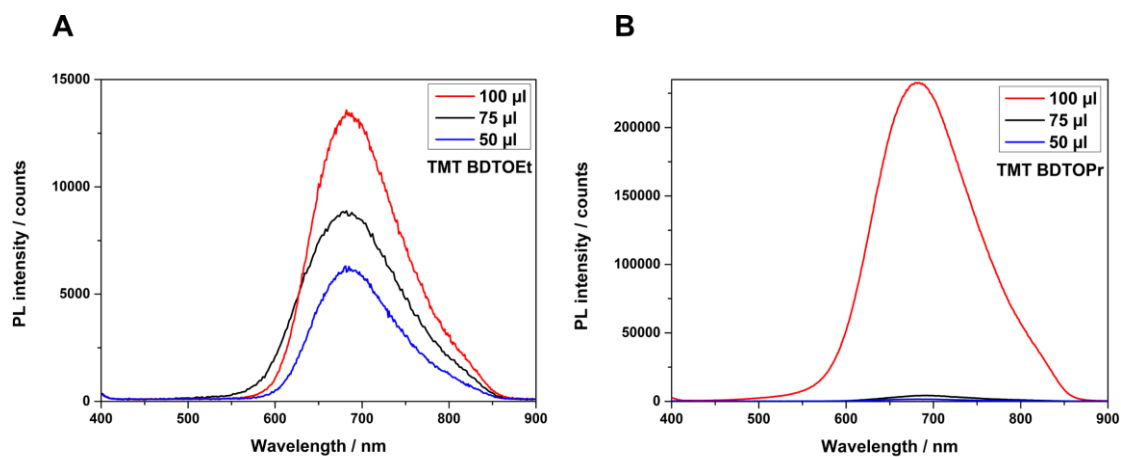


Figure 5.19 PL spectra of VAC films grown on glass of TMT BDTOEt (A) and TMT BDTOPr (B) using different droplet sizes.

5.6.11 Solvatochromic Effect – VAC films

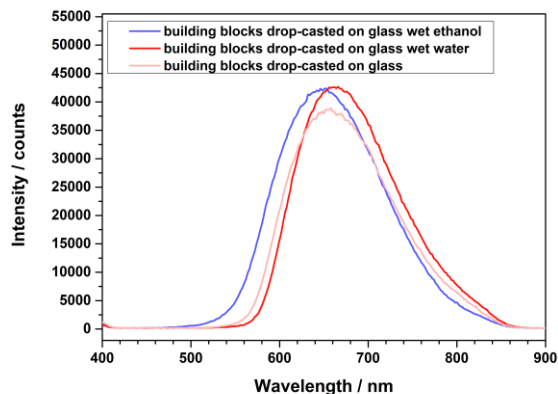


Figure 5.20. PL spectra of the building blocks dropcast on glass substrates after addition of a droplet of ethanol, water and pristine.

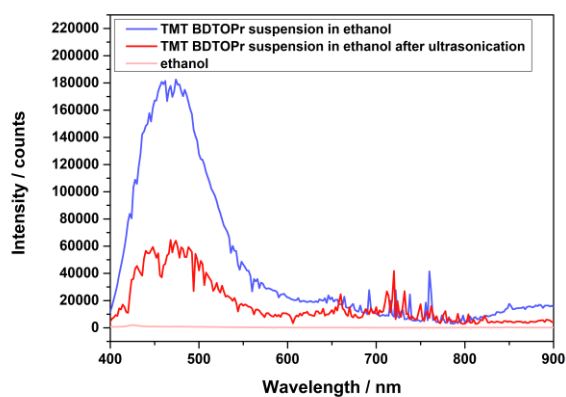


Figure 5.21 PL spectra of TMT BDTOPr bulk powder as suspension in ethanol (blue), after ultrasonication in ethanol (red) and only ethanol as control sample (light red).

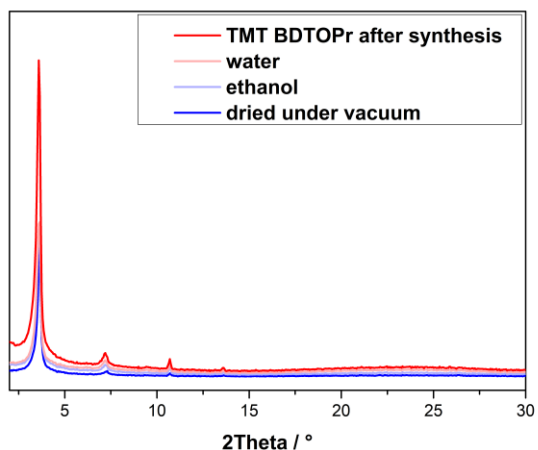


Figure 5.22 XRD patterns of VAC TMT BDTOPr films after synthesis, soaked with water or ethanol and after drying under vacuum.

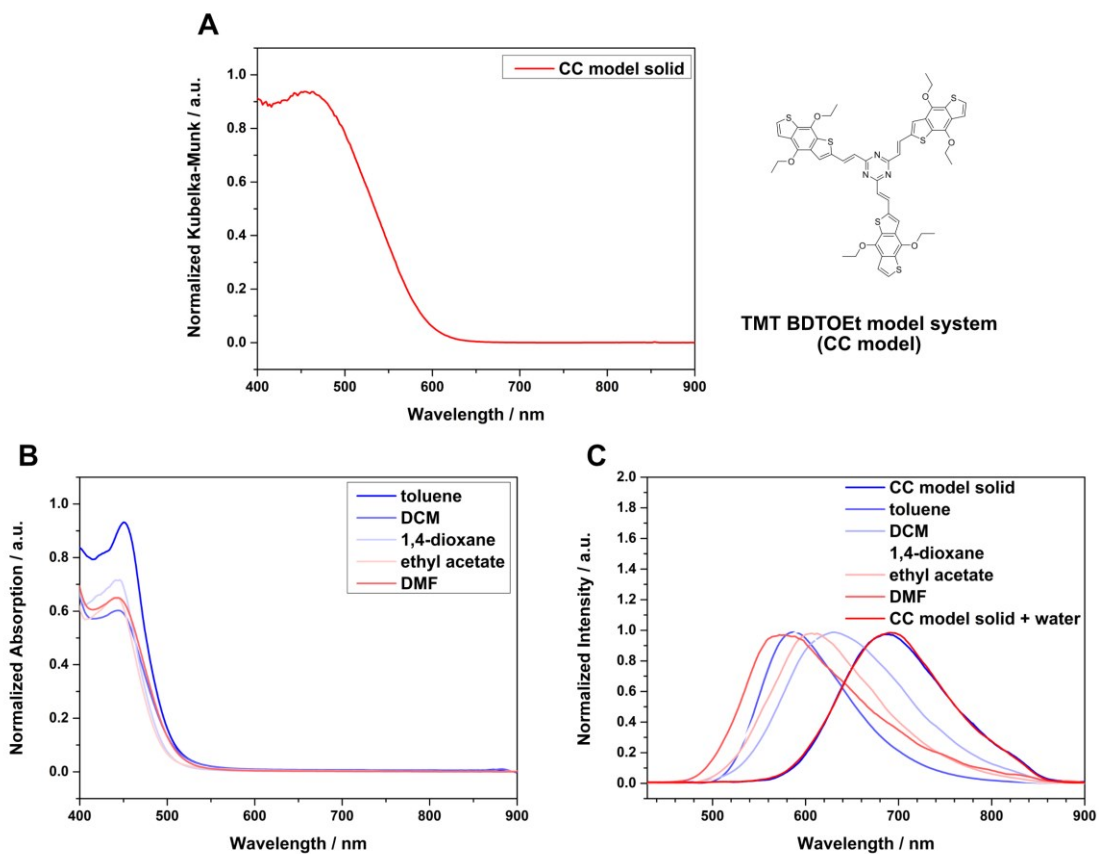


Figure 5.23. A. Normalized UV-vis spectrum of the model system as a solid. B. and C. Normalized UV vis absorption and photoluminescence spectra of the CC model system in different solvents.

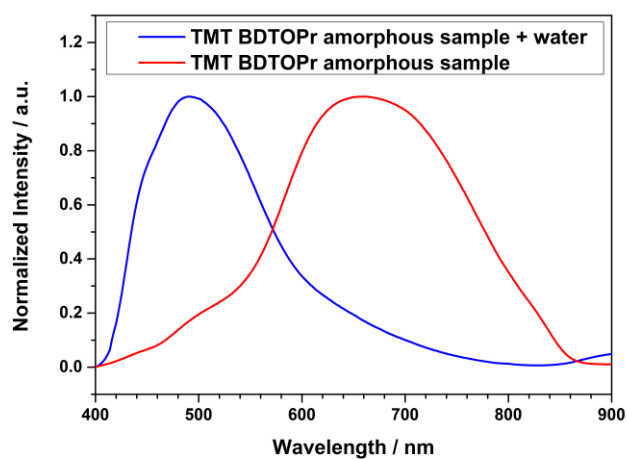


Figure 5.24. Normalized photoluminescence spectra of an amorphous film sample that was synthesized using TMT and BDTOPr and the vapor-assisted conversion method under non-ideal synthesis conditions using only mesitylene in the solvent bath and short reaction times (dry or soaked with water).

5.6.12 References

- (1) N. Xu, R.-L. Wang, D.-P. Li, Z.-Y. Zhou, T. Zhang, Y.-Z. Xie and Z.-M. Su, *New J. Chem.*, **2018**, *42*, 13367–13374.
- (2) T. Sick, J. M. Rotter, S. Reuter, S. Kandambeth, N. N. Bach, M. Döblinger, J. Merz, T. Clark, T. B. Marder, T. Bein and D. D. Medina, *J. Am. Chem. Soc.*, **2019**, *141*, 12570–12580.

6. Benzotrithiophene COF Thin Films – Directional Electrical Conductivity

This chapter is based on the following article:

Oriented Thiophene-Extended Benzotrithiophene Covalent Organic Framework Thin Films – Directional Electrical Conductivity

Published as: Frey, L.,^{†‡} Pöhls, J. F.,[‡] Hennemann, M.,[‡] Mähringer, A.,[†] Reuter, S.,[†] Clark, T.,^{‡*} Weitz, R. T.,^{‡*} Medina, D. D.,^{†*} Oriented Thiophene-Extended Benzotrithiophene Covalent Organic Framework Thin Films: Directional Electrical Conductivity. *Adv. Funct. Mater.* **2022**, 2205949.

[†] Department of Chemistry and Center for Nanoscience (CeNS), Ludwig-Maximilians University (LMU), Buten-andtstraße 11 (E), 81377 Munich, Germany

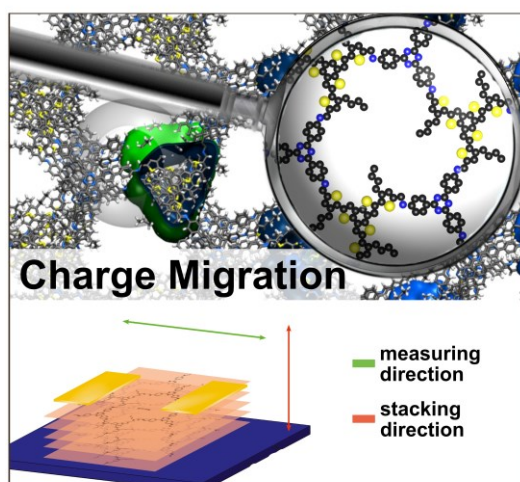
[‡] I. Institute of Physics, Faculty of Physics, Georg-August-University Göttingen, 37077 Göttingen, Germany

[‡] Friedrich-Alexander-University Erlangen-Nürnberg (FAU), Computer-Chemistry-Center, Department of Chemistry & Pharmacy, Naegelsbachstraße 25, 91052 Erlangen, Germany

[‡] International Center for Advanced Studies of Energy Conversion (ICASEC), University of Göttingen, Göttingen, Germany

* Corresponding Authors

‡ These authors contributed equally.



6.1 Abstract

We describe the synthesis of covalent organic frameworks (COFs) based on a novel three-pod, thiophene extended benzotrithiophene (BTT) building block, which, in combination with C_3 -symmetric triazine-based amines affords novel, highly crystalline and porous imine-linked COFs, BTT TTA and BTT TTTBA, with distorted hexagonal pores and surface areas as high as $932 \text{ m}^2 \text{ g}^{-1}$ and $1200 \text{ m}^2 \text{ g}^{-1}$, respectively. Subsequently, the frameworks were grown successfully on different substrates as highly oriented thin films, with varying thicknesses from 320 to 590 nm for BTT TTA and 290 to 480 nm for BTT TTTBA, as indicated by grazing incidence diffraction (GID) and electron microscopy analyses. BTT films on quartz substrate show light absorption in the 300-600 nm spectral region and emission at 740 and 705 nm. Room-temperature in-plane electrical conductivity of up to 10^{-4} S m^{-1} was measured for both COFs. Temperature-dependent electrical conductivity measurements indicate activation energies of $\sim 123.3 \text{ meV}$ for BTT TTA and $\sim 137.5 \text{ meV}$ for BTT TTTBA and trap-dominated charge transport *via* a hopping mechanism for both COFs. Moreover, conductive atomic force microscopy revealed strongly directional, defect-dominated charge transport in the oriented BTT COF films, with a strong preference for the in-plane direction within the molecular 2D-planes over the out-of-plane direction. Quantum mechanical calculations predict BTT TTTBA to conduct holes and electrons effectively in both the in-plane and out-of-plane directions. In-plane, charge carrier transport is of hopping character where the triazine cores represent the barrier. Out-of-plane, a continuous charge-carrier pathway is calculated that is hampered by an imposed structural defect simulated by a rotated molecular COF layer.

6.2 Introduction

Covalent organic Frameworks (COFs) are crystalline, highly ordered, porous polymers that are formed mainly by reversible condensation reactions of a large selection of organic building blocks. The slightly reversible nature of the covalent bond-formation ensures “proof-reading” related to building block assembly faults, leading to the formation of highly structurally defined products.^{1,2} The use of organic building blocks has opened up the opportunity to construct tailor-made COFs, whose key properties such as pore structure, optical properties and conjugation of monomers can be modified by fine-tuning of the chemical structure and geometry of the building blocks. These unique features of COFs provide access to studying chemical character – structural paradigm – performance correlations for a variety of applications such as gas storage^{3,4}, sensing⁵⁻⁷, catalysis^{8,9} and separation^{10,11}. Inspired by photoactive and semiconducting organic polymers, COFs consisting of photoactive building blocks have been synthesized. Typically, the building blocks feature geometries suitable for constructing two-dimensional COF sheets, extended in-plane, upon polymerization. The nascent molecular COF sheets grow in size

and interact, aggregate and fall out of solution as a layered solid. The 2D-COF structure paradigm provides several intriguing structural properties, such as precise positioning of the organic moieties in a columnar manner, in-plane conjugation, accessible pore channels, and a large variety of pore sizes and shapes. In 2D electroactive conjugated COFs, charge migration is expected both in the plane of the conjugated COF sheets and perpendicular thereto *via* the columns. The study of charge migration in 2D-COFs benefits from the deposition with a preferential layer orientation with respect to the surface, which in turn allows charge migration to be probed, both in the conjugated plane and in the non-covalent molecular columns of the COF.¹²

In recent years, research on multi(thiophene) fused aromatic compounds has gained interest owing to their successful implementation as active materials in organic light-emitting diodes,¹³ photovoltaic devices^{14,15} or organic thin-film transistors (OTFTs)¹⁶. Moreover, much effort has been devoted to the synthesis on benzo[1,2-b:4,5-b']dithiophene (BDT) and benzo[1,2-b:3,4-b':5,6-b'']trithiophene (BTT) derivatives as potential organic semiconductors.^{16,17} Benzotrithiophene comprises three thiophenes fused to a central benzene ring, resulting in a planar and electron-rich system.^{18,19} The BTT C_3 -symmetric core and its different isomers have been used successfully as part of a polymeric active layer in organic solar cells,^{15,20} aggregation agent promoting self-assemblies²¹ and 2D-covalent organic frameworks^{22–24}. Extended BTT, and particularly thiophene-extended BTT cores suitable for the formation of COFs has not yet been reported. In the context of COFs, designing an extended BTT photoactive core requires solubility and symmetry to be considered for COF formation. This includes extension of the BTT core in three vertices with the desired functional groups and the installation of solubilizing side chains that synchronize and are compatible with the COF layer stacking.²⁵

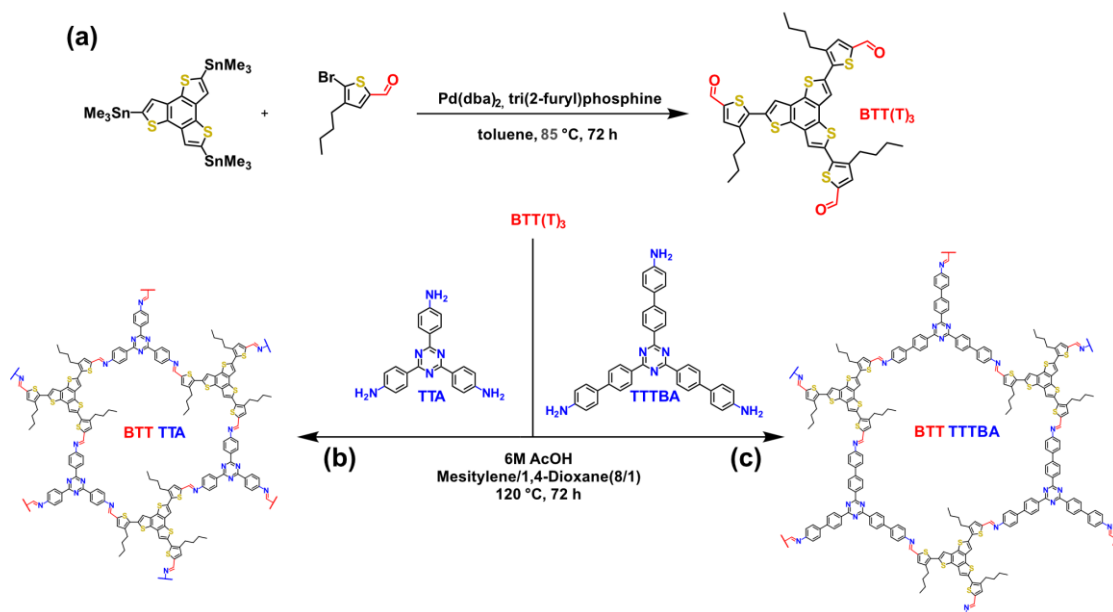
We now describe the synthesis of a novel three-pod thiophene extended benzotrithiophene (BTT)-based tricarbaldehyde that features the central BTT-unit decorated with three peripheral thiophene moieties. Combining the novel BTT building block with multidentate amines, namely (1,3,5-triazine-2,4,6-triyl)trianiline (TTA) or (1,3,5-triazine-2,4,6-triyl)tris((1,1'-biphenyl)-4-amine) (TTTBA)), two novel highly crystalline and porous imine-linked COFs, termed BTT TTA and BTT TTTBA, respectively, are presented. The presence of the peripheral thiophene units at the BTT core building block leads to the formation of squished hexagonal pores. Moreover, highly oriented, crystalline thin films were successfully grown on different substrates, featuring layer orientation parallel to the substrate and thickness of 300-500 nm. BTT TTA and TTTBA films show light absorption in the 300-600 nm wavelength range and photoluminescence (PL) emission at 740 nm and 705 nm for BTT TTA and TTTBA, respectively. Directional electrical conductivity of the BTT COF films was determined by constructing various devices of different electrode architectures. Room temperature in-plane electrical conductivity values as high as 10^{-4} S m^{-1} were determined for BTT TTA and TTTBA. Temperature-dependent electrical conductivity measurements indicate trap-dominated charge transport in-plane.

6.3 Results and Discussion

6.3.1 Synthesis

We aimed at synthesizing COF building blocks containing six conjugated thiophene units. Therefore, initially, the novel terthieno-benzotrithiophene (BTT)-based COF building block, termed BTT(T)₃, was synthesized. First, the BTT core was obtained following a reported protocol.¹⁹ Subsequently, the BTT core was stannylated and coupled to 5-bromo-4-butylthiophene-2-carbaldehyde through a *Stille* coupling reaction (**Scheme 6.1**) to afford the desired C₃-building block BTT(T)₃ (for more information see appendix). The as-prepared BTT(T)₃ building block was suspended in mesitylene and 1,4-dioxane (8:1, v:v) together with (1,3,5-triazine-2,4,6-triyl)trianiline (TTA) or (1,3,5-triazine-2,4,6-triyl)tris((1,1'-biphenyl)-4-amine) (TTTBA) as complementary building blocks. Employing a Schiff-base acid-catalyzed imine condensation reaction under solvothermal synthesis conditions for 72 h at 120 °C resulted in the precipitation of a dark orange powder for BTT TTA and dark yellow powder for TTTBA (**Scheme 6.1**). After the given reaction time, the precipitated powders were filtered under reduced pressure and washed with THF. The wet powders were subjected to supercritical CO₂ extraction for further drying²⁶ (for further information see **Figure 6.6, Section 6.6.2**).

In models, the presence of the peripheral thiophene units at the BTT core results in a rigid and chiral building block, subsequently leading to the formation of highly distorted hexagonal enantiomeric pores (**Figure 6.7**). These two features typically limit the formation of a crystalline product.²⁷ The formation of highly crystalline BTT TTA and TTTBA materials was confirmed using powder X-ray diffraction (PXRD) analysis (**Figure 6.1c, f**). Impressively, the obtained BTT COFs feature long-range order with observed high order bragg reflections. The PXRD diffraction patterns reveal highly defined and intense reflections at 3.8°, 6.6°, 10.1°, 13.1°, 15.2°, 16.6° and 25.7° 2θ for BTT TTA and 2.9°, 5.1°, 5.9° and 7.9° 2θ for BTT TTTBA. For BTT TTA, a reflection associated with the stacking distance at 25.7° 2θ was observed, corresponding to a π-stacking distance of about 3.5 Å. According to the symmetry of the building blocks, structure models were constructed using the Materials Studio software package (Accelrys Inc.), the structure simulations and geometry optimization were carried out using the Forcite module employing the universal force field and *P1* symmetry. The resulting theoretical PXRD patterns were compared to those obtained experimentally. In 2D-COFs, different stacking arrangements of the 2D layers are possible; eclipsed layer stacking (AA), alternating, staggered or unidirectional stacking as well as a random arrangement.²⁸ For both COFs, the simulations show that the eclipsed layer stacking (AA) and unidirectional stacking agree well with the experimental patterns. For both models, unit-cell parameters suggest structures close to a hexagonal crystal system, however, considering the packing of the alkyl side chains, we ruled out a fully overlapped AA stacking of the layers, hence for further refinement of the unit cell we used unidirectional stacking (**Figure 6.1a, b, c, f**).



Scheme 6.1. (a) A *Stille* coupling reaction scheme, affording the tricarbaldehyde BTT(T)₃ building block. Schematic representation of the synthesis of (b) BTT TTA, using 4,4',4''-(1,3,5-triazine-2,4,6-triyl)trianiline (TTA) and (c) BTT TTTBA using 4,4''',4''''-(1,3,5-triazine-2,4,6-triyl)tris((1,1'-biphenyl)-4-amine) (TTTBA) as complementary building blocks.

The simulated unit cells obtained were refined using the Reflex module in the Materials Studio software using the Pawley method for powder refinement according to the experimentally obtained PXRD patterns. Thereby, unit cell parameters of $a = 27.7 \text{ \AA}$, $b = 28.0 \text{ \AA}$, $c = 3.7 \text{ \AA}$, $\alpha = \beta = 90^\circ$, $\gamma = 122^\circ$ for BTT TTA and $a = 34.4 \text{ \AA}$, $b = 35.1 \text{ \AA}$, $c = 4.0 \text{ \AA}$, $\alpha = 89^\circ$, $\beta = 90^\circ$, $\gamma = 120^\circ$ for BTT TTTBA were obtained. Additionally, the observed reflections at the PXRD patterns were indexed and attributed to the corresponding hkl planes. For BTT TTA, hkl (100), (110), (210), (220), (400), (230) and (001) correspond to 3.8° , 6.6° , 10.1° , 13.1° , 15.2° , 16.6° and 25.7° 2θ . For BTT TTTBA, hkl (100), (110), (200) and (210) correspond to 2.9° , 5.1° , 5.9° and 7.9° 2θ . For BTT TTA a reflection associated with the stacking distances at 25.7° 2θ was obtained, corresponding to an interlayer distance of about 3.5 \AA .

The porosity of the two BTT COFs was analyzed by nitrogen gas physisorption at 77 K. For BTT TTA, the nitrogen sorption isotherm shows typical type I sorption profile with a sharp nitrogen uptake at relatively low partial pressure ($p/p_0 < 0.09$ and up to $280 \text{ cm}^3 \text{ g}^{-1}$), which is characteristic for microporous materials. The nitrogen sorption isotherm of BTT TTTBA features type IVb sorption isotherm profile.²⁹ In the isotherm, two steep and well-defined nitrogen uptakes at low partial pressures ($p/p_0 < 0.16$ and up to $320 \text{ cm}^3 \text{ g}^{-1}$) related to the presence of mesoporous materials are shown. In addition, the adsorption isotherm is fully reversible, showing no hysteresis, which is a common feature of materials containing aligned 1D-mesopores with diameter smaller than 40 \AA . Both BTT TTA and BTT TTTBA revealed high calculated and apparent Brunauer-Emmett-Teller (BET) surface areas of $932 \text{ m}^2 \text{ g}^{-1}$ and $1200 \text{ m}^2 \text{ g}^{-1}$, respectively (**Figure 6.1d, g, Figure 6.9**). For the analysis of the pore sizes the quenched solid density

functional theory (QSDFE) model was employed. Thereby, pore sizes of 1.8 nm and 2.6 nm with a narrow pore size distribution were determined for BTT TTA and BTT TTTBA, respectively. (**Figure 6.10, 6.11**).

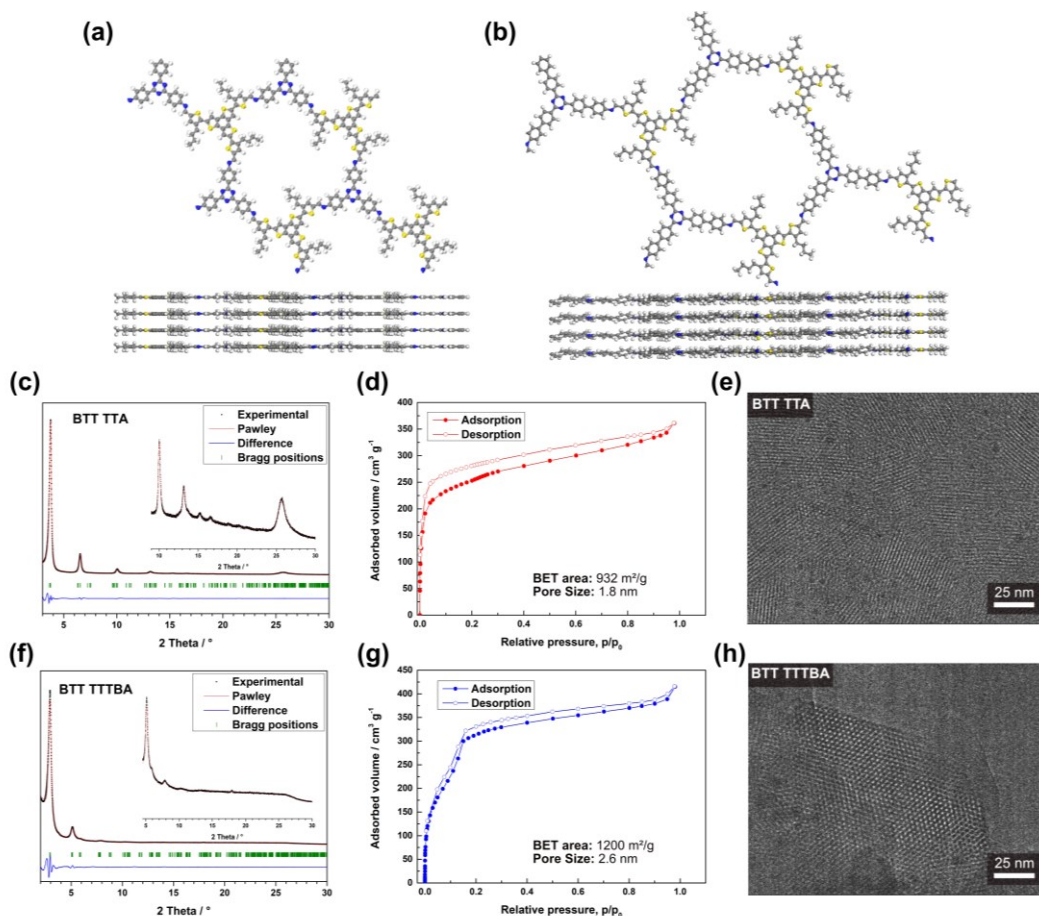


Figure 6.1. (a) and (b) Schematic representation of BTT TTA and BTT TTTBA. (c) and (f) Experimental PXRD pattern (black dots) of BTT TTA and TTTBA, respectively. Pawley refinement (red line), difference plot between the experimental data and the Pawley-refined PXRD pattern (blue line), Bragg positions are indicated by green ticks. The insets in both XRD patterns show a magnified view of $2\theta > 5^\circ$. (d) and (g) Nitrogen physisorption isotherms at 77 K of BTT TTA and BTT TTTBA, respectively. (e) and (h) TEM images of BTT TTA and BTT TTTBA bulk material, respectively.

Thermogravimetric analysis (TGA) under synthetic air flow revealed that both BTT COFs are thermally stable at temperatures up to 350 °C. Here, significant weight loss at around 350 °C associated with the beginning of a structural degradation of the COF materials is detected; at 600 °C the process ceases with complete weight loss (**Figure 6.12**). Notably, the continuous and complete weight loss is an excellent indication for the high purity of the COF materials and the absence of residual synthesis agents originating from ligand synthesis. Scanning electron microscopy (SEM) analysis of the COF powders revealed nanometer-sized COF particles of about 50-150 nm in diameter which aggregate into cauliflower-like assemblies of different sizes (**Figure 6.13**). We note that the majority of the COF crystallites appear spherical. However, in some cases faceted, hexagonally shaped crystallites are clearly

observed, which corresponds well with the high structural definition observed by PXRD and the simulated pseudo-hexagonal structure. Transmission electron microscopy (TEM) analysis of both COFs further supports the highly crystalline nature of the COFs. Projections along the *c*-axis reveal the expected honeycomb structure of the COF (**Figure 6.1e, h**). Electron diffraction patterns of the obtained images further support the formation of highly crystalline COFs, showing high order diffraction lines for a single BTT TTTBA crystallite (**Figure 6.14**).

6.3.2 Oriented Thin Films of BTT TTA and BTT TTTBA

To study and characterize the BTT COF properties regarding their photophysical and electronic properties further, oriented COF thin films were synthesized on various substrates. The synthesis was carried out in glass vessels equipped with a Teflon substrate holder using the non-epitaxy *in-situ* approach under developed solvothermal synthesis protocols for the BTT COFs.^{12,30–32} Thus, the substrates were positioned and immersed horizontally using the Teflon substrate holder into the reaction vessel, charged with the appropriate reactive precursor solution. Subsequently, acetic acid was added, and the reaction vessel was heated to 120° C for a fixed reaction time (ranging from 12 to 72 h, depending on the desired thickness of the film). After removal from the reaction mixture, the substrate was thoroughly washed with dry tetrahydrofuran (THF) and dried under a stream of nitrogen to reveal a homogeneous shimmering layer on the substrate. SEM cross-section and top-view images showed that a continuous and homogeneous coverage of the substrate was obtained (**Figure 6.2d, e, Figure 6.15, 6.16**). Depending on the reaction time, the thickness of the resulting COF layer is tuned, ranging from 320 to 590 nm for BTT TTA and 290 to 480 nm for BTT TTTBA (**Figure 6.16**). A grazing-incidence X-ray diffraction (GIXRD) analysis indicated the preferential parallel orientation of the COF molecular layers with respect to the substrate, with the (001) reflection (at 25.7° and 26.2° 2θ for BTT TTA and BTT TTTBA, respectively) being the only reflection visible in the diffraction pattern (**Figure 6.18**). Complementary to the 1D-diffractogram, grazing-incidence wide-angle X-ray scattering analysis (GI-WAXS) was carried out to examine the crystallinity of the films and to confirm the preferential orientation of the COF crystallites with respect to the substrate. For both COFs, strong distinct reflections at q_y 2.78, 4.89, 7.56, 9.82 nm⁻¹ and q_z 19.13 nm⁻¹ for BTT TTA corresponding to *hkl* (100), (110), (210), (220), (001) and q_y 2.18, 3.86 and 5.85 nm⁻¹ for BTT TTTBA corresponding to *hkl* (100), (110), (210) were obtained. The *q*-values obtained by data-reduction to 1D-plots match those obtained for the bulk powder XRD patterns (**Figure 6.19**). The GIWAXS data of both COF thin films confirm the preferential orientation with the [001]-axis to be oriented orthogonal to the surface (**Figure 6.2a, Figure 6.16a**). The SEM cross-section and top-view images showed that in both cases a homogenous and continuous COF deposit was obtained with residual powder that is attributed to a secondary nucleation on top of the oriented thin films. High-magnification SEM micrographs targeting the crystallites on top of the film revealed hexagonal facets, which is in line with the observed bulk COF

morphology (**Figure 6.2d, e, Figure 6.16**). Additionally, TEM analysis of scratched-off film confirms the formation of highly oriented COF crystallites that form a continuous tile; (**Figure 6.2b, c, Figure 6.16**) projections along the *c*-axis reveal the expected honeycomb structure of the COF. Furthermore, electron diffraction of the non-oriented residual deposit on top of the oriented film reveals highly crystalline COF materials.

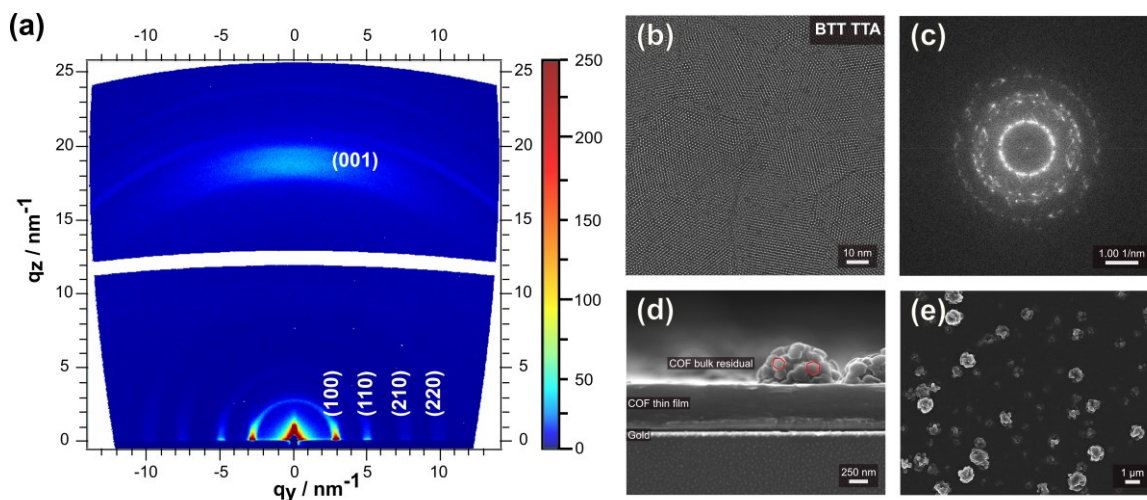


Figure 6.2. (a) GIWAXS 2D patterns of BTT TTA thin film grown on ITO. (b) and (c) TEM and electron diffraction images of BTT TTA thin films on ITO scratched off the substrate. (d), (e) SEM cross-section and top-view images of BTT TTA thin films on gold substrates

6.3.3 Photophysical Properties

Next, we analyzed the photophysical properties of the BTT COFs using UV-vis and photoluminescence (PL) spectroscopies (**Figure 6.3**). For both BTT COF samples examined, the absorption bands are located in the UV and blue spectral regions. Further, the BTT TTA has an absorption onset of around 560 nm. The absorption onset of BTT TTTBA is slightly blue-shifted (550 nm) compared to the BTT TTA. We attribute this effect to the additional benzene rings in TTTBA being rotated out-of-plane, which can affect the extent of conjugation (**Figure 6.3a**). This shift can also be seen in the color of the resulting thin films, with BTT TTA films revealing bright orange and BTT TTTBA films bright yellow colors. Assuming a direct band gap transition, Tauc plots allowed for estimating the optical band gaps of the two structures, yielding band gaps of 2.32 eV for BTT TTA and 2.41 eV for BTT TTTBA (**Figure 6.3b**). Steady-state PL of the BTT COFs was measured at an excitation wavelength of 378 nm. BTT TTA exhibits two distinct emission bands at around 575 and 740 nm, the latter being more intense. For BTT TTTBA, only one distinct emission band was detected at around 705 nm. Both COFs show broad emissions that range from the visible to the near-infrared spectral regions (**Figure 6.3c**). When compared to the PL emissions of the BTT(T)₃ building block a significant red-shift of the emission bands of the corresponding COFs can be detected, indicating the formation of a new electronic structure with extended conjugation on framework COF formation (**Figure 6.20**).

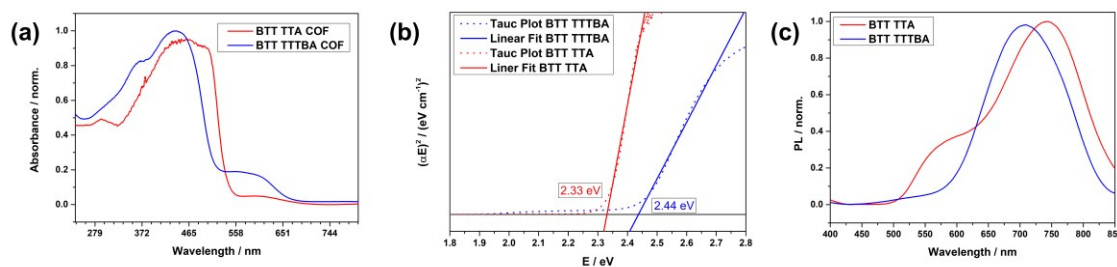


Figure 6.3. (a) Normalized absorption spectra of BTT TTA (red) and BTT TTTBA (blue) thin film on quartz substrates. (b) Tauc plots of the BTT TTA (red) and BTT TTTBA (blue) UV-vis absorbance spectra calculated for a direct band transition model. (c) Normalized PL ($\lambda_{\text{exc}} = 378$ nm) spectra for BTT TTA (red) and BTT TTTBA (blue) thin films.

6.3.4 Electrical Conductivity of BTT TTA and BTT TTTBA COFs

Electrical conductivity measurements were used to assess the charge-transport properties of the BTT COFs, both in-plane along the 2D molecular sheets and out-of-plane across the stacked 2D-COF columns. The temperature-dependent electrical conductivity was determined using two-probe measurements in the temperature range from 296 K to 6 K. The measurements were performed on macroscopic COF films (thickness ~ 500 nm) that had been deposited onto silicon wafers coated with an insulating layer of 300 nm SiO_2 . The voltage sweeps performed for BTT TTA, exemplarily shown for different temperatures in **Figure 6.4b**, are non-linear, which we attribute to the impact of non-ideal injection at the COF-gold contact.³³ The temperature-dependent conductivity values presented in **Figure 6.4a** are therefore determined at drain-source voltage (VDS) = 40 V, since the influence of the contact resistance is less pronounced at such high voltages.³⁴ At room temperature, this results in a conductivity of $\sim 8.7 \times 10^{-4}$ S/m for of BTT TTA and $\sim 1.1 \times 10^{-4}$ S/m for BTT TTTBA, which places them among the most conductive non-doped COFs reported to date.^{35,36} Notably, in-plane conductivity measurements of films of different thicknesses (320, 380 and 590 nm in the case of BTT TTA and 290, 430 and 480 nm in the case of BTT TTTBA) show similar conductivity values.

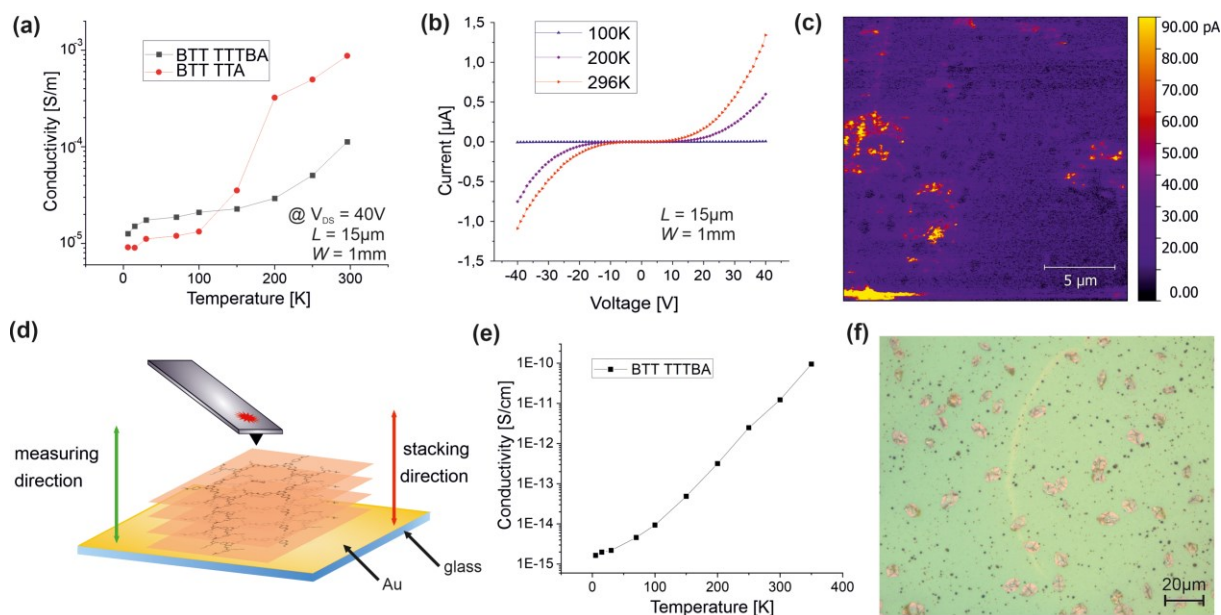


Figure 6.4. (a) Temperature dependent electrical conductivity measurements of BTT TTA and BTT TTTBA in the in-plane direction. Conductivities calculated from two-point measurements in the temperature range from 6 K to 296 K. (b) The underlying I-V-curves, shown for 100 K, 200 K and room temperature for BTT TTA reveal a significant impact of contact resistance. (c) cAFM measurement on the BTT TTTBA film on Au. (d) Schematic representation of the out-of-plane conductive AFM measurements of the thin BTT COF films. (e) Temperature dependence of the out-of-plane conductivity for the BTT TTTBA. (f) The polycrystalline regions in the cAFM can also be observed with an optical microscope.

The temperature-dependent data in **Figure 6.4a** reveal a thermally activated in-plane conductivity for both COFs. Activation energies (E_a) can be derived from fitting an Arrhenius plot of the form $\sigma(T) = \sigma_0 \exp[-(E_a/k_B T)]$ (with the Boltzmann constant k_B) to the conductivity data σ plotted against the inverse of the temperature T^{-1} . The activation energies E_a derived by this method are ~ 123.3 meV for BTT TTA and ~ 137.5 meV for BTT TTTBA. Based on the electrical conductivity data obtained, it is challenging to determine whether the activated behavior arises due to a band gap in the electronic structure or by charge traps in the form of defects. In the case of semiconductors with doping levels below the electrostatically accessible range ($\sim 10^{12}$ cm $^{-2}$ in our geometry), electrical conductivity can be altered by varying the charge-carrier density using a gate voltage. In the case of BTT COFs, such an effect was not observed. This, together with the band gaps obtained from the Tauc plots (**Figure 6.3b**), which are an order of magnitude larger than the activation energies determined, suggests that the activated behavior observed is rather defect related. Such defects might be present at boundaries between single-crystalline grains. Furthermore, the low-temperature conductivity data are in good agreement with the characteristic temperature dependence of Mott variable-range hopping, which could indicate hopping-based transport.

In contrast to the conductivities up to 8.7×10^{-4} S/m reached for the in-plane measurements, charge transport in the out-of-plane direction is strongly suppressed. Two-point measurements on a macroscopic scale with an ITO bottom contact and a gold top contact show a room-temperature conductivity of $\sim 9.5 \times 10^{-11}$ S/m with a strong temperature dependence for the BTT TTTBA (**Figure**

6.4e). A conductivity several orders of magnitude smaller compared to the in-plane direction was also confirmed by conductive AFM measurements on both BTT COF films on gold substrates (**Figure 6.4d**). As shown in **Figure 6.4c**, a current of up to 0.97 nA is observed at the polycrystalline non-oriented COF deposits on the film, where charge transport along the covalent bonds in these areas is possible in all spatial directions (**Figure 6.4f, Figure 6.2b-e**). The strong suppression of charge transport in the out-of-plane direction shown by our experimental measurements, could be the result of structural defects along the molecular stacks. With only weak bonds between the layers in the columnar stacking and a hopping-based transport, these single deviations of the AA stacking can represent barriers that suppress the charge transport effectively.

Overall, the electrical conductivity measurements show strongly directional, defect-dominated charge transport in the BTT COF films and, given the more than five orders of magnitude transport anisotropy, with a strong preference for the in-plane direction within the conjugated 2D-planes over the out-of-plane direction. Both the strong channel length dependence and cAFM in-plane measurements on a microscopic scale suggest that the room temperature conductivities of $\sim 8.7 \times 10^{-4}$ for the BTT TTA and $\sim 1.1 \times 10^{-4}$ S/m for the BTT TTTBA represent only a lower limit, since they were measured on a macroscopic scale and depend strongly on the charge traps in the measured channel.

6.3.5 Charge-Carrier Pathway Simulations

The possible charge-carrier migration pathways in BTT TTTBA were studied using classical molecular-dynamics (MD) simulations and subsequent charge-propagation simulations. The thermal fluctuations of the structure were studied with classical MD using the Universal Force Field (UFF)³⁷ with AM1^{38,39} atomic charges.

A snapshot from the end of the simulation (**Figure 6.5a**) was used for imaginary-time-evolution simulations^{40,41} of electron- and hole-transport. The charge-transport simulations for electrons and holes are based on the local electron affinity^{42,43} (**Figure 6.5b**) and the local average ionization energy⁴⁴ (**Figure 6.5c**), calculated using AM1^{38,39} semiempirical molecular-orbital (MO) theory. The calculated conductance paths for electrons and holes are shown in **Figure 6.5d, e** and **Figure 6.22**, respectively. Details of the simulations are given in the SI.

To estimate the effect of grain boundaries parallel to the plane of the COF between crystallites, a 180° rotation was introduced into the structure at the position of the dashed line in **Figure 6.5f** and **Figure 6.22e**. The charge-transport simulations now show a significant barrier at this boundary (which is far tighter than expected in the real system). This barrier can only be crossed by tunneling. **Figure 6.5f** and **Figure 6.22** show this behavior for an electron and a hole, respectively. The tunneling distance is clearly far larger than that in the in-plane paths between sulfur-rich centers.

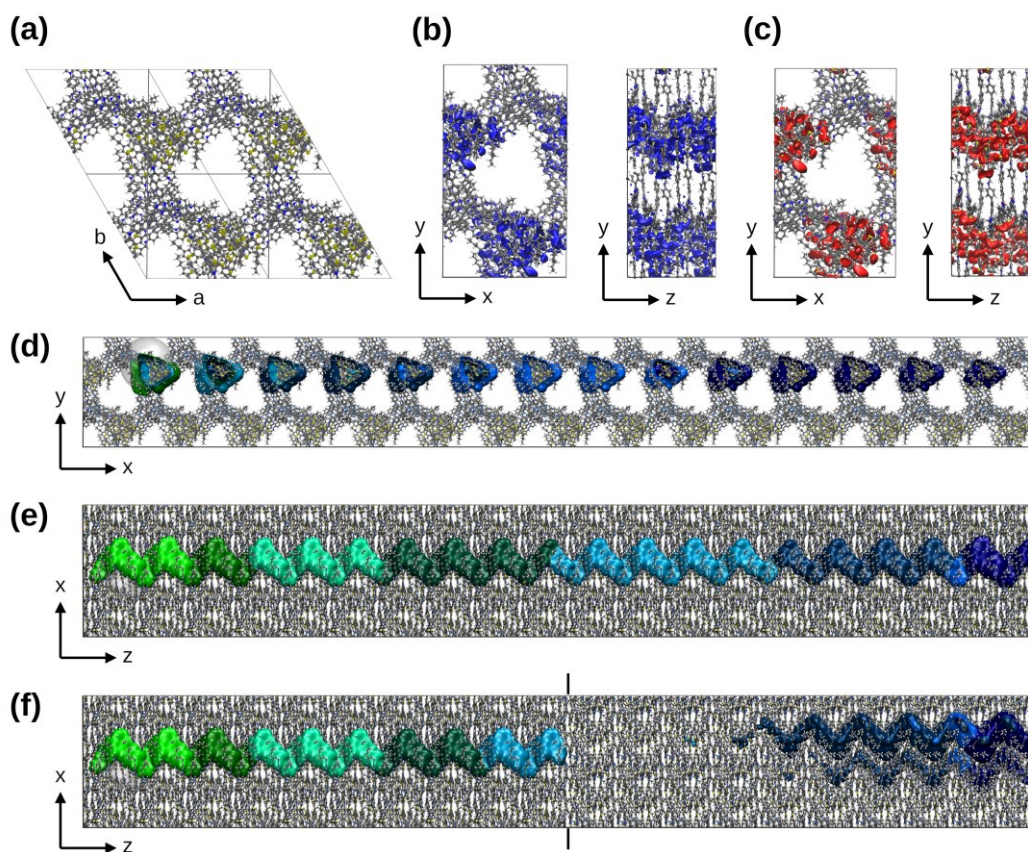


Figure 6.5. (a) Top view of the equilibrated BTT TTTBA after 11 ns MD run. Top and side views of the isovalue-surfaces of the EAL (blue, contour level = -1 eV) (b) and IEL (red, contour level = 14 eV) (c) for BTT TTTBA calculated with AM1. The Cartesian directions (x , y , z) used for the charge-transport simulations relate to the crystallographic axes (a , b , c) in the following manner: $x = a$; $y = 2b + a$; $z = c$. Calculated electron-transport paths for the BTT TTTBA in the Cartesian directions x (d) and z (e). Isocontour plots for eight simulation steps of the electron (green to blue; contour level = 1.2×10^{-5} e-Bohr⁻³). The initial Gaussian functions are shown as transparent spheres. (f) Calculated electron-transport path in the Cartesian z direction for the displaced model structure of the BTT TTTBA.

6.4 Conclusion

In summary, we showed the synthesis of a novel three-pod thiophene-extended BTT-based tricarbaldehyde. In combination with different C_3 -symmetric triazine-based amines we were able to synthesize two new highly crystalline, porous and imine-linked COF structures, namely BTT TTA and BTT TTTBA. To study their transport properties, the frameworks were successfully grown on different substrates using the *in-situ* approach as electroactive, highly oriented thin films and room-temperature in-plane conductivities of up to 10^{-4} S m⁻¹ were measured. Temperature dependent electrical conductivity measurements revealed a temperature dependence indicative of trap-dominated hopping type charge transport. All in all, with our measurements we could see a strongly directional, defect-dominated charge transport in the BTT COF films, with a strong preference for the in-plane direction within the conjugated 2D planes over the out-of-plane direction. Quantum mechanical calculations predict a hopping type

charge transport in the 2D molecular planes, and molecular COF columns perpendicular to the in-plane direction to provide a continuous path. By imposing a grain boundary in the form of a rotated COF layer, dramatically hampered charge transport in this direction. This study emphasizes the role of defect in the overall conductivity performance of COF materials and particularly for BTT COFs presented, where the electrical conductivity values obtained for the latter represent the lower limit and are expected to improve dramatically by defect-controlled synthesis strategies.

6.5 References

- (1) Frey, L.; Jarju, J. J.; Salonen, L. M.; Medina, D. D. Boronic-acid-derived covalent organic frameworks: from synthesis to applications. *New J. Chem.* **2021**, *45* (33), 14879–14907. DOI: 10.1039/D1NJ01269J.
- (2) Lohse, M. S.; Bein, T. Covalent Organic Frameworks: Structures, Synthesis, and Applications. *Adv. Funct. Mater.* **2018**, *28* (33), 1705553. DOI: 10.1002/adfm.201705553.
- (3) Fan, H.; Mundstock, A.; Feldhoff, A.; Knebel, A.; Gu, J.; Meng, H.; Caro, J. Covalent Organic Framework–Covalent Organic Framework Bilayer Membranes for Highly Selective Gas Separation *J. Am. Chem. Soc.* **2018** *140* (32), 10094–10098. DOI: 10.1021/jacs.8b05136.
- (4) Li, Z.; Feng, X.; Zou, Y.; Zhang, Y.; Xia, H.; Liu, X.; Mu, Y. A 2D azine-linked covalent organic framework for gas storage applications. *Chem. Commun.* **2014**, *50* (89), 13825–13828. DOI: 10.1039/C4CC05665E.
- (5) Ascherl, L.; Evans, E. W.; Gorman, J.; Orsborne, S.; Bessinger, D.; Bein, T.; Friend, R. H.; Auras, F. Perylene-Based Covalent Organic Frameworks for Acid Vapor Sensing. *J. Am. Chem. Soc.* **2019**, *141* (39), 15693–15699. DOI: 10.1021/jacs.9b08079.
- (6) Jhulki, S.; Evans, A. M.; Hao, X.-L.; Cooper, M. W.; Feri-ante, C. H.; Leisen, J.; Li, H.; Lam, D.; Hersam, M. C.; Barlow, S.; Brédas, J.-L.; Dichtel, W. R.; Marder, S. R. Humidity Sensing through Reversible Isomerization of a Covalent Organic Framework. *J. Am. Chem. Soc.* **2020**, *142* (2), 783–791. DOI: 10.1021/jacs.9b08628.
- (7) Wang, Y.; Zhao, Z.; Li, G.; Yan, Y.; Hao, C. A 2D covalent organic framework as a sensor for detecting formaldehyde. *J. Mol. Model.* **2018**, *24* (7), 153. DOI: 10.1007/s00894-018-3676-x.
- (8) Wang, Y.; Liu, H.; Pan, Q.; Wu, C.; Hao, W.; Xu, J.; Chen, R.; Liu, J.; Li, Z.; Zhao, Y. Construction of Fully Conjugated Covalent Organic Frameworks via Facile Linkage Conversion for Efficient Photoenzymatic Catalysis. *J. Am. Chem. Soc.* **2020**, *142* (13), 5958–5963. DOI: 10.1021/jacs.0c00923.
- (9) Shen, J.-C.; Jiang, W.-L.; Guo, W.-D.; Qi, Q.-Y.; Ma, D.-L.; Lou, X.; Shen, M.; Hu, B.; Yang, H.-B.; Zhao, X. A rings-in-pores net: crown ether-based covalent organic frameworks for phase-transfer catalysis. *Chem. Commun.* **2020**, *56* (4), 595–598. DOI: 10.1039/C9CC07639E.
- (10) Cui, W.-R.; Zhang, C.-R.; Jiang, W.; Li, F.-F.; Liang, R.-P.; Liu, J.; Qiu, J.-D. Regenerable and stable sp² carbon-conjugated covalent organic frameworks for selective detection and extraction of uranium. *Nat. Commun.* **2020**, *11* (1), 436. DOI: 10.1038/s41467-020-14289-x.

- (11) Khan, N. A.; Zhang, R.; Wu, H.; Shen, J.; Yuan, J.; Fan, C.; Cao, L.; Olson, M. A.; Jiang, Z. Solid–Vapor Interface Engineered Covalent Organic Framework Membranes for Molecular Separation. *J. Am. Chem. Soc.* **2020**, *142* (31), 13450–13458. DOI: 10.1021/jacs.0c04589.
- (12) Medina, D. D.; Petrus, M. L.; Jumabekov, A. N.; Mar-graf, J. T.; Weinberger, S.; Rotter, J. M.; Clark, T.; Bein, T. Directional Charge-Carrier Transport in Oriented Benzodithiophene Covalent Organic Framework Thin Films. *ACS Nano* **2017**, *11* (3), 2706–2713. DOI: 10.1021/acsnano.6b07692.
- (13) Fukazawa, A.; Oshima, H.; Shimizu, S.; Kobayashi, N.; Yamaguchi, S. Dearomatization-Induced Transannular Cyclization: Synthesis of Electron-Accepting Thiophene-S,S-Dioxide-Fused Biphenylene. *J. Am. Chem. Soc.* **2014**, *136* (24), 8738–8745. DOI: 10.1021/ja503499n.
- (14) Budiawan, W.; Lai, K.-W.; Karuppuswamy, P.; Jadhav, T. S.; Lu, Y.-A.; Ho, K.-C.; Wang, P.-C.; Chang, C.-C.; Chu, C.-W. Asymmetric Benzotrithiophene-Based Hole Transporting Materials Provide High-Efficiency Perovskite Solar Cells. *ACS Applied Materials & Interfaces* **2020**, *12* (26). DOI: 10.1021/acsaami.0c02204.
- (15) Molina-Ontoria, A.; Zimmermann, I.; Garcia-Benito, I.; Gratia, P.; Roldán-Carmona, C.; Aghazada, S.; Graetzel, M.; Nazeeruddin, M. K.; Martín, N. Benzotrithiophene-Based Hole-Transporting Materials for 18.2 % Perovskite Solar Cells. *Angew. Chem. Int. Ed.* **2016**, *55* (21), 6270–6274. DOI: 10.1002/anie.201511877.
- (16) Chen, W.; Huang, G.; Li, X.; Li, Y.; Wang, H.; Jiang, H.; Zhao, Z.; Yu, D.; Wang, E.; Yang, R. Revealing the Position Effect of an Alkylthio Side Chain in Phenyl-Substituted Benzodithiophene-Based Donor Polymers on the Photovoltaic Performance of Non-Fullerene Organic Solar Cells. *ACS Appl. Mater. Interfaces* **2019**, *11* (36), 33173–33178. DOI: 10.1021/acsaami.9b07112.
- (17) He, Q.; Shahid, M.; Panidi, J.; Marsh, A. V.; Huang, W.; Daboczi, M.; Kim, J.-S.; Fei, Z.; Anthopoulos, T. D.; Heeney, M. A versatile star-shaped organic semiconductor based on benzodithiophene and diketopyrrolopyrrole. *J. Mater. Chem. C* **2019**, *7* (22), 6622–6629. DOI: 10.1039/C9TC00905A.
- (18) Guo, X.; Puniredd, S. R.; Baumgarten, M.; Pisula, W.; Müllen, K. Benzotrithiophene-Based Donor–Acceptor Co-polymers with Distinct Supramolecular Organizations. *J. Am. Chem. Soc.* **2012**, *134* (20), 8404–8407. DOI: 10.1021/ja302957s.
- (19) Rossi, S.; Bisello, A.; Cardena, R.; Orian, L.; Santi, S. Benzodithiophene and Benzotrithiophene as π Cores for Two- and Three-Blade Propeller-Shaped Ferrocenyl-Based Conjugated Systems. *Eur. J. Org. Chem.* **2017**, *2017* (40), 5966–5974. DOI: 10.1002/ejoc.201701045.
- (20) Gu, C.; Huang, N.; Chen, Y.; Qin, L.; Xu, H.; Zhang, S.; Li, F.; Ma, Y.; Jiang, D. π -Conjugated Microporous Polymer Films: Designed Synthesis, Conducting Properties, and Photoenergy Conversions. *Angew. Chem. Int. Ed.* **2015**, *54* (46), 13594–13598. DOI: 10.1002/anie.201506570.
- (21) Xiao, Q.; Sakurai, T.; Fukino, T.; Akaike, K.; Honsho, Y.; Saeki, A.; Seki, S.; Kato, K.; Takata, M.; Aida, T. Propeller-Shaped Fused Oligothiophenes: A Remarkable Effect of the Topology of Sulfur Atoms on Columnar Stacking. *J. Am. Chem. Soc.* **2013**, *135* (49), 18268–18271. DOI: 10.1021/ja4092769.
- (22) Wei, H.; Ning, J.; Cao, X.; Li, X.; Hao, L. Benzotrithiophene-Based Covalent Organic Frameworks: Construction and Structure Transformation under Ionothermal Condition. *J. Am. Chem. Soc.* **2018**, *140* (37), 11618–11622. DOI: 10.1021/jacs.8b08282.

- (23) Song, Y.; Guo, L.; Du, Y.; Yang, L.; Wang, L. Dual emission N-doped carbon dot@benzotrithiophene tricarbaldehyde-terephthalic dihydrazide covalent organic framework. *Chem. Commun.* **2020**, -. DOI: 10.1039/D0CC06409B.
- (24) Pan, X.; Qin, X.; Zhang, Q.; Ge, Y.; Ke, H.; Cheng, G. N- and S-rich covalent organic framework for highly efficient removal of indigo carmine and reversible iodine capture. *Micropor. Mesopor. Mat.* **2020**, *296*, 109990. DOI: 10.1016/j.micromeso.2019.109990.
- (25) Lohse, M. S.; Rotter, J. M.; Margraf, J. T.; Werner, V.; Becker, M.; Herbert, S.; Knochel, P.; Clark, T.; Bein, T.; Medina, D. D. From benzodithiophene to diethoxy-benzodithiophene covalent organic frameworks – structural investigations. *CrystEngComm* **2016**, *18* (23), 4295–4302. DOI: 10.1039/C6CE00193A.
- (26) Sick, T.; Rotter, J. M.; Reuter, S.; Kandambeth, S.; Bach, N. N.; Döblinger, M.; Merz, J.; Clark, T.; Marder, T. B.; Bein, T.; Medina, D. D. Switching on and off Interlayer Correlations and Porosity in 2D Covalent Organic Frameworks. *J. Am. Chem. Soc.* **2019**, *141* (32), 12570–12581. DOI: 10.1021/jacs.9b02800.
- (27) Bertrand Guillaume H. V.; Michaelis Vladimir K.; Ong Ta-Chung; Griffin Robert G.; Dincă Mircea. Thiophene-based covalent organic frameworks. *PNAS* **2013**, *110* (13), 4923–4928. DOI: 10.1073/pnas.1221824110.
- (28) Mähringer, A.; Medina, D. D. Taking stock of stacking. *Nat. Chem.* **2020**, *12* (11), 985–987. DOI: 10.1038/s41557-020-00568-z.
- (29) Thommes, M.; Kaneko, K.; Neimark, A. V.; Olivier, J. P.; Rodriguez-Reinoso, F.; Rouquerol, J.; Sing, K. S.W. Physisorption of gases, with special reference to the evaluation of surface area and pore size distribution (IUPAC Technical Report). *Pure Appl. Chem.* **2015**, *87* (9-10), 1051–1069. DOI: 10.1515/pac-2014-1117.
- (30) Sick, T.; Hufnagel, A. G.; Kampmann, J.; Kondofersky, I.; Calik, M.; Rotter, J. M.; Evans, A.; Döblinger, M.; Herbert, S.; Peters, K.; Böhm, D.; Knochel, P.; Medina, D. D.; Fattakhova-Rohlfing, D.; Bein, T. Oriented Films of Conjugated 2D Covalent Organic Frameworks as Photocathodes for Water Splitting. *J. Am. Chem. Soc.* **2018**, *140* (6), 2085–2092. DOI: 10.1021/jacs.7b06081.
- (31) Medina, D. D.; Werner, V.; Auras, F.; Tautz, R.; Dogru, M.; Schuster, J.; Linke, S.; Döblinger, M.; Feldmann, J.; Knochel, P.; Bein, T. Oriented Thin Films of a Benzodithiophene Covalent Organic Framework. *ACS Nano* **2014**, *8* (4), 4042–4052. DOI: 10.1021/nn5000223.
- (32) Medina, D. D.; Sick, T.; Bein, T. Photoactive and Conducting Covalent Organic Frameworks. *Adv. Energy Mater.* **2017**, *7* (16), 1700387. DOI: 10.1002/aenm.201700387.
- (33) Liu, Z.; Kobayashi, M.; Paul, B. C.; Bao, Z.; Nishi, Y. Contact engineering for organic semiconductor devices via Fermi level depinning at the metal-organic interface. *Phys. Rev. B* **2010**, *82* (3), 35311. DOI: 10.1103/PhysRevB.82.035311.
- (34) Vladimirov, I.; Chow, C.; Strudwick, A.-J.; Kowalsky, W.; Schwab, M. G.; Kälblein, D.; Weitz, R. T. Bulk transport and contact limitation of MoS₂ multilayer flake transistors untangled via temperature-dependent transport measurements. *Phys. Status Solidi A* **2015**, *212* (9), 2059–2067. DOI: 10.1002/pssa.201532157.
- (35) Yuhao Zhu; Shuyi Jiang; Xuechun Jing; Xiao Feng. Electrically conductive 2D covalent organic frameworks. *Trends Chem.* **2022**, *4* (2), 128–141. DOI: 10.1016/j.trechm.2021.11.006.

- (36) Souto, M.; Perepichka, D. F. Electrically conductive covalent organic frameworks: bridging the fields of organic metals and 2D materials. *J. Mater. Chem. C* **2021**, *9* (33), 10668–10676. DOI: 10.1039/D1TC00750E.
- (37) Rappe, A. K.; Casewit, C. J.; Colwell, K. S.; Goddard, W. A.; Skiff, W. M. UFF, a full periodic table force field for molecular mechanics and molecular dynamics simulations. *J. Am. Chem. Soc.* **1992**, *114* (25), 10024–10035. DOI: 10.1021/ja00051a040.
- (38) Dewar, M. J. S.; Zoebisch, E. G.; Healy, E. F.; Stewart, J. J. P. Development and use of quantum mechanical molecular models. 76. AM1: a new general purpose quantum mechanical molecular model. *J. Am. Chem. Soc.* **1985**, *107* (13), 3902–3909. DOI: 10.1021/ja00299a024.
- (39) Dewar, M. J. S.; Yuan, Y. C. AM1 parameters for sulfur. *Inorg. Chem.* **1990**, *29* (19), 3881–3890. DOI: 10.1021/ic00344a045.
- (40) Kriebel, M.; Sharapa, D.; Clark, T. Charge Transport in Organic Materials: Norm-Conserving Imaginary Time Propagation with Local Ionization Energy as the External Potential. *J. Chem. Theory Comput.* **2017**, *13* (12), 6308–6316. DOI: 10.1021/acs.jctc.7b00568.
- (41) Kriebel, M.; Hennemann, M.; Beierlein, F. R.; Medina, D. D.; Bein, T.; Clark, T. Propagation of Holes and Electrons in Metal–Organic Frameworks. *J. Chem. Inf. Model.* **2019**, *59* (12), 5057–5064. DOI: 10.1021/acs.jcim.9b00461.
- (42) Ehresmann, B.; Groot, M. J. de; Alex, A.; Clark, T. New Molecular Descriptors Based on Local Properties at the Molecular Surface and a Boiling-Point Model Derived from Them. *J. Chem. Inf. Comp. Sci.* **2004**, *44* (2), 658–668. DOI: 10.1021/ci034215e.
- (43) Clark, T. The local electron affinity for non-minimal basis sets. *J. Mol. Model.* **2010**, *16* (7), 1231–1238. DOI: 10.1007/s00894-009-0607-x.
- (44) Sjoberg, P.; Murray, J. S.; Brinck, T.; Politzer, P. Average local ionization energies on the molecular surfaces of aromatic systems as guides to chemical reactivity. *Can. J. Chem.* **1990**, *68* (8), 1440–1443. DOI: 10.1139/v90-220.

6.6 Appendix

Abbreviations

AFM	atomic force microscopy	HRMS	high resolution mass spectroscopy
BET	Brunauer-Emmett-Teller	NIR	near-infrared
BTT	benzotrithiophene	NBS	<i>N</i> -bromosuccinimide
Bu	butyl	PL	photoluminescence
Db	<i>trans,trans</i> -dibenzylideneacetone	PSD	pore size distribution
DCM	dichloromethane	PXRD	powder X-ray diffraction
DFT	density functional theory	rt	room temperature
DMF	<i>N,N</i> -dimethylformamide	SEM	scanning electron microscopy
DMSO	dimethyl sulfoxide	TEM	transmission electron microscopy
EI	electron ionization	THF	tetrahydrofuran
eq.	equivalents	quant.	quantitative

6.6.1 Methods

Nuclear magnetic resonance (NMR) spectra were recorded using Bruker AV 400 and AV 400 TR spectrometers. Chemical shifts are expressed in parts per million (δ scale) and are calibrated using residual (undeuterated) solvent peaks as an internal reference ($^1\text{H-NMR}$: CDCl_3 : 7.26, DMSO-d_6 : 2.50; $^{13}\text{C-NMR}$: CDCl_3 : 77.16, DMSO-d_6 : 39.52). Data for ^1H NMR spectra are reported in the following way: chemical shift (δ ppm) (multiplicity, coupling constant/ Hz, integration). Multiplicities are reported as follows: s= singlet, d= doublet, t= triplet, q= quartet, m= multiplet, or combinations of thereof.

Solid-state ^{13}C cross-polarization magic angle spinning (CP-MAS) NMR spectra were recorded with a Bruker Avance III-500 spectrometer using 4 mm diameter ZrO_2 rotors at a spinning frequency of 12 kHz.

High resolution electron ionization (EI) **mass spectra (MS)** were recorded with a Thermo Finnigan MAT 95 instrument.

Powder X-ray diffraction (PXRD) measurements were performed using a Bruker D8 Discover with Ni-filtered Cu K_α radiation and a LynxEye position-sensitive detector in Bragg-Brentano geometry.

The **structure models of the COFs** were constructed using the Accelrys Materials Studio software package. Structure refinements using the Pawley method were carried out as implemented in the Reflex module of the Materials Studio software.

Nitrogen sorption isotherms were recorded with Quantachrome Autosorb *I* and Autosorb *iQ* instruments at 77 K. The samples were outgassed for 24 h at 120 °C under high vacuum prior to the measurements. Pore size distributions were calculated using the quenched solid density functional theory (QSDFT) model with a carbon kernel for cylindrical pores.

Transmission electron microscopy (TEM) was performed on a FEI Titan Themis instrument equipped with a field emission gun operated at 300 kV.

Scanning electron microscopy (SEM) images were recorded with a FEI Helios NanoLab *G3 UC* scanning electron microscope equipped with a field emission gun operated at 3-5 kV. For the cross-section analysis substrates were partially cut and broken manually to reveal fresh cross-sections. Prior to SEM analysis the samples were coated with a thin carbon layer by carbon fiber flash evaporation in high vacuum.

UV-VIS-NIR spectra were recorded using a Perkin-Elmer Lambda 1050 spectrometer equipped with a 150 mm integrating sphere, photomultiplier tube (PMT) and InGaAs detectors. **Diffuse reflectance spectra** were collected with a Praying Mantis (Harrick) accessory and were referenced to barium sulfate powder as white standard.

2D grazing-incidence small angle X-ray scattering (GISAXS) data were recorded with an Anton Paar SAXSpace system equipped with a GeniX Cu K α microsource and a Dectris Eiger R 1M detector. The samples were positioned at 135 mm sample-detector distance and a tilt angle of 2.1° with respect to the incident beam.

Photoluminescence (PL) data were processed with a FluoTime 300 from PicoQuant GmbH. The samples were photo-excited using a 378 nm laser (LDH-P-C-375, from PicoQuant GmbH). The PL was collected using a high-resolution monochromator and photomultiplier detector assembly (PMA-C 192-N-M, PicoQuant GmbH).

Thermogravimetric analysis (TGA) measurements were performed on a Netzsch Jupiter ST 499 C instrument equipped with a Netzsch TASC 414/4 controller. The samples were heated from room temperature to 900 °C under a synthetic air flow (25 ml min⁻¹) at a heating rate of 10 K min⁻¹.

Conductivity The temperature dependent transport measurements were performed at a Lakeshore CRX-VF probe station at vacuum conditions with $p < 2 \times 10^{-7}$ mbar. The electrical gold contacts (60 nm thickness) were evaporated through a shadow mask. An electrically conductive sample stage was used for gating through the back gate. This stage was thermally coupled to a helium refrigerator allowing for measurements from 6 K to room temperature. Two source meters (Keithley 2450) were used to apply source-drain and gate voltages.

The **conductive AFM (cAFM)** measurements were performed on a Jupiter XR AFM by Oxford Instruments using SCM-PIT conductive AFM tips with PtIr5 coating. The BTT COF films for this analysis were grown on glass substrates covered by a gold layer.

6.6.2 Materials and Building Block Synthesis

General: All materials were purchased from *Sigma Aldrich*, *Acros* or *TCI Europe* in the common purities *purum*, *puriss* or *reagent grade*. The materials were used as received without additional purification and handled in air unless otherwise noted.

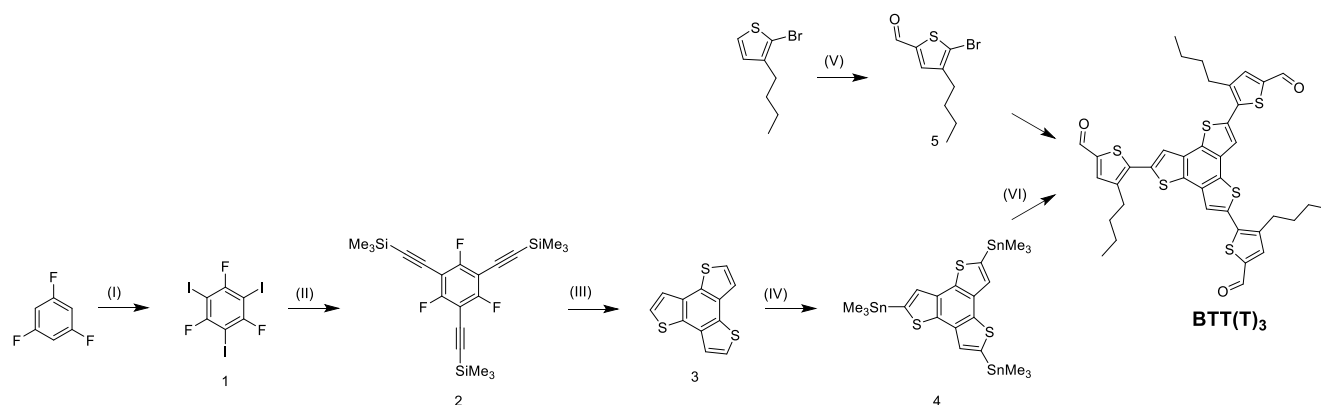


Figure 6.6. Synthesis of BTT(T)₃ building block. (I) H₃IO₆, KI, H₂SO₄, 0 to 70 °C, 87 %. (II) SiMe₃CCH, CuI, PdCl₂(PPh₃)₂, NEt₃, 70 °C, quant. (III) Na₂S, CuI, TMEDA, DMF, 110 °C, 80 %. (IV) n-BuLi, Me₃SnCl, THF, 0 °C to rt, quant. (V) POCl₃, DMF, 70 °C, 62 %. (VI) Pd(dba)₂, tri(2-furyl)phosphine, toluene, 85 °C, 36 %.

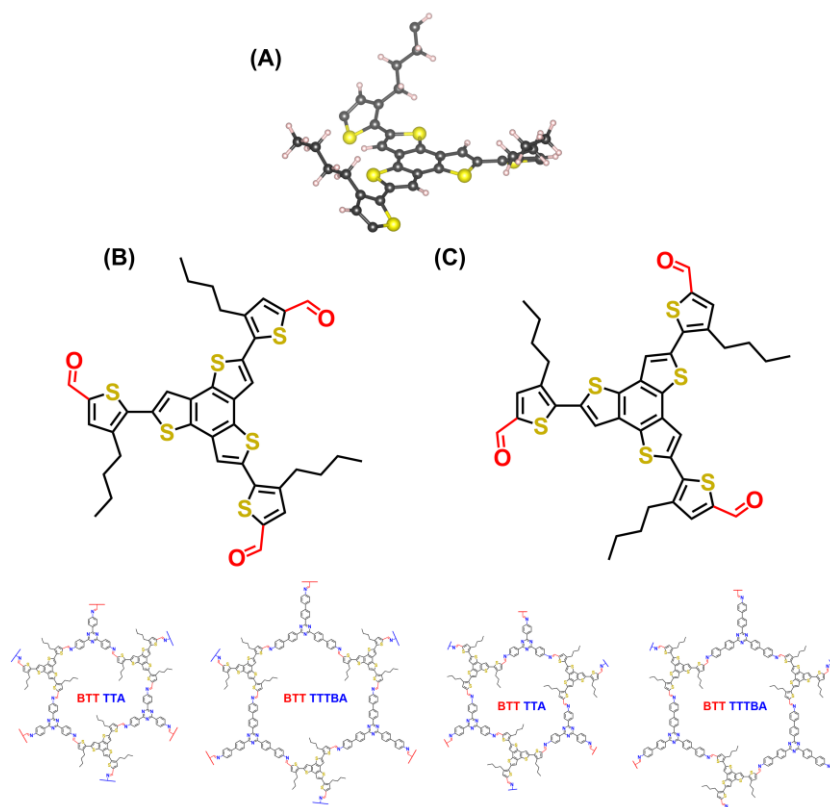
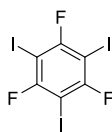
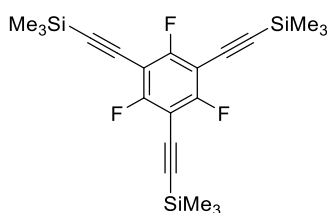


Figure 6.7. A. Structure simulation of BTT(T)₃. B. and C. Schematic illustration of BTT(T)₃ building blocks and the respective COFs BTT TTA and BTT TTTBA.

1,3,5-trifluoro-2,4,6-triiodobenzene (1)¹

Periodic acid (12.9 g, 56.4 mmol) was suspended in concentrated H₂SO₄ and cooled to 0 °C. Potassium iodide (28.4 g, 171 mmol) was added at 0 °C over the course of 5 min. Subsequently, 1,3,5-trifluorobenzene (5.0 g, 38 mmol, 3.9 mL) was added over the course of 15 min at 0 °C and the reaction mixture was heated to 70 °C for 4 h. After completion of the reaction, the mixture was poured onto crushed ice (400 mL) and extracted with diethyl ether. The combined organic phases were washed with aqueous sodium thiosulfate solution, dried over MgSO₄, filtered and the filtrate was concentrated under reduced pressure. The crude product was purified by sublimation *in vacuo* to afford the title compound as slightly brown crystals (16.7 g, 32.8 mmol, 87 %).

HRMS (EI) calcd for C₆F₃I₃ [M]⁺: 509.71; found 509.71.

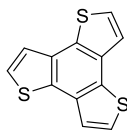
((2,4,6-trifluorobenzene-1,3,5-triyl)tris(ethyne-2,1-diyl))tris(trimethylsilane) (2)²

1,3,5-trifluoro-2,4,6-triiodobenzene (**1**, 1.5 g, 3.0 mmol, 1.0 eq.), PdCl₂(PPh₃)₂ (216 mg, 0.30 mmol, 10 mol %) and CuI (114 mg, 0.60 mmol, 20 mol%) were dissolved in 20 mL THF and 40 mL triethylamine. Ethynyltrimethylsilane (1.45 mL, 10.4 mmol, 3.5 eq.) was added and the reaction mixture was stirred at 70 °C under argon overnight. After the reaction was completed, the mixture was filtered over celite, washed with CHCl₃ and concentrated under reduced pressure. The crude product was purified *via* column chromatography (silica, cyclohexane, *R_f*=0.4) to afford the title compound as colorless powder (947 mg, 2.25 mmol, 75 %).

¹H NMR (400 MHz, CDCl₃) δ = 0.26 (s, 27H).

¹³C NMR (100 MHz, CDCl₃) δ = 164.4, 161.8, 106.9, 88.7, 0.23.

HRMS (EI) calcd for C₂₁H₂₇F₃Si₃ [M]⁺: 420.14; found 420.14

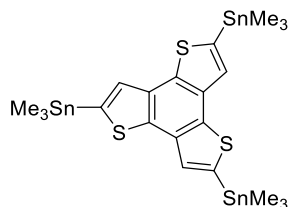
Benzo[1,2-b:3,4-b':5,6-b'']trithiophene (3)²

Compound **2** (210 mg, 0.50 mmol) was dissolved in 37 mL dry DMF. CuI (30.4 mg, 0.16 mmol), TMEDA (34.7 mg, 0.05 mL, 0.30 mmol) and sodium sulfide nonahydrate (1.08 g, 4.49 mmol) were added and the reaction mixture was stirred at 110 °C for 2 h. After completion of the reaction, the mixture was filtered, and the solution was extracted with ethyl acetate. The combined organic phases were washed with brine, dried over MgSO₄, filtered and the filtrate was concentrated under reduced pressure. The crude product was purified *via* column chromatography (silica, cyclohexane, *R_f*= 0.38) to afford the title compound as colorless solid (94.8 mg, 0.38 mmol, 77 %).

¹H NMR (400 MHz, CDCl₃) δ = 7.64 (d, *J*= 5.4 Hz, 3H), 7.54 (d, *J*= 5.4 Hz, 3H).

¹³C NMR (100 MHz, CDCl₃) δ = 131.9, 131.6, 125.1, 122,4.

HRMS (EI) calcd for C₁₂H₆S₃ [M]⁺: 245.96; found 245.96.

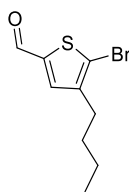
2,5,8-tris(trimethylstannyl)benzo[1,2-b:3,4-b':5,6-b'']trithiophene (4)³

Compound **3** (24.6 mg, 0.10 mmol, 1 eq.) was dissolved in 3 mL dry THF and cooled to -78 °C. *n*-BuLi (0.30 mL, 0.60 mmol, 6.0 eq.) was added and the solution was stirred at -78 °C for 1 h. Subsequently, the reaction mixture was allowed to warm to room temperature and stirred for another 2 h. After cooling to 0 °C, SnMe₃Cl (0.65 mL, 0.65 mmol, 6.5 eq.) was added and the solution was allowed to warm to room temperature overnight. The solvent was removed under reduce pressure to afford the title compound as slightly beige-colored solid (73.5 mg, 0.1 mmol, quant.).

¹H NMR (400 MHz, CDCl₃) δ = 7.69 (s, 3H), 0.47 (s, 27 H).

¹³C NMR (100 MHz, CDCl₃) δ = -8.0, 130.6, 132.9, 136.0, 138.1.

HRMS (EI) calcd for C₂₁H₃₀S₃Sn₃ [M]⁺: 737.86; found 737.86.

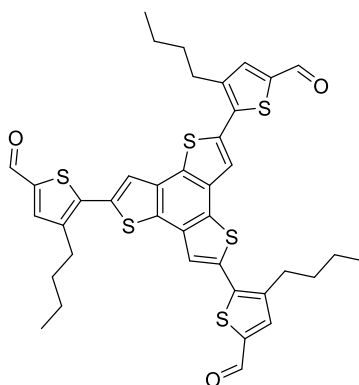
5-bromo-4-butylthiophene-2-carbaldehyde (5)

2-bromo-3-butylthiophene (3.0 g, 13.7 mmol) was dissolved in dry DMF (10 mL). POCl₃ (2.50 mL, 27.4 mmol, 2 eq.) was added slowly and the reaction was heated to 70 °C overnight under argon. After completion of the reaction, the solution was poured onto crushed ice and neutralized using Na₂CO₃. The solution was extracted using DCM and washed with water and brine. The combined organic phases were dried over MgSO₄, filtered and the filtrate was concentrated under reduced pressure. The crude product was purified *via* column chromatography (silica, DCM/cyclohexane 1:2) to afford the title compound as light yellow oil (2080 mg, 8.42 mmol, 62 %).

¹H NMR (400 MHz, CDCl₃) δ = 9.75 (s, 1H), 7.49 (s, 1H), 2.67-2.56 (m, 2H), 1.65-1.54 (m, 2H), 1.42-1.33 (m, 2H), 0.95 (t, J = 7.3 Hz, 3H).

¹³C NMR (100 MHz, CDCl₃) δ = 182.2, 141.5, 139.9, 137.0, 31.6, 29.3, 27.8, 22.4, 14.0.

HRMS (EI) calcd for C₉H₁₁BrOS [M]⁺: 245.97; found 245.97.

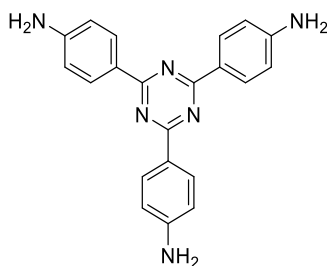
5,5',5''-(benzo[1,2-*b*:3,4-*b'*:5,6-*b''*])trithiophene-2,5,8-triyl(4-butylthiophene-2-carbaldehyde) (BTT(T)₃)

Compound **4** (73.5 mg, 0.10 mmol, 1 eq.) and compound **5** (148 mg, 0.60 mmol, 6 eq.) were dissolved in 6 mL dry toluene. Pd(dba)₂ (8.60 mg, 0.015 mmol, 15 mol%) and tri(2-furyl)phosphine (8.7 mg, 0.0375 mmol, 37.5 mol%) were added and the reaction mixture was heated to 85 °C under argon for two days. After the reaction was complete, the solvent was removed under reduced pressure. The crude product was purified *via* column chromatography (silica, DCM) to afford the title compound as orange solid (26.8 mg, 0.036 mmol, 36%).

HRMS (EI) calcd for $C_{39}H_{36}O_3S_6 [M]^+$: 744.10; found 744.10.

1H NMR (400 MHz, DMSO- d_6) δ = 9.94 (s, 3H), 7.39 (s, 3H), 7.35 (s, 3H) 2.93-3.01 (m, 6H), 1.75-1.68 (m, 6H), 1.28-1.23 (m, 6H), 0.90-0.97 (m, 9H).

4,4',4''-(1,3,5-triazine-2,4,6-triyl)trianiline (TTA)



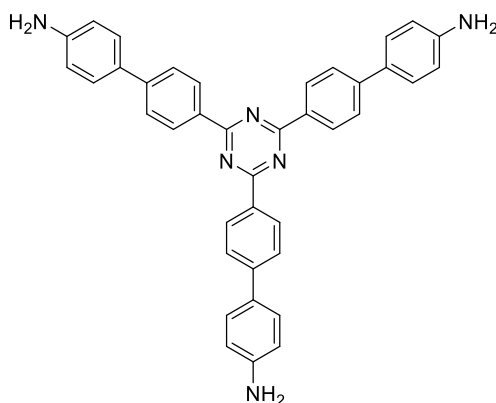
4-aminobenzonitrile (1.55 g, 13 mmol) was dissolved in $CHCl_3$ (5 ml) and stirred at 0 °C for 1 h. Subsequently, trifluoromethanesulfonic acid (4 mL) was added dropwise to the reaction mixture. The mixture was allowed to warm to room temperature and was stirred for 24 h. Crushed ice was added, and the mixture was neutralized using sodium hydroxide. The resulting yellow precipitate was filtered off and washed thoroughly with water. After drying under reduced pressure, the title compound was obtained as light yellow solid (3.6 g, 10.3 mmol, 79 %).

1H NMR (400 MHz, DMSO- d_6) δ = 8.35 (d, J = 8.7 Hz, 1H), 6.69 (d, J = 8.8 Hz, 1H), 5.90 (s, 1H).

^{13}C NMR (100 MHz, DMSO- d_6) δ = 169.5, 152.9, 130.1, 122.9, 113.1.

HRMS (EI) calcd for $C_{21}H_{16}N_6 [M]^+$: 354.16; found 354.16.

4,4''',4''''-(1,3,5-triazine-2,4,6-triyl)tris((1,1'-biphenyl)-4-amine) (TTTBA)



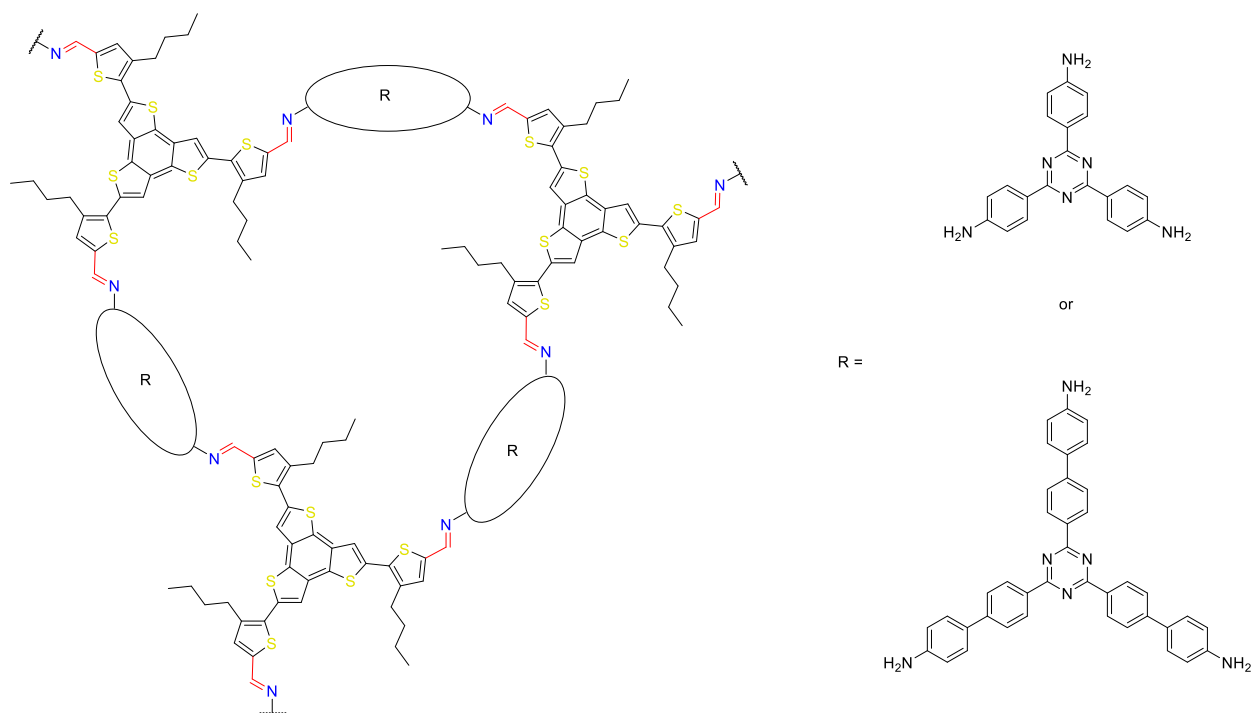
4-(4-aminophenyl)benzotrithiophene (1.7 g, 8.6 mmol) was added to a Schlenk tube and cooled to 0 °C. Trifluoromethanesulfonic acid (2.30 mL, 25.7 mmol) was added dropwise over the course of 20 minutes while maintaining the temperature at 0 °C. The reaction mixture was stirred for 24 h. After the reaction

was complete, distilled water (30 mL) was added to the mixture and the solution was neutralized using sodium hydroxide. The resulting yellow precipitate was filtered off and washed thoroughly with water. After drying under reduced pressure, the title compound was obtained as yellow solid (4.2 g, 7.2 mmol, 84 %).

¹H NMR (400 MHz, DMSO-*d*₆) δ = 8.72 (d, *J* = 8.5 Hz, 6H), 7.84 (d, *J* = 8.6 Hz, 6H), 7.55 (d, *J* = 8.6 Hz, 6H), 6.70 (d, *J* = 8.6 Hz, 6H), 5.44 (s, 6H).

¹³C NMR (100 MHz, DMSO-*d*₆) δ = 114.2, 125.9, 126.4, 128.0, 129.2, 132.6, 144.9, 149.4, 170.6.

HRMS (EI) calcd for C₃₉H₃₀N₆ [M]⁺: 582.25; found 582.25.



Synthesis of BTT TTA

In a 6 mL culture tube, BTT(T)₃ (4.99 mg, 16.7 μmol) and TTA (2.37 mg, 10.0 μmol) were suspended in a mixture of mesitylene and 1,4-dioxane (500 μL, v : v 8:1). After adding 50 μL of acetic acid (aqueous, 6M) the tube was sealed and heated at 120 °C for 72 h. The resulting precipitate was filtered and rinsed with anhydrous THF before Soxhlet extraction with anhydrous THF overnight. After drying under reduced pressure, the final product was obtained as orange-brown powder.

Synthesis of BTT TTTBA

In a 6 mL culture tube, BTT(T)₃ (4.99 mg, 16.7 μmol) and TTTBA (3.9 mg, 10 μmol) were suspended in a mixture of mesitylene and 1,4-dioxane (500 μL, v : v 8:1). After adding 50 μL of acetic acid (aqueous, 6M) the tube was sealed and heated at 120 °C for 72 h. The resulting precipitate was filtered and rinsed with anhydrous THF before Soxhlet extraction with anhydrous THF overnight. After drying under reduced pressure, the final product was obtained as yellow-brown powder.

Synthesis of BTT TTA thin film

The thin films were synthesized using a bottom-up, in-situ, approach. An autoclave equipped with a teflon liner and a substrate was charged with BTT(T)₃ (4.99 mg, 16.7 μmol) and TTA (2.37 mg, 10.0 μmol). Next, a mixture of mesitylene and 1,4-dioxane (2000 μL, v : v 8:1) and 200 μL of acetic acid (aqueous, 6M) were added. The autoclave was sealed and heated at 120 °C for 16 h. After cooling to room temperature, the COF film was rinsed with anhydrous THF and dried under reduced pressure.

Synthesis of BTT TTTBA thin film

An autoclave equipped with a teflon liner and a substrate was charged with BTT(T)₃ (4.99 mg, 16.7 μmol) and TTTBA (3.9 mg, 10 μmol). Next, a mixture of mesitylene and 1,4-dioxane (2000 μL, v : v 8:1) and 200 μL of acetic acid (aqueous, 6M) were added. The autoclave was sealed and heated at 120 °C for 16 h. After cooling to room temperature, the COF film was rinsed with anhydrous THF and dried under reduced pressure.

6.6.3 Structural Analysis**Unit cell parameters (P1) and atomic coordinates for BTT TTA**

$$a = 27.7, b = 28.0, c = 3.7 \text{ \AA}$$

$$\alpha = \beta = 90^\circ, \gamma = 122^\circ$$

Atom	a/x	b/y	c/z
C1	0.21138	0.54317	0.48258
C2	0.23867	0.52539	0.41233
C3	0.28453	0.55216	0.41536
C4	0.30417	0.59740	0.48720
C5	0.27686	0.61521	0.55688
C6	0.23096	0.58836	0.55508
C7	0.47483	0.83792	0.47682
C8	0.50031	0.81826	0.40309
C9	0.48117	0.77239	0.40272
C10	0.43611	0.74526	0.47528
C11	0.41065	0.76498	0.54881
C12	0.42984	0.81083	0.55019
C13	0.50682	0.57500	0.48358
C14	0.46142	0.54920	0.54972
C15	0.43433	0.56805	0.54721
C16	0.45199	0.61324	0.47936
C17	0.49740	0.63899	0.41249
C18	0.52442	0.62010	0.41400
C19	0.71631	0.44999	0.46245
S20	0.66446	0.44255	0.46770
C21	0.68775	0.49867	0.46237

Benzotrithiophene COF Thin Films – Directional Electrical Conductivity

C22	0.73285	0.52166	0.45687
C23	0.74937	0.49356	0.45691
C24	0.60064	0.17234	0.48886
S25	0.60795	0.12758	0.49070
C26	0.55215	0.09481	0.49774
C27	0.52936	0.11719	0.49860
C28	0.55735	0.16198	0.49347
C29	0.87671	0.33403	0.45403
S30	0.92126	0.38622	0.44694
C31	0.95377	0.36287	0.44523
C32	0.93146	0.31751	0.44986
C33	0.88695	0.30082	0.45495
C34	0.09717	0.44458	0.61245
C35	0.14291	0.47209	0.62067
C36	0.16268	0.51451	0.48022
C37	0.13561	0.52914	0.33658
C38	0.08979	0.50159	0.32892
C39	0.07022	0.45888	0.46072
C40	0.35282	0.62584	0.48641
N41	0.37892	0.60752	0.48501
C42	0.42335	0.63342	0.47941
N43	0.44163	0.67799	0.47520
C44	0.41587	0.69669	0.47654
N45	0.37149	0.67045	0.48216
C46	0.53581	0.55513	0.48765
C47	0.49494	0.88652	0.47611
C48	0.52153	0.51317	0.34944
C49	0.54929	0.49504	0.34821
C50	0.59196	0.51852	0.48091
C51	0.60590	0.56001	0.62766
C52	0.57818	0.57811	0.62951
C53	0.53659	0.91361	0.62017
C54	0.55495	0.95942	0.62452
C55	0.53192	0.97887	0.48892
C56	0.49079	0.95188	0.33582
C57	0.47244	0.90616	0.33133
N58	0.61982	0.49910	0.46867

C59	0.66228	0.52121	0.46347
C60	0.75419	0.36483	0.46371
C61	0.77683	0.34143	0.46292
C62	0.75403	0.29574	0.46762
C63	0.70806	0.27291	0.47319
C64	0.68544	0.29578	0.47401
C65	0.70878	0.34202	0.46923
C66	0.69148	0.36936	0.46930
C67	0.72493	0.41301	0.46373
S68	0.77726	0.42076	0.45841
C69	0.82136	0.35889	0.45779
C70	0.83128	0.32529	0.45876
S71	0.78657	0.27262	0.46589
C72	0.68083	0.22811	0.47825
C73	0.63745	0.21806	0.48285
S74	0.62984	0.26298	0.48103
C75	0.52969	0.04660	0.50255
N76	0.55161	0.02600	0.50167
C77	0.00220	0.38855	0.44958
N78	0.02305	0.43139	0.44456
C79	0.79848	0.51240	0.45128
C80	0.82579	0.56227	0.44592
C81	0.87328	0.57596	0.44073
C82	0.90002	0.62501	0.43548
C83	0.53868	0.19254	0.49349
C84	0.48910	0.17007	0.49938
C85	0.47556	0.20416	0.49872
C86	0.42680	0.18194	0.50451
C87	0.85650	0.25142	0.46057
C88	0.87876	0.22401	0.46004
C89	0.84481	0.17622	0.46589
C90	0.86683	0.14939	0.46535

Unit cell parameters (P1) and atomic coordinates for BTT TTTBA

a = 34.4, b = 35.1, c = 4.0 Å

$$\alpha = 89^\circ, \beta = 90^\circ, \gamma = 120^\circ$$

Atom	a/x	b/y	c/z
C1	0.21138	0.54317	0.48258
C2	0.23867	0.52539	0.41233
C3	0.28453	0.55216	0.41536
C4	0.30417	0.59740	0.48720
C5	0.27686	0.61521	0.55688
C6	0.23096	0.58836	0.55508
C7	0.47483	0.83792	0.47682
C8	0.50031	0.81826	0.40309
C9	0.48117	0.77239	0.40272
C10	0.43611	0.74526	0.47528
C11	0.41065	0.76498	0.54881
C12	0.42984	0.81083	0.55019
C13	0.50682	0.57500	0.48358
C14	0.46142	0.54920	0.54972
C15	0.43433	0.56805	0.54721
C16	0.45199	0.61324	0.47936
C17	0.49740	0.63899	0.41249
C18	0.52442	0.62010	0.41400
C19	0.71631	0.44999	0.46245
S20	0.66446	0.44255	0.46770
C21	0.68775	0.49867	0.46237
C22	0.73285	0.52166	0.45687
C23	0.74937	0.49356	0.45691
C24	0.60064	0.17234	0.48886
S25	0.60795	0.12758	0.49070
C26	0.55215	0.09481	0.49774
C27	0.52936	0.11719	0.49860
C28	0.55735	0.16198	0.49347
C29	0.87671	0.33403	0.45403
S30	0.92126	0.38622	0.44694
C31	0.95377	0.36287	0.44523
C32	0.93146	0.31751	0.44986
C33	0.88695	0.30082	0.45495

Benzotrithiophene COF Thin Films – Directional Electrical Conductivity

C34	0.09717	0.44458	0.61245
C35	0.14291	0.47209	0.62067
C36	0.16268	0.51451	0.48022
C37	0.13561	0.52914	0.33658
C38	0.08979	0.50159	0.32892
C39	0.07022	0.45888	0.46072
C40	0.35282	0.62584	0.48641
N41	0.37892	0.60752	0.48501
C42	0.42335	0.63342	0.47941
N43	0.44163	0.67799	0.47520
C44	0.41587	0.69669	0.47654
N45	0.37149	0.67045	0.48216
C46	0.53581	0.55513	0.48765
C47	0.49494	0.88652	0.47611
C48	0.52153	0.51317	0.34944
C49	0.54929	0.49504	0.34821
C50	0.59196	0.51852	0.48091
C51	0.60590	0.56001	0.62766
C52	0.57818	0.57811	0.62951
C53	0.53659	0.91361	0.62017
C54	0.55495	0.95942	0.62452
C55	0.53192	0.97887	0.48892
C56	0.49079	0.95188	0.33582
C57	0.47244	0.90616	0.33133
N58	0.61982	0.49910	0.46867
C59	0.66228	0.52121	0.46347
C60	0.75419	0.36483	0.46371
C61	0.77683	0.34143	0.46292
C62	0.75403	0.29574	0.46762
C63	0.70806	0.27291	0.47319
C64	0.68544	0.29578	0.47401
C65	0.70878	0.34202	0.46923
C66	0.69148	0.36936	0.46930
C67	0.72493	0.41301	0.46373
S68	0.77726	0.42076	0.45841
C69	0.82136	0.35889	0.45779
C70	0.83128	0.32529	0.45876

S71	0.78657	0.27262	0.46589
C72	0.68083	0.22811	0.47825
C73	0.63745	0.21806	0.48285
S74	0.62984	0.26298	0.48103
C75	0.52969	0.04660	0.50255
N76	0.55161	0.02600	0.50167
C77	0.00220	0.38855	0.44958
N78	0.02305	0.43139	0.44456
C79	0.79848	0.51240	0.45128
C80	0.82579	0.56227	0.44592
C81	0.87328	0.57596	0.44073
C82	0.90002	0.62501	0.43548
C83	0.53868	0.19254	0.49349
C84	0.48910	0.17007	0.49938
C85	0.47556	0.20416	0.49872
C86	0.42680	0.18194	0.50451
C87	0.85650	0.25142	0.46057
C88	0.87876	0.22401	0.46004
C89	0.84481	0.17622	0.46589
C90	0.86683	0.14939	0.46535

6.6.4 IR Spectroscopy

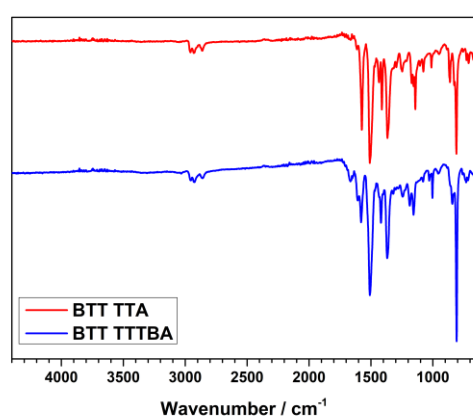


Figure 6.8. FT-IR spectra of BTT TTA (red) and BTT TTTBA (blue) confirming the formation of the COFs with the imine bonds appearing at $\sim 1580\text{ cm}^{-1}$ in both COFs.

6.6.5 Sorption

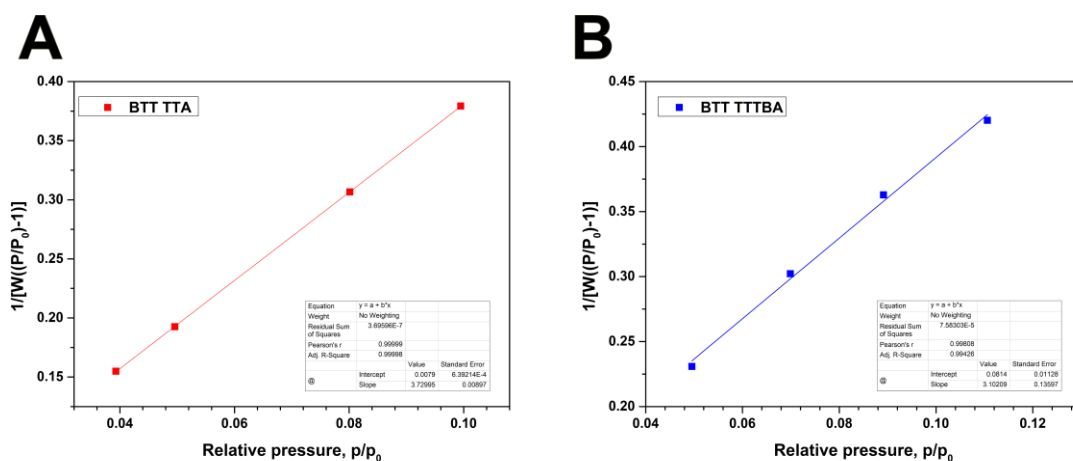


Figure 6.9 A. and B. Multi-point BET plots and linear fits of BTT TTA and BTT TTTBA, respectively.

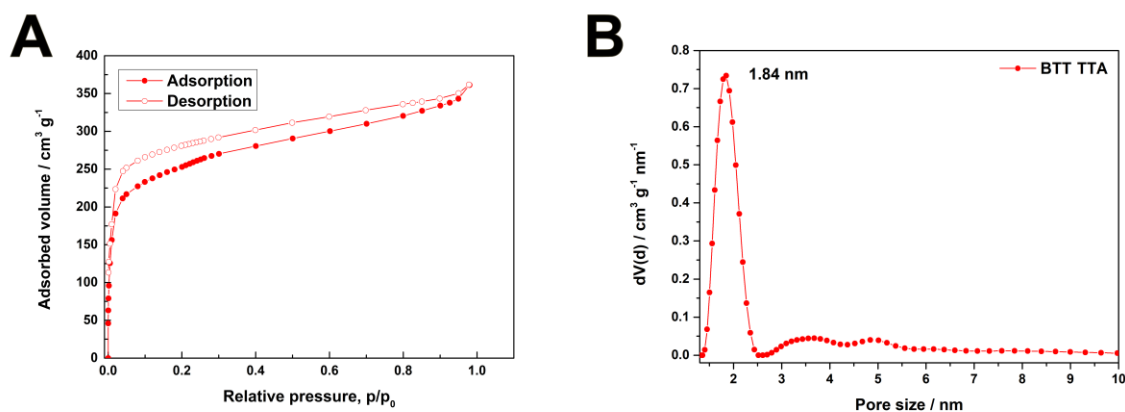


Figure 6.10. A. Nitrogen adsorption and desorption isotherms of activated BTT TTA measured at 77 K representing a Type I(a) isotherm according to IUPAC. B. The corresponding calculated pore size distribution obtained by DFT.

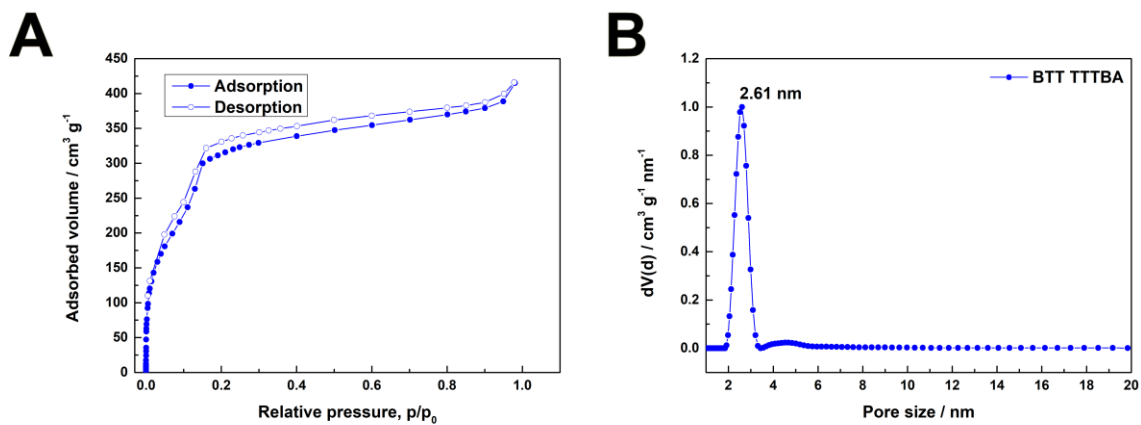


Figure 6.11. A. Nitrogen adsorption and desorption isotherms of activated BTT-TTTBA measured at 77 K representing a Type IV(b) isotherm according to IUPAC. B. The corresponding calculated pore size distribution obtained by DFT.

6.6.6 Thermogravimetric Analysis

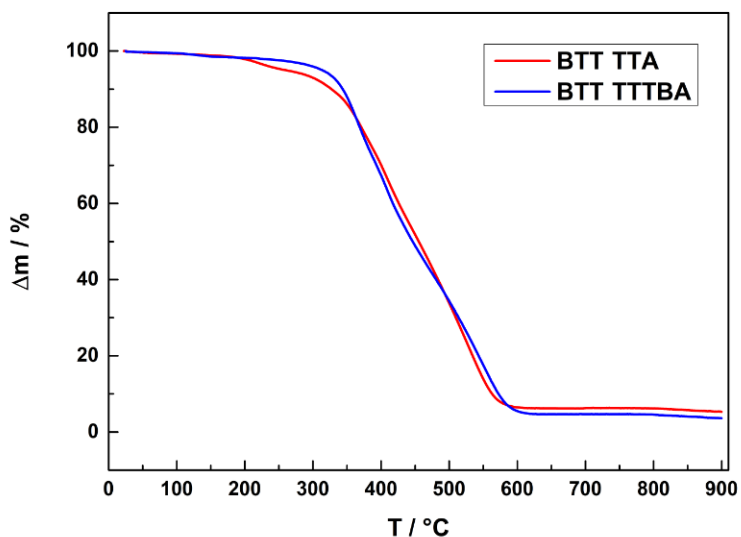


Figure 6.12. Thermogravimetric Analysis (TGA) of BTT TTA and BTT TTTBA measured for bulk materials.

6.6.7 Electron Microscopy

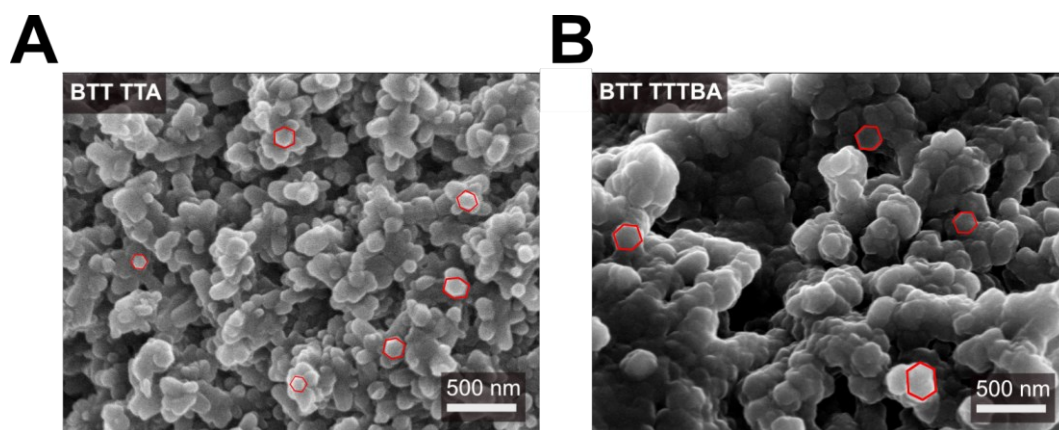


Figure 6.13. A. and B. SEM images of BTT TTA and BTT TTTBA bulk powders.

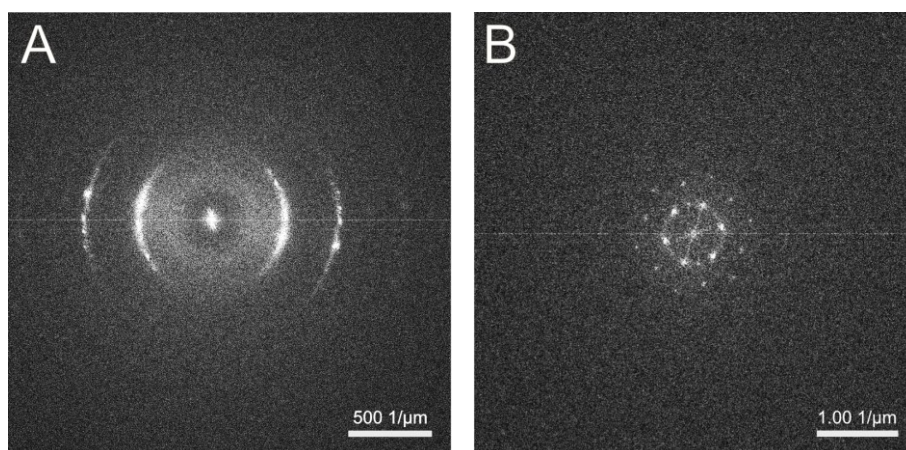


Figure 6.14. A. and B. Additional TEM images of BTT TTA and BTT TTTBA.

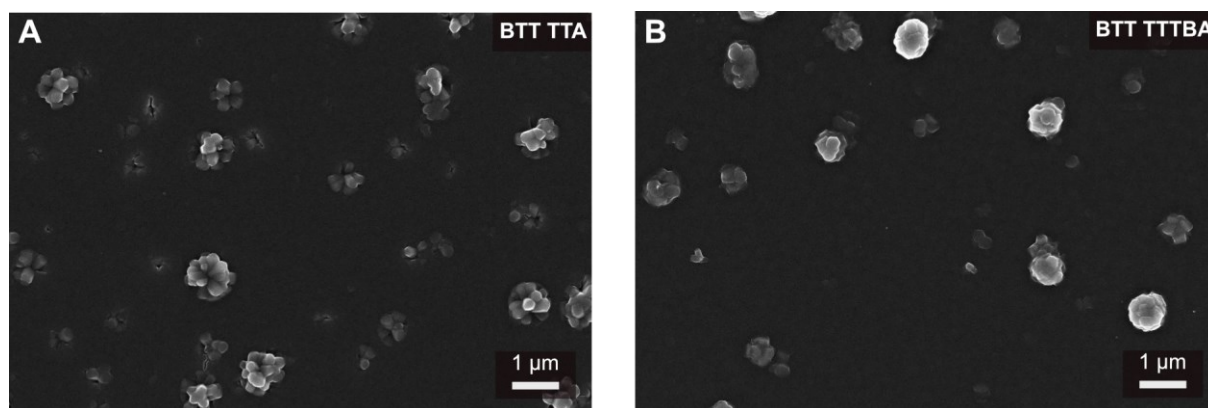


Figure 6.15. A. and B. SEM Top-View images of BTT TTA and TTTBA thin films grown on ITO.

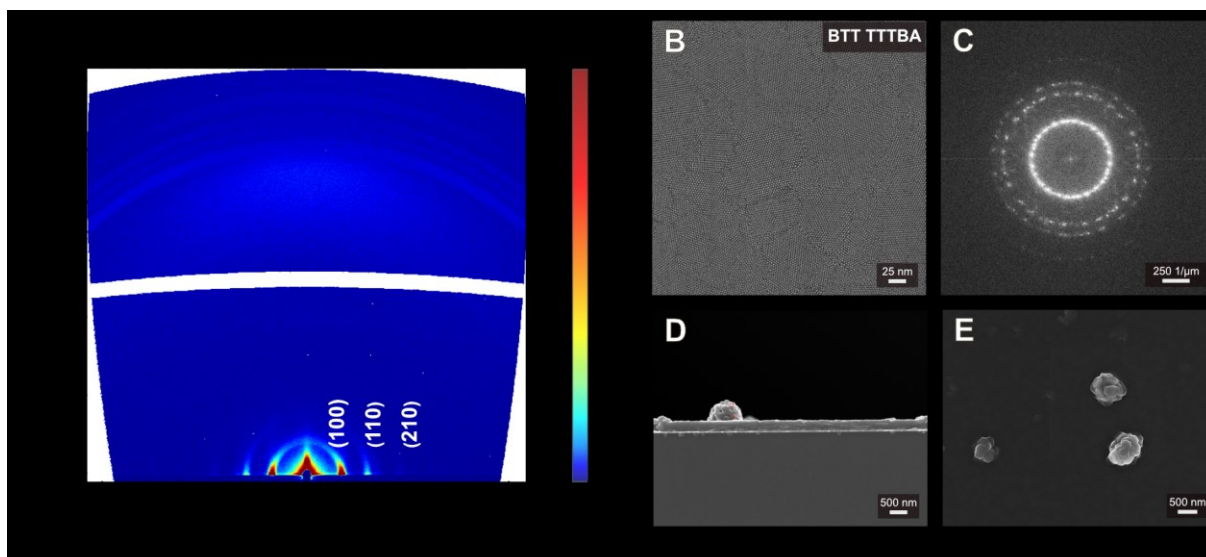


Figure 6.16. A. GIWAXS 2D pattern of BTT TTTBA thin film grown on ITO. B. and C. TEM and electron diffraction images of BTT TTTBA thin films grown on ITO, scratched off the substrate. D., E. SEM cross-section and top-view images of BTT TTTBA thin films on gold substrates, respectively.

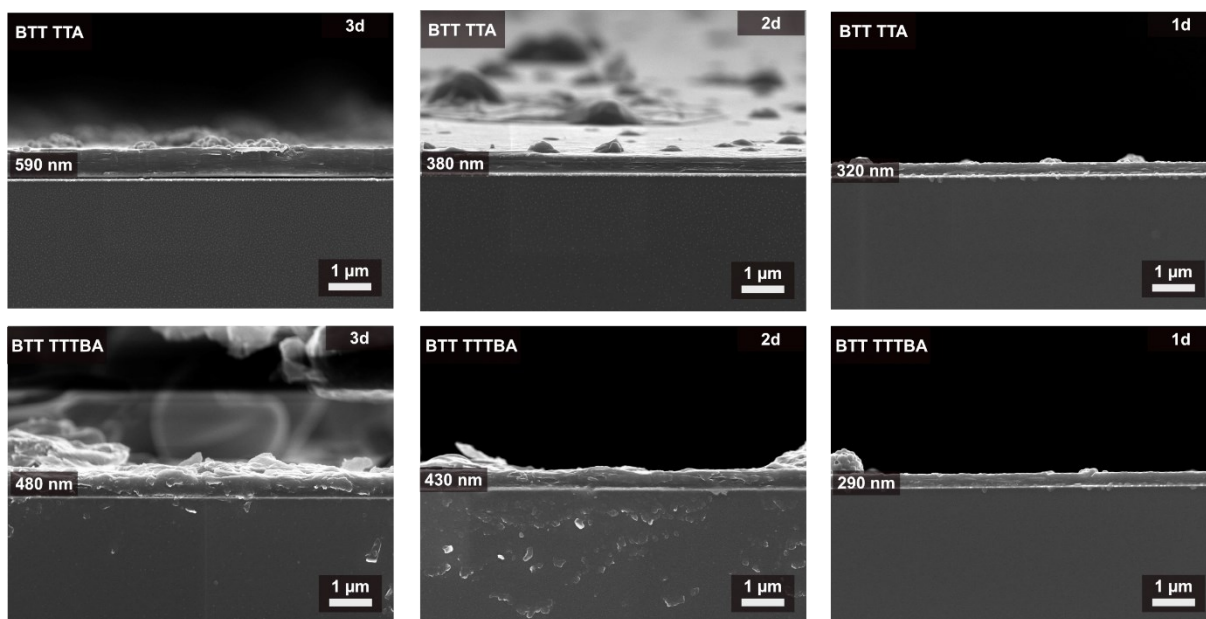


Figure 6.17. SEM cross-section images of BTT TTA and TTTBA thin films grown on gold substrates showing different thicknesses depending on the reaction times that were used.

6.6.8 Grazing Incidence Diffraction Patterns

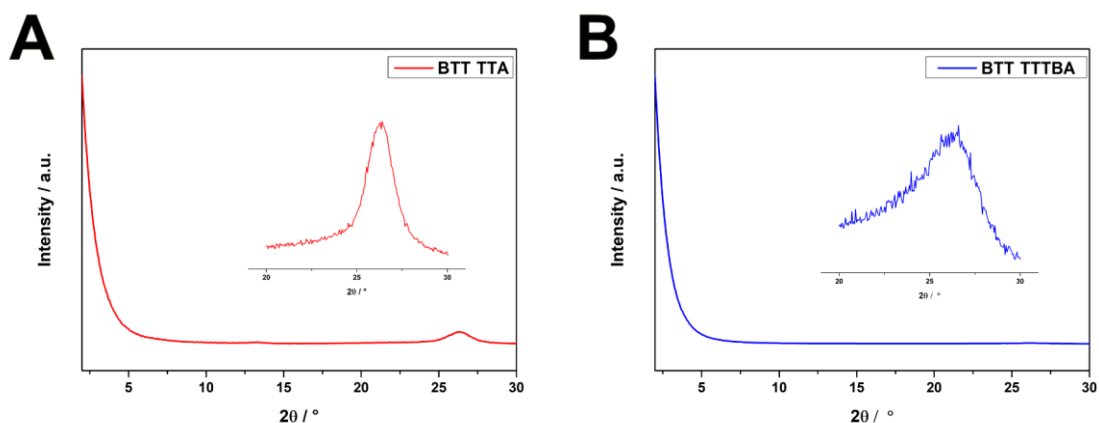


Figure 6.18. **A.** and **B.** depicting the XRD patterns of BTT TTA and BTT TTTBA films grown on gold substrates, indicating the high degree of crystal orientation. The strongest reflection in the respective pattern at about 26° is attributed to the interlayer distance of successive COF layers, these are shown as insets.

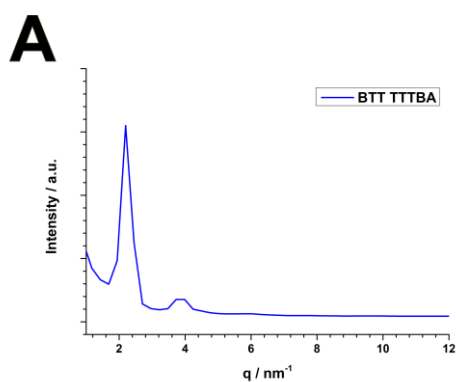


Figure 6.19. A. Data reduction plot of the obtained GIWAXS data for a BTT TTTBA thin film.

6.6.9 Photoluminescence Spectroscopy

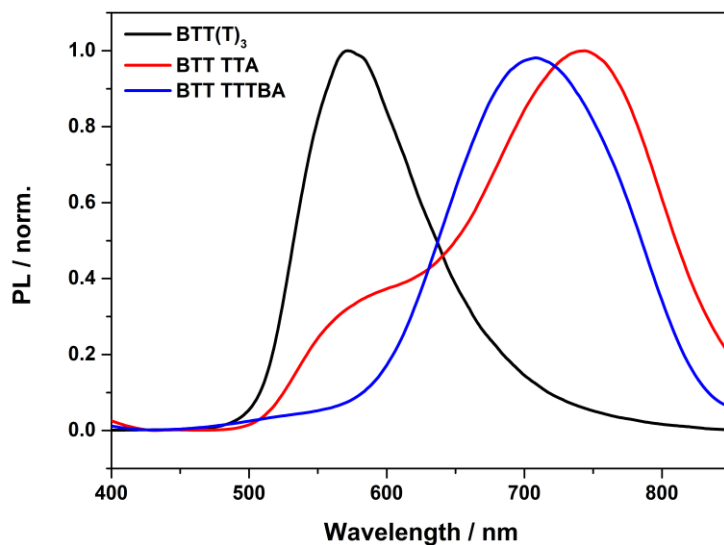


Figure 6.20. Photoluminescence spectra of the building block BTT(T)₃ (black) and the corresponding COFs BTT TTA (red) and BTT TTTBA (blue) in comparison.

6.6.10 Electrical Conductivity – Stability Measurements

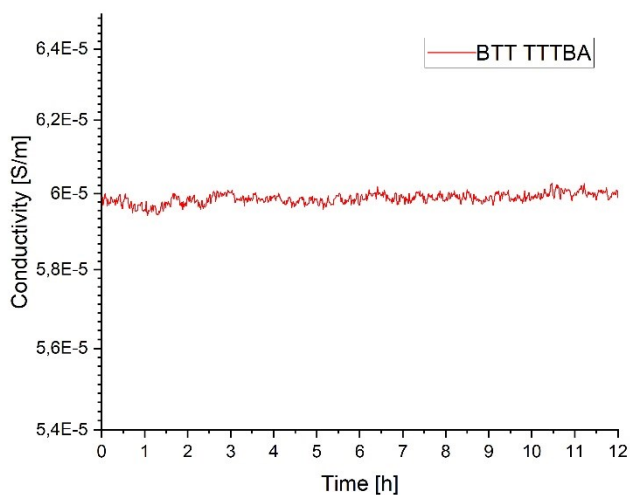


Figure 6.21. Conductivity stability measurement at room temperature of a 430 nm BTT TTTBA film with a constant source drain voltage of 10V for 12 hours.

6.6.11 Computational Simulations

A hexagonal simulation cell of dimensions $35.0 \times 35.0 \times 32.0$ Å was constructed for BTT TTTBA by stacking eight unit cells. The UFF force field with AM1 Coulson charges was used for the classical molecular-dynamics (MD) simulations. The system was prepared using slightly modified tools developed by Boyd et al.^{4,5} A cutoff of 12.5 Å was used for the nonbonding interactions; Coulomb interactions beyond this distance were treated using a particle–particle Ewald approach.⁶ The system was equilibrated for 1 ns and an additional 10 ns simulation using a Nosé–Hoover thermostat and barostat in the anisotropic NPT ensemble (1 fs time step, 298 K, 1 atm, 100 timesteps temperature damping, 10.000 timesteps pressure damping), using LAMMPS.^{7,8} A Snapshot taken at the end of the simulation was used for further processing.

Semiempirical molecular-orbital (MO) single-point calculations with periodic boundary conditions using the AM1 Hamiltonian within the restricted Hartree–Fock formalism were carried out using the cluster version of EMPIRE 20.^{9–12} The calculations were performed on the nearly hexagonal simulation cell of BTT TTTBA of dimensions $34.4 \times 34.1 \times 25.0$ Å consisting of 1,200 atoms. Three-dimensional local electron affinity and local-ionization energy maps were generated with EH5cube 20¹³ and stored in Gaussian cube-file format¹⁴ as orthogonal cells of $34.4 \times 59.1 \times 25.0$ Å.

Propagation of the hole- or electron density in imaginary time used an in-house program.¹⁵ Simulations of electron and hole charge-transport in the different Cartesian directions were performed on supercells of the electron affinity and local-ionization energy maps by applying a linear term describing a homogeneous electric field in the appropriate direction to the external potential, as described in reference 15.

The results were visualized using Vpster v1.19.1b¹⁶ and VMD 1.9.1.^{17,18}

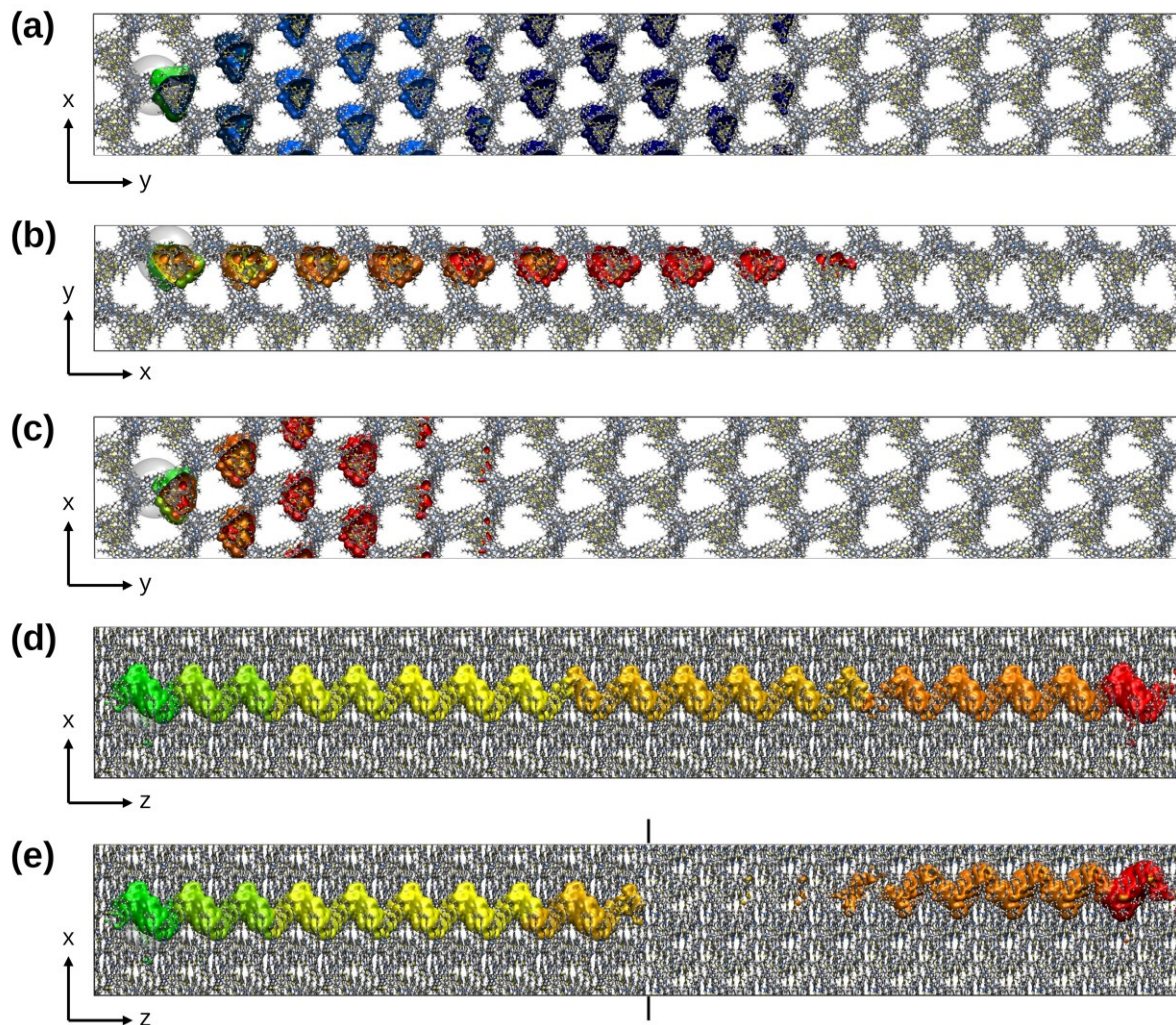
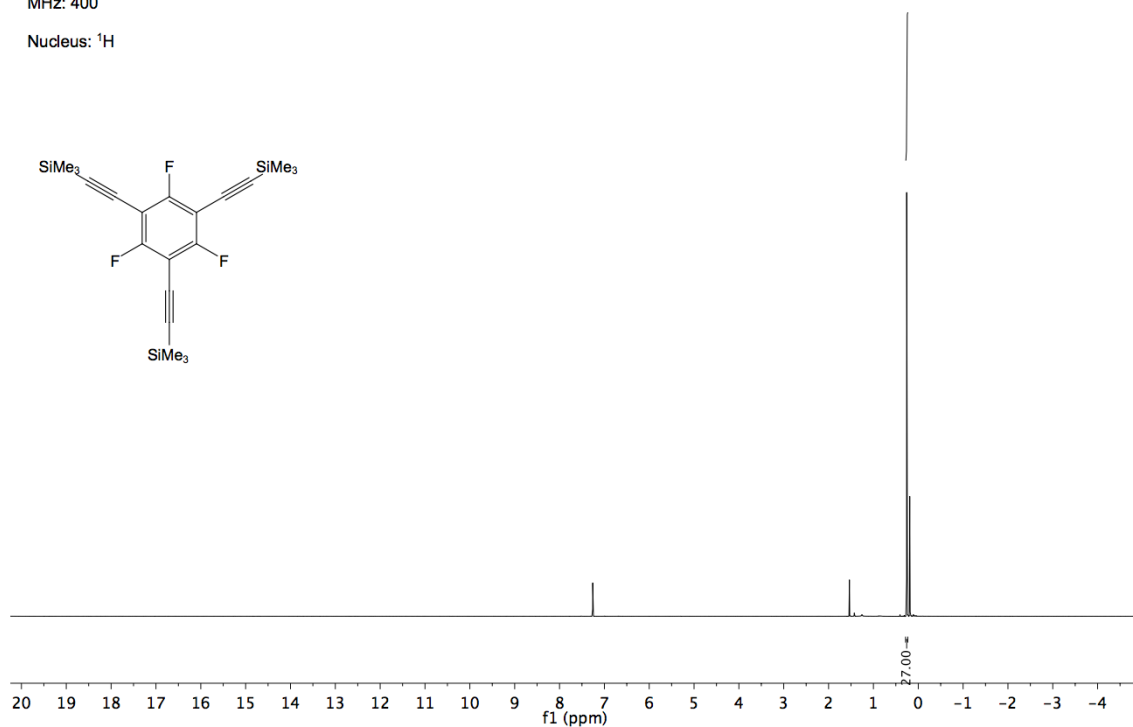


Figure 6.22. a. Calculated electron-transport paths for the BTT TTTBA in the Cartesian direction y . Calculated hole-transport paths for the BTT TTTBA COF in the three Cartesian directions x (b), y (c) and z (d). Isocontour plots for eight simulation steps of the hole (green to red; contour level = 1.2×10^{-5} e-Bohr $^{-3}$). The initial Gaussian functions are shown as transparent spheres. Calculated hole-transport path (e) in the Cartesian z direction for the displaced model structure of the BTT TTTBA. Isocontour plots for eight simulation steps of the electron (green to blue) and hole (green to red; contour level = 1.2×10^{-5} e-Bohr $^{-3}$).

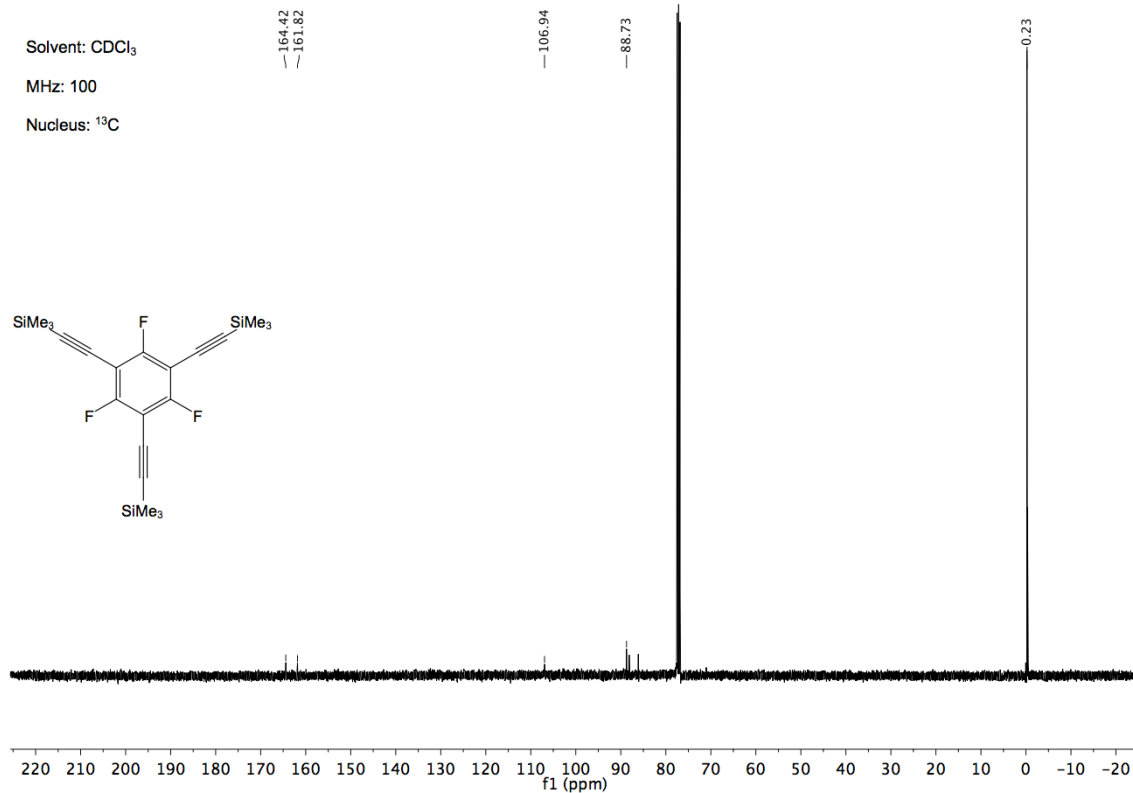
6.6.12 NMR Spectra

Solvent: CDCl₃

MHz: 400

Nucleus: ¹HSolvent: CDCl₃

MHz: 100

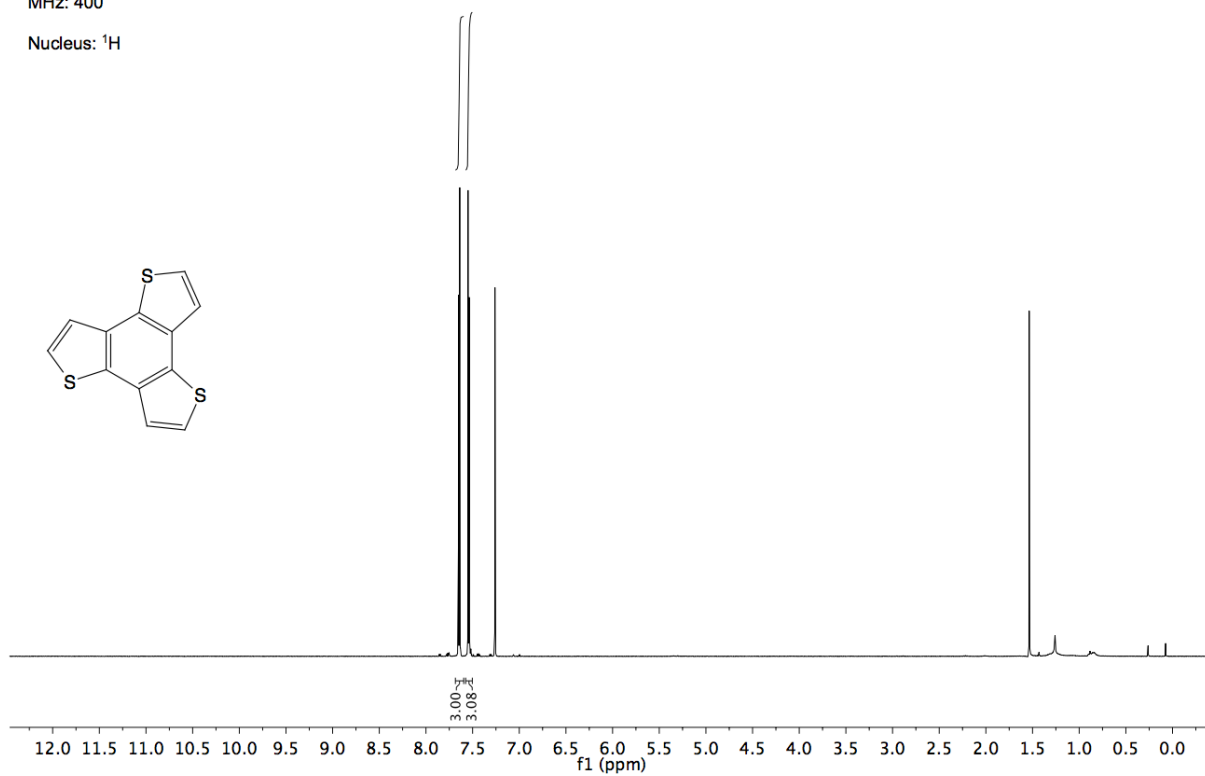
Nucleus: ¹³C

Benzotrithiophene COF Thin Films – Directional Electrical Conductivity

Solvent: CDCl_3

MHz: 400

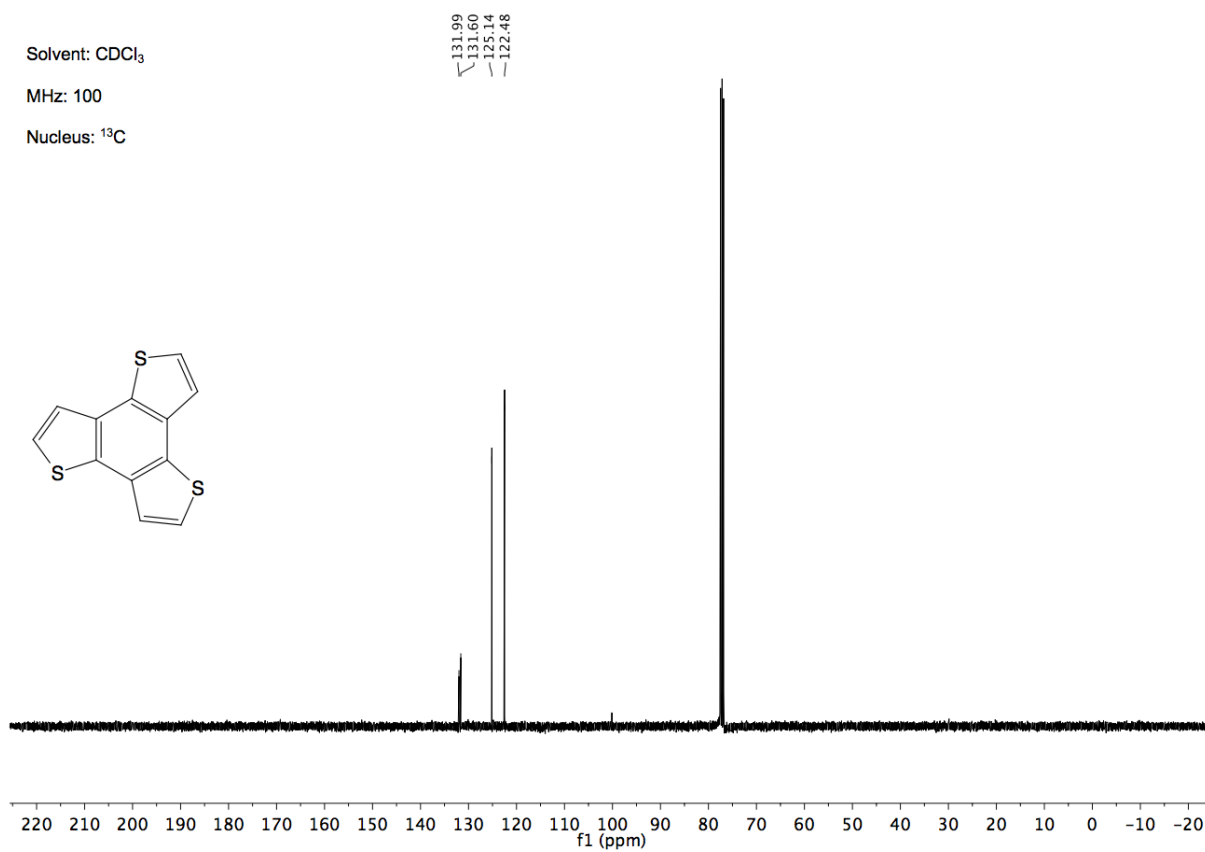
Nucleus: ^1H



Solvent: CDCl_3

MHz: 100

Nucleus: ^{13}C

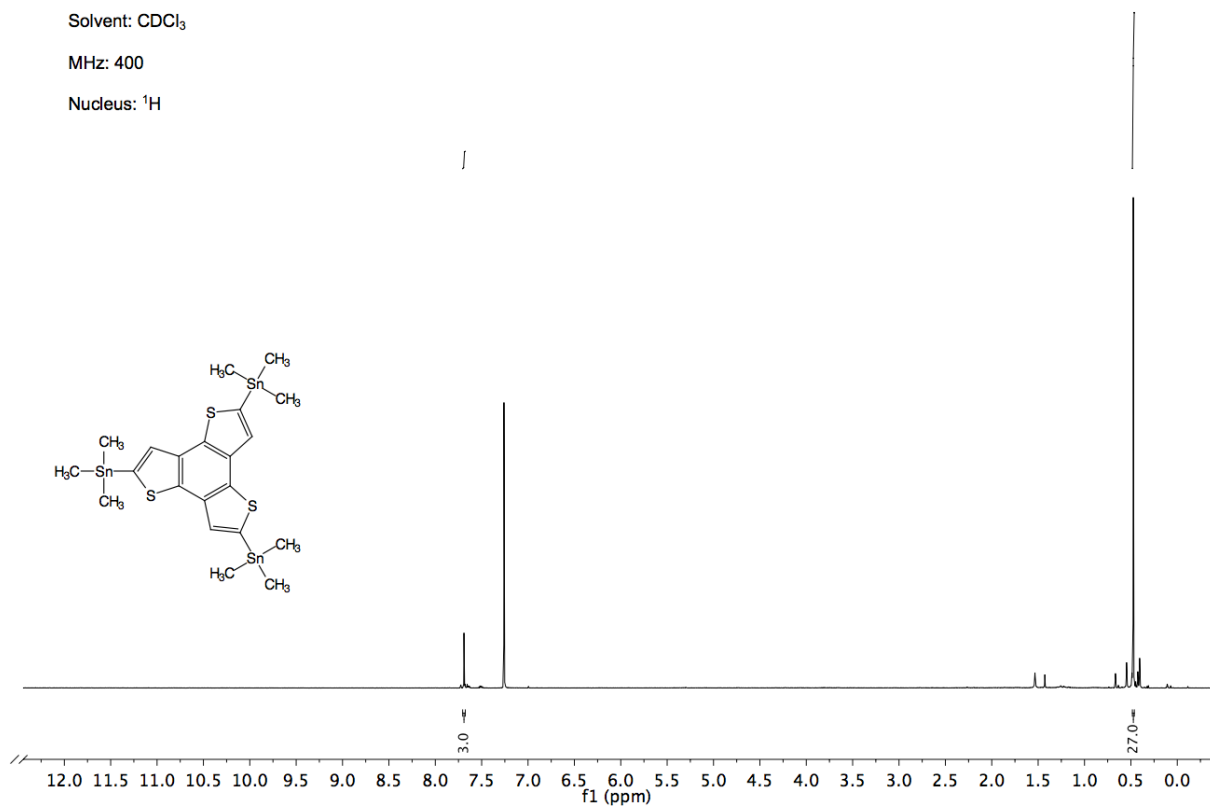


Benzotrithiophene COF Thin Films – Directional Electrical Conductivity

Solvent: CDCl₃

MHz: 400

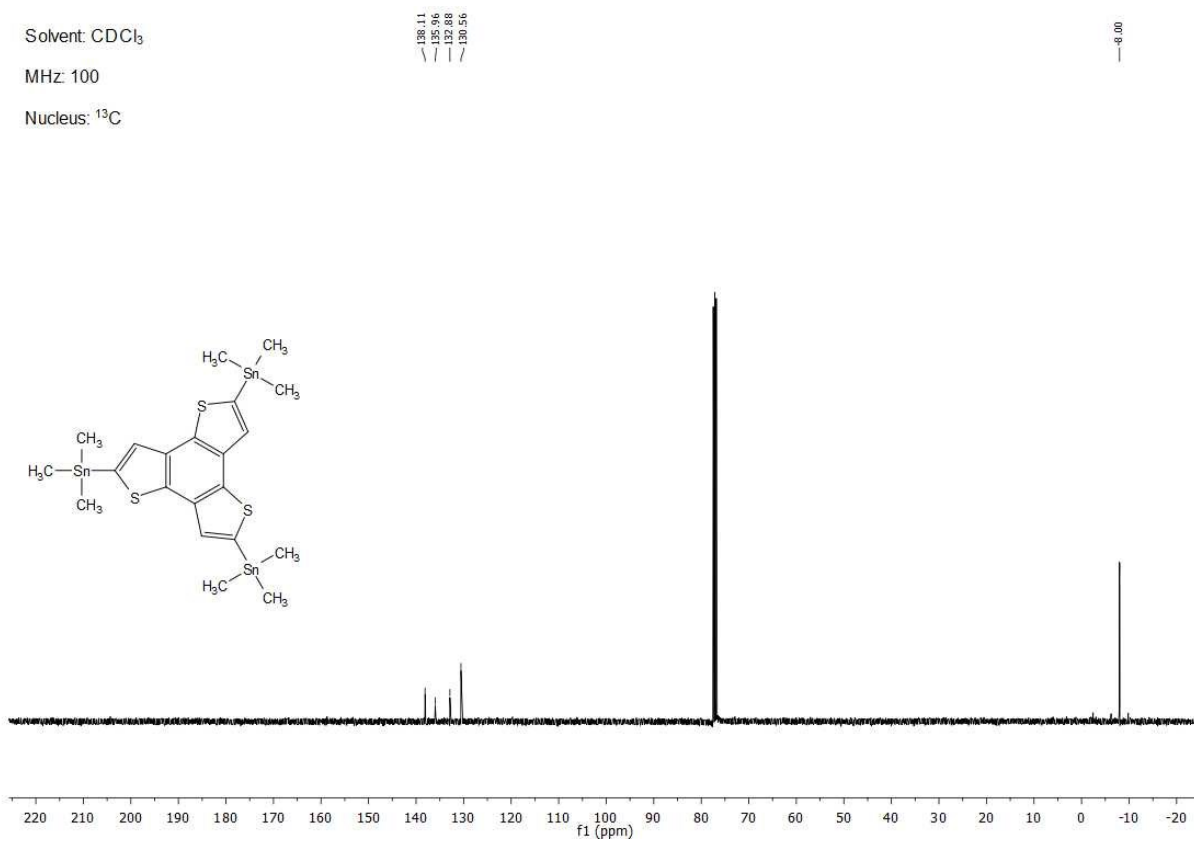
Nucleus: ¹H



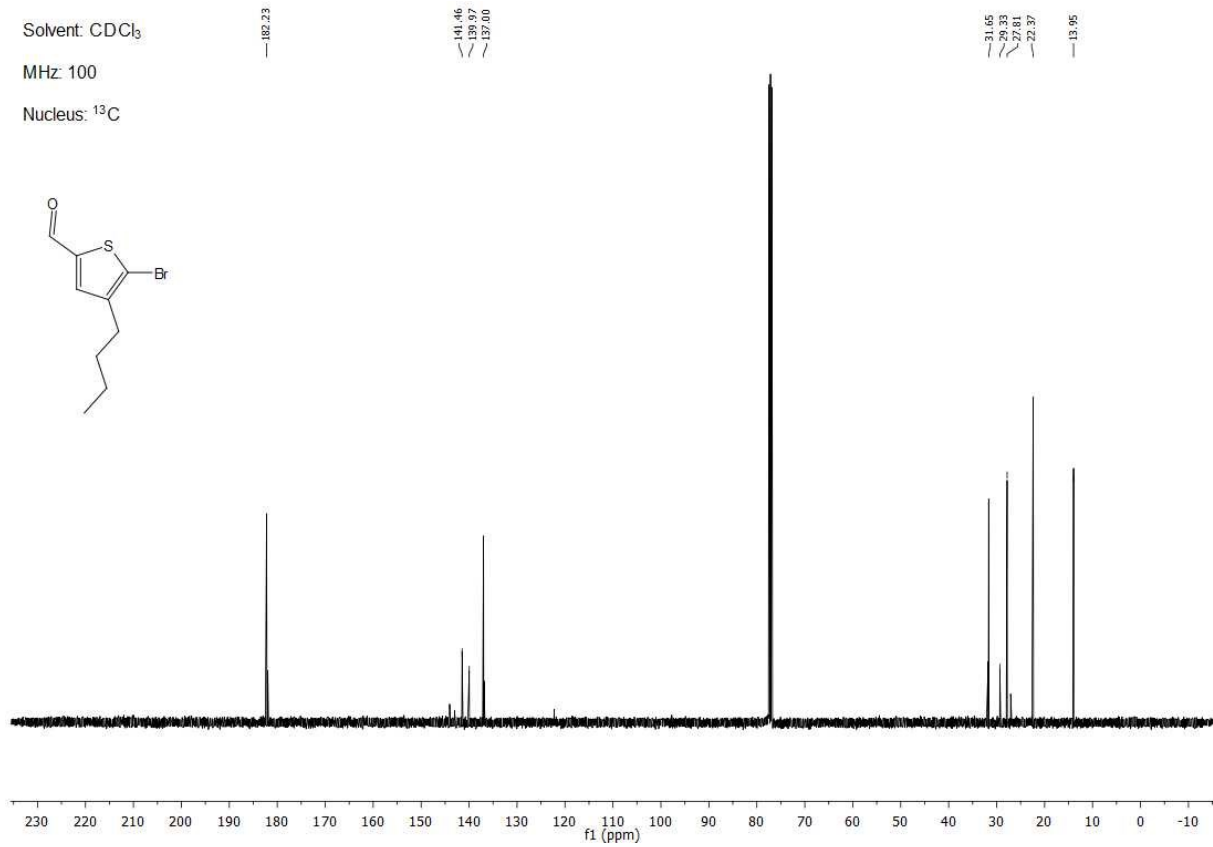
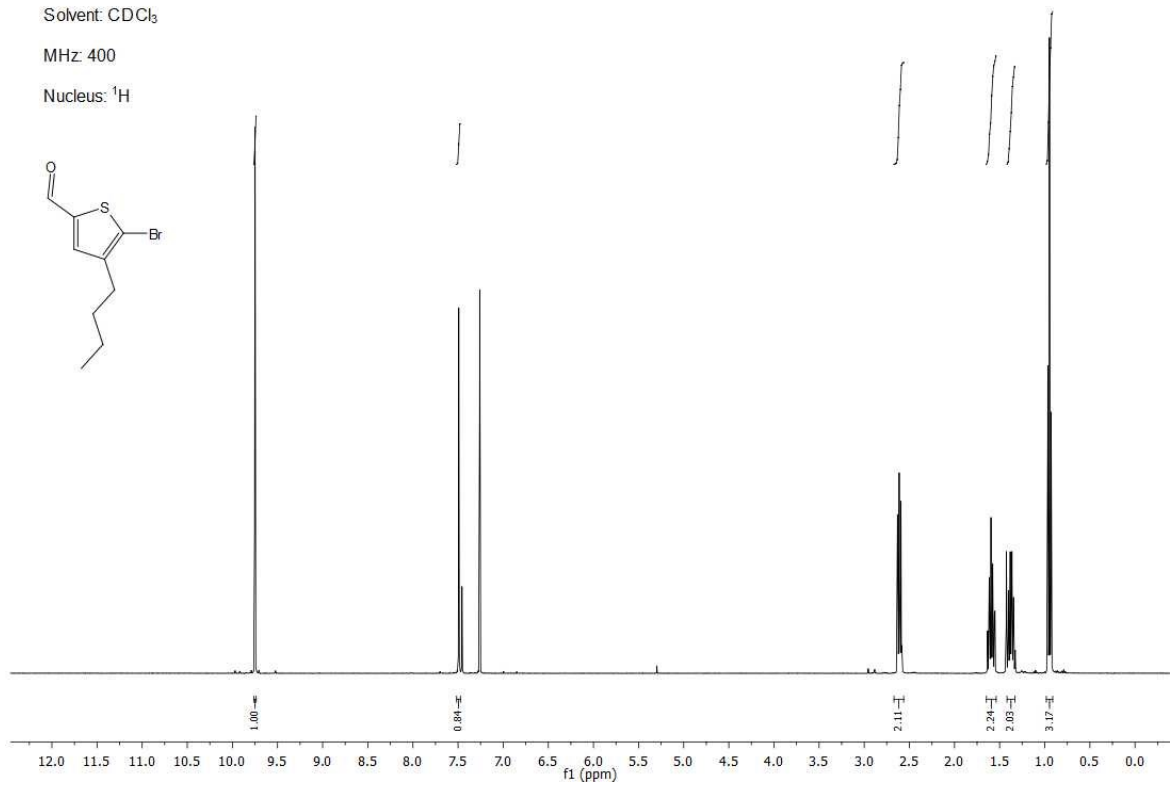
Solvent: CDCl₃

MHz: 100

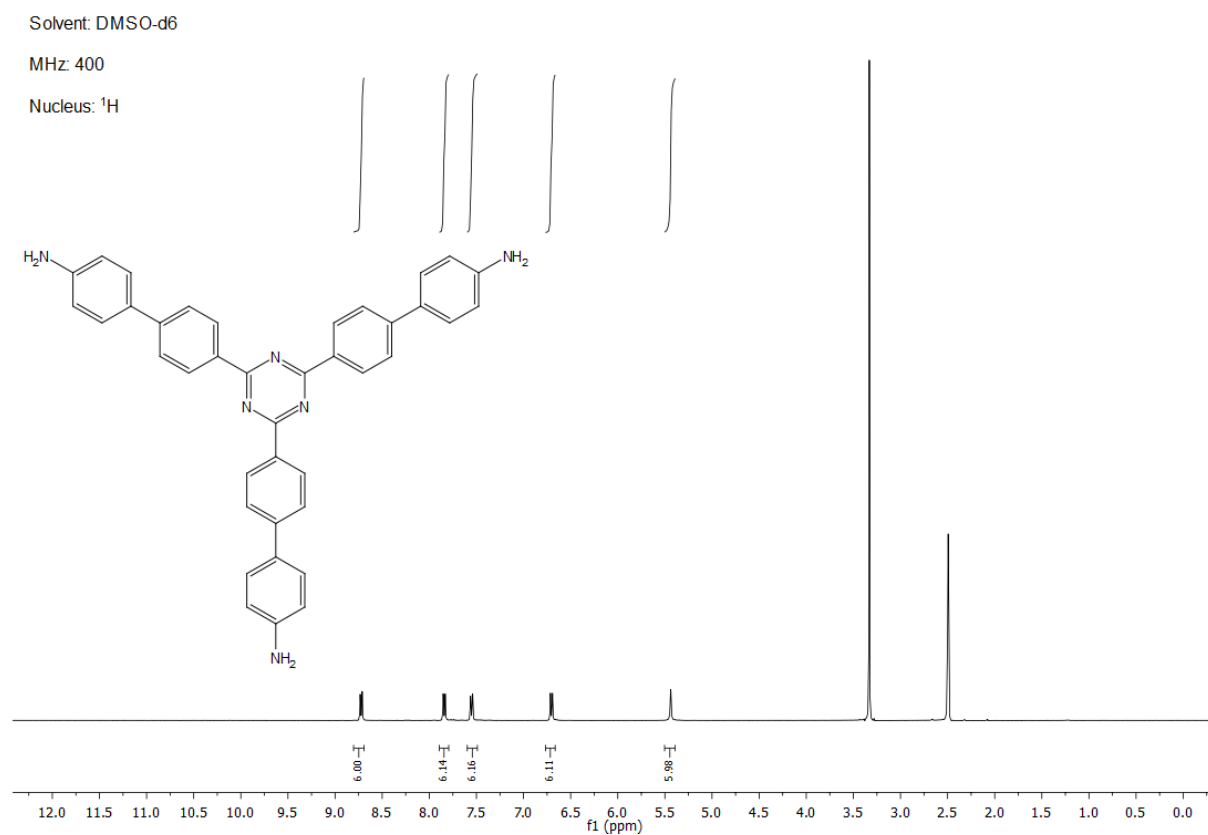
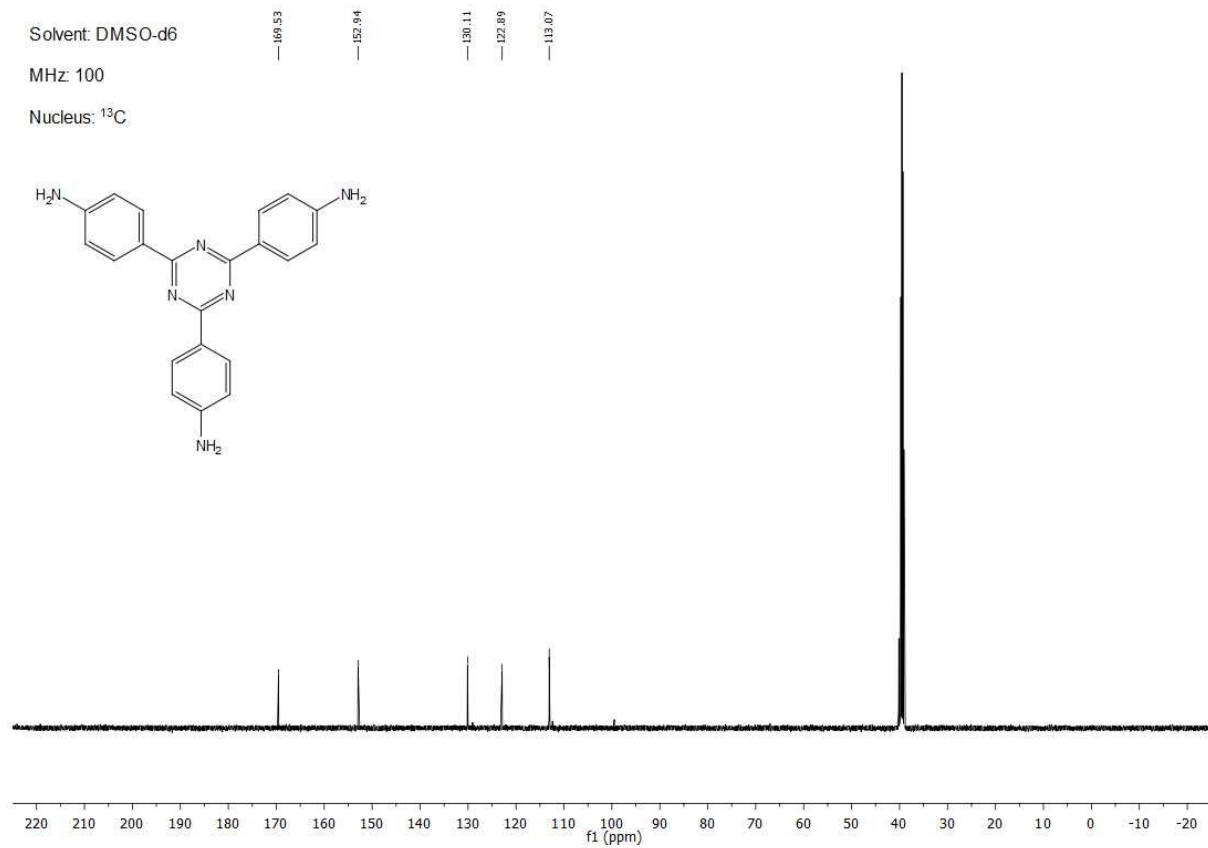
Nucleus: ¹³C

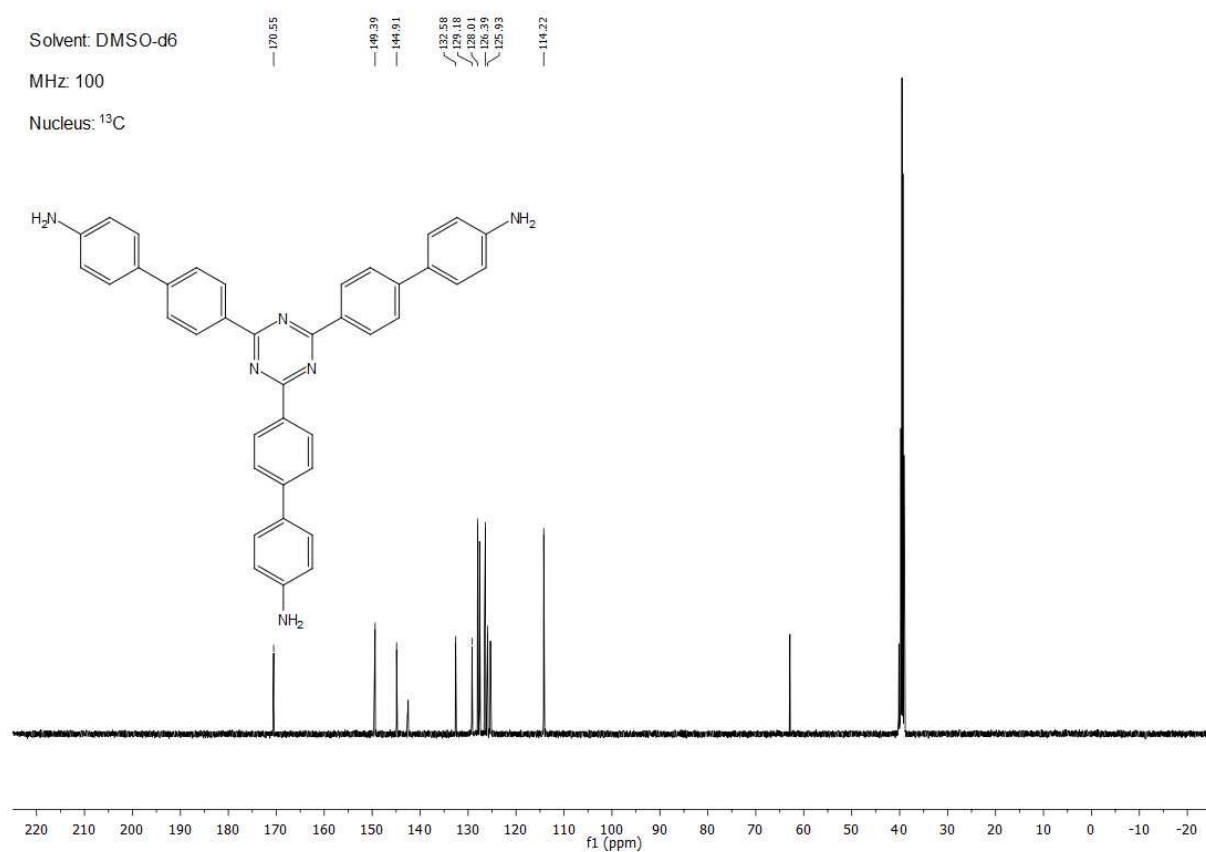


Benzotrithiophene COF Thin Films – Directional Electrical Conductivity



Benzotrithiophene COF Thin Films – Directional Electrical Conductivity





6.6.13 Solid-state NMR Spectra

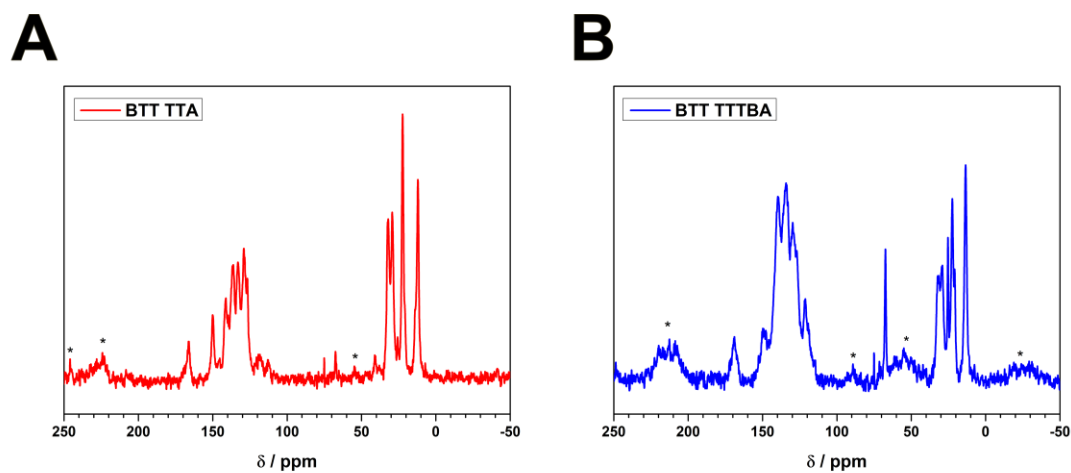


Figure 6.23. A. and B. Solid-state ^{13}C cross-polarization magic angle spinning (CP-MAS) NMR spectra of BTT TTA and BTT TTTBA, respectively. The absence of a peak corresponding to the aldehyde functions at around 190 ppm in combination with the peak at around 170 ppm corresponding to the formation of a C=N bond is in line with the formation of a framework. The well-defined peaks below 50 ppm can be attributed to the butyl chains of the BTT(T)₃ linker and the signals in the range of 150-100 ppm correspond to the aromatic framework.¹⁹ The signals marked with asterisks correspond to spinning sidebands.

6.6.14 References

- (1) Wenk, H. H.; Sander, W. Generation of Fluorinated m-Benzyne Derivatives in Neon Matrices. *Eur. J. Org. Chem.* **2002**, 2002, 3927–3935.
- (2) Rossi, S.; Bisello, A.; Cardena, R.; Orian, L.; Santi, S. Benzodithiophene and Benzotrithiophene as π Cores for Two- and Three-Blade Propeller-Shaped Ferrocenyl-Based Conjugated Systems. *Eur. J. Org. Chem.* **2017**, 2017, 5966–5974.
- (3) Liu, H.; Zhang, Z.; Huang, M.; Zhao, B.; Zhang, J.; Tan, S. A trilobal non-fullerene electron acceptor based on benzo[1,2-b:3,4-b':5,6-b''] trithiophene and perylene diimide for polymer solar cells. *Synth. Met.* **2017**, 227, 122–130.
- (4) https://github.com/peteboyd/lammps_interface. *LAMPPS Interface 0.2.2*.
- (5) Boyd, P. G.; Moosavi, S. M.; Witman, M.; Smit, B. Force-Field Prediction of Materials Properties in Metal-Organic Frameworks. *J. Phys. Chem. Lett.* **2017**, 8, 357–363.
- (6) Darden, T.; York, D.; Pedersen, L. Particle mesh Ewald: An $N \cdot \log(N)$ method for Ewald sums in large systems. *J. Chem. Phys.* **1993**, 98, 10089–10092.
- (7) <http://lammps.sandia.gov>. *LAMMPS version 12 Dec 2018*.
- (8) Plimpton, S. Fast Parallel Algorithms for Short-Range Molecular Dynamics. *J. Comput. Phys.* **1995**, 117, 1–19.
- (9) <http://ceposinsilico.de/products/empire.htm>. *EMPIRE 20, Cepas InSilico GmbH Obermichelbach*.
- (10) Hennemann, M.; Clark, T. EMPIRE: a highly parallel semiempirical molecular orbital program: 1: self-consistent field calculations. *J. Mol. Model.* **2014**, 20, 2331.
- (11) Margraf, J. T.; Hennemann, M.; Clark, T. EMPIRE: a highly parallel semiempirical molecular orbital program: 3: Born-Oppenheimer molecular dynamics. *J. Mol. Model.* **2020**, 26, 43.
- (12) Margraf, J. T.; Hennemann, M.; Meyer, B.; Clark, T. EMPIRE: a highly parallel semiempirical molecular orbital program: 2: periodic boundary conditions. *J. Mol. Model.* **2015**, 21, 144.
- (13) <http://ceposinsilico.de/products/empire.htm>. *EH5cube 20, Cepas InSilico GmbH Obermichelbach*.
- (14) <https://gaussian.com/cubegen/> (accessed March 10, 2022).
- (15) Kriebel, M.; Sharapa, D.; Clark, T. Charge Transport in Organic Materials: Norm-Conserving Imaginary Time Propagation with Local Ionization Energy as the External Potential. *J. Chem. Theory Comput.* **2017**, 13, 6308–6316.
- (16) S. Gsänger, <http://github.com/sgsaenger/vipster>, <https://sgsaenger.github.io/vipster/index.html>. *Vipster 1.19.1b*.
- (17) <http://www.ks.uiuc.edu/Research/vmd/>. *VMD 1.9.1*.
- (18) Humphrey, W.; Dalke, A.; Schulten, K. VMD: visual molecular dynamics. *J. Mol. Graphics* **1996**, 14, 33–8, 27–8.

7. Conclusion

This thesis was focused on the development of new synthetic tools for the construction of tailor-made two-dimensional COFs, with the overarching goal to encode optoelectronic characteristics and induce charge carrier transport in crystalline organic matter. To achieve this goal, a confluence of several disciplines in chemistry ranging from organic chemistry to material science is required. Hereby, in this thesis, several of these aspects are addressed. Particularly, the development of diverse synthesis approaches to chemically modify COF powders and films while maintaining the key properties of framework materials, namely high order and surface area. Thereby, COFs of different linkage motifs ranging from boronate ester-based (chapter 3 and 4), imine-linked (chapter 6) to vinylene-linked COFs (chapter 5) are studied as platforms to accommodate photoactive or semi-conductive building blocks. These COFs were designed to display nitrogen-rich and thiophene-containing building units. For the latter, prominently, a novel star-shaped building block consisting of six thiophene units based on a benzotrithiophene core is presented. In combination with nitrogen-rich counterparts, BTT-COFs are obtained as highly crystalline powder and films and their charge-carrier transport was examined.

In the first two chapters, (chapter 3 and 4) different synthetic strategies (post-synthetic modification and three-component one-pot modification) are developed to include large area fused aromatic building blocks in COFs, namely pyrene-fused azaacenes. The impact of the systematic alteration of the frameworks 'chemical nature i.e., the extension of the π -system, on the optical properties of the resulting COFs was studied. Thereby, in chapter 3 a simple, catalyst-free cyclocondensation PSM synthesis for reactive boronic-ester-based COFs to form pyrene-fused azaacene moieties is presented. Hereby, Dione-COF serving as precursor has been modified using linear amines, i.e. *o*-phenylenediamine (Ph) and 2,3-diaminonaphthalene (Naph), to give two COFs termed Dione-Ph-COF and Dione-Naph-COF. Through a PSM scheme, dione moieties, an integral part of the COF constructing pyrene dione building block, are modified in up to 33% yield to form the corresponding azaacene while crystallinity and porosity of the pristine Dione-COF are maintained. A subsequent and systematic alteration of the light absorption properties was evidenced in the UV-vis spectra where COFs bearing elongated azaacenes show a red-shift of the absorption onsets for Dione-Ph-COF and Dione-Naph-COF compared to the pristine Dione-COF. Interestingly, the Dione-COF series is PL-inactive. This is attributed to an internal charge transfer between pyrene-dione building block or derivatives and HHTP evidenced by the PL quenching of pyrene dione building block in a solid mixture with HHTP.

In chapter 3 a PSM approach resulted in COFs consisting of a mixture of pyrene dione moieties and converted pyrene azaacenes. To boost the reaction yield and to obtain COFs with a uniform chemical characteristic, a novel one-pot, three-component methodology for the functionalization of covalent organic framework bulk and films was discovered. Here, small-sized building components are included

in the reaction mixture which react exclusively at particular sites to form large building blocks and frameworks at a similar time frame. Using the well-known di-boronic acid pyrene dione, linear amines and catechol building blocks, COFs exclusively built up from pyrene azaacenes corresponding to a 100 % conversion yield of dione moieties, termed Aza-COFs, are formed. Upon the inclusion of diamines in the reaction mixture, an extension of the aromatic system of the pyrene dione building block is obtained, where aromatization is considered to be one of the driving forces for diamines to react exclusively with diones in the three-component reaction. Strikingly, this methodology is suitable to construct the fragile boronate-ester based COFs, where catechols and boronic acids react undisturbed despite the presence of strong competing amine nucleophiles. The way COF building blocks interact between successive layers is one of the most urgent matters to achieve a fundamental understanding of charge dynamics. Here, the pyrene dione building block yields asymmetric pyrene azaacenes where fully overlapped or anti parallel stacking scenarios are considered. Powder X-ray diffraction analysis of the obtained COF implies that Aza-COFs comprise mainly antiparallel aligned pyrene azaacenes in the successive layers. Furthermore, the newly developed methodology was applied for thin film synthesis where oriented and crystalline Aza COF thin films are obtained by the one-pot three-component synthesis. The photophysical properties of the resulting Aza-COFs were determined. In line with the extension of the π -conjugation, for Aza-2Ph- to Aza-Ph- and Aza-Naph-COF a gradual red-shift of the absorption maximum is evident. This approach is an important addition to the toolkit of COF bulk and film synthesis methodologies.

Switching from boronate-ester-linked COFs to vinylene-linked COFs, in chapter 5 we showed the synthesis of two novel highly crystalline thiophene-based vinylene-linked COF structures, namely TMT BDTOEt and TMT BDTOPr, which were formed *via* base-catalyzed Knoevenagel condensation reaction upon combination of trimethyl-triazine (TMT) and different functionalized benzodithiophene (BDT) aldehydes. To date, the synthesis of new vinylene-linked COF structures with control over crystallinity and porosity is a great challenge mainly due to the poor reversibility of the employed condensation reactions. Even though the elementary construction principles of vinylene-linked COFs have been illustrated in literature, the development of synthesis approaches and optimizing reactions conditions under which ordered vinylene-linked COFs are obtained are highly desired targets. In this chapter, for the first time, vinylene-linked COFs are formed in high crystallinity and porosity under conditions that differ from the common solvothermal conditions. Here, the VAC-method was employed to form vinylene-linked COF deposits with good control over thickness and crystallinity. Thereby, different reaction conditions such as temperature, reaction time and solvent vapor sources were assessed and their influence on the film crystallinity was probed using X-ray diffraction analysis. The new COF structures emerge even under mild reaction conditions, such as 40 °C or short reaction times of only 30 minutes. Further, these vinylene-linked COFs feature interesting photophysical properties. They feature light absorption in the 300-610 nm wavelength range and direct band gaps of 2.0 eV. Photoluminescence (PL)

spectroscopy revealed strong photon emission at 690 nm for both COFs which could be largely blue-shifted up to 480 nm upon interaction with different solvents such as water or ethanol, possibly resulting from a solvatochromic effect. Moreover, after addition of the solvents the lifetimes for the largest contributions drastically changed from 0.69 ns (58%) to 8.16 ns (63%) and 9.97 ns (87%) upon interaction with ethanol and water, respectively.

The last section of this thesis (chapter 6) dealt with charge carrier migration in COFs. Here, we developed the synthesis of a novel star-shape thiophene-extended BTT-based tricarbaldehyde. In combination with different tridentate triazine-based amines we were able to synthesize two novel highly crystalline, porous and imine-linked COF structures, namely BTT TTA and BTT TTTBA. To study their transport properties, the frameworks were successfully grown on different substrates using the *in situ* approach as electroactive, highly oriented thin films and room-temperature in-plane conductivities of up to 10^{-4} S m⁻¹ were measured. Temperature dependent electrical conductivity measurements revealed a temperature dependence indicative of trap-dominated hopping type charge transport. All in all, with our measurements we could see a strongly directional, defect-dominated charge transport in the BTT COF films, with a strong preference for the in-plane direction within the conjugated 2D planes over the out-of-plane direction. Quantum mechanical calculations predict a hopping type charge transport in the 2D molecular planes, and molecular COF columns perpendicular to the in-plane direction to provide a continuous path. Imposing a grain boundary in the form of a rotated COF layer dramatically hampered charge transport in this direction. This study emphasizes the role of defects in the conductivity of COF materials and particularly for the BTT COFs presented, where the electrical conductivity values obtained for the latter represent the lower limit and are expected to further improve through defect-controlled synthesis strategies.

In conclusion, this thesis has been focused on the development of synthetic strategies to tailor photophysical properties of covalent organic frameworks as well as the generation of novel covalent organic frameworks featuring different linkage motifs. Different methods have been shown to yield COFs with tailor-made optical properties such as a post-synthetic modification approach, and a three-component synthesis approach. Further, COFs were developed featuring interesting optical properties upon interaction of the COFs with different solvents. In addition to the characterization of the optical properties, the electrical properties of the COFs were of particular interest.

8. Appendix

8.1 Curriculum Vitae

Name: Laura Frey

Date of birth/-place: 29th of November, 1993/ Ingolstadt, Germany

Education

03.2019 – today	Ludwig Maximilians University of Munich, Munich, Germany - PhD in physical chemistry, Prof. Bein
10.2016 – 01.2019	Ludwig Maximilians University of Munich, Munich, Germany - M.Sc. Chemistry - Main subjects: Physical and organic chemistry - Minor subject: Informatics - Master thesis: “Design and synthesis of extended star-shape benzotrithiophene-based linkers for Covalent Organic Frameworks”
04.2017 – 09.2017	Merck Schuchardt OHG, Hohenbrunn, Germany - Student trainee - Topics: Development of a site-wide concept for the evaluation of safety hazards; implementation of site-wide risk assessments
08.2016 – 12.2016	University of Glasgow, Glasgow, Scotland - Physical chemistry internship - Group of M. Kadodwala
03.2016 – 05.2016	Ludwig Maximilians University of Munich, Munich, Germany - Research assistant in organic chemistry, Magauer group - Topic: De novo construction of substituted indoles
10.2012 – 10.2016	Ludwig Maximilians University of Munich, Munich, Germany - B.Sc. Chemistry and biochemistry - Bachelor thesis: “Conformational cycle of the Hsp70 chaperone BiP”

09.2004 – 06.2012 **Gymnasium Beilngries, Beilngries, Germany**
- Abitur

8.2 Publications

1. *Boronic-acid-derived covalent organic frameworks: from synthesis to applications*

Laura Frey,^{‡a} Jenni J. Jarju,^{‡b} Laura M. Salonen^{*b} and Dana M. Medina^{*a}

Published as: Laura Frey,^{‡a} Jenni J. Jarju,^{‡b} Laura M. Salonen^{*b} and Dana M. Medina^{*a}, *New J. Chem.*, **2021**, *45*, pp 14879-14907.

2. *A post-synthetic modification strategy for the synthesis of pyrene-fused azaacene covalent organic frameworks*

Soraia P. S. Fernandes,^{‡[a,b]} **Laura Frey**,^{‡[c]} Krystal M. Cid-Seara,^[a,d] Orlando Oliveira,^[a] Noelia Guldris,^[a] Enrique Carbó-Argibay,^[a] Carlos Rodríguez-Abreu,^[c] Yury V. Kolen'ko,^[a] Artur M. S. Silva,^[b] Dana D. Medina,^{*[c]} and Laura M. Salonen^{*[a]}

Published as: S. P.S. Fernandes, L. Frey, K. M. Cid-Seara, O. Oliveira, N. Guldris, E. Carbó-Argibay, C. Rodríguez-Abreu, Y. V. Kolen'ko, A. M.S. Silva, D. D. Medina et al., *Micropor. Mesopor. Mat.* **2022**, 112162.

3. *Oriented Thiophene-Extended Benzotrithiophene Covalent Organic Framework Thin Films – Directional Electrical Conductivity*

Laura Frey,^{†‡} Jonas F. Pöhls,[‡] Matthias Hennemann,¹ Andre Mähringer,[†] Stephan Reuter,[†] Timothy Clark,^{1*} R. Thomas Weitz,^{‡1*} Dana D. Medina^{†*}

Published as: Frey, L., Pöhls, J. F., Hennemann, M., Mähringer, A., Reuter, S., Clark, T., Weitz, R. T., Medina, D. D., Oriented Thiophene-Extended Benzotrithiophene Covalent Organic Framework Thin Films: Directional Electrical Conductivity. *Adv. Funct. Mater.* **2022**, 2205949.

4. *Building Blocks and COFs formed in chorus – Three-Component Synthesis of Pyrene-Fused Azaacene Covalent Organic Framework Bulk and Films*

Laura Frey,^{‡[a]} Orlando Oliveira,^{‡[b]} Soraia P. S. Fernandes,^[b,c] Krystal M. Cid-Seara,^[b,d] Roman Guntermann,^[a] Laura M. Salonen^{*[b,e]} and Dana D. Medina^{*[a]}

Manuscript in preparation.

5. *Isomer-Change Induced Modification of Photophysical Properties of Thienothiophene-based Covalent Organic Frameworks*

Laura Frey,^{†‡} Roman Guntermann,^{†‡} Thomas Bein,^{†*} Dana D. Medina^{†*}

Manuscript in preparation.

6. *Thiophene-Based Vinylene-Linked Covalent Organic Framework Films*

Laura Frey,[†] Alexander Biewald,[†] Roman Guntermann,[†] Achim Hartschuh,[†] Dana D. Medina^{†*}

Manuscript in preparation.

7. *Synthetic Strategy for Metallophthalocyanine Covalent Organic Frameworks for Electrochemical Water Oxidation*

Jenni J. Jarju; Aida M. Díez; **Laura Frey**; Viviana Sousa; Enrique Carbó-Argibay; Dana D. Medina; Oleg I. Lebedev; Laura M. Salonen, Yury V. Kolen'ko*

Published as: J.J. Jarju, A.M. Díez, L. Frey, V. Sousa, E. Carbó-Argibay, L.P.L. Gonçalves, D.D. Medina, O.I. Lebedev, Yu.V. Kolen'ko and L.M. Salonen, *Materials Today Chemistry*, **2022**, 26, pp 101032.

8. *A cubic coronene-based MOF*

Patricia I. Scheurle,^{†‡} **Laura Frey**,^{†‡} Marina Schönherr,^{†‡} Markus Döblinger,[†] Marta-Martínez-Abadía,¹ Andre Mähringer,[†] Lena Harms,¹ Gunter Wittstock,¹ Aurelio Mateo-Alonso,¹ Thomas Bein,[†] Dana D. Medina^{†*}

Manuscript in preparation.

[‡]These authors contributed equally.

8.3 Conference Contributions

1. Alkoxy-Functionalized Wurster-Type Covalent Organic Frameworks
Nanosystems Initiative Munich (NIM) summer retreat 2019, Seon, Germany
2. Alkoxy-Functionalized Wurster-Type Covalent Organic Frameworks
Center of NanoScience (CeNS) workshop 2019, Venice, Italy.
3. A post-synthetic modification strategy for the synthesis of pyrene-fused azaacene covalent organic frameworks
Deutsche Zeolith Tagung (DZT) 2022, Frankfurt, Germany.
4. A post-synthetic modification strategy for the synthesis of pyrene-fused azaacene covalent organic frameworks
International Conference on Metal-Organic Frameworks (MOF) 2022, Dresden, Germany